



Terms and Conditions of Use of Digitised Theses from Trinity College Library Dublin

Copyright statement

All material supplied by Trinity College Library is protected by copyright (under the Copyright and Related Rights Act, 2000 as amended) and other relevant Intellectual Property Rights. By accessing and using a Digitised Thesis from Trinity College Library you acknowledge that all Intellectual Property Rights in any Works supplied are the sole and exclusive property of the copyright and/or other IPR holder. Specific copyright holders may not be explicitly identified. Use of materials from other sources within a thesis should not be construed as a claim over them.

A non-exclusive, non-transferable licence is hereby granted to those using or reproducing, in whole or in part, the material for valid purposes, providing the copyright owners are acknowledged using the normal conventions. Where specific permission to use material is required, this is identified and such permission must be sought from the copyright holder or agency cited.

Liability statement

By using a Digitised Thesis, I accept that Trinity College Dublin bears no legal responsibility for the accuracy, legality or comprehensiveness of materials contained within the thesis, and that Trinity College Dublin accepts no liability for indirect, consequential, or incidental, damages or losses arising from use of the thesis for whatever reason. Information located in a thesis may be subject to specific use constraints, details of which may not be explicitly described. It is the responsibility of potential and actual users to be aware of such constraints and to abide by them. By making use of material from a digitised thesis, you accept these copyright and disclaimer provisions. Where it is brought to the attention of Trinity College Library that there may be a breach of copyright or other restraint, it is the policy to withdraw or take down access to a thesis while the issue is being resolved.

Access Agreement

By using a Digitised Thesis from Trinity College Library you are bound by the following Terms & Conditions. Please read them carefully.

I have read and I understand the following statement: All material supplied via a Digitised Thesis from Trinity College Library is protected by copyright and other intellectual property rights, and duplication or sale of all or part of any of a thesis is not permitted, except that material may be duplicated by you for your research use or for educational purposes in electronic or print form providing the copyright owners are acknowledged using the normal conventions. You must obtain permission for any other use. Electronic or print copies may not be offered, whether for sale or otherwise to anyone. This copy has been supplied on the understanding that it is copyright material and that no quotation from the thesis may be published without proper acknowledgement.

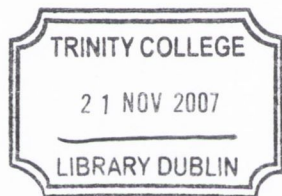
Implications of antiphase boundaries
(APBs) on the strain relaxation and
magnetotransport properties of Fe_3O_4
hetero-epitaxial thin films

A thesis submitted to the University of Dublin, Trinity College,
in application for the degree of Doctor of Philosophy

by

R.G. Sumesh Sofin

School of Physics
Trinity College Dublin
October 2006



THESIS
8224

Dedicated to

My father R.G. Pillai and mother Sobhana Kumari

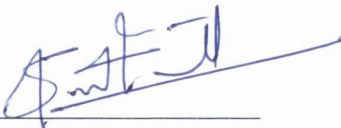
Declaration

This thesis is submitted by the under signed for the degree of Doctor in Philosophy at the University of Dublin.

It has not been submitted as an exercise for a degree at any other university.

Apart from the advice, assistance and joint effort mentioned in the acknowledgements and in the text, this thesis is entirely my own work.

I agree that the library may lend or copy this thesis freely on request.

A handwritten signature in blue ink, appearing to read 'R. G. Sumesh Sofin', is written over a horizontal line.

R. G. Sumesh Sofin

October 2006

Acknowledgments

It was a fine morning in July 2000, when I joined in the Physics department of University of Pune as a Junior research fellow, my supervisor Prof. R.C. Aiyer handed over me a thesis to read. When I was just leafing through the thesis, I was actually dreaming about the day I would write a thesis for my Ph.D. Well! finally, the day has come and I am feeling immense happiness and gratitude towards those who helped me to accomplish my dream.

First I would like to thank my supervisor Prof. Igor Shvets for giving me an opportunity to work in his group. He gave me timely advice and apt suggestions during the entire course of this study. I am indebted to him in my whole life for his constant support and encouragement.

I am grateful to Dr. Sunil K Arora, who co-supervised the entire work and trained me to perform all of the experimental techniques used in this work. I benefited a lot from his years of research experience and in depth knowledge in the subject. Without his critical reading and suggestions this thesis would not have been in this form. I am thankful to Mrs. Happy Arora for the support and encouragement.

I am thankful to Dr Martina Luysberg, Institut für Festkörperforschung, Forschungszentrum Jülich GmbH, D-52425 Jülich, Germany, for the TEM measurements. I am very much thankful to Dr. M Venkitesan, Magnetism and Spin-electronics group Trinity College, for the SQUID measurements and for clearing doubts in magnetism, timely help and advices. I am very much thankful to Mr. Han Chun for doing some of the experiments to reconfirm the results and teaching me how to count in Chinese language. My sincere thanks to Dr. Sivakumar Balakrishnan, School of Chemistry, Trinity College for his help during the Raman measurements. I am very much indebted to him for

treating me like his own brother and for his great help and support during my stay in Ireland.

I am obliged to Mr Ciaran McEvoy for the critical reading of this thesis and all of our research papers. I will always remember the days we spent in the noisy MBE room. I am thankful to Mr. Barry Heffernan for reading my thesis and giving valuable suggestions. I would like to thank Miss. Marie Kinsella for doing all the administrative work in time and for her kind support. I am thankful to Mr. Floriano Cuccureddu for his support and timely jokes which made life very refreshing. I would like to extend my special thanks to him for the Italian lessons with a complete set of hand signs and the hot discussions which gave me lot of insight in to diverse fields like science, movies, philosophy, art and culture. Thanks to Mr. Rafael Ramos for the scientific discussions on AMR research papers and arranging coffee breaks. Thanks to Mrs. Aldara Rico for her kind support and delicious Spanish cuisines. I would like to thank little Noa for bringing joyful moments in our hectic life with her occasional visits to the college. I am thankful to Dr. Shane Murphy for his timely advice and help, Dr. Guido Mariotto for his good company and especially for the barbeque, Dr. Roman Kantor for clarifying the problems with electronics, Dr Giuseppe Manai for the nice company, helping to sort out problems labview programmes, and showing me the jewel in the crown, Dr. Ken Jordan for his help and support, Dr Sergio Ceballos for his sincere advice and help, Mr. Kevin Radican for his good company and sorting problems with labview programming, Dr Jin Xuesong and Dr Yang Zhou for the help they provided during the experiments, Dr. Maina Karzenova for the discussion on XRD measurements, Dr. Alex Cazacu for his support and discussion on art and science, Mr. Anthony M^cCoy for his support and for proof reading the research papers. I would like to thank Mr. Barry Laffoy and Miss. Louise McGuigan and Mr. Chris Smith for their support and help.

Special thanks to Miss. Julie Jacob from Surface Science group, Trinity College for her support and encouragement. I will always remember the help she extended during the difficult times. I am thankful to Dr. Balakrishnan Kannan for his help and company during my stay in Ireland. My special thanks to C. Gopalakrishnan for his help especially during my initial days in Ireland. Sincere thanks to my housemate Dr. Vamsi Komarala for his support and encouragement especially during the writing of this thesis. I could really learn

many things from his vast experience and knowledge. I am thankful to Dr. Sibu Pathmanabhan (Pulee) and Mrs. Reena Sibu for their support and encouragement. His amazing sense of humour made many moments to cherish. Special thanks to Dr. Manjula Devi and Dr Satheesh Krishnamoorthy for their support. My sincere thanks to Mr. Vikram Pakrashi and Miss. Bidisha Ghosh from Civil Engineering department, Trinity College, for their help and company during my stay in Ireland. My sincere thanks to Kumar Kumarappan for his help during writing the thesis. Thanks to Mr. Pradeepan Periyat, Mr. Rajath Varma and Mr. Uttam Manna for their support and company.

I am thankful to Dr. K. Mohanan Pillai, Principal, D.B Pampa College, Kerala, who actually motivated me to go in to the research field during my undergraduate studies. I am very much thankful to my supervisor in University of Pune, Prof. R.C Aiyer who is a guiding light in my life. I am grateful to my intimate friend Dr. Abey Issac with whom I started the journey into the academic life. I would like to thank Mr. Rajeev, Vaishak Industries, India, for his constant encouragement. I am thankful to Dr. Mahesh Abegaonkar, IIT Delhi, India for his brotherly affection and support. Sincere thanks to Dr. Rahul Puranthare, PRL, Ahemmadabad, India for his kind support, help and taking me to the Chandrama restaurant .

I am thankful to Arya, Athira, Viky Vishnu, Nanthu, Shambu, Sreejith Sreenath, Suraji, Kannan, Vinichttan Sinitha chechi, for their love and support. My sincere thanks to my brother Vineeth Kumar who helped, supported and encouraged me all these years. He always has a special place in my heart. I am thankful to Pradeep, my sister's fiancé for his support.

My sincere thanks and love to my sisters Indu and Anu for their support, love, and caring. I am thankful to my fiancé Parvathi for her support, love, caring and patience especially during the writing of this thesis. I am grateful to my in-laws achen, amma and Ayyappan for their encouragement. Last but not the least I would like to thank my parents R.G Pillai and Sobhana Kumari for their love, caring, support and encouragement.

*Be sure you take a good look at them; they are the most valuable
discovery of my life*

Einstein 1915

Summary

The strain relaxation and magneto transport properties of epitaxial magnetite (Fe_3O_4) thin films were studied. Epitaxial Fe_3O_4 films were grown on MgO and MgAl_2O_4 substrates using an Oxygen plasma assisted Molecular beam epitaxy (MBE) system. Characterisation of the films were done using techniques such as Reflection high energy electron diffraction (RHEED), High resolution X-ray diffractometer (HRXRD), Vibrating sample magnetometer (VSM), Low temperature resistivity measurements, and Raman Spectroscopy. Our studies on strain relaxation behaviour of epitaxial Fe_3O_4 thin films grown on MgO (100) substrates reveal that the films do not exhibit strain relaxation up to 700 nm thickness, which is much larger than the strain relaxation critical thickness, t_c , (70nm) predicted by the most accepted model based on mismatch strain. In contrast, the model predictions of strain relaxation behaviour are consistent with our results for Fe_3O_4 films grown on MgAl_2O_4 (100). The observed anomalous strain relaxation behaviour is attributed to the presence of antiphase boundaries (APBs) which lead to the formation of areas within the film that have opposite sign of stress. The stress compensation by the APBs reduces the effective stress experienced by the films. Even though APBs are not expected in Fe_3O_4 films grown on MgAl_2O_4 , TEM studies revealed the presence of APBs. We suggest that these APBs are formed not because of symmetry difference but because of the stacking faults generated by strain relaxation due to the large mismatch between the thin film and substrate.

The magnetoresistance (MR) behaviour of epitaxial Fe_3O_4 film grown on low-vicinal (low miscut) and high-vicinal (high miscut) MgO substrates is compared. The MR is significantly higher (12.2% at 2 Tesla) for a 45 nm Fe_3O_4 film on a high vicinal substrate than that observed (7.2% at 2 Tesla) for the film on low-vicinal substrate. A strong anisotropy in the MR is observed in correlation with the direction of the atomic step edges. The observed modification in the magneto-transport behaviour of epitaxial Fe_3O_4 films is attributed to an enhanced spin scattering arising due to the presence of atomic height steps that lead to the formation of a greater density of antiferromagnetically coupled APBs. The effect of pre deposition annealing duration of vicinal substrates on MR properties of the Fe_3O_4 films was studied.

VIII

Our results suggest that substrate annealing modifies the surface properties which in turn affects the density of APB.

A detailed study of the crystallographic direction dependence of MR in Fe_3O_4 (110) films of different thickness grown on MgO (110) substrates were performed. Structural characterisation revealed that the films were epitaxial and partially strain relaxed. MR studies as a function of temperature and thickness on these films reveal that the field dependency of MR shows drastically different features when measured along the $\langle \bar{1}10 \rangle$ and $\langle 001 \rangle$ directions. MR measurement along the $\langle 001 \rangle$ direction showed 9.5% MR at T_v (116K) with 1 Tesla field and showed 4% MR when measured along $\langle \bar{1}10 \rangle$ direction for a 200nm film. The MR observed at T_v along the $\langle 001 \rangle$ direction is very high compared to MR values reported for Fe_3O_4 films at 1 Tesla field with the exception of films deposited on vicinal MgO substrates. To explain the large MR anisotropy, we proposed three different mechanisms. The first one is related to the crystallographic directional dependents on the formation of strong antiferromagnetically coupled APBs due to the difference in the symmetry between the film and substrate. The second one is related to the formation of APBs induced by the misfit dislocations (MDs). Our analysis showed a greater probability for the formation of APBs along $\langle 001 \rangle$ direction compared to the $\langle \bar{1}10 \rangle$ direction. The spin polarised electron transport across these highly dense antiferromagnetically coupled APBs formed along $\langle 001 \rangle$ direction compared to $\langle \bar{1}10 \rangle$ direction could be one of the reasons for the observed MR anisotropy. Another mechanism proposed for the observed MR anisotropy is related to the strain induced modification of the band structure of Fe_3O_4 films. Band structure calculations reported for strained and unstrained magnetite thin films shows that, the half-metallic behaviour of the cubic magnetite eventually turns into normal metal behaviour in the high-strain states. A difference in spin polarisation due to anisotropic strain along with a high density of antiferromagnetically coupled APB formed due to strain relaxation induced misfit dislocations could be another reason for the enhancement of MR observed in the $\langle 001 \rangle$ direction compared to the $\langle \bar{1}10 \rangle$ direction. In conclusion our studies reveal that the strain relaxation and magnetotransport properties of Fe_3O_4 thin films are strongly related to the formation of antiphase boundaries within the film.

Publications

“Anomalous strain relaxation behaviour of Fe₃O₄/MgO (100) hetero-epitaxial system grown using molecular beam epitaxy”

S.K. Arora, **R.G.S. Sofin**, I.V. Shvets and M. Luysberg, J. Appl. Phys 100 073908 (2006)

“Influence of substrate pre-deposition annealing on step edges induced magnetoresistance in epitaxial magnetite films grown on vicinal MgO (100) substrates”

R.G.S Sofin, S K Arora and I.V Shvets, J. Magn. Mater, **316**, e969 (2007)

“Study of magnetoresistance of epitaxial magnetite films grown on vicinal MgO (100) substrate”

R.G.S Sofin, S K Arora and I.V Shvets. J. Appl. Phys **97** (10): 10D315 (2005)

“Magnetoresistance enhancement in epitaxial magnetite films grown on vicinal substrates”

S K Arora, **R.G.S Sofin** and I.V Shvets, Phys. Rev. B, **72**, 134404 (2005)

“Influence of antiphase boundary density on the conduction noise properties of epitaxial magnetite thin films”

S.K Arora, **R.G.S Sofin** I.V. Shvets. R.Kumar, M.W.Khan,J.P. Srivastava, J. Appl. Phys **97** (10), 10C310 (2005)

“Antiphase boundaries-induced exchange coupling in epitaxial Fe₃O₄ thin films”

S.K Arora, **R.G. S Sofin**, A. Nolan and I.V. Shvets. J.Magn. Mater.**286**, 463-467 (2005)

“Swift heavy ion irradiation-induced modifications in structural, magnetic and electrical transport properties of epitaxial magnetite thin films”

R. Kumar, M.W. Khan, J.P. Srivastava, S.K. Arora, **R.G.S. Sofin**, R. J Choudhary and I. V Shvets. J. Appl. Phys, **100** (3), 033703 (2006)

“Anisotropy of magnetoresistance in epitaxial Fe₃O₄ (110) films grown on MgO (110) substrates”

R.G.S Sofin, S K Arora and I.V Shvets, communicated

“Strain relaxation and magnetotransport properties of (110) oriented Fe₃O₄ films deposited on MgO (110) substrates”

R.G.S Sofin, S K Arora and I.V Shvets, in preparation.

“Formation of strain induced antiphase boundaries in Fe₃O₄ films grown on MgAl₂O₄ (100) substrates”

R.G.S Sofin, S K Arora and I.V Shvets, in preparation.

Patents

“Magnetoresistive medium including nanowires” I.V Shvets, S K Arora and **R.G.S Sofin**. United States Patent Application No 20050264958

List of abbreviations

A- atomic weight

AFM -antiferromagnetic

AGFM- alternating gradient field magnetometer

a- lattice constant

AMR- anisotropic magneto resistance

APB - antiphase boundaries

DWs- Domain walls

DWMR- domain wall magnetoresistance

FM- ferromagnetic

FWHM- full width at half maximum

G- reciprocal lattice vector

GMR- giant magnetoresistance

H_A-anisotropy field

HMFM - Half metallic ferromagnetic

HRXRD-high resolution X-ray diffraction

J- Exchange integral

k- Boltzmann constant

K₀ - wave vector

MBE- molecular beam epitaxy

MD- misfit dislocation

MR- Magneto resistance

- MRAM**- magnetic random access memory
- M_S – saturation magnetisation
- MTJ**- Magnetic tunnel junctions
- N_A - Avogadro number
- NMR**- nuclear magnetic resonance
- nn* - nearest-neighbour
- OMR**- ordinary magneto resistance
- P**- spin polarization
- Φ -inter-planar angle
- Q(x)**-reciprocal lattice vectors
- ρ - density
- RHEED**-reflection high energy electron diffraction
- RLP**- reciprocal lattice point,
- S**- Spin angular momentum
- SP**- Small polaron
- SPT**- spin polarised tunneling
- t*- transfer integral
- T_C - Curie temperature
- t_c - strain relaxation critical thickness,
- TEM**-transmission electron microscopy
- TMR**- tunnelling magnetoresistance
- T_V - Verwey transition temperature
- U(r)**- electrostatic potential
- UHV**- ultra high vacuum
- VSM**-vibrating sample magnetometer

XRD - X-Ray diffraction

Z- number of electrons per atom.

List of Figures

2.1	Magnetite unit cell.....	10
2.2	Electronic configuration of the Fe^{2+} ion and Spin polarised electron bands of Fe_3O_4	13
2.3	Schematic drawing of main magnetic exchange interactions in Magnetite.....	16
2.4	MgO unit cell.....	18
2.5	Schematic of antiphase boundaries (APBs) formed due to $1/2\langle 100 \rangle$ type of in-plane shifts.....	20
2.6	Schematic of antiphase boundaries (APBs) formed due to $1/4\langle 110 \rangle$ type of in-plane shifts.....	21
2.7	Schematic of antiphase boundaries (APBs) formed due to $1/4\langle 101 \rangle$ type of out-plane shifts.....	22
2.8	Schematic of magnetic exchange interactions formed across antiphase boundaries (APBs) in Fe_3O_4 films grown on MgO (100) substrate.....	24
3.1	Schematic of the entire MBE system.....	33
3.2	Schematic of the MBE deposition chamber layout.....	35
3.3	Schematic of the MBE Load-Lock chamber layout.....	38
3.4	Schematic of the Molybdenum sample holder, Cup and transfer tool.....	41

3.5 Schematic of the RHEED system configuration.....	42
3.6 Schematic of the requirements necessary for the RHEED diffraction conditions to be fulfilled.....	44
3.7. Schematic of the RHEED diffraction geometry.....	45
3.8. Schematic of the correlation of surface coverage with idealized RHEED oscillations.....	48
3.9. Ray paths of electrons leaving the crystal through terrace planes and step edges.....	49
3.10. Scattering geometry of X-rays probing a plane having an inter planar angle ϕ with the surface plane.....	51
3.11. Schematic of the diffraction geometry for a vicinal a surface.....	53
3.12. Typical rocking curve for a symmetrical ω - 2θ scan.....	54
3.13. Asymmetric grazing exit (GE) and grazing incidence (GI) diffraction geometries.....	56
3.14. Schematic of a fully strained substrate – film system.....	56
3.15. Representation of asymmetric grazing exit diffraction geometry.....	57
3.16. Representation of the shifts of (622) and (6-2-2) reciprocal lattice points from the ω - 2θ diffraction line.....	58
3.17. Representation of the grazing exit diffraction geometry.....	60
3.18. Representation of the grazing incidence diffraction geometry.....	61
3.19. Representation of the grazing exit (GE) and incidence (GI) reciprocal space mapping.....	63
3.20. Representation of the grazing exit (GE) and incidence (GI) diffraction geometries.....	64
3.21 Schematic of a typical asymmetrical ω - $n\theta$ scans.....	65
3.22 Scattering geometry used in XRR measurements.....	67

3.23. Schematic of the reflection and refraction of X-rays incident upon a plane boundary between mediums with refractive index n_1 and n_2	67
3.24. Schematic of the typical XRR spectrum from a homogeneous layer on a substrate.....	68
3.25. Schematic of the diffractometer layout.....	70
3.26. Photograph of the components of the High Resolution X-Ray diffractometer.....	71
3.27. Schematic of the operation of a transmission electron microscope.....	74
3.28. Schematic of the bright field imaging and dark field imaging.....	75
3.29. Energy level diagram for Raman scattering.....	77
3.30. Schematic representation of the Raman spectrometer.....	78
3.31. A typical hysteresis loop of a ferromagnet with applied field H in the direction of easy axis.....	80
3.32. Schematic of a VSM measurement setup.....	81
3.33. Schematic of a AGFM measurement setup.....	82
3.34. Schematic of the CCR Resistivity Measurement system.....	85
3.35. Photograph of the CCR 2 system in MR measurement configuration....	86
4.1 RHEED pattern of MgO substrate and 70 nm thick Fe_3O_4 film.....	94
4.2 RHEED intensity oscillations observed during the growth of Fe_3O_4 film on MgO substrate.....	95
4.3 Raman shifts observed for Fe_3O_4 films having various thicknesses grown on MgO substrate.	96
4.4 Magnetization curve obtained for a 700 nm epitaxial magnetite film grown on MgO substrate.....	97
4.5 Verwey transition observed for Fe_3O_4 films having various thicknesses grown on MgO substrate.....	98

4.6 The ω - 2θ scans for Fe_3O_4 films with different thickness on MgO (100) substrates.....	100
4.7. The ω - $n\theta$ scans for Fe_3O_4 films with different thickness on MgO (100) substrates.....	101
4.8 Reciprocal space map of 700 nm thick Fe_3O_4 film on MgO.....	102
4.9 Cross-sectional TEM image of 400 nm $\text{Fe}_3\text{O}_4/\text{MgO}$	104
4.10 Plan- view bright field electron micrograph of a 200 nm and 700 nm Fe_3O_4 film grown on MgO substrate.....	104
4.11 Plan- view bright field electron micrograph of a 400 nm Fe_3O_4 film grown on MgO substrate.....	105
4.12 High resolution cross-section TEM image of 400 nm $\text{Fe}_3\text{O}_4/\text{MgO}$	105
4.13 Dislocation geometries in multilayers.....	106
4.14 Comparison of experimentally observed values of the in-plane strain, $\epsilon_{ }$, with the FKR model predictions for the Fe_3O_4 films grown on MgO (100) substrates.....	108
4.15 Schematic diagram of an antiphase boundary formed in Fe_3O_4 films grown on MgO (100) substrate.....	110
4.16 Schematic diagram of a rotational type antiphase boundary.....	111
4.17 Reciprocal space maps around the (311)/(622) Bragg reflection in grazing exit geometry for 700 nm thick Fe_3O_4 thin films on MgO (100) s substrate.....	114
4.18 RHEED patterns of MgAl_2O_4 substrate, 5 nm and 120 nm thick Fe_3O_4 films.....	117
4.19 Raman shifts observed for Fe_3O_4 films having various thicknesses grown on MgAl_2O_4 substrate.....	119
4.20 Variation of most intense Raman peak position with thickness.....	119

4.21 Magnetization curve obtained for 120 nm epitaxial magnetite film grown on MgAl ₂ O ₄ substrate.....	120
4.22 Verwey transition observed for 70 and 120 nm Fe ₃ O ₄ films grown on MgO substrate.....	121
4.23. The ω -2 θ scans of 15, 60 and 120 nm Fe ₃ O ₄ film on (100) MgAl ₂ O ₄ substrate.....	122
4.24. The ω -n θ scans of 60 and 120 nm Fe ₃ O ₄ film on (100) MgAl ₂ O ₄ substrate measured for asymmetric (622) Bragg reflection. measured in the grazing exit geometry..	123
4.25 Comparison of experimentally observed values of the in-plane strain, $\epsilon_{ }$, with the FKR model predictions for the Fe ₃ O ₄ films grown on MgAl ₂ O ₄ (100) substrates.....	124
4.26 Plan-view TEM images of 70nm and 200nm Fe ₃ O ₄ thin films grown on MgAl ₂ O ₄ substrates.....	125
4.27 The cross-section TEM image of 70nm Fe ₃ O ₄ film on MgAl ₂ O ₄	126
4.28 Schematic diagram of an antiphase boundary formed in Fe ₃ O ₄ films grown on MgAl ₂ O ₄ (100) substrate.....	126
4.29 Schematic diagrams of two possible configurations of antiphase boundaries formed in Fe ₃ O ₄ films grown on MgAl ₂ O ₄ (100) substrate..	127
5.1. Example for the formation of a step induced APB.....	135
5.2 Two possible combinations of step induced APB formation of which one forms APB and other does not.....	136
5.3 RHEED images of high-vicinal MgO (100) substrate after the UHV heat treatment.....	140
5.4 RHEED images of 45nm Fe ₃ O ₄ film grown on high-vicinal MgO (100) substrate.....	141

5.5 The ω - 2θ scans of Sample 1 and Sample 2 measured relative to the (200) Bragg reflection of MgO.....	142
5.6 The ω - $n\theta$ grazing exit scans of Sample 1 and Sample 2 measured relative to the (311) Bragg reflection of MgO..	143
5.7 The reflectivity scans of Sample 1 and Sample 2.....	143
5.8 Hysteresis loops of Sample 1 and Sample 2 measured at room temperature.....	145
5.9 Magnetoresistance of sample 1 at 150K and 108K.....	147
5.10 Magnetoresistance of sample 1 measured at Verwey transition temperature (108K).....	148
5.11 Resistivity as a function of temperature measured along and perpendicular to the step edges for sample 2.....	148
5.12 Magnetoresistance as a function of applied in-plane magnetic field for Sample 2.....	149
5.13 Temperature dependence of the MR perpendicular and along the step-edges for Sample 2.....	151
5.14 The difference in MR observed along and perpendicular to the step edge directions.....	152
5.15 RHEED images of high vicinal MgO substrate (Sample 3).....	153
5.16 The ω - 2θ scans of Sample 2 ,Sample 3 Sample 4 and Sample 5.....	154
5.17 Resistivity as a function of temperature measured along and perpendicular to the step edges for Sample 2, Sample 3, Sample 4 and Sample 5.....	155
5.18 Magnetoresistance MR of Sample 2, Sample 3, Sample 4 and Sample 5.....	156

5.19 Magnetoresistance MR of Sample 2, Sample 3, Sample 4 and Sample 5.....	157
5.20 Magnetoresistance MR of Sample 2, Sample 3, Sample 4 and Sample 5.....	158
5.21 Magnetoresistance MR at 2 Tesla field of <i>Sample C</i> as a function of temperature.....	159
5.22 Difference in Magnetoresistance measured along and across the step edges (MR_{SE}) of Sample 2, Sample 3, Sample 4 and Sample 5.....	159
5.23 Magnetoresistance as a function of applied magnetic field for sample 2.....	161
5.24 Magnetoresistance of sample 2 along with the bulk magnetization normalized to the saturation magnetization.....	162
5.25 Spin structures of one of the magnetic sublattices of magnetite across an antiphase boundary.....	163
6.1 RHEED pattern of MgO (110) substrate.....	174
6.2 Raman shifts observed for Fe_3O_4 (110) films having various thicknesses grown on MgO (110) substrate.....	175
6.3 Variation of most intense Raman peak position with thickness.....	176
6.4 The reflectivity scans for of Fe_3O_4 films grown on MgO (110) substrates with thickness.....	177
6.5 The ω - 2θ scans for Fe_3O_4 films with different thickness on MgO (110) substrates.....	178
6.6 Variation of out of plane lattice constant (a_{\perp}) with thickness.....	179
6.7 The ω - $n\theta$ scans for Fe_3O_4 films with different thickness on MgO (110) substrates.....	179
6.8 The ω - $n\theta$ scans for Fe_3O_4 films with different thickness on MgO (110)	

substrates.	180
6.9 Variation of in-plane lattice constant ($a_{ }$ along $\langle -110 \rangle$ direction) with thickness.....	181
6.10 Variation of in-plane lattice constant ($a_{ }$ along $\langle 001 \rangle$ direction) with thickness.....	181
6.11 Verwey transition observed for Fe_3O_4 films having various thicknesses grown on MgO (110) substrate in $\langle \bar{1}10 \rangle$ and $\langle 001 \rangle$ directions.....	182
6.12 Magnetization curve obtained for 20 nm magnetite film grown on MgO (110) substrate.....	184
6.13 Magnetization curve obtained for 30 and 60nm magnetite films grown on MgO (110) substrate.....	185
6.14 Magnetization curve obtained for 90 and 200 nm magnetite film grown on MgO (110) substrate.. ..	185
6.15 Magnetoresistance curves measured at different temperatures for a 200 nm magnetite film grown on MgO (110) substrate.....	186
6.16 Magnetoresistance curves measured at different temperatures for a 20 nm magnetite film grown on MgO (110) substrate.....	187
6.17 MR% observed for magnetite films grown on MgO (110) substrate....	187
6.18 $\Delta\text{MR}\%$ (width of the switching) observed at the switching field for magnetite films having different thickness grown on MgO (110) substrates.....	188
6.19 Magnetoresistance curves measured at different temperatures for a 200 nm magnetite film grown on MgO (110) substrate.....	189

6.20 Magnetoresistance curves measured at different temperatures	
for a 20 nm magnetite film grown on MgO (110) substrate.....	189
6.21 MR% observed for magnetite films grown on MgO (110) substrate.....	190
6.22 Variation of the separation (ΔH) between the symmetric peak values of	
MR% observed for magnetite films having different thickness grown on,	
MgO (110) substrates, as a function of temperature.....	191
6.23 Schematic illustration of APB formation for a (110) oriented Fe_3O_4 films	
grown on MgO (110) substrates.....	192
6.24 Magnetoresistance curve obtained at room temperature for a	
20 nm Fe_3O_4 film.....	194
6.25 Magnetoresistance curve obtained at room temperature for a 200 nm	
Fe_3O_4 film.....	194
6.26 Magnetoresistance curve obtained at 180K for a 200 nm film	
Measured along $\langle 001 \rangle$ hard axis direction superimposed with	
schematic model of magnetized domains.....	196
6.27 Changes in the domain structure during the increase in magnetic field	
along $\langle 001 \rangle$ hard axis.....	197
6.28 Magnetization curves obtained for a 200nm Fe_3O_4 film along $\langle 001 \rangle$	
direction.....	203
6.29 Magnetization curves obtained for a 200nm Fe_3O_4 film along $\langle \bar{1}10 \rangle$	
direction.....	204
6.30 Formation of misfit dislocation due to the missing of one row of	
Oxygen leading to the formation of APB.....	206
7.1 Cross sectional view of the proposed magneto-resistive medium.....	219

List of Tables

Table 2.1	Summary of the Magnetic exchange interactions across APBs....	25
Table 4.1	Summary of the Raman shifts observed from a Fe_3O_4 films.....	96
Table 4.2	Summary of the magnetization measurements on Fe_3O_4 films.....	97
Table 4.3	Summary of the resistivity measurements on Fe_3O_4 films.....	99
Table 4.4	Summary of the predicted and observed strain relaxation values.....	116
Table 4.5	Summary of the Raman shifts observed on Fe_3O_4 films.....	120
Table 4.6	Summary of the magnetization measurements on Fe_3O_4 films.....	121
Table 4.7	Summary of the predicted and observed strain relaxation values.	125
Table 6.1	Summary of the Raman shifts observed on Fe_3O_4 films	163
Table 6.2	Summary of the resistivity measurements on Fe_3O_4 films.....	183
Table 6.3	Summary of the magnetization measurements. on Fe_3O_4 films ...	183
Table 6.4	Summary of the magnetization measurements. on Fe_3O_4 films....	184

Contents

1) Introduction	1
Bibliography.....	7
2) Physical properties of magnetite	9
2.1) Introduction.....	9
2.2) Properties of Bulk Fe ₃ O ₄	10
2.2.1 Crystallographic structure	10
2.2.2 Magnetic exchange interactions.....	14
2.2.3 Electrical conductivity	16
2.3) Properties of epitaxial Fe ₃ O ₄ films.....	18
2.3.1 Substrate.....	18
2.3.2 Formation of anti-phase domain boundaries.....	19
2.3.3 Magnetic exchange interactions in Fe ₃ O ₄ thin film.....	23
2.3.4 Conductivity in epitaxial Fe ₃ O ₄ films.....	25
2.3.5 Magnetoresistance in epitaxial Fe ₃ O ₄ films.....	26
Bibliography.....	28
3) Experimental Details	31

3.1 Introduction	31
3.2 Molecular beam epitaxy (MBE).....	31
3.2.1 Ultra high vacuum (UHV) system.....	34
3.2.1.1 Deposition chamber.....	34
3.2.1.2 Load-Lock Chamber.....	38
3.2.1.3 Plasma source.....	39
3.2.1.4 Water Cooling system and Interlock	
System.....	39
3.2.1.5 Sample Preparation and Loading.....	40
3.2.2 <i>In situ</i> sample characterisation	42
3.2.2.1 Reflection High Energy Electron	
Diffraction (RHEED).....	42
3.2.2.2 Basic principles of RHEED.....	43
3.2.2.3 Instrumentation details of RHEED on the	
MBE system.....	49
3.3 <i>ex situ</i> sample characterisation.....	50
3.3.1 High Resolution X-Ray Diffraction (HRXRD).....	50
3.3.1.1 Basic principles of HRXRD.....	51
3.3.1.2 Determination of Lattice parameters	
using HRXRD.....	52
3.3.1.3 X-ray Reflectivity measurements.....	66
3.3.1.4 Tilt Analysis or miscut angle	
Measurement.....	69
3.3.1.5 Instrumentation details of HRXRD.....	70
3.3.2 Transmission electron microscopy (TEM).....	72
3.3.2.1 Imaging methodology.....	73

3.3.2.2 Instrumentation details.....	75
3.3.3 Raman spectroscopy.....	76
3.3.3.1 Basic principles of Raman spectroscopy	76
3.3.3.2 Instrumentation details of Raman Spectrometer.....	78
3.3.4 Vibrating sample magnetometer (VSM) and Alternating gradient field magnetometer (AGFM)...	79
3.3.4.1 Theory of operation.....	80
3.3.4.2 Details of VSM and AGFM used in the present work.....	83
3.3.5 Electrical resistivity measurements.....	84
Bibliography.....	88
4) Strain relaxation behaviour of (100) oriented Fe₃O₄ thin films	91
4.1 Introduction.....	91
4.2 Experiment.....	92
4.3 Results and discussion.....	94
4.3.1 Studies on Fe ₃ O ₄ (100)/MgO (100) system.....	94
4.3.1.1 RHEED measurements.....	94
4.3.1.2 Raman spectroscopy.....	95
4.3.1.3 Magnetization measurements.....	96
4.3.1.4 Resistivity measurements.....	98
4.3.1.5 HRXRD measurements.....	99
4.3.1.6 TEM Studies.....	103
4.3.1.7 Discussion.....	106

4.3.2 Studies on $\text{Fe}_3\text{O}_4(100)/\text{MgAl}_2\text{O}_4(100)$ system.....	117
4.3.2.1 RHEED measurements.....	117
4.3.2.2 Raman spectroscopy.....	118
4.3.2.3 Magnetization measurements.....	120
4.3.2.4 Resistivity measurements.....	121
4.3.2.5 HRXRD measurements.....	122
4.3.2.6 Discussion.....	124
4.4 Conclusions.....	128
Bibliography.....	130
5) Magnetoresistance enhancement in epitaxial magnetic films grown on vicinal substrates	133
5.1 Introduction.....	133
5.1.1 Calculation of the probability of APB Formation.....	134
5.2. Experiment.....	138
5.3 Results and discussion.....	140
5.3.1 RHEED measurements.....	140
5.3.2 HRXRD measurements.....	142
5.3.3 Magnetization measurements.....	144
5.3.4 Magnetoresistance measurements.....	146
5.3.5 Effects of substrate pre-deposition annealing on the MR behaviour of Fe_3O_4 films grown on vicinal MgO (100) substrate.....	152
5.3.6 Discussion	160
5.4 Conclusion.....	167
Bibliography.....	169

6) Strain relaxation behaviour and magnetotransport	
properties of (110) oriented Fe₃O₄ thin films	171
6.1 Introduction.....	171
6.2. Experiment.....	172
6.3 Results and discussion.....	173
6.3.1 RHEED measurements.....	173
6.3.2 Raman spectroscopy.....	174
6.3.3 HRXRD measurements.....	176
6.3.4 Resistivity measurements.....	182
6.3.5 Magnetization measurements.....	183
6.3.6 Magnetoresistance measurements.....	186
6.3.7 Discussion.....	191
6.4 Conclusion.....	208
Bibliography.....	211
7) Conclusions	213
Future work.....	218
Bibliography.....	221

Nature is showing us only the tail of the lion, but I have no doubt that the lion belongs to it even though, because of its large size, it cannot totally reveal itself all at once. We can see it only the way a louse that is sitting on it would.....

Einstein 1914

Chapter 1

Introduction

Feynman in his 1960 article, titled '*There's plenty of room at the bottom*' [1], pointed out that if a bit of information requires only 100 atoms, then all the books ever written could be stored in a cube with sides 0.02 inches long. Even though in recent years researchers have been able to write bits of information in two dimensions using even fewer than 100 atoms by using scanning tunnelling microscope [2], only less than 1% of the total information ever recorded in the world is stored in electronic format. About 4% of the information is stored on photographic microfiche and the remaining 95% is on paper [3]. The huge demand for high density information storage, high speed information retrieval and processing technologies by rapidly developing fields such as bioinformatics, genetic engineering, telecommunication industries, internet and software companies, digital movie industries, scientific research etc are bringing multi billion dollar revenue to information storage and processing industries. No wonder, the storage and high speed processing of information on an ever finer scale have become the most important aspect of the rapidly growing field of nano-materials in which researchers are trying to control the fine-scale structure of materials [3].

The incredible developments currently being made in the fields of electronics and information technologies have been made possible by exploiting the properties of electron charge and spin. Conventional electronic circuits used for data processing use the charge of electrons in semiconductors, while data storage media such as hard disks use the spin of electrons in a magnetic material. The idea of injecting, transporting and controlling the

electronic spin to implement novel functions, led to the development of a new field called spin-electronics or spintronics.

Magnetic oxides are one of the most promising categories of materials for spin-electronics applications and have attracted considerable interest in the recent past [4, 5, 6]. These materials exhibit a rich complexity in magnetic and electronic properties due to strong cation-anion bonding, which is not found in metals. In addition, oxide surfaces are more complex than those of metals and semiconductors. There are added complexities due to the fact that some oxide surfaces are polar meaning that they are likely to reconstruct to reduce their surface Coulomb energy [7]. Representative examples of investigations of two such magnetic oxide surfaces are magnetite (Fe_3O_4) (100) and Fe_3O_4 (111) [8, 9].

The spin electronic devices such as spin valves and magnetic tunnel junctions (MTJ) are realized by separating two ferromagnetic (FM) electrodes by a normal metal or an insulating barrier respectively [10, 11]. Half metallic ferromagnetic (HMFM) materials possess 100% spin polarization and are expected to play an important role in spin-electronic devices. Some examples of half metallic ferromagnetic materials are rare earth doped manganites, double perovskites, CrO_2 , Fe_3O_4 , several Heusler alloys etc [12, 13, 14]. Out of the small number of known half metallic materials with high Curie temperatures (>300 K) more than half are oxides. Magnetite, Fe_3O_4 is a common and stable half metallic oxide. Due to its relatively high Curie Temperature ($T_C = 858$ K) and its electronic properties, Fe_3O_4 , represents one of the promising materials for spin electronic devices [15]. Most of these applications will employ this material in the form of thin films. Thin films are widely used in many applications, including microelectronics, optics, corrosion resistant coatings, micro-mechanics etc [16]. To realize these applications, one requires good control over the stoichiometry and precise knowledge of the strain status of the films. The stoichiometry, strain, defect structure etc are expected to play a crucial role in determining the magneto-transport and magnetic properties of Fe_3O_4 films.

There are several reports on the pseudomorphic growth of magnetite films on a variety of substrates [17-23]. MgO is an ideal substrate for epitaxy of magnetite due to the small lattice mismatch (-0.344%). The epitaxial growth of Fe_3O_4 on MgO substrate suffers from the formation of antiphase boundaries

(APB) which are formed as a natural growth defect due to difference in the translational and rotational symmetry between Fe_3O_4 on MgO [19,24,25]. Fe_3O_4 (100) films on MgO (100) substrates remain coherent up to a thickness much greater than the critical thickness, t_c , for strain relaxation estimated from mismatch strain. On the other hand Fe_3O_4 films, grown on MgAl_2O_4 (100) substrates (which have the same crystal structure of Fe_3O_4 and a higher lattice mismatch, 3.9%) show behaviour consistent with the widely accepted model predictions. Films grown on MgO (110) show a partial strain relaxation much below the critical thickness. In the case of Fe_3O_4 films grown on MgAl_2O_4 substrates, formation of APBs are not expected. However, the presence of APBs in $\text{Fe}_3\text{O}_4/\text{MgAl}_2\text{O}_4$ systems have been reported [26]. In this work we point out that, the presence of APBs plays a key role in the strain relaxation behaviour of hetero-epitaxial magnetite thin films and is an important issue in tailoring nano-structured devices based on magnetite. Thus a systematic study of the strain relaxation behaviour of epitaxial Fe_3O_4 thin films grown on (100) oriented MgO , MgAl_2O_4 and (110) oriented MgO substrates are presented in this thesis. Other main issues addressed in this thesis are given below.

As mentioned in the previous paragraph, spin valves consist of a multilayer of magnetic materials, separated by a thin non magnetic material. The current in the magnetic materials is spin polarised. The resistance through the structure is high when the magnetic coupling between the magnetic materials is anti-ferromagnetic. On application of an external magnetic field the two magnetic layers align ferromagnetically and consequently the resistance decreases. An understanding of the mechanisms which govern the magnetoresistance (MR) in these systems is complicated since they depend on many factors such as magnetic impurities, structural disorder, band structure, interfacial roughness etc [27,28]. Application of Fe_3O_4 in spin valves, as a ferromagnetic magnetic electrode, has not been very successful until now, as the observed magneto resistance effect was very low [29]. Presence of APBs have a strong influence on the spin polarised conduction electrons of Fe_3O_4 because of the anti-ferromagnetic coupling present across a significant fraction of these boundaries. But, APBs open up a new type of spin valve application [17]. The APBs themselves can act like a spin valve, giving rise to MR within a single layer. The advantages of this type of spin valves is that it does not require a multilayer structure, thus reducing the number of interfaces and the

domains on both sides of the boundary have the same band structure. The magnetic properties of adjacent domains are strongly coupled. The MR behaviour of Fe_3O_4 thin films has been widely studied in films on different substrates like MgO and MgAl_2O_4 [17, 30-32]. However, due to the random network of APBs formed in the epitaxial Fe_3O_4 films, the magnitude of MR observed in epitaxial films has not exceeded 8% for a magnetic field strength of 2 Tesla. In order to exploit the presence of APBs to control the MR properties of Fe_3O_4 thin films, we used vicinal MgO substrates. These substrates when treated under appropriate annealing conditions form an array of atomic terraces of atomic step height, whose width can be controlled by selecting the correct miscut angle. Fe_3O_4 films grown on vicinal substrates are expected to have greater density of APB formed due to atomic step and are highly oriented. We exploited this to control the density and orientation of APBs which essentially gives higher MR. In addition to increased MR, a strong anisotropy in correlation with atomic step direction is also observed.

Previous reports of magnetoresistance (MR) behaviour of Fe_3O_4 (110) epitaxial films grown on MgO (110) substrate, show a small (0.65%) MR at 120°C (Verwey temperature, T_v) with an applied field of 0.1 Tesla [33]. Here, we present a detailed study of the crystallographic direction dependence of MR in partially strain relaxed Fe_3O_4 (110) films of different thickness grown on MgO (110) substrates. MR studies as a function of temperature and thickness on these films reveal that the field dependency of MR shows drastically different features when measured along the $\langle \bar{1}10 \rangle$ and $\langle 001 \rangle$ directions. MR along the $\langle 001 \rangle$ direction is found to be higher compared to MR measured along the $\langle \bar{1}10 \rangle$ direction and to MR values reported for Fe_3O_4 films at 1 Tesla field except for films deposited on vicinal MgO substrates. The observed anisotropy in MR behaviour of Fe_3O_4 films is related to the strain status, APB formation and magnetocrystalline anisotropy of Fe_3O_4 films.

In conclusion, it is very clear that, for future technological applications of Fe_3O_4 thin films, a complete knowledge of the structural, electronic and magnetic properties of Fe_3O_4 hetero-epitaxial systems are needed. The work presented here addresses the study of strain relaxation behaviour and magneto transport behaviour of $\text{Fe}_3\text{O}_4/\text{MgO}$ (100) $\text{Fe}_3\text{O}_4/\text{MgAl}_2\text{O}_4$ (100) and $\text{Fe}_3\text{O}_4/\text{MgO}$ (110) hetero-epitaxial systems grown using molecular beam epitaxy (MBE). A detailed study of magneto transport behaviour of Fe_3O_4 thin

films on vicinal MgO (100) substrates is also presented. We have written the thesis in such a way that each chapter can be read independently although cross referencing is used to minimise repetition. An outline of the details presented in the thesis is given below.

Chapter 2: In this chapter we discuss the fundamental physical properties of magnetite bulk and thin films. In section §2.2, the details of crystal structure, magnetic properties, electrical conductivity etc of bulk magnetite is provided and in section §2.3 the details of magnetite thin films are given. In sub-section §2.3.1 we discuss the details of the substrates (MgO and MgAl₂O₃) used for the growth of magnetite thin films in the present work and in sub-section §2.3.2 we give a detailed description of the formation of antiphase boundaries (APBs) in magnetite thin films grown on MgO (100) substrates. The magnetic properties and electrical conductivity of magnetite thin films are given in sub-sections §2.3.3 and §2.3.4. The mechanism of magnetoresistance is described in sub-section §2.3.5

Chapter 3: In this chapter we discuss the thin film growth technique and various characterization techniques used in the present work. In section §3.2 details of the molecular beam epitaxy (MBE) system is given. In sub-section §3.2.2 the details of *in situ* Reflection high energy electron diffraction (RHEED) technique is discussed. In section §3.3 details of *ex situ* characterisation techniques such as High resolution X-ray diffraction (HRXRD) (§3.3.1), Transmission electron microscopy (TEM) (§3.3.2), Raman spectroscopy (§3.3.3), Vibrating sample magnetometer (VSM) and Alternating gradient field magnetometer (AGFM) (§3.3.4) and details of electrical resistivity measurements (§3.3.5), are furnished.

Chapter 4: In this chapter we discuss the Strain relaxation behaviour of (100) oriented Fe₃O₄ thin films grown on MgO and MgAl₂O₄ substrates. The Fe₃O₄ films grown on MgO show no strain relaxation even up to a thickness ten times higher than the critical thickness predicted for the relaxation. But films grown on MgAl₂O₄ show strain relaxation in line with the theoretical predications. The anomalous strain relaxation observed in Fe₃O₄ films on MgO substrates is attributed to the presence of APBs. A model is proposed for the formation of

APBs due to misfit dislocations generated by strain relaxation in the case of Fe_3O_4 films grown on MgAl_2O_4 substrates.

Chapter 5: This chapter deals with the magnetoresistance enhancement in epitaxial magnetite films grown on vicinal MgO (100) substrates. MR properties of Fe_3O_4 films grown on vicinal and non vicinal MgO substrates are compared. A strong anisotropy in the MR in close correlation with the direction of current and step-edges was observed. MR properties of epitaxial Fe_3O_4 films on vicinal MgO substrate show a direct dependence on the substrate annealing duration. The observed difference in MR along two equivalent crystallographic directions on the surface is explained on the basis of spin dependent electron scattering along the APBs and difference in the reduction of magnetisation values along and across the APBs resulting from the difference in magnetoelastic properties.

Chapter 6: In this chapter we discuss the strain relaxation behaviour and magnetotransport properties of (110) oriented Fe_3O_4 thin films grown on MgO (110) substrates. Structural characterization shows that the films are strain relaxed and Magnetoresistance and magnetization measurements show different behaviour in the $\langle 001 \rangle$ and $\langle \bar{1}10 \rangle$ directions. The possibility of the formation of APBs in Fe_3O_4 on a MgO (110) substrate due to the difference in symmetry (between film and substrate) and due to the misfit dislocations arising because of strain relaxation are explored. The observation of high MR and temperature dependence of the MR curves along the $\langle 001 \rangle$ direction compared to the $\langle \bar{1}10 \rangle$ is explained on the basis of strain status, APB formation and magnetocrystalline anisotropy of Fe_3O_4 films.

Chapter 7: The main results described in this thesis are summarised in this chapter. A discussion on the extension of the work for the future is also given.

Bibliography

- [1] R. P Feynman, Eng. Sci. **23** 22,(1960); reprinted in 1992 J Micromech. Systems **1** 60.
- [2] D. M Eigler and E. K Schweizer, Nature **344** 524, (1990).
- [3] K. G. Ashar, Magnetic Disk Drive Technology: Heads, Media, Channel, Interfaces, and Integration, Wiley-IEEE Press (1996)
- [4] I. Zutic, J. Fabian and S. Das Sarma, Rev. Mod. Phys. **76**, 323 (2004).
- [5] M. Ziese, Rep. Prog. Phys. **65**, 143 (2002).
- [6] J.M.D. Coey, M. Venkatesan, J. Appl. Phys. **91**, 8345 (2002)
- [7] C. Noguera, J. Phys. Condens. Matter **12**, R367 (2000)
- [8] R. Wiesendanger, I.V. Shvets, D. Burgler, G. Tarrach, H.J. Guntherodt, J.M.D. Coey and S. Graser, Science **255**, 583 (1992)
- [9] I.V. Shvets, N. Berdunov, G. Mariotto and S. Murphy, Euro Phys. Lett. **63**, 867 (2003)
- [10] G.A. Prinz, J. Magn. Magn. Mat. **200**, 57 (1999).
- [11] R. Jansen, J.Phys. D Appl. Phys. **36**, 289 (2003).
- [12] J.M.D. Coey, M. Viret and S. von Molnar, Adv. Phys. **48**, 167 (1999).
- [13] W.E. Pickett and D.J. Singh, Phys. Rev. B **53**, 1146 (1996).
- [14] R.A. de Groot, F.M. Mueller, P.G. van Engen and K.H.J. Buschow, Phys. Rev. Lett. **50**, 2024 (1983).
- [15] J. S. Moodera, J. Nassar and G. Mathon Annu. Rev. Mater. Sci., **29**:381, (1999).
- [16] L.B Freund and S. Suresh, Thin Film Materials, Cambridge University Press, (2003).
- [17] W. Eerenstein, T.T.M. Palstra, S.S. Saxena and T. Hibma Phys. Rev. Lett. **88**, 247204 (2002)
- [18] T. Fuji, M. Takano, R. Katano, Y. Isozumi, and Y. Bando, J. Magn. Magn. Mater. **130**, 267 (1994).
- [19] D. T. Margulies, F. T. Parker, F. E. Spada, R. S. Goldman, J. Li, R. Sinclair and A. E. Berkowitz, Phys. Rev. B **53**, 9175 (1996).
- [20] F .C. Voogt, T. Hibma, P. Smulders and L. Niesen, J. Cryst. Growth **174**, 440 (1997).
- [21] M. Ziese, Phys. Rev. B **62**, 1044 (2000).

- [22] S. Kale, S. M. Bhagat, S. E. Loafland, T. Scabarozzi, S. B. Ogale, A. Orozco, S. R. Shinde, T. Venkatesan, B. Hannover, B. Mercey and W. Prellier, *Phys. Rev. B.* **64**, 205413 (2001).
- [23] M. Ziese, R. Hohne, C. Semmelhackh, H. Reckentin, N.H. Hong and P. Esquinazi, *Eur. Phys. J. B* **28**, 415 (2002).
- [24] F.C. Voogt, T.T.M. Palstra, L. Niesen, O.C. Rogojanu, M.A. Janes and T. Hibma, *Phys. Rev. B.* **57**, 8107 (1998).
- [25] W.Eerenstein, T.T.M Palstra, and T. Hibma, *Phys. Rev. B.* **68**, 014428 (2003).
- [26] M. Ziese, R. Hohne, P. Esquinazi and P. Busch, *Phys. Rev. B.* **66**, 134408 (2002).
- [27] E.Y. Tsymbal, O.N. Mryasov, and P.R. LeClair, *J. Phys. Condens. Mat.* **15**, 109 (2003).
- [28] A. Fert, A. Barthelemy, J. Ben Youssef, J.P. Contour, V. Cros, J.M. De Teresa, A.Hamzic, J.M. George, G. Faini, J. Grollier, H. Jaffres, H. Le Gall, F. Montaigne, F.Pailloux and F. Petroff, *Mat. Sci. Eng. B-Solid* **84**, 1 (2001).
- [29] P.J. van der Zaag, P.J.H. Bloemen, J.M. Gaines, R.M. Wolf, P.A.A. van der Heijden, R.J.M. van de Veerdonk and W.J.M. de Jonge, *J. Magn. Magn. Mat.* **211**, 301 (2000).
- [30] M. Ziese and H.J. Blyte, *J. Phys. Cond. Matter* **12**, 13 (2000).
- [31] X.W. Li, A. Gupta, Gang Xiao and G.Q. Gong, *J. Appl. Phys.* **83**, 7049 (1998).
- [32] S.B. Ogale, K. Ghosh, R.P. Sharma, R.L. Greene, R. Ramesh and T. Venkatesan, *Phys. Rev. B* **57**, 7823 (1998).
- [33] H. Matsuda, H. Sakakima, H. Adachi, A. Odagawa and K. Setsune, *J. Mater. Res.*, **17**, 1985(2002).

*The truth of a theory can never be proven, for one never knows if
future experience will contradict its conclusions*

Einstein 1919

Chapter 2

Physical properties of magnetite

2.1 Introduction

'Magnesia' is the name of the southeastern area of Thessaly in central Greece. It is believed that around 4000 years ago people in Magnesia were bewitched by the discovery of a black mineral with peculiar attractive properties. They called this mineral 'magnet', which means "magnesian stone" in Greek. Later this mineral was identified as 'magnetite' with chemical formula Fe_3O_4 . Magnetite is magnetic at room temperature, in fact it is ferrimagnetic (meaning that the crystallographic planes are antiferromagnetically arranged, but there is a different amount of spins in each plane, giving rise to a sizeable magnetic moment) with high Curie temperature of 858 K [1]. Not only it is magnetic at room temperature, Fe_3O_4 is also conducting and exhibits the metal to insulator transition at about 120K, known as Verwey transition, which is far from being fully understood [2,3]. Band structure calculations predict the conduction electrons to be fully spin polarised [4,5]. Because of these fundamental properties, much interest has been directed towards Fe_3O_4 as a potential candidate for spin electronics devices such as spin valves and spin tunnel junctions [6,7].

Besides the natural abundance of Fe_3O_4 , it has also been synthesized, both as a single crystal and in thin film form. In addition to many experimental studies determining the crystal structure, magnetic properties and electrical conductivity, a lot of theoretical work has been performed in order to understand the band structure [4,5,8,9] and electrical conductivity properties [10-12]. As a potential candidate for magnetic planar devices and spin

electronic device applications, Fe_3O_4 thin films prepared by a variety of methods have been widely studied [13]. Thin films of Fe_3O_4 have properties that deviate from those of the bulk. The magnetisation does not saturate in high fields [14] and ultra thin films below 5nm become super-paramagnetic [15]. The resistivity is increased with respect to the bulk [16, 17] and epitaxial films exhibit magneto resistance [18-20]. Despite years of thorough research, many of the properties of Fe_3O_4 are still far from fully understood. The following sections discuss the properties of bulk and thin films of magnetite in detail.

2.2 Properties of Bulk Fe_3O_4

2.2.1 Crystallographic structure

Since the early decades of the 20th century, with the X-Ray diffraction (XRD) measurements performed by Bragg [21], Fe_3O_4 is known to crystallize in the inverse spinel structure with a lattice constant, $a=0.83987$ nm. This consists of a cubic closed packing of oxygen anions arranged in a face-centred lattice. Fe_3O_4 belongs to $\text{Fd}\bar{3}\text{m}$ symmetry group [22]. Two kinds of interstices are available for the metal cations: tetrahedral, conventionally indicated as A-type, and octahedral, conventionally indicated as B-type.

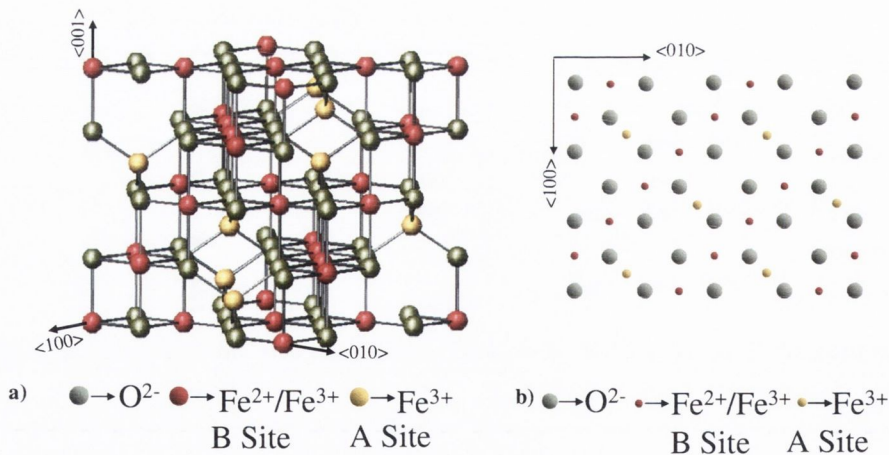


Figure 2.1. (a) 3D view of the unit cell of Fe_3O_4 containing 32 oxygen anions (white) 16 octahedral iron ions (red) and 8 tetrahedral iron ions (blue) (b) (001) plane of Fe_3O_4 . The tetrahedral iron ions (blue) are half way between two planes of octahedral iron ions (red) and oxygen ions.

The unit cell of Fe_3O_4 is composed of 32 O^{2-} that embrace 64 tetrahedral interstices, (A-type), and 32 octahedral interstices, (B-type). Normal

spinels are formed when 1/8 of the A sites are occupied by 8 divalent ions and 1/2 of the B sites are occupied by 16 trivalent ions. Instead, in Fe_3O_4 , 8 of the 16 Fe^{3+} ions in the unit cell are placed in A sites, whereas the other 8, together with the 8 Fe^{2+} ions, occupy the B sites in the inverse spinel structure, see Figure 2.1(a). The unit cell consists of four (001) layers, each layer containing the oxygen anions and the octahedral iron ions. The tetrahedral sites are located halfway between these layers. The B site cations run in strings in the $\langle 110 \rangle$ directions. In a (001) plane, alternating strings are occupied, see Figure 2.1(b). The strings in the next layer are rotated by 90° with respect to the one below it via a screw axis.

The very first studies on Fe_3O_4 performed by Verwey [23,24], suggested that the high conductivity at room temperature (about $200 \Omega^{-1}\text{cm}^{-1}$ as compared to low values for normal spinels of about $10^{-5} \Omega^{-1}\text{cm}^{-1}$) is the consequence of a random distribution of the iron ions in the octahedral planes. According to crystal field theory, it is possible to represent the state of the octahedral (B) sites of Fe_3O_4 as shown in Figure 2.2a [25]. The five d orbitals split in to two levels consisting of two e_g levels and three t_{2g} levels. The two different iron ions are present in the octahedral sites, Fe^{2+} (d^6) and Fe^{3+} (d^5). The Fe^{3+} ions are in a high spin state, with the 5 electrons arranged in parallel, in accordance with Hund's rule. The antiferromagnetic (AFM) alignment of the two consecutive crystallographic planes cause the magnetic moment associated with these Fe^{3+} ions in the B-site to be cancelled by the one of the Fe^{3+} ions in the A-site. There are three electronic configurations possible for a Fe^{2+} ion, see figure 2.2b. The configuration with 4 unpaired electrons is believed to be correct because it is in agreement with the value of the magnetisation measured experimentally of $4 \mu_B$ per formula unit. The additional spin down electron of the Fe^{2+} ion in the octahedral site can easily hop to a neighbouring Fe^{3+} site provided their spins are parallel. In the magnetically ordered state only the spin-down electron can easily move, resulting in spin-polarised electron transport. The electron transport is restricted to the B-sites. B-site spins are oriented ferromagnetically because of their mutual anti-ferromagnetic coupling to the A-site spins. The magnetic coupling will be further discussed in the next subsection. Figure 2.2c shows the electron bands of Fe_3O_4 obtained from the Local Spin Density Calculation (LSDA) by Zhang et al. [26] From their analysis the exchange splitting between the spin-up and spin-down d electrons

on the Fe atom is roughly 3.5 eV. In addition to the exchange splitting Δ_{ex} , the five fold d levels are split into t_{2g} and e_g orbitals by the crystal field. The crystal field splitting Δ_{CF} , generated because of differences in covalent mixing and electrostatic interaction with neighbouring atoms, is approximately 2eV for the Fe(B) atom while it is less than a few tenths of an eV for the Fe(A) atom. This difference is attributed to the large covalent mixing of the Fe (B) orbitals with its six nearest neighbours of the same kind. The calculated net magnetic moment is $4.0 \mu_B / \text{Fe}_3\text{O}_4$ formula unit. The high-spin state of the Fe atoms is consistent with the argument that a high-spin state is indicated if the exchange splitting Δ_{ex} is greater than the crystal field splitting Δ_{CF} . Also their calculation suggests that the magnetic moments on the A and B sublattices are antiferromagnetically aligned. The remarkable feature of the spin-polarised bands is that the spin up bands (majority spins) are semiconducting while the spin down bands (minority spins) are metallic. Only spin down electrons are present at the Fermi energy and these electrons have predominantly Fe(B) character.

Around a temperature of 120K, the electrical resistivity of stoichiometric magnetite crystals suddenly increases by two orders of magnitude which is called Verwey transition (T_v) [2]. At this transition the structure distorts from its cubic symmetry [24] and a charge ordering occurs at the B sites [27] thus reducing the conductivity. Other properties of the crystal such as magnetisation, magnetostriction, thermal expansion and heat capacitance, also exhibit a sudden variation at T_v [28]. The exact transition temperature depends on the purity of the crystal [29, 30]. Nonstoichiometry depresses the transition temperature which is a maximum for pure stoichiometric Fe_3O_4 . For extreme levels of cation deficiency a second order transition is observed at 120K [30].

Despite the fact that the Verwey transition had been first detected 80 years ago, and extensively studied since the late 1940s, its mechanism is still matter of discussion and controversy [3, 31, 32]. In recent years there were numerous studies searching for the charge ordering taking place along the B site. There are mainly four different mechanisms supported in the literature. The first one proposes the charge ordering of Fe^{2+} and Fe^{3+} on the same octahedral planes and is supported by nuclear magnetic resonance (NMR)

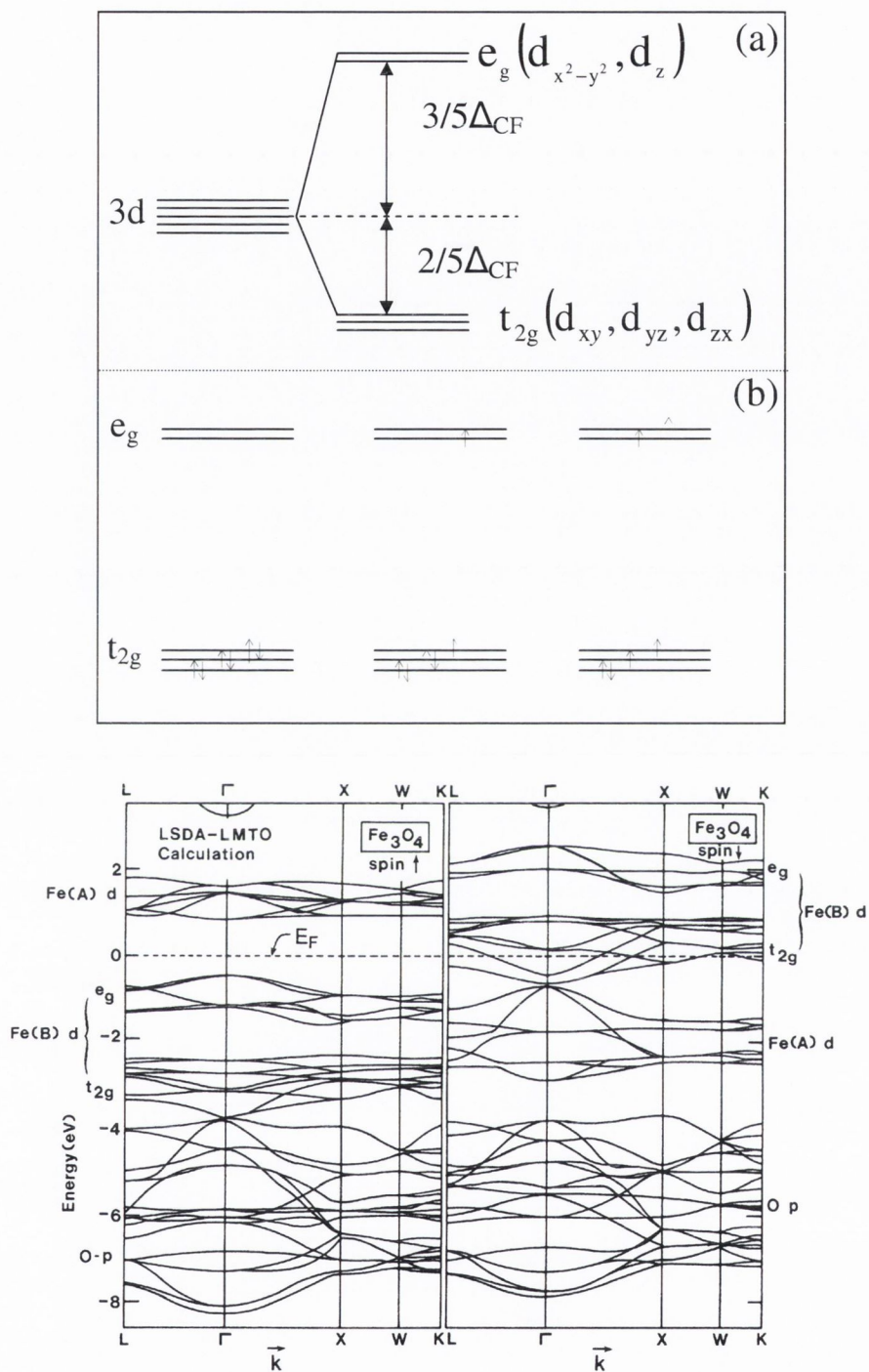


Figure 2.2. (a) Schematic representation of the splitting of the 5d electronic orbitals of an isolated iron ion in an octahedral crystal field (b) The three different possible electronic configurations of Fe^{2+} in an octahedral site. (c) Spin polarised electron bands of Fe_3O_4 by local spin density calculation. (Zhang et al. Ref 26)

[33, 34], high energy transmission electron diffraction [35] and high resolution neutron and synchrotron X-ray resonant scattering [36] experiments. The second hypothesis suggests the ordering of electrons in the B sites in terms of condensation of phonons, and is supported by X-ray resonant scattering [37, 38] and more recent NMR [39] experiments. The third one is the charge density transfer, or coordination-crossover (CC) transition from inverse to normal spinel, characterized by a specific temperature, T_{CC} , and the fourth one is the [32] first-order structural phase transition, from a cubic to a distorted-cubic phase [32] characterized by a specific transition temperature designated T_{dist} . The detailed XRD measurements carried out by Rozenberg et al [32], at isobaric and isothermal conditions show that the metallic state of magnetite is stable in the cubic structure, whereas the insulating phase is stable in the distorted-cubic structure. Their conclusion is that the opening of a gap in the electronic band structure within the distorted-cubic phase is associated with the particular electronic band structure emanating from this crystallographic structure. But there exist several questions to be answered: (i) Why is magnetite a good conductor within the cubic-spinel structure? (ii) Within the distorted-cubic phase, which bands are responsible for the gap opening? (iii) Why is the distorted-cubic phase stable below the T_{dist} ?

As all these hypotheses do not bring enough evidence to give a conclusive description of the mechanism of the Verwey transition, more work and experiments are needed.

2.2.2 Magnetic exchange interactions

In Fe_3O_4 , there are several magnetic exchange interactions that have to be taken into account. The magnetic exchange interaction between two neighbouring spins is described by the Heisenberg exchange Hamiltonian:

$$\mathbf{H}_{ex} = -\sum_{i,j} \mathbf{J}_{ij} \mathbf{S}_i \cdot \mathbf{S}_j \quad (2.1)$$

Where \mathbf{S}_i and \mathbf{S}_j are spin angular momentum of two electrons on neighbouring atoms. \mathbf{J}_{ij} is a constant called the *exchange integral*. If \mathbf{J}_{ij} is positive, the energy is lowest when the two spins are parallel to each other and is called *ferromagnetic* interaction. For \mathbf{J}_{ij} negative, moments of adjacent atoms point in opposite directions which results in the lowest energy state and is

called *antiferromagnetic* interaction. The sign and strength of the effective exchange integral J_{ij} depends on the distance, angle, spin and electronic configuration of the neighbouring moments and can result from cation-cation interactions and cation-anion-cation interactions. The latter type of interaction is referred to as super-exchange [40]. Out of several magnetic exchange interactions present in Fe_3O_4 , three most important interactions are:

Cation-cation interactions: - The most important interaction is the *double exchange* interaction between the iron ions in the octahedral site [41]. Since the spin of the extra electron of Fe^{2+} is oppositely directed to the electrons of Fe^{3+} , electron transfer is only possible when both ions are aligned ferromagnetically. This then increases the bandwidth or delocalisation of the extra electron, thereby decreasing its kinetic energy and favouring a ferromagnetic alignment.

Cation-Oxygen-cation interactions (superexchange):- The strength and sign of this exchange interaction depends on the angle between the ions and on the filling of the orbitals. Exchange between the two iron ions via the intervening oxygen requires overlap of the orbitals. Overlap only occurs between orbitals with similar symmetry. On the Oxygen ions three p -orbitals contribute, of which two have a π -type symmetry and one has σ -type symmetry [40,42]. Of the five d -orbitals of iron, three possess a π -type symmetry (the three t_{2g} -orbitals) and two a σ -type symmetry (the two e_g -orbitals). The e_g -orbitals thus overlap with the oxygen p -orbitals with σ -type symmetry and the t_{2g} -orbitals with the oxygen p -orbitals with π -type symmetry. Because the σ -overlap is generally larger than π -overlap [40], the σ -exchange is stronger.

a) 125 degree iron-oxygen-iron exchange: This is acting between the Fe^{3+} ions on the octahedral and tetrahedral sites. This is a strong anti-ferromagnetic coupling, largely due to overlap of the e_g orbitals on the B site and t_{2g} orbitals on the A sites. This exchange is responsible for the high Curie temperature of 858 K.

b) 90 degree iron-oxygen-iron exchange: The angle between the octahedral iron ions and the intervening oxygen is 90 degrees. This leads to a ferromagnetic coupling between the iron ions, but this coupling is much

weaker than the anti-ferromagnetic coupling between the A and B sublattices. Since the orbital overlap between the iron t_{2g} and oxygen p is weak, this exchange is difficult to separate from the double exchange. The main interactions are shown in Figure 2.3

Due to the strong antiferromagnetic coupling between Fe^{3+} ions on A and B sites the net magnetic moment in Fe_3O_4 is simply that of the Fe^{2+} ion in B site, which is $4\mu_B$ and shows a saturation magnetisation 480emu/cm^3 . The magnetic behaviour of Fe_3O_4 at low temperature was extensively studied [28, 43]. As the temperature is lowered the magnetisation increases and undergoes an abrupt decrease in the value near Verwey transition which is associated with the charge ordering below Verwey transition.

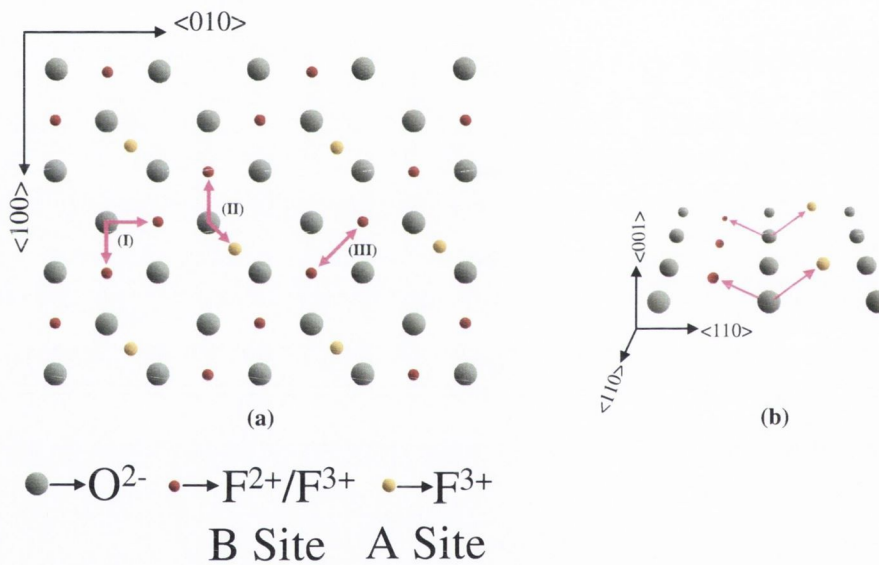


Figure 2.3. (a) Schematic drawing of a (001) plane in Fe_3O_4 . The magnetic exchange interactions are indicated in the figure. (I) 90° superexchange interaction at the octahedral site (II) Superexchange interaction between iron ions on the octahedral and tetrahedral lattice. (III) double exchange between iron ions on the octahedral lattice. (b) 3D view of super exchange between iron ions on the octahedral lattice and tetrahedral lattice.

2.2.3 Electrical conductivity

The electron transport is restricted to the B sites in Fe_3O_4 . The additional spin down electron in Fe^{2+} can easily hop to a neighbouring Fe^{3+} ion

if their spins are parallel. The extra electron of the Fe^{2+} ions is in the spin-down t_{2g} band at the B sites which is separated from the occupied spin-up t_{2g} band by a gap of around 3.5eV [44]. Ihle and Lorenz have performed a quantitative calculation of the conductivity in Fe_3O_4 [11]. They used perturbation theory and the Hamiltonian is written as:

$$\mathbf{H} = -\mathbf{E}_b \sum_i \mathbf{n}_i + 1/2 \sum_{i \neq j} \mathbf{U}_{ij} \mathbf{n}_i \mathbf{n}_j + \sum_{q\nu} \omega_{q\nu} \tilde{\mathbf{b}}_{q\nu}^\dagger \tilde{\mathbf{b}}_{q\nu} + \sum_{i \neq j} \mathbf{t}_{ij} \varphi_{ij} \tilde{\mathbf{c}}_{ij}^\dagger \tilde{\mathbf{c}}_{ij} \quad (2.2)$$

where \mathbf{E}_b is the small polaron (SP) binding energy, \mathbf{U}_{ij} the effective SP-SP interaction energies and \mathbf{n}_i the electron occupation number. $\omega_{q\nu}$ is the phonon energy and $\tilde{\mathbf{b}}_{q\nu}$ is the phonon creation operator. The last term in the equation (1.2) is the perturbation term where \mathbf{t}_{ij} are the nearest-neighbour (nn) transfer integrals, φ_{ij} the vibrational overlap integral and $\tilde{\mathbf{c}}_{ij}$ the small polaron creation operator.

The conductivity is then calculated using the Kubo formula. The total conductivity is the summation of the band and hopping conductivities. But below room temperature the band conductivity is the main contribution to the conductivity which is given by:

$$\sigma_b = t^2 \frac{C_b}{kT} \exp(-U_1/2k_0T) \exp(-4S_0k_bT/\omega_0) \quad (2.3)$$

in the limit of small $U_1/2kT$ and large $\omega_0/2kT$. Where constant C_b contains temperature independent terms, U_1 is the nn Coulomb repulsion, \mathbf{K} is Boltzmann constant, \mathbf{T} temperature, ω is the phonon energy, and \mathbf{S}_0 contains the electron-phonon coupling strength. This equation suggests that band conduction first increases due to the thermal activation and then reaches its maximum value after which it decreases due to the decrease of \mathbf{t} . With increasing temperature, the probability for multi-phonon processes increases and the hopping conduction starts to dominate the conductivity process. The hopping conductivity is given by:

$$\sigma_h = t^2 \frac{C_h}{kT} \exp(-U_1/2K_0T) \exp(S_0\omega_0/2k_0T) \quad (2.4)$$

As both the band and the hopping conductivity are proportional to t^2 , the total conductivity is also proportional to t^2 , i.e. $\sigma_T \propto t^2$.

2.3 Properties of epitaxial Fe_3O_4 films

2.3.1 Substrate

Magnesium oxide, MgO possesses the rock-salt crystal structure as shown in Figure 2.4 and belongs to the space group $\text{Fm}\bar{3}\text{m}$. The lattice constant is 0.4213nm. The lattice mismatch with Fe_3O_4 is only -0.3% which makes MgO a suitable substrate for the growth of Fe_3O_4 films. The almost perfect epitaxial relationship between Fe_3O_4 and MgO is due to the common fcc oxygen sub-lattice. In this work we have used polished MgO (100), MgO(110) and vicinal MgO (100) (miscut azimuth directed along $\langle 011 \rangle$) oriented substrates for the growth of Fe_3O_4 (100) and Fe_3O_4 (110) epitaxial films. ‘Vicinal substrates’ are substrates which are a few degrees off cut from their crystal plane. Details of the growth process are discussed in chapter 4.

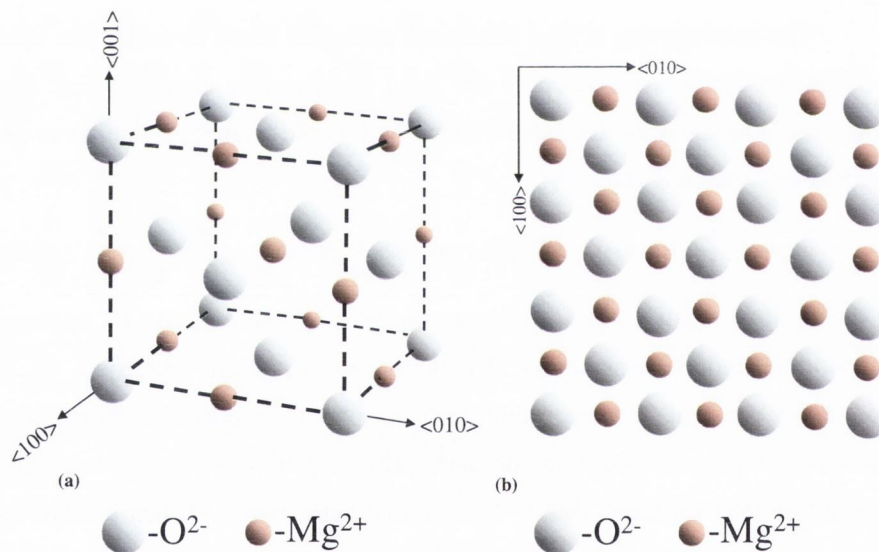


Figure 2.4. 3D view of the unit cell of MgO containing oxygen anions and magnesium ions.

The other substrate used in the present work is MgAl_2O_4 which has the normal spinel structure and a lattice constant of 0.808nm. This results in a larger mismatch of 4%. In the normal spinel structure the Mg^{2+} ions occupy the tetrahedral sites and the Al^{3+} ions occupy the octahedral sites.

2.3.2 Formation of anti-phase domain boundaries

Physical properties of epitaxial Fe_3O_4 films deviate from those of the bulk such as larger electrical resistivity [17], magneto resistance [20,45] and magnetization which does not saturate in high magnetic fields [14]. These differences are attributed to the presence of antiphase boundaries (APBs) which are natural defects occurring during growth of $\text{Fe}_3\text{O}_4/\text{MgO}$ thin films [14, 44]. In the first stages of growth, islands of Fe_3O_4 are deposited on MgO. However, because of the difference in unit cell parameter and crystal symmetry, the different islands can be related by a shift vector, which is not a lattice translation vector [14,15]. APBs are formed when islands of Fe_3O_4 on the MgO surface coalesce and the neighbouring islands are shifted with respect to each other [46]. The oxygen sub-lattice is more or less undisturbed across the APBs and only the cation lattice is shifted. The APB shifts in these films are a consequence of two distinct forms of symmetry breaking between MgO and Fe_3O_4 . The first is due to the lattice parameter of MgO (0.4213nm) being half that of Fe_3O_4 (0.8397nm) and because of this, adjacent Fe_3O_4 monolayers may be shifted by $1/4\langle 110 \rangle$, $1/4\langle \bar{1}\bar{1}0 \rangle$ or $1/2\langle 100 \rangle$ which are called in-plane shifts. The structure at the boundary is determined by the type of shift and by the direction of the shift with respect to the plane of the boundary i.e. whether the shift is parallel or perpendicular to the boundary plane. Some examples of APB formations due to in-plane shifts are shown in figure 2.5 and Figure 2.6. The other APB shifts are a result of the lower symmetry of Fe_3O_4 monolayers compared to the MgO substrate surface. Consequently, adjacent Fe_3O_4 islands on the same MgO surface may be rotated by 90° , as shown in Figure.2.7. In combination with the screw symmetry element of the spinel structure this gives rise to the $1/4\langle 101 \rangle$, $1/4\langle 10\bar{1} \rangle$, $1/4\langle 011 \rangle$ and $1/4\langle 0\bar{1}\bar{1} \rangle$ shifts which are designated as out-of-plane shifts. Eerenstein *et al.* have reported a detailed transmission electron microscopy (TEM) study on the APB domain sizes in Fe_3O_4 films [47]. They found that the domain size increases significantly with film thickness and shows a parabolic relation $D \propto \sqrt{t}$, where t is the deposition time which is proportional to the thickness of the film

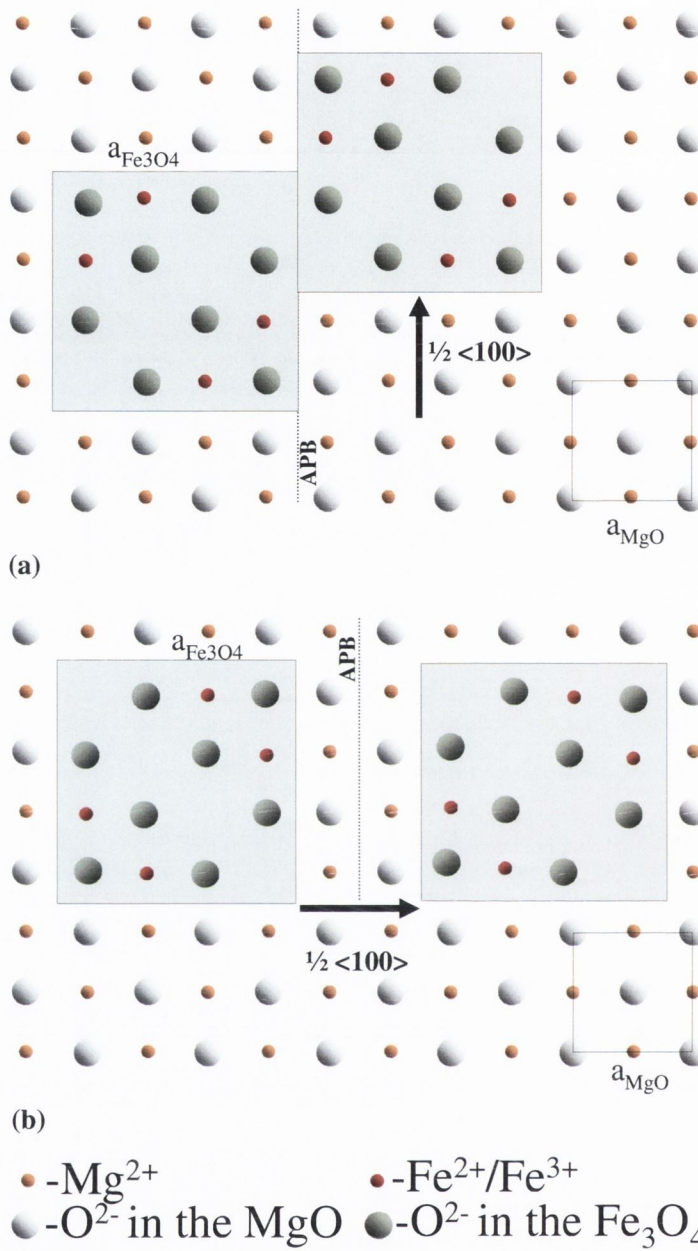


Figure 2.5. Schematic of antiphase boundaries (APBs) formed due to $1/2\langle 100 \rangle$ type of in-plane shifts (a) shift parallel to boundary plane (b) shift perpendicular to the boundary plane. The boundary at which the two nucleation sites meet and form the APB is indicated by the dashed line.

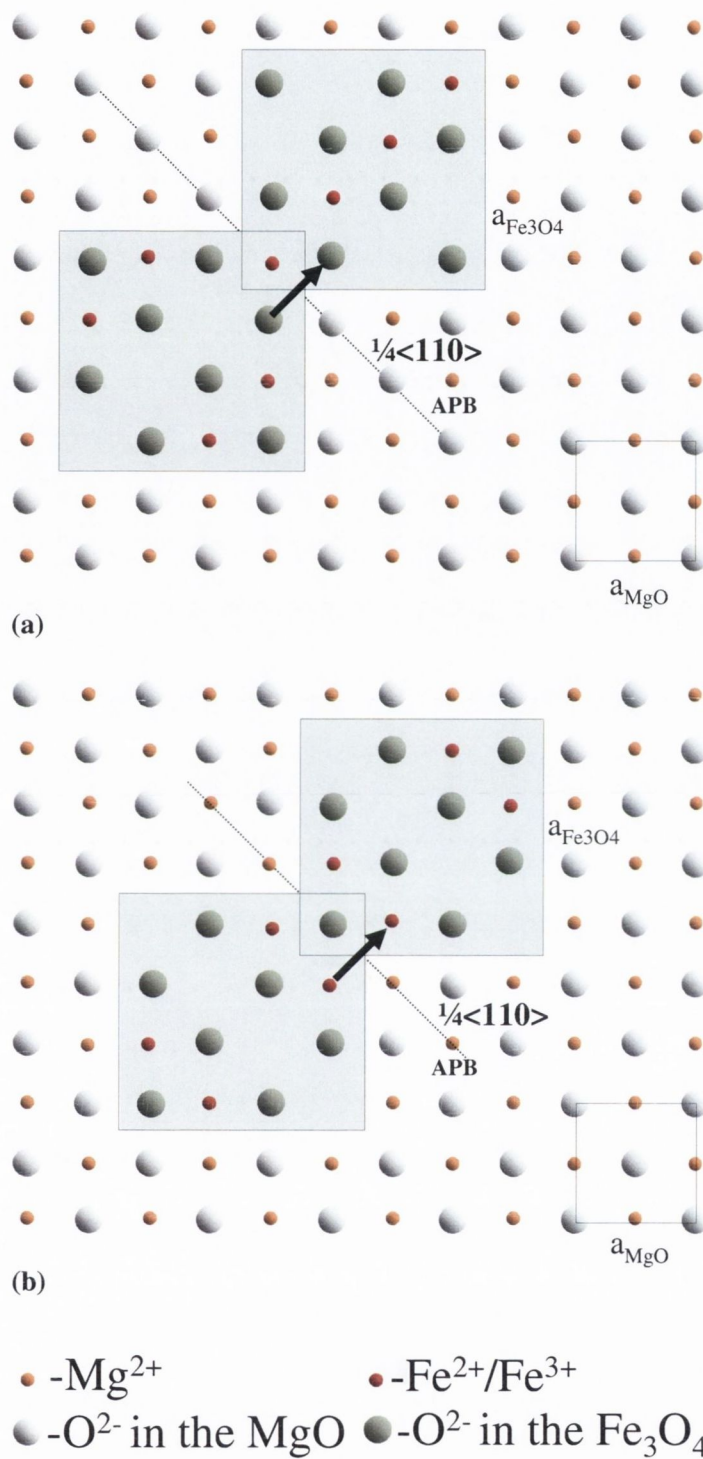


Figure 2.6. Schematic of antiphase boundaries (APBs) formed due to $1/4\langle 110 \rangle$ type of in-plane shifts (a) shift parallel to boundary plane (b) shift perpendicular to the boundary plane. The boundary at which the two nucleation sites meet and form the APB is indicated by the dashed line.

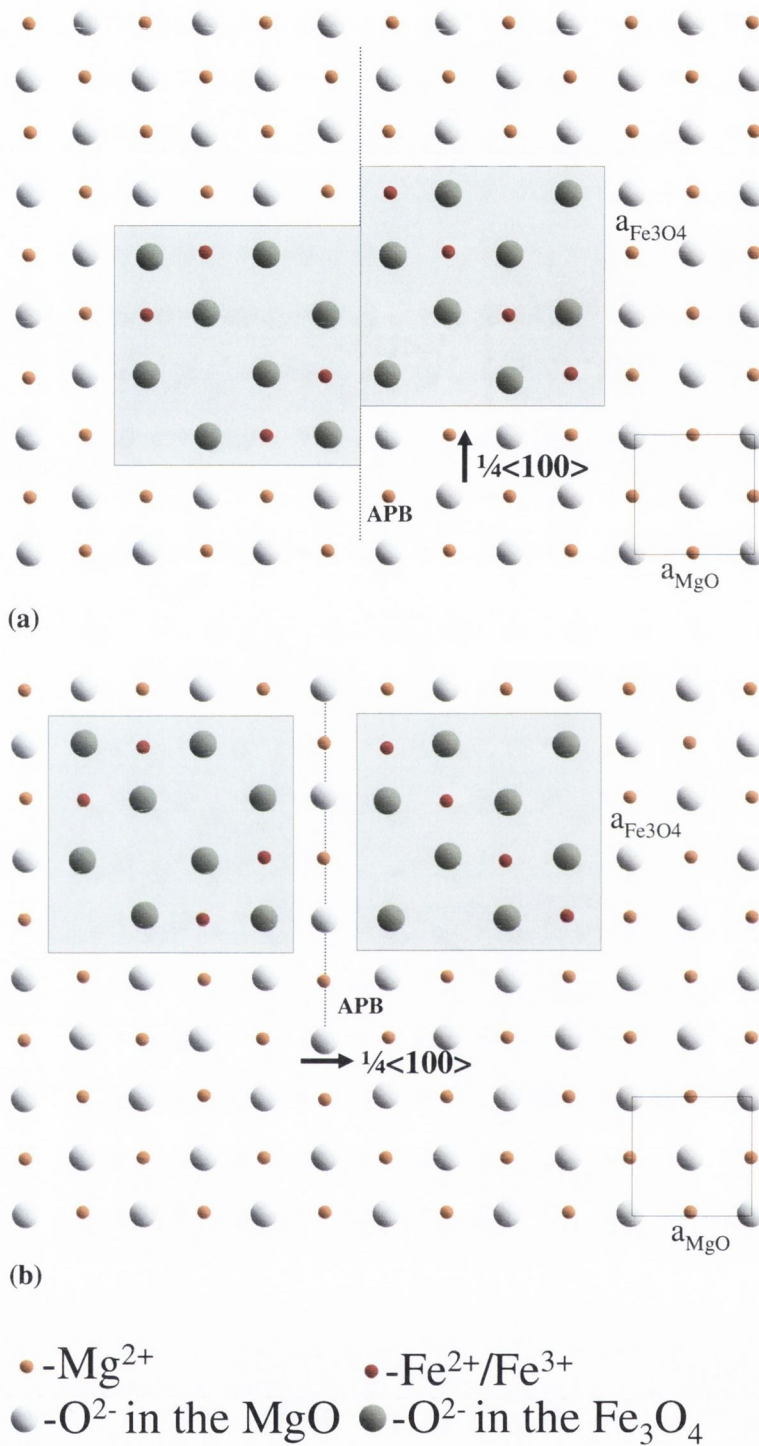


Figure 2.7. Schematic of antiphase boundaries (APBs) formed due to $1/4\langle 101 \rangle$ type of out-plane shifts (a) $1/4\langle 100 \rangle$ shift parallel to boundary plane (b) $1/4\langle 100 \rangle$ shift perpendicular to the boundary plane. The boundary at which the two nucleation sites meet and form the APB is indicated by the dashed line.

deposited. They have also shown that the increase in domain size with thickness is not by the growth of larger domains on top of the small domains in the first monolayer, but is due to the diffusive migration of APBs, which were found to anneal out during the post annealing studies. The free energy of the thin films are higher due to the presence of APBs and therefore there is a large affinity to remove APBs. Post annealing of these films helps the boundaries to migrate such that a local equilibrium at the boundaries can be achieved. With annealing the boundaries are found to have become straighter and the number of junctions significantly reduced [47].

Since Fe_3O_4 and MgAl_2O_4 possess the same spinel type structure and symmetry, APB formation is not anticipated during the growth of Fe_3O_4 on MgAl_2O_4 substrates. But the presence of APBs in this system is reported [48]. An important factor to be noticed in this system is relaxation of the film due to higher misfit around 4%. A detailed description of APBs and misfit dislocations and connection between them are given in chapter 4.

2.3.3 Magnetic exchange interactions in Fe_3O_4 thin film

The magnetic exchange interactions across the APBs are very important because they can affect the physical properties of the epitaxial Fe_3O_4 films. An anti-ferromagnetic coupling will have a strong influence on the magnetization [14] and on the magnetoresistance properties [20]. A detailed study of different magnetic exchange interactions across the APBs which are not present in the bulk Fe_3O_4 is reported by Celotto *et al.* [44]. Their analysis shows that across the APBs there can be new, 180 degree strong antiferromagnetic octahedral–oxygen–octahedral super exchange, 90 degree weak ferromagnetic octahedral–oxygen–octahedral super exchange (which exists in addition to the 90 degree ferromagnetic super exchange in the bulk), additional double exchange interactions between octahedral iron ions etc. All these interactions, their relative strength and presence have been summarised in Table.2.1. Also some of the new exchange interactions across the APBs are shown in Figure 2.8. It is clear that the majority of strong interactions present in thin film are anti-ferromagnetic in nature [44].

The magnetic properties the films grown by sputter deposition, molecular-beam epitaxy and evaporation differ from those expected for single crystal Fe_3O_4 with bulk behaviour [14]. In order to saturate the magnetization

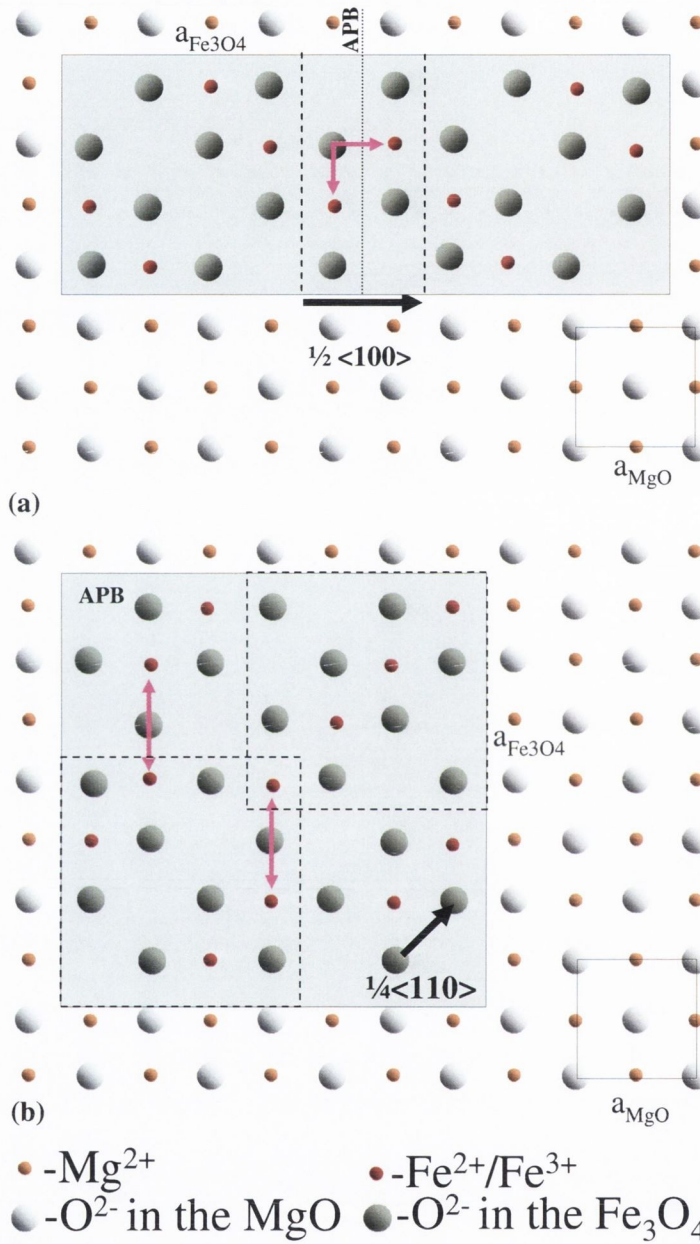


Figure 2.8. Schematic of magnetic exchange interactions formed across antiphase boundaries (APBs) in Fe₃O₄ films grown on MgO (100) substrate (a) $1/2\langle 100 \rangle$ shift parallel to boundary plane. 90 degree ferromagnetic super exchange is indicated with arrows in violet colour (b) $1/4\langle 110 \rangle$ shift perpendicular to the boundary plane. 120 degree antiferromagnetic super exchange is indicated with arrows in violet colour.

in Fe_3O_4 , the magnetic field must be large enough to align all B site spins parallel to the field direction, while A site spins are antiparallel due to AB exchange coupling. In bulk crystals this occurs at relatively low fields (anisotropy field ~ 310 Oe) which only needs to be large enough to overcome the anisotropy and dipolar fields. But in the case of thin films, in order to create this collinear arrangement of the spins the field must be large enough to overcome the strong exchange coupling across the APB which favours antiparallel B spins and antiparallel A spins on either side of the boundary. Since the exchange fields are very large, films remain unsaturated in fields as large as 70 kOe [14]. Since the presence of the APBs results directly from the growth process of Fe_3O_4 thin films grown on MgO substrates, the anomalous magnetic properties are intrinsic to the films, independent of preparation technique.

Exchange Interaction	Type and angle	Strength and sign	Presence
oct-ox-oct	super, 180°	AF, strong	At APB
tet-ox-tet	super, $\sim 140^\circ$	AF, strong	At APB
oct-ox-tet	super, $\sim 120^\circ$	AF, strong	Bulk and at APB
oct-ox-oct	super, $\sim 90^\circ$	FM, weak	Bulk and at APB
tet-ox-tet	super, $\sim 70^\circ$	AF, weak	At APB
oct-oct	direct	FM, weak	Bulk and at APB
tet-tet	direct	AF, weak	At APB
oct-tet	direct	FM, weak	At APB

Table 2.1. Magnetic exchange interactions across anti-phase boundaries in epitaxial Fe_3O_4 films grown on MgO, listed according to their relative strength.

2.3.4 Conductivity in epitaxial Fe_3O_4 films

The resistivity of Fe_3O_4 thin films is higher than the bulk and increases with decreasing thickness. This can be explained by the presence of antiphase boundaries which strongly modify the conductivity in Fe_3O_4 thin films. The magnetic coupling over the majority of these boundaries can be antiferromagnetic. The conductivity of Fe_3O_4 is proportional to the square of the transfer integral: $\sigma \propto t^2$. Previous studies have shown that the transfer integral t , depends on the angle between two spins on neighbouring ions [49, 50], which is given by:

$$t = t_0 \cos \frac{\varphi}{2} \quad (2.5)$$

where φ is the angle between the two spins. In the case of ferromagnetic alignment, the two spins are parallel and the transfer integral has its maximum value t_0 . In the case of anti-ferromagnetic alignment the transfer integral becomes zero. This is the case at the APBs when an anti-ferromagnetic coupling is present. The epitaxial films are made up of structurally shifted domains, within which the conduction resembles bulk behaviour, and at the boundary regions the conduction is strongly reduced. The enhancement in resistivity with reduction in film thickness is due to a decrease in APB domain size or increase in APB density with reduction in thickness [47].

2.3.5 Magnetoresistance in epitaxial Fe_3O_4 films

The epitaxial films exhibit large negative MR around and below T_v . Coey et al have studied the MR of Fe_3O_4 in polycrystalline thin films, powder compact and single crystals. It has been suggested that MR in these systems are associated with spin polarised electron transport across the adjacent ferromagnetic grains with misaligned magnetisation due to the decoupled magnetic exchange [45]. Li et al have studied the low field MR behaviour of a polycrystalline Fe_3O_4 film grown on polycrystalline SrTiO_3 substrate and compared it with an epitaxial film grown on $\text{MgO}(100)$ substrate [51]. The two films showed comparable resistivity and exhibited very similar temperature dependence. MR behaviour of the two films were also similar with a peak occurring in both cases close to T_v , which is due to the abrupt changes in the thermodynamic quantities accompanied with the first order Verwey transition. Eerenstein et al have studied the MR of epitaxial Fe_3O_4 films grown on $\text{MgO}(100)$ substrate and the effect was attributed to the spin polarised transport across the antiferromagnetically coupled APBs [20,52]. As explained in the previous section the conductivity in the films are proportional to transfer integral, $\sigma \propto t^2$, and if the spin on a neighbouring ion is rotated over an angle φ the transfer integral is reduced to Equation 2.5. Therefore transfer of the conduction electron between ions with antiparallel spins at an antiferromagnetically coupled APB is blocked and conductivity is zero. When a magnetic field is applied, the spins at the boundaries will align themselves to

some degree with the magnetic field so that the electron transfer across the boundaries will increase [20,52]. Considering two spin chains separated by an antiferromagnetic boundary, they obtained the relation:

$$\cos^2 \varphi_{AF} = \frac{HM_s}{W_{AF}} \quad (2.6)$$

Where \mathbf{H} is the applied magnetic field, \mathbf{M}_s is the saturation magnetisation and $W_{AF} = A_{AF}^2 / A_F d^2$ (where A_F is the exchange stiffness constant, A_{AF} is the exchange stiffness constant for antiferromagnetic exchange interaction at the boundary and d is the distance between two neighbouring spin chains along the boundary). This analysis shows that transport through an antiferromagnetically coupled APB will be zero if no magnetic field is applied and increases approximately linearly with a magnetic field. This is the cause of the magnetoresistance behaviour in these films. The magnetoresistance behaviour of Fe_3O_4 films will be discussed in detail in chapter 5 and 6.

Bibliography

- [1] M.L. Glasser and F.J. Milford, Phys. Rev. **130**, 1783 (1963).
- [2] E.J.W. Verwey, Nature (London), **144**, 327 (1939).
- [3] F. Walz, J. Phys. Condens. Matter **14**, R285 (2002).
- [4] A. Yanase and K. Saratori, J. Phys. Soc. Jap. **53**, 312(1984).
- [5] A. Yanase and N. Hamada, J. Phys. Soc. Jap. **68**, 1607(1999).
- [6] K Ghosh, S.B Ogale, S.P Pai, M. Robson, Eric Li, I. Jin, Zi-wen Dong, R.L Greene, R. Ramesh, T. Venkitesan, and M. Johnson, Appl. Phys. Lett. **73**, 689 (1998).
- [7] P. Sensor, A. Fert, J.L. Maurice, F. Montaigne, F. Petroff, and A. Vaures, Appl. Phys.Lett. **74**, 4017 (1999).
- [8] J.R. Cullen and E.R Callen, J. Appl. Phys. **41**, 879 (1970).
- [9] J.R. Cullen and E.R Callen, Phys. Rev. B **7**, 397 (1973).
- [10] D. Ihle, Phys. Stat. Sol. B **121**,217 (1984).
- [11] D. Ihle and B. Lorenz, J. Phys. C **19**, 5239 (1986).
- [12] D. Ihle and B. Lorenz, Phil. Mag. B **42**, 337 (1980).
- [13] C. A. Kleint, H.C. Semmelhack, M. Lorenz and M.K. Krause, J. Magn. Magn. Mater.**140-144**, 725 (1995).
- [14] D.T. Margulies, F.T. Parker, M.L. Rudee, F.E. Speda, J.N. Chapman, P.R. Aitchison and A.E. Berkowitz. Phys. Rev.Lett.**79**,5162 (1997).
- [15] F.C Voogt, T.T.M. Palstra, L. Niesen, O.C. Rogojanu, M.A. James and T. Hibma, Phys. Rev. B. **57**, 08107 (1998).
- [16] R.J.M. van de Veerdonk, M.A.M. Gijs, P.A.A. van der Heijden, R.M. Wolf and W.J.M. de Jonge, Mat. Res. Soc. Symp. Proc. **401**,455 (1996).
- [17] W. Eerenstein, T.T.M. Palstra, T. Hibma and S. Celotto Phys. Rev. B **66**, 201101 (R)(2002).
- [18] A. Gupta, G.Q. Gong, G. Xiao, P.R. Duncombe, P. Lecoeur, P. Trouilloud, Y.Y. Wang, V.P. Dravid and J.Z. Sun, Phys. Rev. B **54**, R15629 (1996).
- [19] M. Ziese and H.J. Blyte, J. Phys. Cond. Matter **12**, 13 (2000).
- [20] W. Eerenstein, T.T.M. Palstra, S.S. Saxena and T. Hibma Phys. Rev. Lett. **88**, 247204(2002).
- [21] W.H. Bragg, Phyl. Mag.,**30**:305,1915

- [22] International Crystallography Tables, Phys.Lett.**1**, 251 (1962).
- [23] E.J.W. Verwey, P.W. Haayman. Physica, **8**:979,1941.
- [24] E.J.W. Verwey, P.W. Haayman and C.W.Romenijn, J. Chem. Phys.,**14**:181,1947.
- [25] D. Khomskii. Electronic Structure, Exchange and magnetism in Oxides. Springer- Verlag Berlin Heidelberg, 2001.
- [26] Z. Zhang and S. Satpathy, Phys. Rev. B **44**, 319 (1991)
- [27] J.P. Wright, J.P. Attfield and P.G. Radaelli, Phys. Rev. Lett. **87** 266401 (2001).
- [28] C.A Domenicali, Phys.Rev.,**78**(4):458,1950
- [29] W. Kunding and R.S. Hargrove, Solid State Comm. **7**, 223 (1969).
- [30] R. Aragón, D.J. Buttrey, J.P. Sheperd and J.M. Honig, Phys. Rev. B **31**, 430 (1985).
- [31] J García and G. Subaís, J.Phys.Cond. Matter, **16**,R145,2004.
- [32] G. Kh. Rozenberg, M.P. Pasternak, W.M.Xu, Y. Amiel, M. Hanfland, M. Amboage, R.D.Taylor and R. Jeanloz. Phys. Rev. Lett, **96**,045705,2006.
- [33] S. Iida, K. Mizusuma, M.Mizouchi, K.Kose, K.Kato, K.Yanai, N.Goto and S. Yumoto, J. Appl. Phys, **53**,2164,1982.
- [34] M. Mizoguchi, J. Phys. Soc. Jap, **44**,1501,1978.
- [35] J. M. Zuo, J.C.H. Spence and W. Petuskey, Phys. Rev. B, **42**,8451,1990.
- [36] J.P. Wright, J.P. Attfield and P.G. Radaelli, Phys. Rev. B, **66**, 214422, 2002.
- [37] J García , G. Subaís, M.G. Proietti, J.Blasco, H.Renevier, J.l.Hodeau and Y.Joly, Phys. Rev. B, **63**, 054110,2001.
- [38] G. Subaís, J García , J.Blasco ,M.G. Proietti, H.Renevier, and M.C. Sanchez. Phys. Rev. Lett, **93**,156408,2004.
- [39] M. Mizoguchi, J. Phys. Soc. Jap, **70**(8),2333,2001.
- [40] J. B. Goodenough, Magnetism and Chemical Bond, Wiley New York 1963.
- [41] P.A. Cox, Transition Metal Oxides, Oxford University Press, Oxford 1995, 221-223.
- [42] P.W. Atkins, Physical Chemistry 5th edition, Oxford University Press 1994.
- [43] B.A Calhoun, Phys.Rev.,**94**(6):1577,1954
- [44] S. Celotto, W.Erenstein, and T Himba. Eur.Phys. J.B, **36**:271,2003.

- [45] J.M.D. Coey, A.E. Berkowitz, Li. Balcells, F.F.Putris, and F.T.Parker
Appl. Phys. Lett., **72**:734, 1998.
- [46] T. Hibma, F.C. Voogt, L.Niesen, P.A.A. van der Heijden, W.J.M. de
Jonge, J.J.T.M. Donkers, P.J. vab der Zaag, J. Appl. Phys, **85**, 5291
(1999).
- [47] W. Eerenstein, T.T.M. Palstra, and T. Hibma, Phys. Rev. B **68**, 014428
(2003)
- [48] C.A. Kleint, M.K. Krause, R.Hhne, M. Lorenz, H.C. Semmelhack, A.
Schneider, D. Hesse, H Sieber, J. Taubert and W. Andr, J.Phys. **IV**, **7**
C1,593 (1997)
- [49] P.W. Anderson and H. Hasegawa, Phys. Rev. **100**, 675 (1955).
- [50] K. Kubo and N. Ohata, J. Phys. Soc. Japan **33**, 21 (1972).
- [51] X.W. Li, A.Gupta, G.Xiao, G.Q. Gong, J. Appl. Phys, **83** (1998) 7049.
- [52] W. Eerenstein, T.T.M. Palstra, and T. Hibma, Thin solid films, **400**, 90
(2001)

A concept exists for a physicist only when there is a possibility of finding out in a concrete case whether or not the concept applies.

Einstein 1920

Chapter 3

Experimental Details

3.1 Introduction

The rapid advancements in the study and application of ultra-thin films over the last few decades are due to improvements in ultra high vacuum technology and deposition techniques. In this chapter we give a detailed description of the thin film growth methods and the techniques used to characterize the films. The chapter is divided into two main sections. In the first section (§3.2), The thin film growth using molecular beam epitaxy (MBE) and *in situ* analysis of the samples using reflection high energy electron diffraction (RHEED) are discussed. In the second section (§3.3), *ex situ* characterisation of samples using different methods such as high resolution X-ray diffraction (HRXRD), vibrating sample magnetometer (VSM), low temperature magneto transport measurements, Raman spectroscopy, and transmission electron microscopy (TEM) are discussed.

3.2 Molecular beam epitaxy (MBE)

‘Epitaxy’ is a specialized thin-film deposition technique. The term epitaxy (Greek; "epi" "upon" and "taxis" "in ordered manner") describes an ordered crystalline growth on a crystalline substrate. It involves the growth of crystals of one material on the crystal face of another (hetero-epitaxy) or the same (homo-epitaxy) material. Epitaxy forms a thin film whose material lattice structure and orientation or lattice symmetry is identical to that of the substrate on which it is deposited.

Molecular beam epitaxy is a sophisticated form of vacuum evaporation. Molecular beams of the constituent elements are generated from sources and travel without scattering to a substrate where they combine to form an epitaxial film. In solid source MBE, material is evaporated from solid ingots by heating or with an electron beam. The rate of growth depends on the flux of material in the molecular beams which can be controlled by the evaporation rate and, most importantly, switched on and off with shutters in a fraction of the time required to grow one monolayer. The basic principle of epitaxial growth is that atoms on a clean surface are free to move around until they find a correct position in the crystal lattice to bond. In practice there will be more than one nucleation site on a surface and so growth is by the spreading of islands. The mobility of an atom on the surface will be greater at higher substrate temperature resulting in smoother interfaces, but higher temperatures also lead to a lower "sticking coefficient" and more migration of atoms within the layers already grown. Clearly there will be a compromise temperature to achieve the best results. Using MBE thin films can be grown with very precise control over the film thickness and stoichiometry, thus enhancing the reproducibility of quality thin film production.

In our MBE system a molecular beam of a metal species is created by the evaporation of the source material using a beam of high energy electrons. The molecular beam subsequently condenses on a substrate and the thin film grows epitaxially. By controlling the flux of the molecular beam and by controlling the energy of the evaporating e-beam, one can control the growth rate of the thin film. Metal oxides may also be grown by MBE by simply adding the appropriate gas into the deposition chamber. The gas may be added in molecular form or, using a plasma generator, may be added in atomic form. In this manner we were able to produce the magnetite films for this research work. The low background pressure possible due to the advances in high vacuum technology ensure that the growing film remains contamination free for the time necessary to deposit the films and analyse them *in situ*.

All of the films grown and investigated during the course of the research outlined in this thesis were deposited using a DCA MBE M600 Molecular Beam Epitaxy System. The system comprised of two separate chambers connected via a gate valve. The chambers were designated the Load-

Lock chamber and the Deposition chamber. Substrates and samples were transferred between the chambers using a magnetically coupled transfer arm, which had a transfer cup attached. The transfer cup facilitated transfer of the bare substrate/sample from the Load-Lock chamber to the Deposition chamber and vice versa. The deposition chamber was fitted with a reflection high energy electron diffraction (RHEED) system for *in situ* sample analysis. Construction of the system was in all parts UHV compatible while all parts were fitted with standard ConFlat (CF) type flanges for use with flat Copper gaskets. The base pressure of the Load-Lock chamber was of the order 5×10^{-7} Torr while the base pressure of the Deposition chamber was of the order of 5×10^{-10} Torr. The detailed description of different parts of MBE is given in the following sections. A photograph of the system layout is given in Figure 3.1 below.

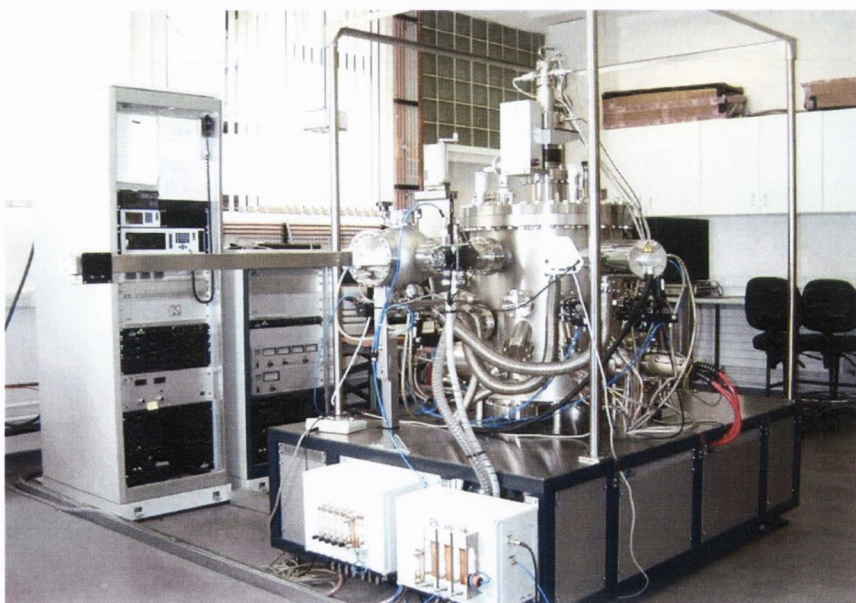


Figure 3.1. The entire MBE system, including the load-lock chamber, the deposition chamber, the transfer arm and the assorted power electronics cabinets.

3.2.1 Ultra high vacuum (UHV) system

3.2.1.1 Deposition chamber

The deposition chamber associated with the MBE system was a vertical 600 mm ID chamber with a wire sealed removable top flange. A schematic of the chamber is shown in Figure 3.2 below. The system was fitted with a low wobble substrate manipulator which consisted of a heavy duty Z-manipulator, a hollow shaft inverted rotary motion feed-through and a high temperature heater stage. The substrate manipulator was located vertically in the centre of the chamber meaning that, once loaded the substrate was facing downwards during all processes and manipulations. The rotary drive consisted of two concentric tubes of which the inner was stationary and the outer could be rotated, using magnetic coupling. All electrical wiring (thermocouple and power) were conducted through the inner stationary tube.

The substrate manipulator featured a new design for the heater electrical contacts and the support bearings. The heater stage was a high temperature heater stage with a PBN/PG/PBN cup heater element. The element was surrounded by a radiation shield. A C-type thermocouple (W/Rh) was located in the space between the filament and the substrate. The temperature was controlled via a EURO THERM 2408 controller used in conjunction with a DC power supply. All pre-deposition annealing was done *in situ* using the substrate manipulator heater avoiding the need for a separate annealing chamber. This improved the quality of the cleaned substrates and minimised possible contaminants that may have arisen as a result of the transfer procedure between adjacent chambers. The heavy duty Z-stage was used for loading and RHEED alignment purposes. The manipulator also allowed the substrate to be lowered to any height above the main shutter thus increasing the effectiveness of the main shutter in interrupting all e-beams. The substrates were loaded into Molybdenum holders which in turn were loaded into the substrate manipulator with a minimum of stress and the active substrate surfaces were pointing down and held in place by gravity alone. The Molybdenum holder allowed for low electron beam incident angle RHEED measurements to be made. Details of the attachment of the substrates to the sample manipulator and the RHEED system alignment will be discussed in later sections.

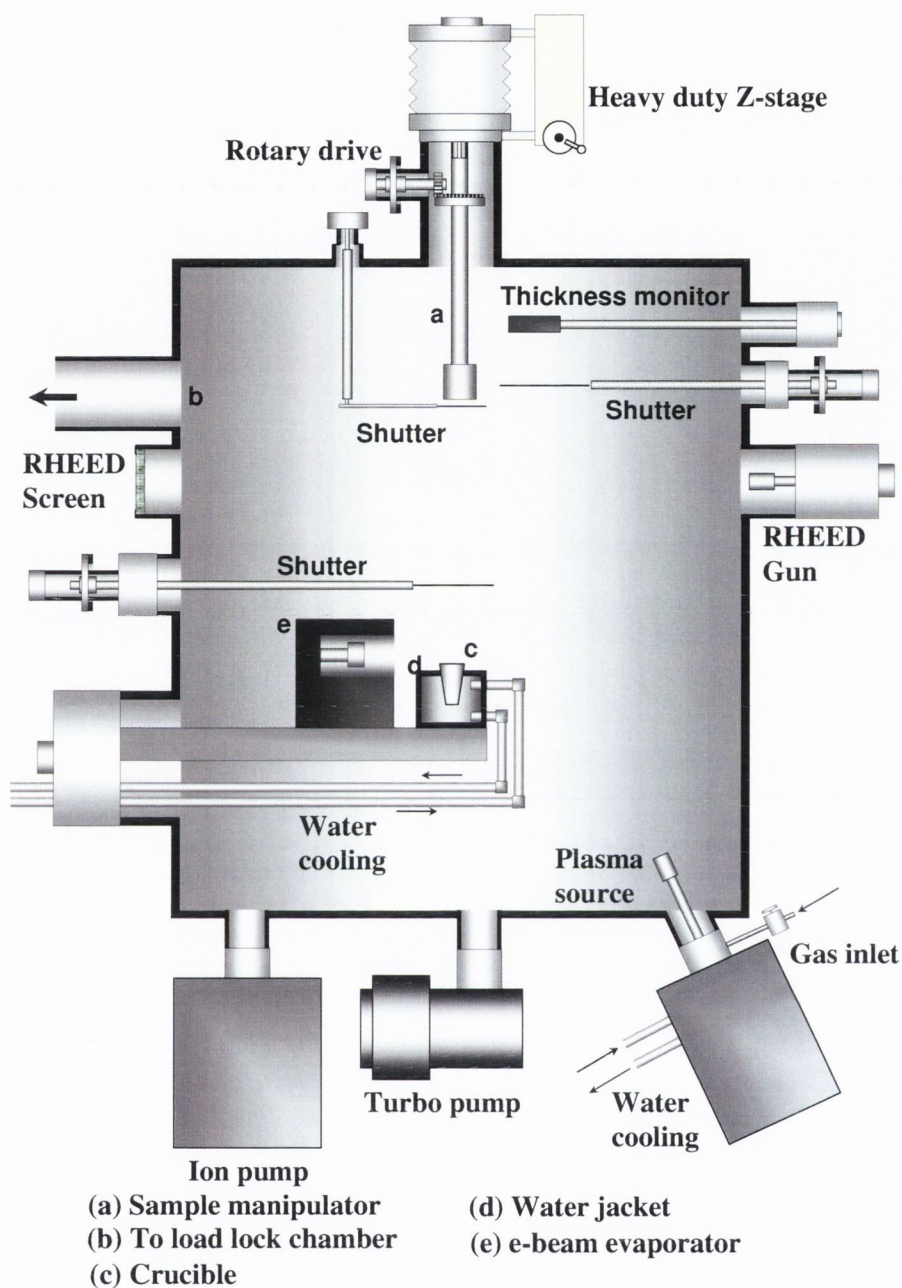


Figure 3.2. Schematic of the MBE deposition chamber layout, depicting the RHEED system, the e-gun and the associated shutters and thickness monitor head, and the vacuum system.

While the chamber was equipped with two electron guns (e-guns), one magnetron gun and five effusion cells only the one e-gun was utilised for this work. The source materials for evaporation were loaded into individual crucibles, with the composition of the crucible compatible to the source material to preclude the risk of damage or contamination. The e-guns were

mounted on NW200CF flanges allowing easy access for cleaning. The e-guns were also equipped with external support rails which allowed easy removal of the e-guns and crucibles from the deposition chamber thus facilitating re-filling and servicing. One of the e-guns, designated e-gun-1, (the one which was used in this work) was used in conjunction with a single, large crucible which typically contained Fe pellets. The second e-gun, designated e-gun-2, was used in conjunction with a moveable Molybdenum plate which housed four individual small crucible holders. Each crucible was filled with a different source material and the plate, and hence the crucibles, were positioned in relation to the electron beam (e-beam) by means of a feed-through screw. Thus, at any one time the deposition chamber was primed with up to five different source materials.

The electron beam generated by each e-gun was controlled by a sweeper mechanism, which allowed the electron beam characteristics to be adjusted. This allowed the frequency at which the electron beam swept the relevant crucible to be controlled along with the X- and Y-axis travel of the beam over the crucible surface. This was achieved by controlling the voltage applied to plates within the e-gun architecture, thus controlling the deflection of the electron beam. The relevant values were adjusted using a separate, handheld control panel. When the sweeper functionality was in an off position the electron beam fell on only one point of the crucible.

The e-gun power and hence the deposition rates were monitored and controlled using an INFICON IC/5 deposition rate controller. In general, the higher the power applied to the e-gun the more intense the electron beam and thus the higher the deposition rate. Alternatively, the deposition rate could be controlled using the sweeper module. The energy density of the electron beam could be controlled by adjusting the area of the crucible upon which the electron beam fell. The smaller the X- and Y- travel of the beam the higher the electron beam density and so, the same deposition rate could be achieved for a lower power rating. In general this method was not used as the electron beam was set to sweep the entire crucible surface to try and maintain uniform heating of the source material and minimise the effects of local hot spots.

Each e-gun had a port associated with it to house a quartz crystal monitor head. These crystal monitor heads were positioned such that they were shielded from other sources. Each crystal monitor head was further

shielded by a shutter which, when used correctly, acted to prolong the lifetime of the monitor head. Each e-gun also had an associated shutter positioned over the relevant crucible evaporation position. This shutter acted to allow material impact on the crystal monitor head but not on the substrate. This in effect allowed the system to be stabilised before deposition commenced. Also associated with each e-gun was a unique beam spot observation system based on a rotatable mirror configuration. Thus, the respective mirrors could be hidden during deposition, to avoid damage or contamination, by means of a rotary feed-through.

The shutter system as described above was a linear electro-pneumatic shutter system. The shutter blades were moved outside the vacuum with a pneumatic actuator. The construction was designed to give enough driving force even after heavy contamination of the shutter blade. The shutter operation was completely controlled using Festo controllers which allow for easy adjustment of the shutter motion via adjustable pressure valves. The shutters were run in soft-mode to minimise vibrations and flake fallings. The deposition chamber also consisted of a main shutter positioned directly below the substrate manipulator. This shutter allowed all beams to be interrupted at once, no matter the source. This shutter was only opened during the loading of a substrate and during deposition. At all other times it was kept closed to prevent any unwanted material or contaminate impinging on the substrate.

The electron gun area was separated from the main body of the deposition chamber by a water cooled roof. The lower part of the deposition chamber was fitted with a water cooled shroud that effectively separated the growth area from the e-guns. At the lower end of the water panel the source positions were separated from each other with double wall Mo beam separator plates. These plates were in good thermal contact with the water panel and the double walled design effectively prevented any thermal or chemical cross talk between different sources.

The deposition chambers pumping system consisted of a VARIAN Triode ion pump with a pumping speed of 500 ls^{-1} , a VARIAN V1000 1000 ls^{-1} turbo pump and a VARIAN Tri Scroll 600 dry scroll vacuum pump. The turbo pump was separated from the deposition chamber with an electro-pneumatic gate valve via a NW200CF flange. The vacuum system thus described allowed

base pressures of the order of 5×10^{-10} Torr to be achieved in the deposition chamber.

3.2.1.2 Load-Lock Chamber

The Load-Lock chamber facilitates the loading and transferring of the sample to deposition chamber, using a magnetically coupled transfer arm, without breaking the ultra high vacuum condition maintained in the deposition chamber. The Load-Lock chamber design utilises a small volume chamber consisting of a 200 mm ID spherical vessel. The substrate holder is introduced into the Load-Lock chamber via a VITON sealed quick access door (top loader). The Load-Lock chamber is equipped with a 70 ls^{-1} VARIAN turbo pump and a VARIAN Dry Scroll pump. The chamber is vented through a Nupro vent valve and/or the automatic VARIAN vent valve mounted on the turbo pump. The chamber is vented using either nitrogen or argon gas. The vacuum monitoring includes a GRANVILLE – PHILLIPS control unit with a Convectron gauge head and a nude ion gauge head.

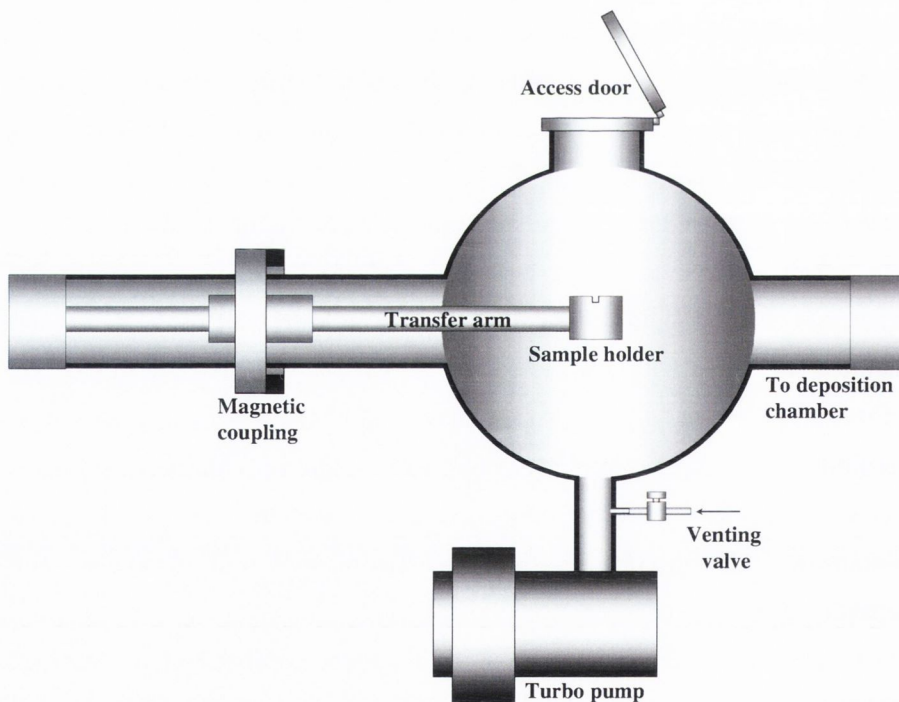


Figure 3.3. Schematic of the MBE Load-Lock chamber layout, depicting the Sample holder, magnetically coupled transfer arm and the vacuum system.

The maximum baking temperature for the Load-Lock chamber was 150 °C, limited by the VITON sealed quick access door. Schematic of the MBE Load-Lock chamber is shown in Figure 3.3.

3.2.1.3 Plasma source

The MBE system was fitted with an Oxford Scientific OSPrey Plasma Source set to operate in Atomic Mode. The specially designed aperture plate inhibits ions from escaping from the plasma, yet allows reactive neutrals to escape and form the dominant beam fraction. The emitted particles are largely thermalised through multiple collisions on passing through the aperture. The plasma source was fitted to the deposition chamber via a CF100 port. Microwaves with a frequency of 2.45 GHz were generated by a microwave magnetron operating at a magnetron power of 10-250W. The microwaves were then coupled through a resonant coupler into a coaxial feed-through structure which guided the microwaves into the vacuum and up into the plasma chamber. The plasma was excited in this chamber and the microwaves absorbed. The plasma was confined to this chamber. Further enhancement of the plasma density was provided by a magnetic quadrupole arranged around the discharge chamber which generates an 87 mT field inside the plasma. At this field strength electrons in a 2.45 GHz microwave field undergo electron cyclotron resonance motion. The spiralling motion greatly enhanced the electron path length and therefore the probability of collisions leading to the creation of ions was increased. The open end of the plasma chamber was fitted with aperture plates with a number of small holes. These acted to reduce the number of ions leaving the plasma chamber thus effectively reducing the ion current. The beam leaving the plasma chamber consisted mainly of molecular and atomic particles. In this manner molecular oxygen (O₂) was converted into atomic oxygen and subsequently introduced into the deposition chamber. The atomic oxygen impinged on the surface of the substrate in the same manner as the metallic species and in such a manner thin film metallic oxides were deposited. For this work the only metallic oxide deposited was magnetite.

3.2.1.4 Water Cooling system and Interlock system

All of the water-cooled equipment associated with the MBE system had its own separate water-cooling circuits. The main water-cooled pieces of

equipment were the e-guns and the substrate manipulator. The cooling lines were controlled by manual ball valves located in a cooling block. Namur type sensors monitor the water lines to ensure there was sufficient water to cool the respective equipment. There was a safety interlock system to ensure sufficient water cooling. A compressed air line was used to ensure sufficient air pressure to provide sufficient water pressure. Failures of the water pressure lead to tripping of the interlock and system shutdown.

3.2.1.5 Sample Preparation and Loading

Each substrate (MgO substrate) was de-greased in an ultra sonic bath for 15 minutes in each of Methanol, Iso-Propanol and Acetone. The substrate was then boiled in Acetone for several minutes prior to being loaded into the Molybdenum (Mo) substrate holder, shown in Figure.3.4 (a) below. The Mo holder had a 10mm × 10mm size square hole in the centre, which was designed in such a way to hold the sample, and three protruding parts separated radially at 120 degrees apart. The Mo holder was placed on a stainless steel cup (see Figure.3.4 (b)) which had three square slots aligned with the three protruding parts in the Mo holder. The substrate was loaded with the polished side facing down on the Mo holder and was lifted out of the cup using a specially designed transfer tool that accompanied the MBE system which is shown in Figure.3.4 (c). The transfer tool had two co-axial rings inside the main cylindrical tube. The bottom ring had three square slots (marked as (i) in the Figure.3.4 (c)) similar to the ones in the sample cup, which was aligned with the three protruding parts in the Mo holder. The transfer tool was then inserted in to the cup by aligning the protruding parts of Mo holder with the slots in the transfer tool. The transfer tool was rotated in clockwise direction so that the protruding parts of Mo holder moved within the rings of transfer tool and locked at a stopping screw which is marked as (ii) in the Figure 3.4 (c). The Mo holder, and substrate, was then transferred to the transfer cup (similar to the one which was used before) in the Load-Lock chamber via the VITON sealed quick access door (top loader).

Once loaded the Load-Lock chamber was pumped until the pressure reached $\sim 5 \times 10^{-7}$ Torr, at which point the gate valve was opened and the transfer arm was moved to a position in the centre of the Deposition chamber. The substrate manipulator was lowered over the transfer cup until it coupled

with the Mo substrate holder. The manipulator was then turned through a pre-set angle into the lock position at which point the Mo holder was deemed to be

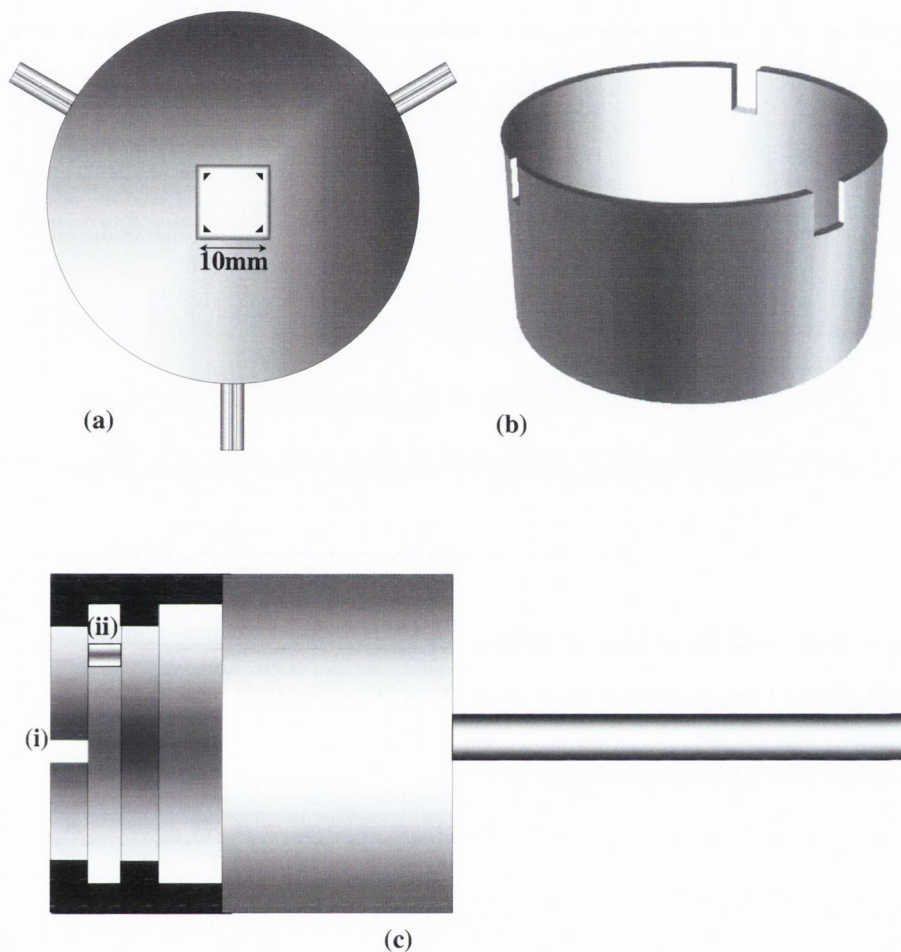


Figure 3.4. (a) Molybdenum sample holder (b) Cup (c) transfer tool (i) rectangular slot (ii) stopping screw

locked into the substrate manipulator by the same mechanism explained before in the case of transfer tool. The substrate manipulator was then raised again and the transfer arm, and transfer cup, withdrawn from the Deposition chamber. Once the transfer arm was completely removed from the Deposition chamber the gate valve was closed and the two chambers were essentially independent from each other again.

Once the substrate and Mo holder was loaded in the substrate manipulator the Deposition chamber was pumped until it again reached its base pressure of $\sim 5 \times 10^{-10}$ Torr. Only at this point did the *in-situ* annealing

commence. Generally the substrates were annealed at 600°C in UHV for 30 minutes and in an oxygen environment of 1×10^{-5} Torr at 600°C for 180 minutes. The substrates were annealed in an oxygen environment to ensure that any oxygen vacancies that may have arisen due to the UHV annealing were corrected for. On completion of the annealing the substrate surface was checked using RHEED to ensure the surface was smooth, clean and well ordered. In the event of any problem with the surface the substrate was annealed for a longer duration until a satisfactory RHEED image was obtained. The substrate was then deemed ready for deposition. The annealing procedures and deposition parameters used in the present work will be discussed in the following chapters.

3.2.2 *In-situ* sample characterisation

3.2.2.1 Reflection High Energy Electron Diffraction (RHEED)

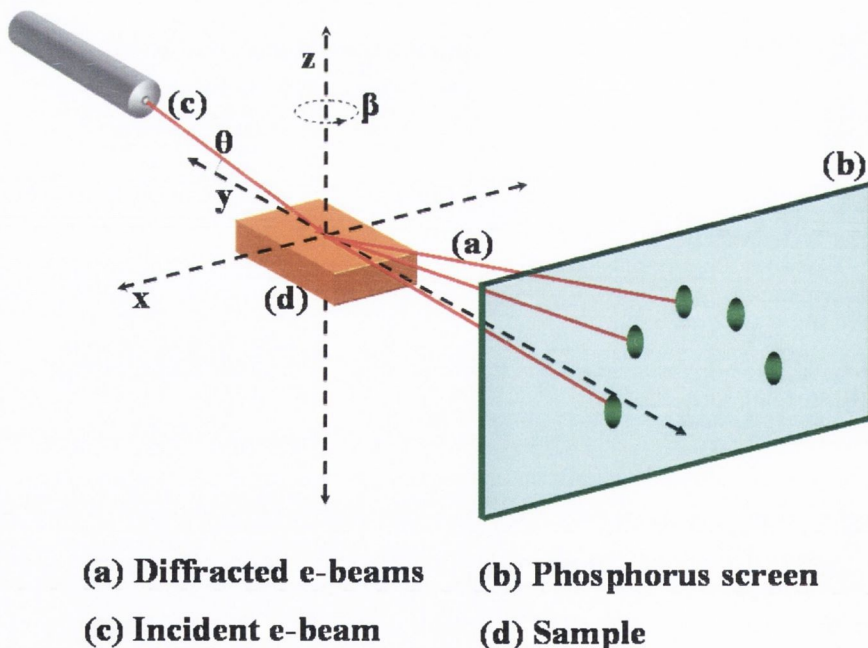


Figure 3.5. Schematic of the RHEED system configuration. The e-gun and the screen lie along the same radial axis of the deposition chamber thus the diffraction conditions are met and a diffraction image appears on the phosphor screen.

Reflection high energy electron diffraction (RHEED) is one of the most important *in situ* sample characterisation tools for the crystal structure and thickness of the film [1,2,3].

In a typical RHEED system a high energy electron beam (10-50 KeV) arrives at a sample surface under grazing incident angle (0.1-5 degree), see figure 3.5. At such higher energies the electrons can penetrate any material for several hundreds of nanometers. However, due to a grazing angle of incidence, the electrons only interact with the topmost layer of atoms (1-2nm) at the surface which makes the technique very surface sensitive. The scattered electrons collected on a phosphorus screen form a diffraction pattern characteristic for the crystal structure of the surface and also contain information concerning the morphology of the surface. The main reasons for the popularity of RHEED are accessibility of the sample during the deposition (the electron beam falls from the side and the flux of the depositing material is directed perpendicular to the sample surface) in relatively high pressure environment and the observation of intensity oscillation of the specular spot during deposition which allows determination of growth rate and growth mode [4]. A brief description of the basic principles and analysis of RHEED is given in the following section.

3.2.2.2 Basic principles of RHEED

Impinging electrons on the sample surface interacts with the electrostatic potential $U(\mathbf{r})$ of the solid. After the scattering some electrons lose energy (inelastic scattering) while some electrons retain their energy (elastic scattering). Inelastically scattered electrons forms the features in a RHEED pattern called Kikuchi patterns [1]. The main part of elastic electrons scatters at the outermost atomic layer and consequently very surface sensitive.

However, inelastic electrons are often indistinguishable from the elastic ones and contribute significantly to the total detected intensity. In Kinematical scattering theory, where only single scattering events are considered, the possible reflections are determined when the Bragg diffraction condition:

$$\mathbf{K}' - \mathbf{K}_0 = \mathbf{G} \quad (3.1)$$

is satisfied, where \mathbf{K}_0 is the wave vector for incident beam, \mathbf{K}' is the wavevector for diffracted beam and \mathbf{G} is the reciprocal lattice vector. This

implies that the conditions for diffractions are met when the incident and diffracted wave vectors differ by a reciprocal wave vector. In the case of elastic scattering, which means that $|\mathbf{K}'| = |\mathbf{K}_0|$, this diffraction condition can be cast into the geometrical construction of the Ewald sphere in reciprocal space. In this construction the tip of \mathbf{K}_0 is attached to a reciprocal lattice point. The sphere around the origin of \mathbf{K}_0 with radius $|\mathbf{K}_0|$ then defines the Ewald sphere, see Figure 3.6. Reflections can occur for all \mathbf{K}' connecting the origin of the sphere and a reciprocal lattice point on the sphere.

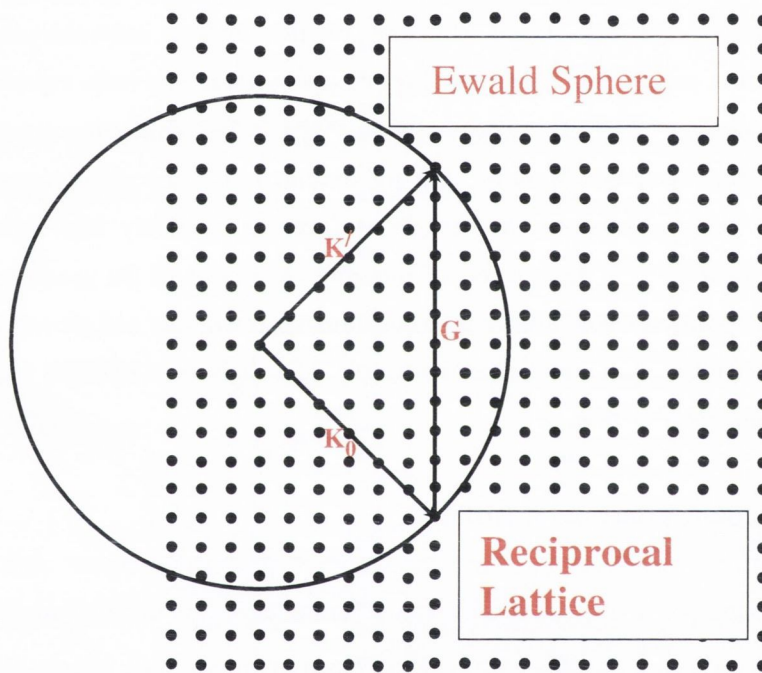


Figure 3.6. Schematic of the requirements necessary for the RHEED diffraction conditions to be fulfilled. The Ewald sphere is a sphere of radius \mathbf{K}_0 .

The surface normal component \mathbf{K}_{0z} of the incident wave vector which determines the penetration into the material can be carried over a large range of values by changing the incidence angle θ . For low incidence angles the sampling depth of RHEED can be very small. This implies that the periodic part of the crystal beneath the surface can usually be neglected and therefore we can approximate the sampled volume in the reciprocal lattice by a two dimensional layer. The reciprocal lattice then degenerates into a set of one-

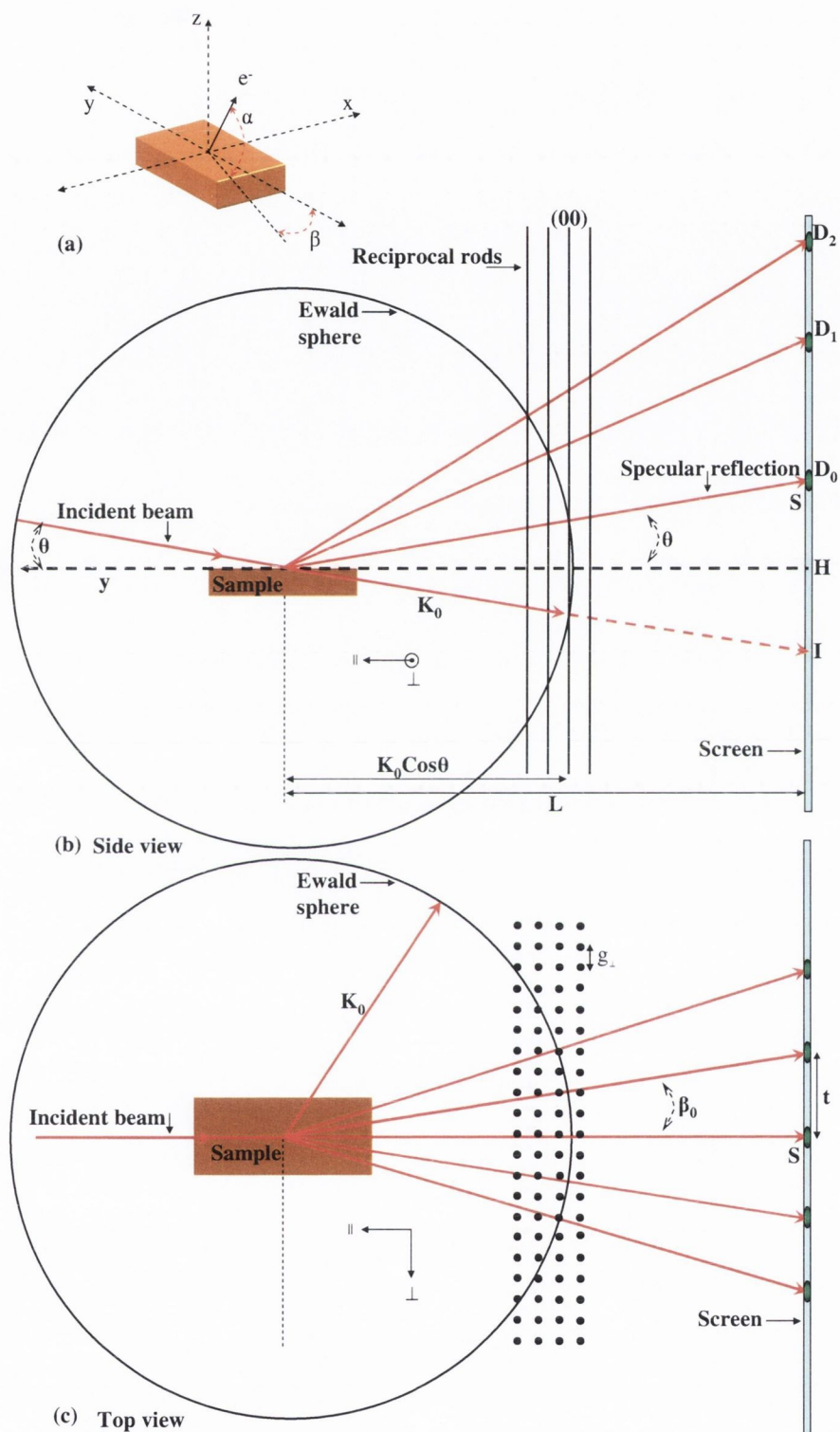


Figure 3.7. Schematic of the RHEED diffraction geometry. (a) orientation of the sample with the beam (b) side view of the intersections of Ewald sphere with the reciprocal lattice rods. (c) Projection of the Ewald sphere on a Plane parallel to the sample surface.

dimensional rods along the z direction perpendicular to the surface. In RHEED, the Ewald sphere is large enough to produce an almost planar cut through the first few Brillouin zones of the reciprocal lattice. Thus, the intersection of the Ewald sphere with a reciprocal lattice rod is almost tangential. This leads to the elongated streaks associated with a clean, well ordered sample surface. Any degradation of the streaks observed is an indication of a rough, and possibly dirty, surface.

Since the reciprocal lattice consists of continuous rods every rod produces a reflection in the diffraction pattern as shown in the Figure 3.7 (b). The reflections occur on so-called Laue circles of radius D_n centered at \mathbf{H} . Diffracted beams are observed in the angular directions α and β as shown in the Figure 3.7 (a). The specular reflection or specular spot \mathbf{S} is located at the intersection of the zeroth-order Laue circle with the (00) rod. The origin of the reciprocal lattice is projected on to \mathbf{I} , where for some sample geometries the part of the incident beam that misses the sample becomes visible [1]. A quantitative method to determine the lattice constant of the sample from the RHEED pattern is given by Hernández-Calderón et al [5].

In a typical RHEED experiment with an electron wave vector $\mathbf{K}_0 \sim 10^2 \text{ \AA}^{-1}$ and reciprocal surface vector \mathbf{g} , the characteristic value of $\mathbf{g}/\mathbf{K}_0 \sim 10^{-2}$ this means that the Ewald sphere will touch a few rods at both sides of the (00) rod, see Figure 3.7 (b) and (c). The angles between these reflections will practically be same and are given by

$$\beta_0 = \tan^{-1} \left[\frac{\mathbf{g}_\perp}{\sqrt{(\mathbf{K}_0^2 - \mathbf{g}_\perp^2)}} \right] = \tan^{-1} \left(\frac{\mathbf{t}}{\mathbf{L}} \right) \quad (3.2)$$

where \mathbf{g}_\perp is the reciprocal lattice rod separation perpendicular to the beam. \mathbf{L} is the sample to screen distance and \mathbf{t} is the distance between streaks. Since $\mathbf{g}_\perp = 2\pi/\mathbf{d}_\parallel$, where \mathbf{d}_\parallel is the distance between equivalent rows of atoms parallel to the incident beam and $\mathbf{g}_\perp \ll \mathbf{K}_0$, where $\mathbf{K}_0 = 2\pi/\lambda_0$, the relation

$$\mathbf{d}_\parallel \mathbf{t} = \mathbf{L} \lambda_0 \quad (3.3)$$

is obtained from Equation (1) where λ_0 is the wavelength of the electron in the relativistic approximation. For a fixed electron beam energy and geometry

configuration, the parameter $L\lambda_0$ can be calibrated with a sample whose lattice constant is well known. In this way a precision in the determination of lattice constants of 10^{-3} can be easily obtained.

The intensity of specular spot in the RHEED pattern generally exhibits very regular oscillations as a function of time, under the growth conditions that lead to layer-by-layer growth or Frank-van der Merwe growth [6-9]. In the layer-by-layer growth mode one layer is essentially completed before material is added to the following layer. This periodic variation of the surface morphology is generally accepted as the reason for RHEED oscillations. The intensity of the specular spot of the clean substrate is maximum and when deposition starts, islands are formed on the surface resulting in an increase of the roughness and a corresponding decrease in intensity due to diffuse scattering [10]. After the completion of one monolayer the surface is again smooth and the intensity increases. This process is shown in the figure 3.8. RHEED oscillations are used to determine growth rates, layer thicknesses and alloy compositions [9]. For Fe_3O_4 one monolayer corresponds to a quarter of the unit cell which is 0.21nm. When the oscillation period is known, the thickness of the film can be calculated accurately from the deposition time.

The RHEED images obtained for a vicinal surface shows distinct features when beam directed along the step edges and perpendicular to the step edges. In the first case RHEED images shows vertical lattice rods and sharp Kikuchi lines are observed and in the second case RHEED images shows sharp horizontal kikuchi lines which are not observed in the first case.

This is because of the increased inelastic scattering due to the presence of atomic steps. The horizontal Kikuchi lines are generally slightly tilted with respect to the shadow edge due to the miscut of the sample surface. On a stepped surface there exist several reciprocal lattice sub-rods that run along the normal to the average miscut surface plane, representing the reciprocal lattice of the step edge, apart from the rods perpendicular to the singular planes between the steps [1]. When the Ewald sphere cuts these rods close to an out-of-phase condition, there are either multiple reflections or an intensity maximum displaced from the average centre of the rod resulting in splitted spots. The mechanism responsible for the spitting by the exit geometry of the electrons at a vicinal surface is shown in the Figure 3.9.

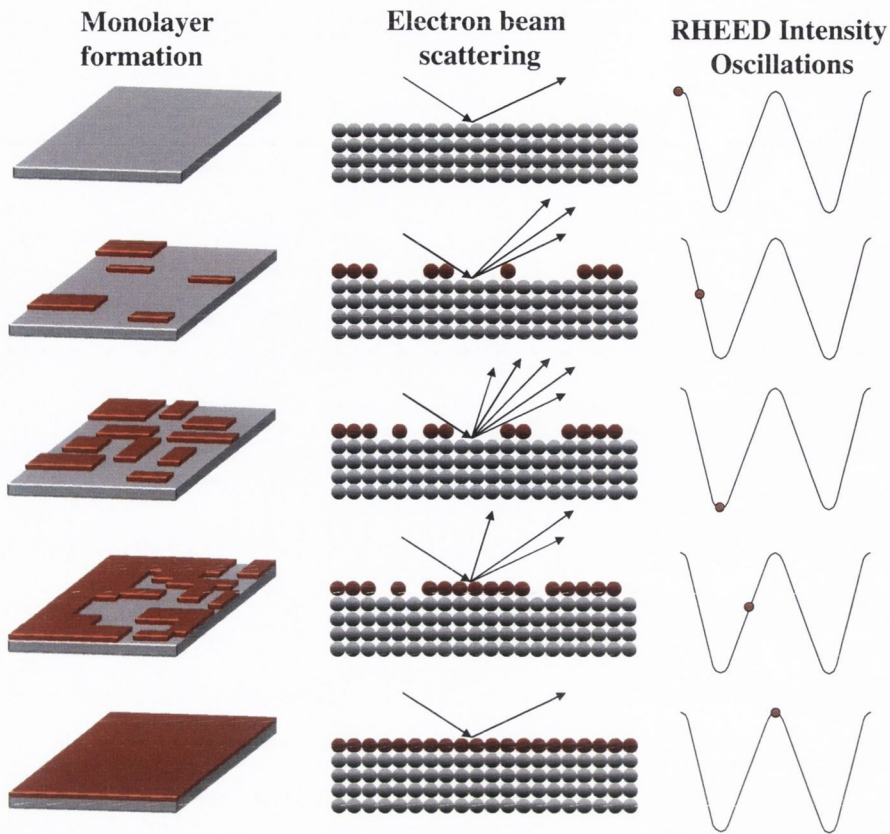


Figure 3.8. Schematic of the correlation of surface coverage with idealized RHEED oscillations.

When the electron crosses the potential step, its momentum perpendicular to the local surface orientation is reduced. If the electron exits at a step face, the momentum change is along the beam, and its direction remains basically unchanged whereas a significant deviation occurs for an exit path through the terrace top face. The two lines of the doublet therefore relate to different scattering geometries, and difference in intensities of the unrefracted and refracted lines leads to split spots [1]. The average surface tilt or miscut angle can be calculated from the spot separation using the following equation:

$$\theta_c = \frac{\langle \theta_e \rangle}{2\pi/sd - 1} \quad (3.4)$$

where $\langle \theta_e \rangle$ is the average exit angle of the two diffraction spots, d is the planer spacing and s denotes the spot separation in reciprocal lattice units. For the incident beam direction perpendicular to the step edges there are additional

features observed like slashes alongside the vertical rods due to the additional periodicity arising from the terrace width.

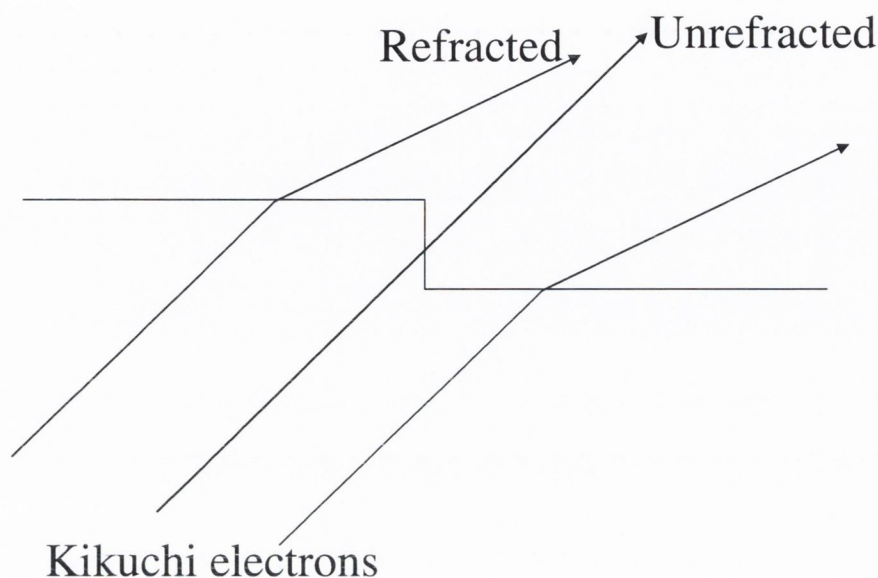


Figure 3.9. Ray paths of electrons leaving the crystal through terrace planes and step edges. The difference in refraction leads to split spots.

3.2.2.3 Instrumentation details of RHEED on the MBE system

The MBE deposition chamber was fitted with a Staib Instrumente Reflection High Energy Electron Diffraction (RHEED) RH 30 system. The system consisted of an electron gun (e-gun) fitted to one of the spare radial deposition chamber ports and a phosphor screen located diagonally across from the e-gun, fitted to one of the other spare deposition chamber ports. A CCD camera was mounted behind the screen to capture the RHEED images. The electron beam source and detector, effectively the e-gun and the phosphor screen, were located along the same axis as was required for the proper operation of the RHEED system. A general schematic of the RHEED configuration is given in Figure 3.5. The RHEED system was capable of working in UHV and also in a vacuum of the order of 5×10^{-5} Torr, though at this pressure the RHEED electron gun (e-gun) was pumped under a differential arrangement by the load-lock turbo pump. This was done in order to prevent oxidation of the RHEED e-gun element. Specifics of the RHEED system included:

- a small focus spot ($< 100 \mu\text{m}$)

- the beam size remains constant even over large working areas
- a small beam divergence (under 0.2 mrad) could be obtained

The RHEED system was equipped with an electron optical system specially designed for RHEED applications, i.e. it was equipped with an electron optical diaphragm system thus producing as shallow angle electron beam as possible. For all the RHEED images presented in this work the RHEED system was operated at a voltage of 20 kV and a filament current of 1.6 Amps. It must be noted that due to the proximity of e-gun-1 to the RHEED e-gun high quality RHEED images could not be produced while e-gun-1 was operating. This was due to the effect of the e-gun sweeper fields on the RHEED electron beam. Thus, RHEED images for films grown using e-gun-1 were only taken on completion of the deposition, with the sweeper in the off position.

To complete a RHEED analysis the substrate had to be rotated to ensure the correct crystal orientation was presented to the electron beam. This was achieved by rotating the substrate manipulator through pre-defined angles in order to present the $\langle 110 \rangle$ and the $\langle 100 \rangle$ directions to the e-beam. To ensure reproducibility the substrate manipulator was rotated through a multiple of angles to ensure several manifestations of the same crystal directions were investigated.

3.3 *ex-situ* sample characterisation

3.3.1 High Resolution X-Ray Diffraction (HRXRD)

The conventional high resolution X-ray diffraction has been developed in to a powerful tool for the nondestructive *ex-situ* investigation of epitaxial layers of heterostructures and superlattice systems. Wide range of information can be gathered from the diffraction patterns like composition and uniformity of epitaxial layers, their thickness, the built in strain and relaxation etc. The details of high resolution X-ray diffraction measurements employed in the present work and instrumentation details are given below.

3.3.1.1 Basic principles of HRXRD

Any measurements of lattice spacing are in principle determined by the Bragg's law :

$$d_{hkl} = \frac{n\lambda}{2\sin\theta} \quad (3.5)$$

where d_{hkl} is the spacing of lattice planes with Miller indices (hkl), θ is the corresponding Bragg angle, λ the wavelength of X-ray used, and n is an integer. In Figure 3.10 the scattering geometry is shown. Φ denotes the angle between the lattice plane (hkl) and the surface, \mathbf{K}_i and \mathbf{K}_s are the incident and the scattered wavevectors. \mathbf{p} is the surface normal and \mathbf{q} is the normal on reflecting planes. ω_+ is the angle between the surface plane and incident wavevector whereas ω_- is the angle between the surface plane and scattered wavevector. ω_+ is referred to as ω here after.

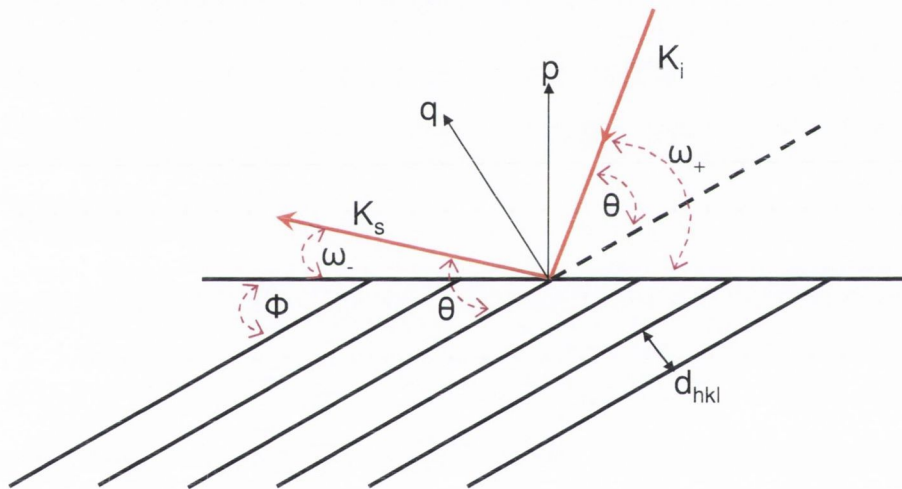


Figure 3.10. Scattering geometry of X-rays probing a plane having an interplanar angle ϕ with the surface plane.

In epitaxial systems typically lattice constant variations ($\Delta d/d$) between 10^{-2} to 10^{-4} have to be measured. The corresponding angular changes $\Delta\theta$ in the Bragg angle follow from the differentiation of Bragg's law (Equation 3.5) as

$$\frac{\Delta d}{d} = \frac{\Delta\lambda}{\lambda} - \frac{\Delta\theta}{\tan\theta} \quad (3.6)$$

It is clear from Equation 3.6 that for high precision measurements of lattice constants the wave length spread $\Delta\lambda$ has to be minimised and to achieve this,

the simple powder diffractometers using a focussing path for the X-Rays are replaced by double and triple-axis spectrometers equipped with multiple crystal or channel cut monochromators and analyzers. In a double axis spectrometer two crystals are used. The first one is often a dislocation free Ge or Si crystal, (sometimes cut to use an asymmetric Bragg diffraction for extremely high resolution), used as the beam conditioner. The second one is the sample to be investigated. In a triple-axis spectrometer apart from the beam conditioner and sample crystal, channel cut crystal is used as an analyser. The advantages of the triple-axis spectrometer are the following

- 1) Improved angular resolution permits the observation of weak diffraction satellites.
- 2) The triple-axis diffractometer allows Bragg plane tilts and dilatations to be determined independently.
- 3) Diffuse scattering e.g. originating from distorted interfaces can easily be separated from coherent Bragg scattering.

The disadvantage of triple axis in comparison with double-axis spectrometer is the analyser crystals reduce the intensity and thus longer measurement time results. The adjustment procedure is quite difficult in triple axis spectrometers comparison with the double-axis

3.3.1.2 Determination of Lattice parameters using HRXRD

During the epitaxial growth the unit cell of thin films can distort due to elongation or compression of in-plane lattice constants in the orthogonal directions depending on the sign of the lattice mismatch ϵ which is given below:

$$\epsilon = \frac{\mathbf{a}_{TF} - \mathbf{a}_s}{\mathbf{a}_s} \quad (3.7)$$

where \mathbf{a}_s and \mathbf{a}_{TF} are the substrate and thin film lattice constants. If the in-plane lattice constant of thin film is equal to the in plane lattice constants of the substrate with a corresponding change in the out-of-plane lattice constant, then the epitaxial system is said to be in a 'strained state'. During the growth the strain induced energy built up within the thin film can reach a threshold value at a particular film thickness called critical thickness (t_c) and cause the film to

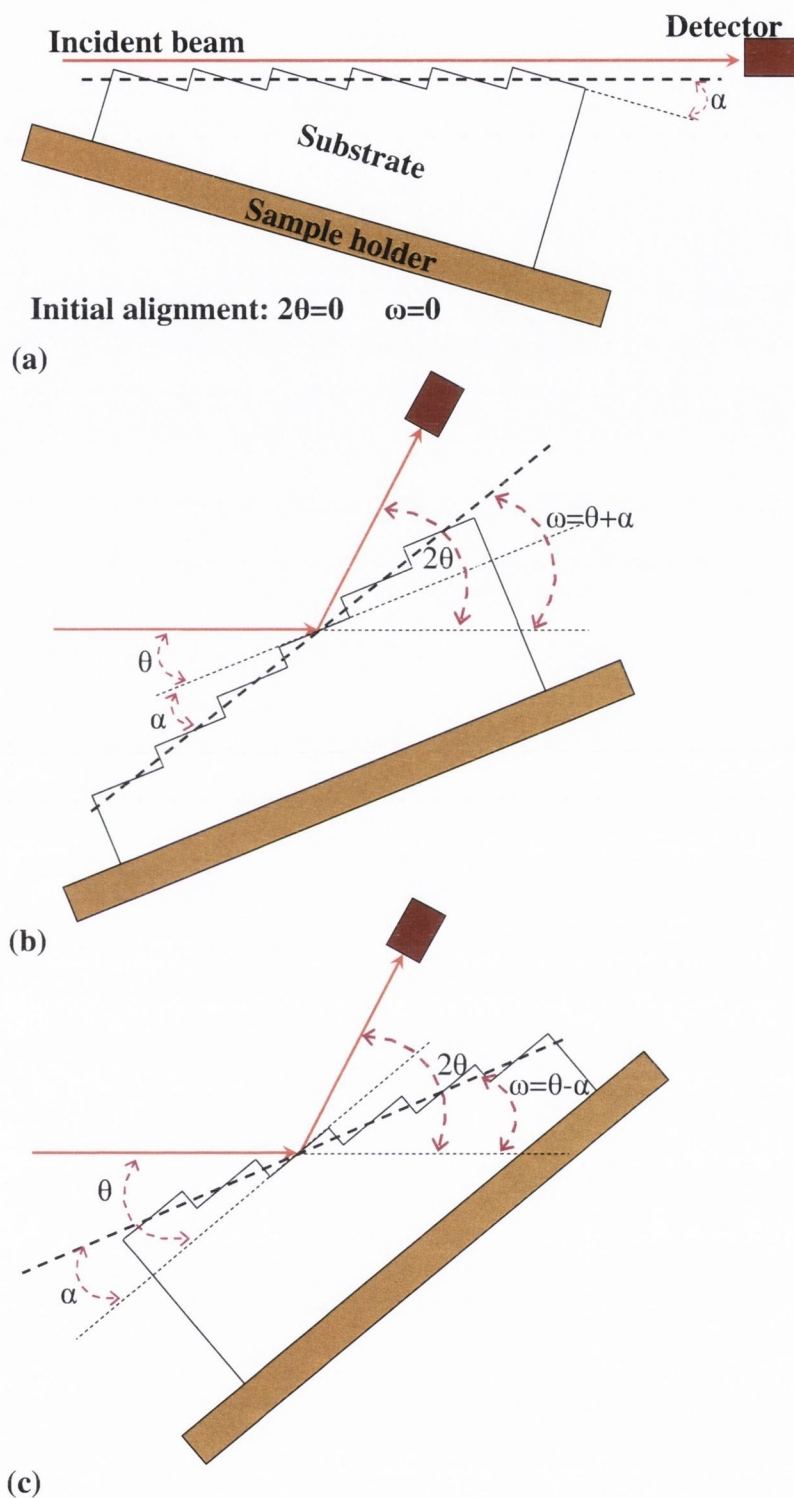


Figure 3.11. Schematic of the diffraction geometry for a vicinal surface. (a) and (b) shows symmetric diffraction when miscut minimum facing the incident beam and when miscut maximum facing the incident beam respectively.

relax to its bulk lattice parameters. To understand the strain status of the film it is necessary to measure the out-of-plane lattice constant or perpendicular lattice constant (a_{\perp}) and in-plane lattice constant (a_{\parallel}) of the film which lies parallel to the surface plane. To measure a_{\perp} and a_{\parallel} , the following methods are employed.

Symmetric scans

If $\Phi = 0$ i.e. the reflecting lattice planes are parallel to the surface, the Bragg diffraction is called 'symmetric'. For $\Phi \neq 0$ the Bragg diffraction is defined as 'asymmetric'. In the case of epitaxial thin films the symmetric scan can be used to find the out-of-plane lattice constant or perpendicular lattice constant (a_{\perp}). To find a_{\perp} a symmetric scan is performed on appropriate surface planes of thin film and substrate.

Ideally ω is half of $2\theta_s$ value but can be $\theta_s \pm \alpha$ for vicinal substrates with a miscut angle α . $\omega = \theta_s + \alpha$ is in the case when miscut minimum is facing the incident beam or the incident beam is in the step up direction as shown in the Figure 3.11 (b) and $\omega = \theta_s - \alpha$ is in the case when miscut maximum is facing the incident beam or incident beam is in the step down direction as shown in the Figure 3.11 (c).

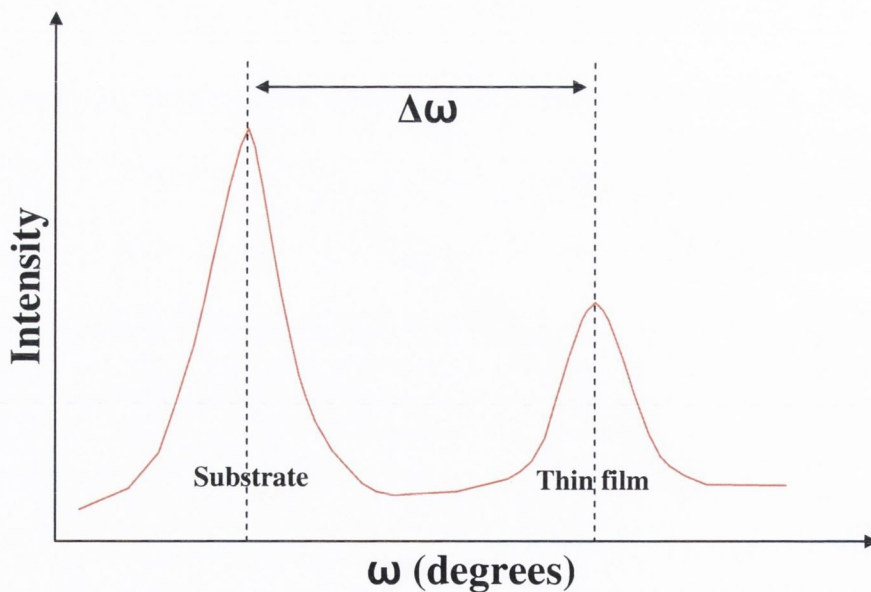


Figure 3.12. Typical symmetrical ω - 2θ scan.

After the optimisation of ω and $2\theta_s$ for the diffraction plane an ω - 2θ scan is performed in which the detector follows twice the angular increment of ω . A typical rocking curve obtained for a symmetrical ω - 2θ scan is shown in Figure 3.12. The high intensity peak is from the substrate and low intensity peak is from the thin film. The diffraction peak of thin film comes right to the substrate peak if the lattice constant of the thin film is smaller than the lattice constant of the substrate.

The Bragg angle for the thin film is calculated by adding the separation between substrate peak and thin film peak ($\Delta\omega$) to the Bragg angle of substrate θ_s as shown below.

$$\theta_{TF} = \theta_s + \Delta\omega \quad (3.8)$$

Substituting θ_{TF} obtained from Equation 3.8, into Equation 3.5 gives the lattice spacing d_{hkl} . The out-of-plane lattice constant a_{\perp} for a cubic crystal (which is the case in the present study of Fe_3O_4 thin films) can be calculated using the following equation:

$$a_{\perp} = d_{hkl} \sqrt{h^2 + k^2 + l^2} \quad (3.9)$$

Asymmetric scans

Asymmetric scans are performed on two accessible opposite inner planes ($h k l$) and $(-h-k l)$ with an inter-planar angle Φ with surface plane as shown in the Figure.3.13 (a). The asymmetric scans performed on these planes are called grazing incidence (GI) and grazing exit (GE) on the respective planes as shown in Figure 3.13 (a). For the grazing exit and grazing incidence diffraction geometries the detector is optimised at $2\theta_s$ position, where θ_s is the Bragg angle for the corresponding (hkl) plane of the substrate. The sample is rotated to a position $\omega = \theta_s + \Phi_s$ for grazing exit diffraction geometry and $\omega = \theta_s - \Phi_s$ for grazing incidence geometry. Φ_s is the inter-planar angle between (hkl) plane and surface plane of the substrate. This is again clearly shown in Figure 3.13 (a) and (b).

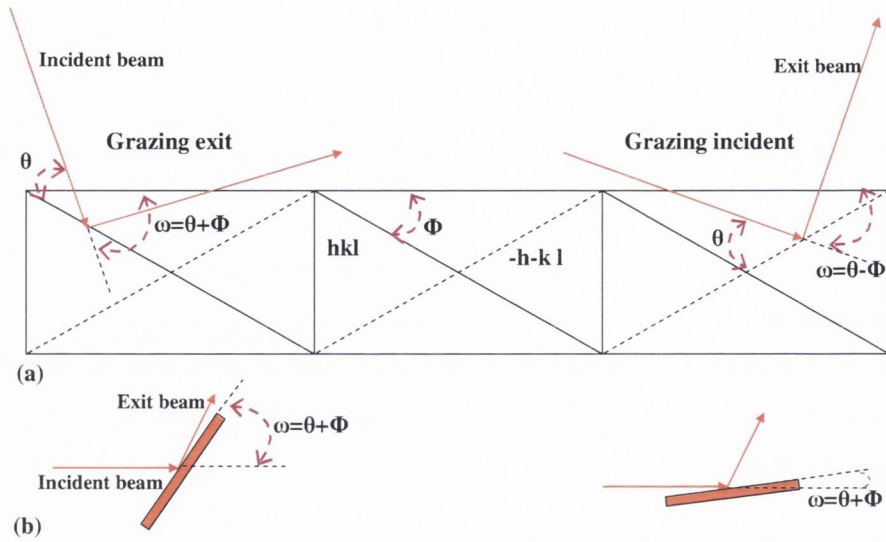


Figure 3.13. (a) Asymmetric grating exit (GE) and grating incidence (GI) diffraction geometries (b) more realistic view of GE and GI diffraction geometries.

In a strained epitaxial film inner (hkl) diffracting planes will not be parallel to the corresponding (hkl) planes of the substrate. Performing an asymmetric ω - 2θ scan from the optimised $2\theta_s$ and ω positions will not gather the thin film intensity. This is due to the different value of inter-planar angle between the (hkl) plane and surface plane of the thin film which is Φ_{TF} compared to the substrate. The difference between inter-planar angles is given as $\Delta\Phi = \Phi_{TF} - \Phi_s$. This is represented in Figure 3.14 in the case of a fully strained system.

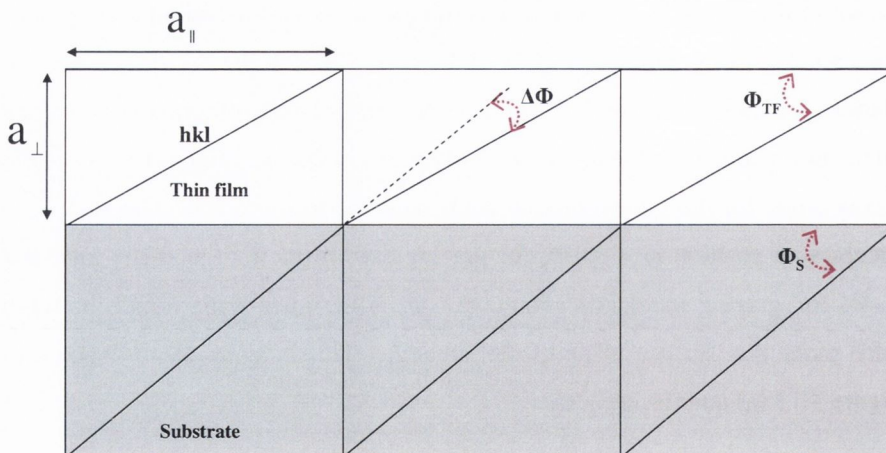


Figure 3.14. Schematic of a fully strained substrate – film system.

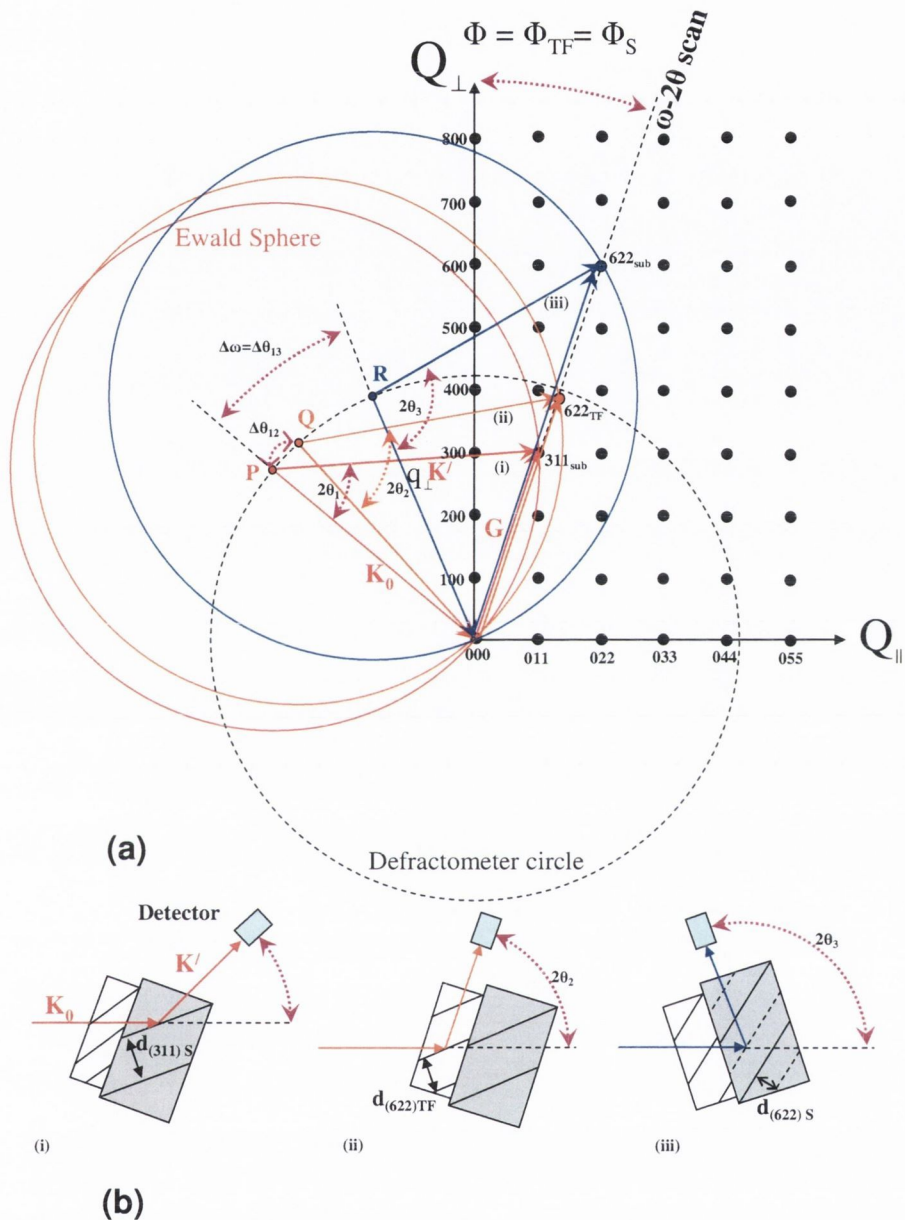


Figure 3.15. Representation of asymmetric grazing exit diffraction geometry for ω - 2θ scans on a fully relaxed $Fe_3O_4(100) / MgO(100)$ system from (311) set of planes in (a) reciprocal lattice space and (b) real space.

For a better explanation let us consider the case of epitaxial $Fe_3O_4(100)$ thin film grown on $MgO(100)$ substrate which is used in the present study. Since Fe_3O_4 unit cell has nearly double the lattice constant of MgO ($a_{Fe_3O_4} = 0.8397\text{nm}$, $a_{MgO} = 0.4123\text{nm}$), Fe_3O_4 grows upon four unit cells of MgO . Lattice constant of two MgO unit cells together is higher than the lattice constant of Fe_3O_4 and therefore the Fe_3O_4 unit cell is tetragonally distorted

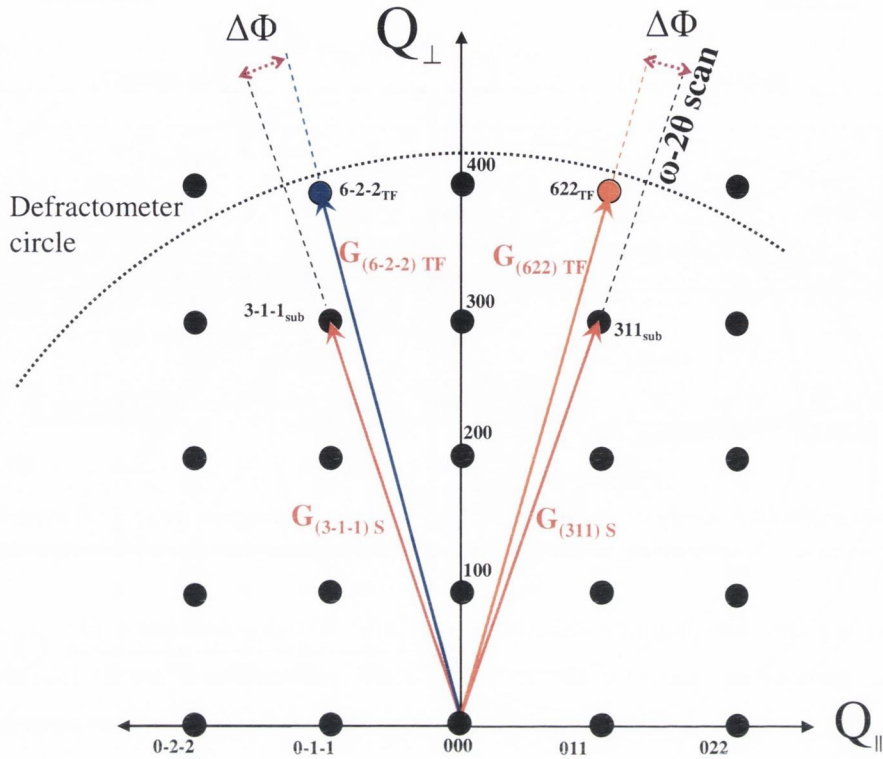


Figure 3.16. Representation of the shifts of (622) and (6-2-2) reciprocal lattice points from the ω - 2θ diffraction line.

with its in-plane lattice constant increased to a value equal to that of MgO and out of plane lattice constant decreased to a lower value compared to the bulk value of Fe_3O_4 . To measure the in plane lattice constant, diffraction peaks of (311) plane of MgO (which is having an inter-planar angle $\Phi_S = 25.23^\circ$ with the (100) surface plane) and (622) plane of Fe_3O_4 whose lattice spacing (d_{622}) is smaller but comparable to the lattice spacing (d_{311}) of MgO, are used. When the system is fully relaxed the (311) and (622) planes are parallel i.e. $\Phi_{TF} = \Phi_S = 25.23^\circ$ or $\Delta\Phi = 0$, performing an asymmetric grazing exit or grazing incidence ω - 2θ scan from the optimised diffraction peak of (311) can fetch the thin film intensity from (622) diffraction plane. The grazing exit ω - 2θ scan is described in Figure 3.15 by using the diffraction geometry in reciprocal

lattice space and real space. During the scan the tip of scattered wave vector \mathbf{K}' moves along the ω - 2θ diffraction line (which is indicated by black dotted line in the Figure 3.15) while the diffraction condition $\mathbf{K}' - \mathbf{K}_0 = \mathbf{G}$ is

satisfied. \mathbf{K}_0 is the incident wave vector and \mathbf{G} is the reciprocal lattice vector (\mathbf{G} is shifted from the original position in the case of (622) planes of substrate and thin film for clarity). The locus of the vertex of \mathbf{K}' and \mathbf{K}_0 traces a circle called the diffractometer circle (see the points P, Q and R in the Figure 3.15).

Three diffraction conditions are identified in the Figure 3.15, as (i),(ii) and (iii). In case (i) the diffraction condition for (311) plane of substrate is satisfied with a Bragg angle θ_1 . In case (ii) the diffraction condition for (622) plane of thin film, which lies in the ω - 2θ diffraction line, is satisfied with a Bragg angle θ_2 . The difference between the Bragg angles θ_1 and θ_2 which is $\Delta\theta_{12}$ is shown in the diffractometer circle. In case (iii) the diffraction condition for (622) plane of substrate is shown with the Bragg angle θ_3 . The difference between θ_1 and θ_3 , which is $\Delta\theta_{13}$ is also shown. All the three cases in the real space diffraction geometry are also shown in the Figure 3.15

In the case of a fully strained system the (622) reciprocal lattice point will no longer lie in the ω - 2θ diffraction line. Instead it will be radially shifted to left or right side of the ω - 2θ diffraction line depending on the value of Φ_{TF} which can be greater than or less than Φ_s . In the case of $\text{Fe}_3\text{O}_4(100)/\text{MgO}(100)$ system, the value Φ_{TF} is smaller than Φ_s , and therefore (622) reciprocal lattice point shifts to the left side of the ω - 2θ diffraction line which is in the grazing exit diffraction geometry. The (6-2-2) reciprocal lattice point will be shifted to right side of the ω - 2θ diffraction line which is in the grazing incidence diffraction geometry. This is represented in Figure 3.16.

In the grazing exit geometry, when the diffraction condition for (622) planes of thin film is satisfied, the detector lags by $2\Delta\Phi$ and misses the thin film intensity. This is shown in the Figure 3.17 (a) using the reciprocal lattice space and (b) the real space diffraction geometry. Case (i) in Figure 3.17(a) and (b) shows the diffraction condition for (311) planes of substrate and case (ii) (with in red circle) shows the lagging of detector when diffraction condition for 622 planes of the thin film is satisfied. The angular rotation of sample stage from the diffraction condition of substrate to the position where diffraction condition of the thin film is satisfied is $\Delta\omega = \Delta\theta - \Delta\Phi$ and is shown in the Figure 3.17 (a).

Figure 3.18 shows the case of grazing incidence diffraction geometry (a) using the reciprocal lattice space and (b) the real space diffraction

film systems. From the Figure 3.17 it is clear that the case of grazing exit diffraction geometry the detector has to move in a faster pace say, ' $n_{GE}\theta$ ' instead of 2θ (where $n_{GE}>2$), from the diffraction condition of (311) planes of substrate in order gather the thin film intensity from (622) planes.

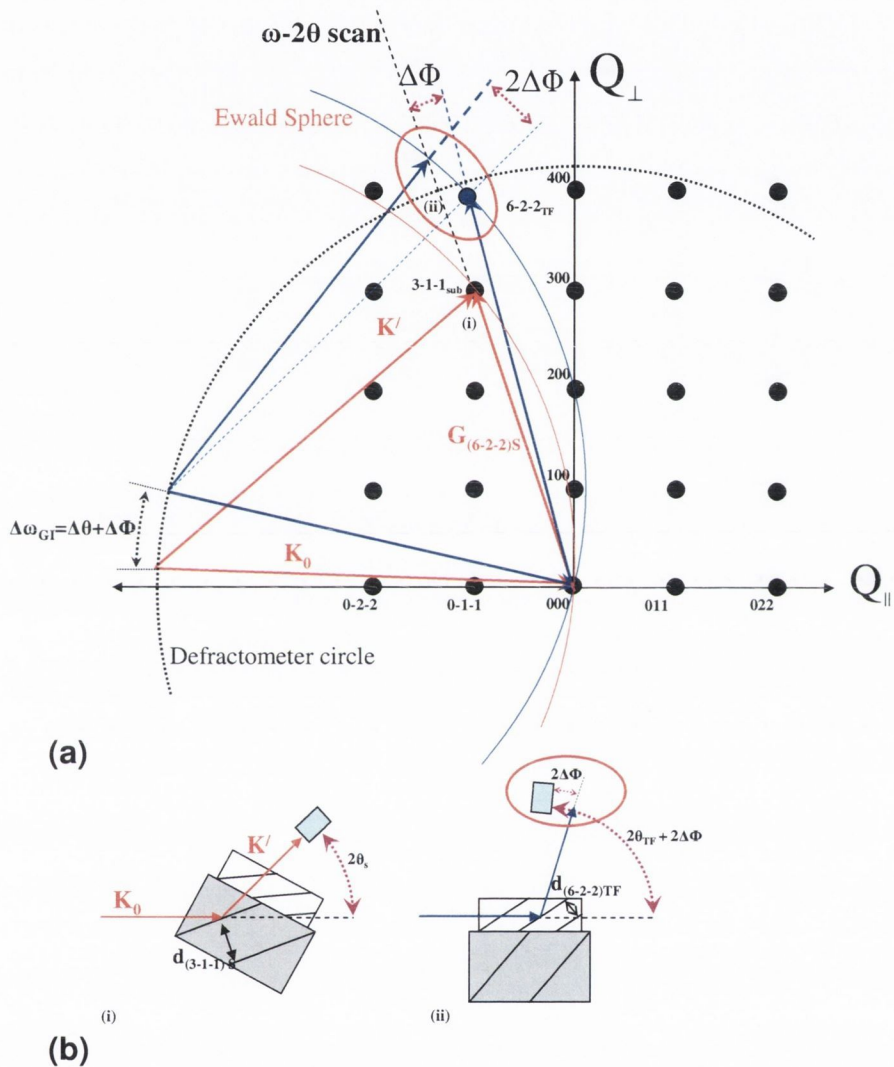


Figure 3.18. Representation of the grazing incidence diffraction geometry for (3-1-1) planes of substrate (case (i)) and (6-2-2) planes of thin film (case (ii)) in (a) reciprocal lattice space and (b) real space. In case (ii) the detector leads by $2\Delta\Phi$ when the diffraction condition for 6-2-2 planes of thin film is satisfied.

Figure 3.18 indicates that the detector has to move in a slower pace say ' $n_{GI}\theta$ ' instead of 2θ (where $n_{GI}<2$), from the diffraction condition of (3-1-1) planes of substrate in order to get the thin film intensity from (6-2-2) planes. Now the

prime task is to find the values of \mathbf{n}_{GE} and \mathbf{n}_{GI} , and this is explained in the following paragraph.

One way to find \mathbf{n}_{GE} and \mathbf{n}_{GI} is to perform a two dimensional intensity mapping obtained by measuring a number of ω - 2θ scans along the reciprocal lattice vector for (311) planes of substrate for different ω offsets which eventually will include (622) reciprocal lattice point of the thin film (This is in the GE diffraction geometry and if it done along (3-1-1) direction it will be in GI diffraction geometry). This is represented in Figure 3.19(a) for GE and GI diffraction geometries. The scan is called 'reciprocal space map'(RSM) and in Figure 3.19 (b) and (c) a typical contour plot of RSM in GE and GI diffraction geometries are represented with ω along x axis and ω - 2θ along y axis. The conversion of peak intensity position in reciprocal coordinates is given by [11]:

$$Q_{\perp} = \frac{2}{\lambda} \sin\theta \cos(\omega - \theta) \quad (3.10)$$

$$Q_{\parallel} = \frac{2}{\lambda} \sin\theta \cos(\omega - \theta) \quad (3.11)$$

From any of the RSM contour plots, approximate values of $\Delta\theta$ and $\Delta\Phi$ are obtained. The values are further refined in the following way.

In GE (or GI) diffraction geometry the detector is moved by $2\Delta\theta$ from the 311 (or 3-1-1) position and the sample stage is rotated by $\Delta\omega_{GE} = \Delta\theta - \Delta\Phi$ ($\Delta\omega_{GI} = \Delta\theta + \Delta\Phi$), where $\Delta\theta$ and $\Delta\Phi$ are the approximate values obtained from the RSM. After this thin film peak is optimized for the maximum intensity and two independent rocking curves of 2θ and ω are performed (i.e the detector moves while the sample stage is fixed and the sample stage rotates while detector is fixed) on the thin film peak and substrate peak. The difference between the detector positions at the thin film and substrate gives a more accurate value of $2\Delta\theta$ and the difference between sample stage positions at the thin film and substrate gives $\Delta\omega_{GE} = \Delta\theta - \Delta\Phi$ ($\Delta\omega_{GI} = \Delta\theta + \Delta\Phi$). From these optimized values we can calculate the values of \mathbf{n}_{GE} and \mathbf{n}_{GI} using the following equations:

$$\mathbf{n}_{GE} = \frac{2\Delta\theta}{\Delta\theta - \Delta\Phi} \quad (3.12)$$

$$\mathbf{n}_{GI} = \frac{2\Delta\theta}{\Delta\theta + \Delta\Phi} \quad (3.13)$$

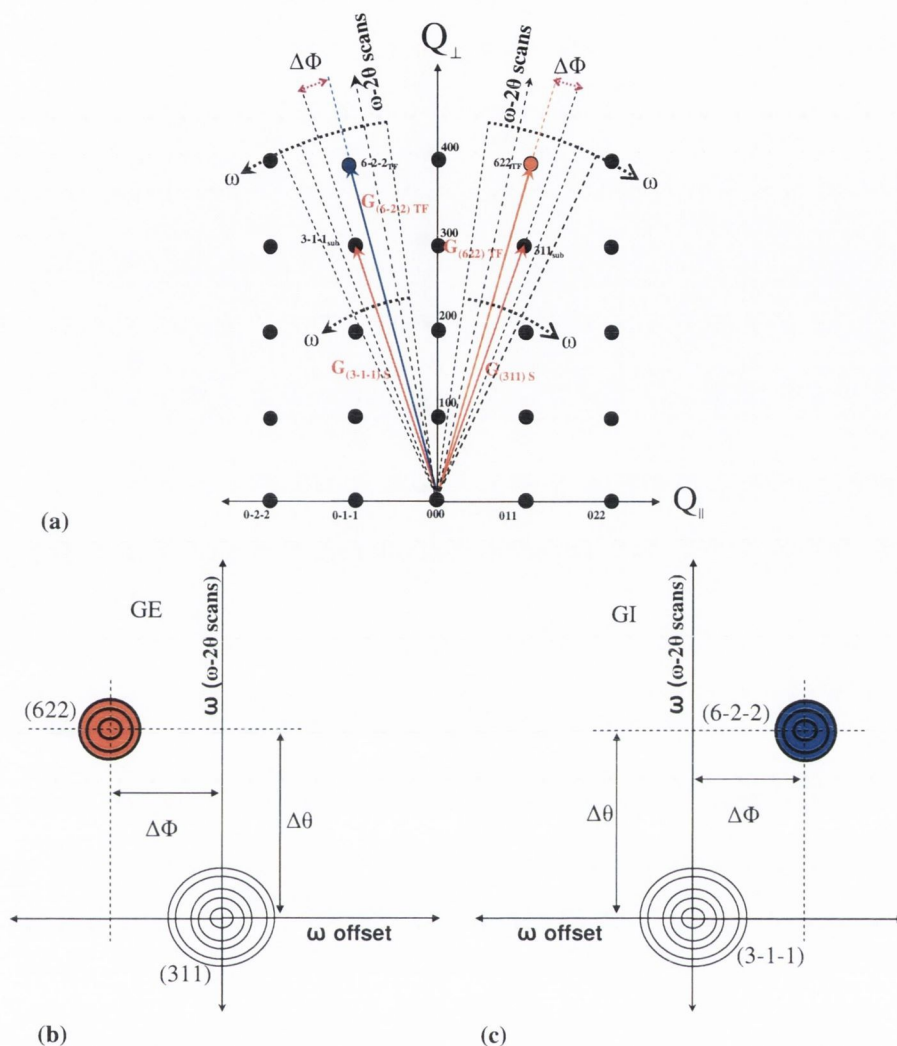


Figure 3.19. (a) Representation of the grazing exit (GE) and incidence (GI) reciprocal space mapping. (b) typical contour plot of reciprocal space map (ω - ω - 2θ scans) in GE diffraction geometry and (c) in GI diffraction geometry.

“PeakSplit” software supplied by Bede Scientific Instruments Ltd. can perform a calculation of \mathbf{n}_{GE} and \mathbf{n}_{GI} by taking into account the strain present in the system as determined from the measurement of \mathbf{a}_{\perp} and using a pre-defined value of the Poisson ratio ν (For Fe_3O_4 , $\nu = 0.3$). The version of PeakSplit used in the present work (PeakSplit Version 1.00 for Windows[®]) supports calculations only for (100) orientated cubic structures. Therefore

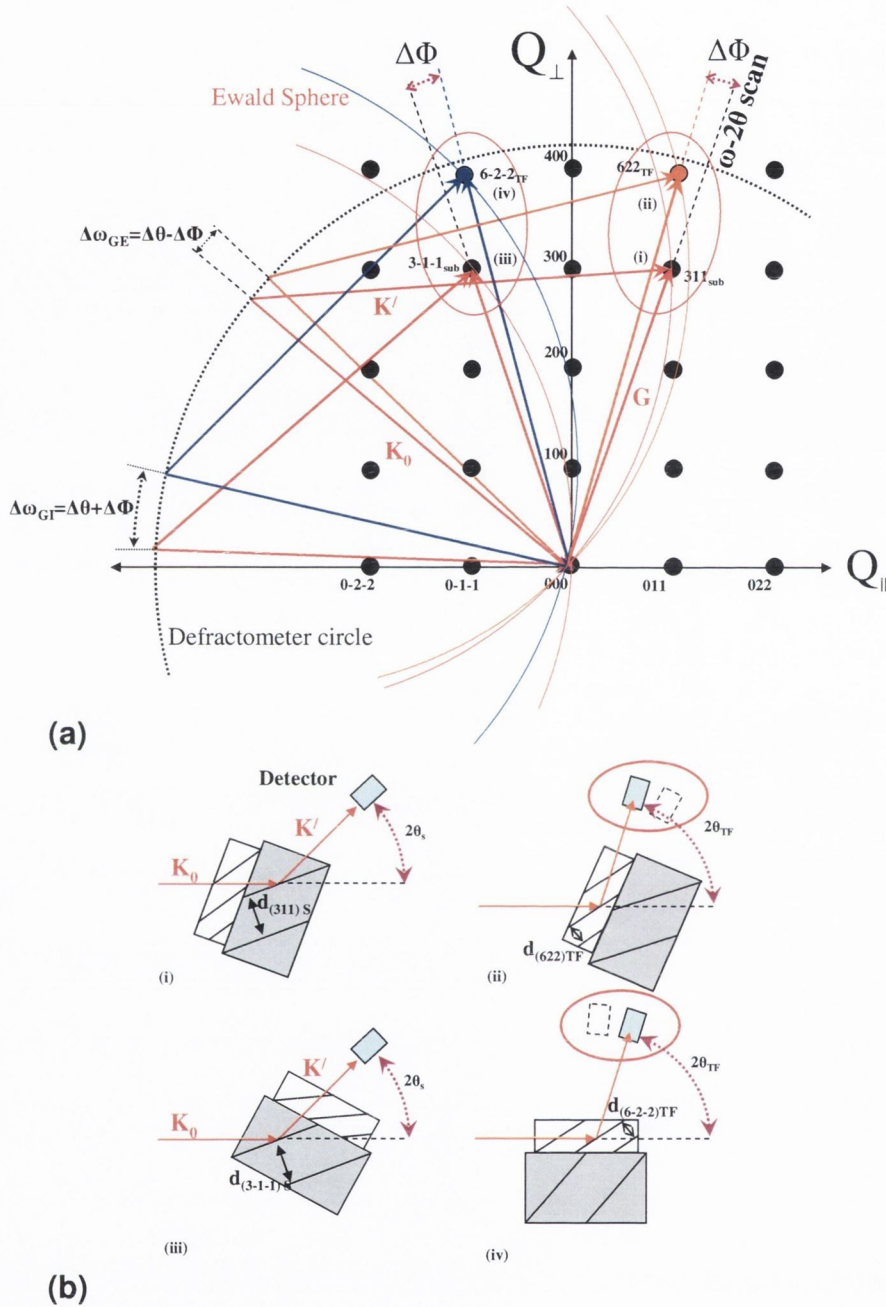


Figure 3.20. (a) Representation of the grazing exit (GE) and incidence (GI) diffraction geometries for (311) and (3-1-1) planes of the substrate (case (i) and (iii)) and (622) and (6-2-2) planes of the thin film (case (ii) and (iv)) in (a) reciprocal lattice space and (b) real space during ω - $n\theta$ scans.

PeakSplit software was used in the case of (100) oriented samples and the method explained above was used for other orientations like (110) to calculate \mathbf{n}_{GE} and \mathbf{n}_{GI} .

Once the values of \mathbf{n}_{GE} and \mathbf{n}_{GI} are determined, the ω - $\mathbf{n}_{GE}\theta$ and ω - $\mathbf{n}_{GI}\theta$ asymmetric scans are performed from the respective substrate diffraction positions (i.e. (311) for GE and (3-1-1) for GI). Diffraction geometries of ω - $\mathbf{n}_{GE}\theta$ and ω - $\mathbf{n}_{GI}\theta$ asymmetric scans in reciprocal space are shown in Figure 3.20 (a). Various diffraction conditions at substrate and thin film are clearly identified as (i), (ii), (iii) and (iv). Figure 3.20(b) represents all the cases in real space diffraction geometries. Typical rocking curves obtained during ω - $\mathbf{n}_{GE}\theta$ and ω - $\mathbf{n}_{GI}\theta$ asymmetric scans are shown in Figure 3.21 (a) and (b). The separation $\Delta\omega_{GE}$ and $\Delta\omega_{GI}$ are then used to calculate accurate values of $\Delta\theta$ and $\Delta\Phi$ using following equations:

$$\Delta\theta = \frac{\Delta\omega_{GE} + \Delta\omega_{GI}}{2} \quad (3.14)$$

$$\Delta\Phi = \frac{\Delta\omega_{GI} - \Delta\omega_{GE}}{2} \quad (3.15)$$

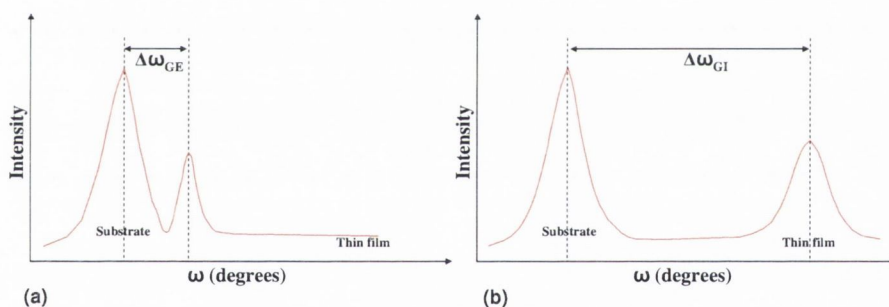


Figure 3.21. Typical rocking curve for a asymmetrical ω - $\mathbf{n}\theta$ scans for (a) grazing exit (b) grazing incidence diffraction geometries.

The in-plane lattice constant \mathbf{a}_{\parallel} of the thin film is determined by substituting $\Delta\theta$ and $\Delta\Phi$ in the following equation:

$$\mathbf{a}_{\parallel} = \mathbf{a}_s \left[\frac{\sin \theta_s}{\sin(\theta_s + \Delta\theta)} \times \frac{\sin \Phi_s}{\sin(\Phi_s + \Delta\Phi)} \right] \quad (3.16)$$

where \mathbf{a}_s is the substrate lattice constant, θ_s and Φ_s are the substrate Bragg angle and interplanar angle between the asymmetric sample plane and sample surface.

3.3.1.3 X-ray Reflectivity measurements

In the present work the X-ray reflectivity (XRR) technique is used for the measurement of thickness of the thin films. Refraction and reflection are two important optical phenomena and are described by Snell's law and the Fresnel equations. The X-ray reflectivity essentially consists of measuring the reflected intensity of X-rays from a sample surface at near glancing incidence [12]. Typical scattering geometry is shown in Figure 3.22. The incident angle is equal to the reflected angle ($\theta = \theta_i = \theta_r$) and is usually less than 6° . A brief theoretical background for finding thickness from XRR is furnished below.

The refractive index of a medium in X-ray range can be written as [12]:

$$\mathbf{n} = 1 - \delta - i\beta \quad (3.17)$$

where δ and β represent the dispersion and absorption terms, which can be given by the expressions:

$$\delta = \frac{r_0 \lambda^2}{2\pi} \mathbf{n}_e \quad (3.18)$$

where r_0 is the Bohr atomic radius, λ is the X ray wave length and \mathbf{n}_e is the

electron density given by $\mathbf{n}_e = Z \frac{N_A}{A} \rho$ (3.19)

where Z is the number of electrons per atom, N_A is Avogadro's number, A the atomic weight and ρ density. Z is usually replaced with a complex atom form factor $f = f_0 + f' + if'' = Z + f' + if''$. The term $f' + if''$ is due to dispersion and absorption and represents X-ray absorption edge. From these considerations δ and β can be represented as:

$$\delta = \frac{r_0 \lambda^2}{2\pi} (Z + f') \frac{N_A}{A} \rho \quad (3.20)$$

$$\beta = \frac{r_0 \lambda^2}{2\pi} f'' \frac{N_A}{A} \rho \quad (3.21)$$

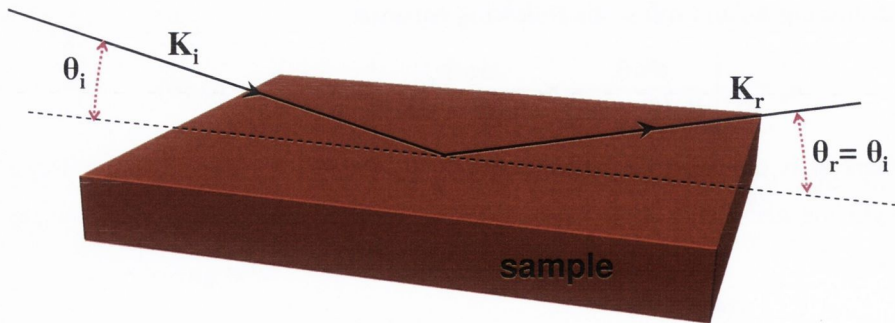


Figure 3.22. Scattering geometry used in XRR measurements.

The real part of refractive index $n, 1 - \delta$, is connected to the phase-lag of the propagating wave and the imaginary part, β , corresponds to the decrease of the wave amplitude. δ and β are small positive quantities of order 10^{-5} to 10^{-7} for X-ray wavelengths at about 1.5\AA [13]. Therefore from Equation (3.16) it is clear that the refractive index is slightly less than 1 and the transmitted wave will be refracted from the normal as shown in the Figure (3.23).

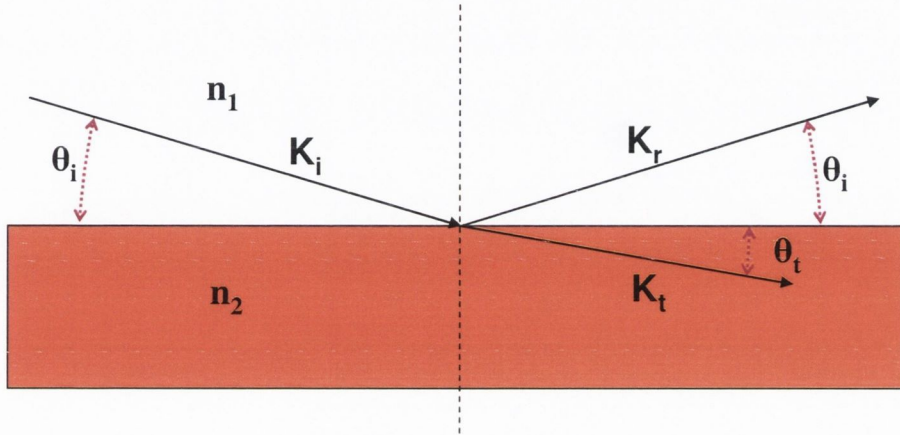


Figure 3.23. Reflection and refraction of X-rays incident upon a plane boundary between mediums with refractive index n_1 and n_2 .

From Snell's law:

$$n_1 \cos \theta_i = n_2 \cos \theta_t \quad (3.22)$$

The critical angle θ_c is the angle at which X-ray will undergo total internal reflection when propagating from a medium of high refractive index to a medium of low refractive index. Considering the case of an absorption free film ($\beta = 0$) and air ($n_1 = 1$) interface, the X-ray critical angle is given by:

$$\cos \theta_c = n_2 = 1 - \delta \quad (3.23)$$

Expansion of cosine for small angles leads Equation (3.23) to

$$1 - \frac{\theta_c^2}{2} \approx 1 - \delta \quad (3.24)$$

$$\theta_c \approx \sqrt{2\delta} \quad (3.25)$$

For incident angles greater than θ_c ($\theta > \theta_c$) the X-ray beam penetrates inside the film. Reflection therefore occurs at the top and the bottom surfaces of the film. The interference between the rays reflected from the top and the

bottom of the film surfaces results in interference fringes as shown in Figure (3.24).

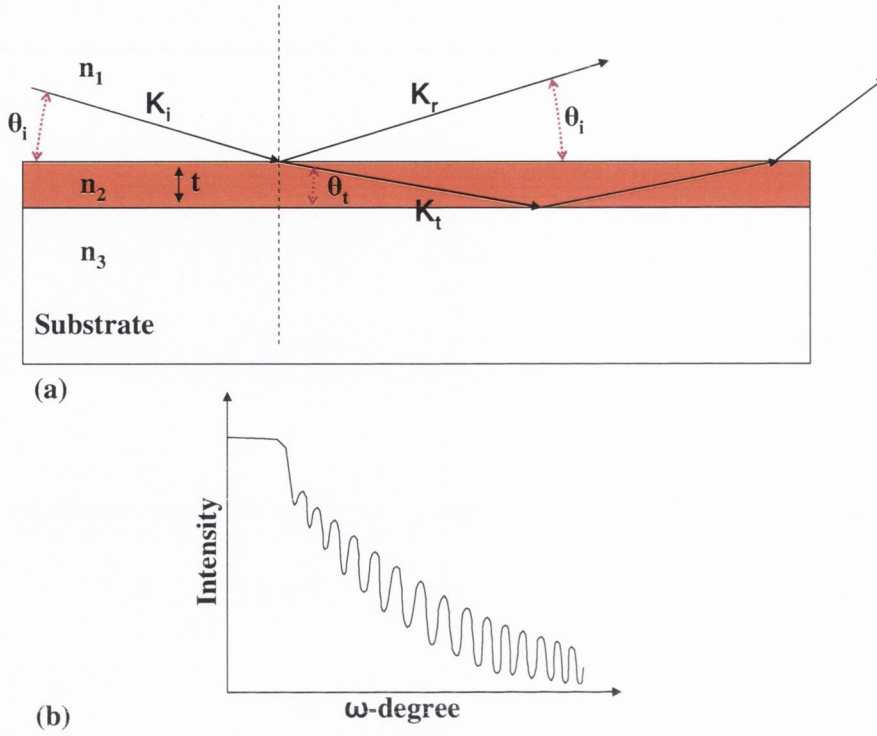


Figure 3.24. (a) Reflection of X-rays from top and bottom surface of the thin film. (b) Typical XRR spectrum from a homogeneous layer on a substrate.

The relation between the thickness t of the thin film and intensity maxima positions θ_m is given by [13]

$$\frac{1}{2}(2m+1)\lambda = 2t\sqrt{\theta_m^2 - 2\delta} \quad (3.26)$$

$$\frac{1}{2}(2m+1)\lambda = 2t\sqrt{\theta_m^2 - \theta_c^2} \quad (3.27)$$

where m is an integer. Considering two neighbouring m and $m+1$ maxima and employing equation (3.27) we get:

$$\frac{1}{2}(2m+1)\lambda = 2t\sqrt{\theta_m^2 - \theta_c^2} \quad (3.28)$$

$$\frac{1}{2}(2m+3)\lambda = 2t\sqrt{\theta_{m+1}^2 - \theta_c^2} \quad (3.29)$$

Subtracting equation (3.28) from (3.29) gives

$$t = \frac{\lambda}{2} \left[\frac{1}{\sqrt{\theta_{m+1}^2 - \theta_c^2} - \sqrt{\theta_m^2 - \theta_c^2}} \right] \quad (3.30)$$

For $\theta_m \gg \theta_c$ equation (3.30) becomes

$$t = \frac{\lambda}{2} \left[\frac{1}{\theta_{m+1} - \theta_m} \right] = \frac{\lambda}{2} \frac{1}{\Delta\theta_m} \quad (3.31)$$

where $\Delta\theta_m$ is the fringe spacing obtained from intensity oscillation during the reflectivity measurements. The thickness is often determined with a precision better than 1 Å. The procedure for following the thickness measurement is described below.

The alignment of the sample stage and detector with X-ray beam is very important for the XRR measurements. This is achieved with the following steps. At first 2θ is calibrated for the zero position by bringing detector in line with the incident X-ray beam for the maximum intensity and keeping the sample stage far out of the beam by moving in the $-ve$ z direction. After the optimisation of 2θ , sample stage is brought in to the beam at a z position where detector shows 20% of the maximum intensity i.e intensity without sample stage. Then ω and χ are optimised for the maximum and minimum intensity respectively and calibrated to zero. The sample stage is moved out of the beam by moving in the $-ve$ z direction and brought to a position at which the detector shows 50% of the maximum intensity. After this the detector is brought to a position less than 0.8 degrees and sample stage is moved to a position at half the value of the detector position. Then a ω rocking curve is performed by moving sample stage with a fixed detector position. The maximum intensity position of ω is calibrated to exactly half the value of detector position in the case there is an offset. The sample stage and detector are moved back to the zero position and a ω - 2θ scan is performed up to 2 degrees. The intensity oscillations obtained are then analysed with the Bede PeakSplit software which incorporates a utility for analysing such data.

3.3.1.4 Tilt Analysis or miscut angle measurement

The tilt or miscut angle of the sample can be measured using HRXRD. Because of the miscut, the ω positions at which diffraction is found vary as the specimen is rotated about its surface normal (rotation of ϕ). A detailed

explanation of this is given during the description of symmetric scans (page number 54) and Figure 3.11 (b) and (c) shows two extreme cases. The ω positions for different positions of ϕ are optimised. A sine curve can be fitted on the plot of peak positions obtained during ω scans against the corresponding values of ϕ . The miscut angle is the angle amplitude of the sine wave and the position of ϕ for the maximum peak position gives the direction of the miscut. The Bede PeakSplit software incorporates a utility for analysing such data. The function used for the fitting is

$$\omega = \omega_0 + \alpha \cos(\phi + \text{offset}) \quad (3.32)$$

where α is the miscut of the substrate or layer and 'offset' is the direction of the miscut.

3.3.1.5 Instrumentation details of HRXRD

The high resolution x-ray diffractometer used to perform all of the high resolution x-ray diffraction (HRXRD) measurements in this work was a Bede D1 diffractometer. A schematic of the system layout is given in Figure 3.25, while a photograph of the actual system is given in Figure 3.26. The entire system was housed in a safety case with access to the relevant elements via an assisted opening lid coupled to an interlock system. Essentially the system comprise three main elements, the source stage, the sample stage and the detector stage.

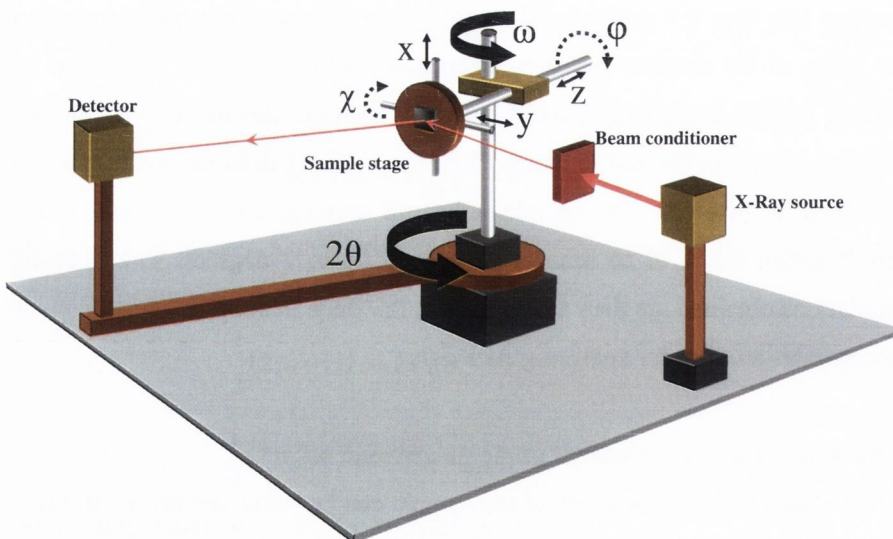


Figure 3.25. Schematic of the diffractometer layout. All of the angles of rotation as described in the main text are outlined

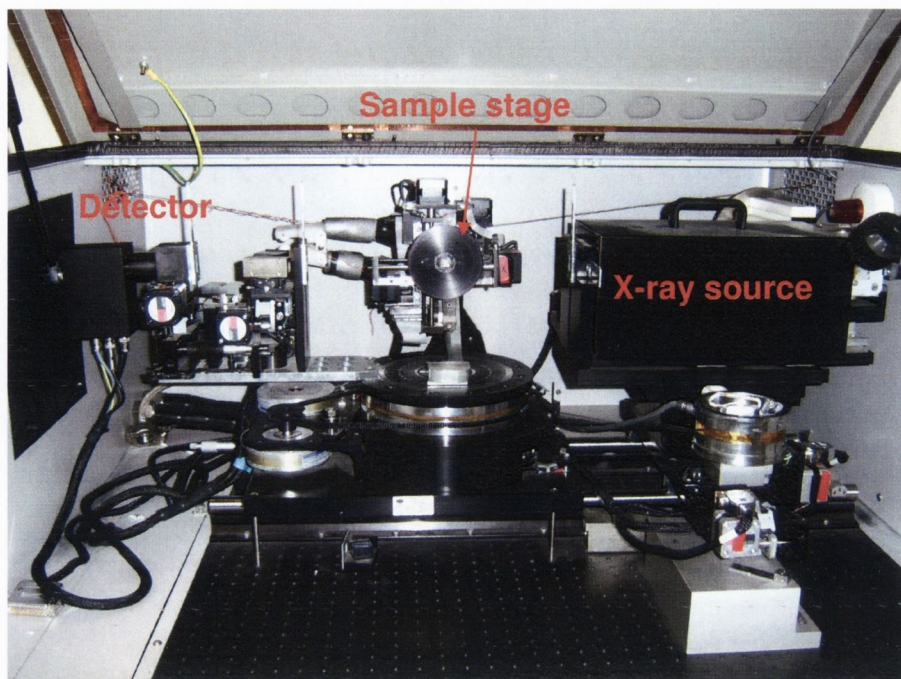


Figure 3.26. Photograph of the components of the High Resolution X-Ray Diffractometer. The sample stage, including the metal sample holder, and the detector stage are visible. The safety lid (open) is also visible.

The source or beam stage was fixed to the system housing and comprised all the beam conditioning mechanisms and the related optics required to ensure a homogeneous X-ray beam of small angular dispersion. A channel cut crystal acted as the beam conditioner in front of the X-ray source. With correct optimisation of the source stage optics a sub-millimetre beam could be achieved that maintained its integrity over long distances (~150 cm). The x-rays were produced from a Cu $K\alpha_1$ transition and had a wavelength of 1.5406 Å. The intensity of the X-ray beam could be controlled via a system of removable metal slits that could be placed in front of the source stage. The relevance of this shall become apparent shortly.

The sample stage was a two part system with the main part mounted on a moveable table that allowed it to move in three separate directions, as indicated in Figure 3.10. The sample stage was completed by a removable metal disk whose centre was marked via cross hairs etched into its surface. The sample for analysis was mounted onto the metal disk using double sided tape. The metal disk was magnetically coupled to the main sample stage. The three angles of movement were denoted ω , ϕ and χ . The ω angle was the angle

through which the sample stage could move around the x -axis and it had a range of $\sim 90^\circ$ with a resolution of 0.18 arcsecond. The ϕ angle was denoted the rotation of the sample and referred to rotation of the sample around the z -axis. It had a range of 280° and a resolution of 0.18 arcsecond. The χ angle was denoted the tilt of the sample and referred to rotation of the sample around the y -axis. It had a range of 40° and a resolution of 0.0025° . Adjustment of these three parameters constituted alignment of the diffraction planes in relation to the source x-ray beam.

The detector stage was also mounted on a moveable platform and was also capable of rotation through a range of angles denoted 2θ . The detector axis rotation range was 235° with a resolution of 0.18 arcsecond. The Bede D1 system was fitted with an Enhanced Dynamic Range detector (EDR detector) with a dynamic range of 0.5 cps to 50 Mcps, though the best results were obtained when the beam intensity was conditioned to give 250,000 cps. The beam intensity could be controlled using the metal slits mentioned above. The system was remotely controlled with all parameters chosen using the Bede Control software provided with the system. All the analysis software was also provided with the system. A channel cut crystal stage was positioned in front of the detector (analyzer) to increase the resolution. The measurements which utilise the channel cut crystal stage are called Triple axis scans and measurements that don't utilise channel cut crystal stage are called Double axis scans. It was only possible to perform triple axis scans when the signal strength was sufficiently strong.

3.3.2 Transmission electron microscopy (TEM)

Transmission electron microscopy is a powerful method for obtaining information regarding microstructural defects such as dislocations, grain boundaries, twin boundaries, anti phase boundaries through diffraction patterns and images of the sample. The high energy electrons (100-300 KeV) used in electron microscopy possess wavelengths of about 4 pm which is much smaller than the wavelength of visible light ($\sim 500\text{nm}$), and gives a much higher resolution than an optical microscope. A lot of information can be gathered from the sample by using an electron microscope since electrons have a much stronger interaction with matter than either visible light or X-rays. More details about TEM can be found in references [14] and [15]. In the following sections

a brief qualitative description of the TEM imaging methodology and instrumentation details of the TEM used in the present work are given .

3.3.2.1 Imaging methodology

The main parts of TEM consist of a vacuum system, a high voltage source and a column that consists of an electron gun, a condenser lens and apertures, a specimen holder, an objective lens system and objective aperture intermediate and projector lens systems and an image recording facility. The vacuum in the column is maintained below 10^{-6} mbar using various pumps. Schematic of the TEM imaging is shown in Figure 3.27.

The electrons emitted from a tungsten (W) filament are accelerated by the high voltage source to an energy range of 200KeV. The accelerated electrons are then collected and focused to the sample by the condenser lens system. The condenser lens system provides control over the brightness of the images. The focused electrons pass through the sample which is held in a holder capable of providing specific diffraction conditions by tilting the sample about two axes. The transmitted electrons then pass through the objective lens. The objective lens is the key lens system which determines the ultimate resolution of the instrument. All the lens systems used are electro-magnetic and are subject to aberrations.

The electrons transmitted through the sample can either be diffracted or scattered in the forward direction. This facilitates two modes of imaging by selecting which electrons are used to make up the image and are called *diffraction mode* and *image mode*. This is done using an objective aperture. In *diffraction mode* the diffracted electrons from the sample pass through the objective lens and are focussed in the back focal plane producing the diffraction pattern. This is shown in Figure 3.27(a). A selected area diffraction aperture is used to select electrons from a certain region such that the diffraction pattern can be related to a specific area. Further magnification occurs in the intermediate and projector lens system which also plays a crucial role in determining whether a diffraction pattern or an image is formed. The diffraction pattern formed in the back focal plane of the objective lens becomes the object plane of the intermediate lens which further magnifies the diffraction pattern [15]. The back focal plane of the intermediate lens becomes the object

plane of the projector lens and the final pattern is formed on a screen or photographic plate placed at the back focal plane of the projector lens.

In the *image mode* electrons from objective lens pass through an objective aperture and the image formed at the image plane of objective lens becomes the object plane of the intermediate lens and further magnification is achieved. This is shown in Figure 3.27(b). The image plane of the intermediate

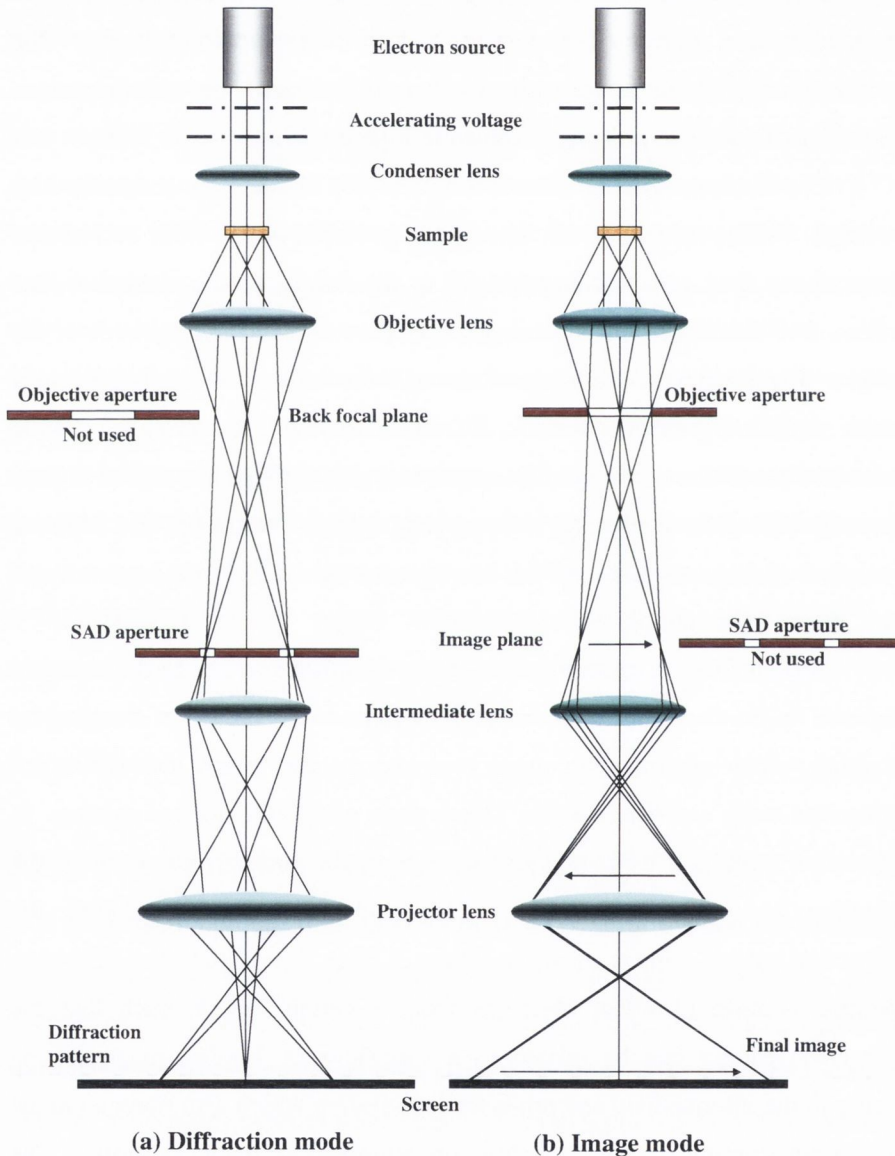


Figure 3.27. Schematic of the operation of a transmission electron microscope in (a) diffraction mode and (b) in image mode. Reproduced from [16].

lens forms the object plane for the projector lens and the final image is formed on a screen or photographic plate placed at the image plane of the projector lens. There are two main modes of imaging called *bright field imaging* and *dark field imaging*. The electrons which are scattered by the sample in the forward direction form the direct beam and this direct beam is used in *brightfield* imaging. This is shown in Figure 3.28 (a). In *bright field imaging* defects in the sample will scatter the direct beam and will appear as dark features in the image. In *dark field imaging*, the diffracted beam or the scattered electrons from the reflecting planes are used. This is shown in Figure 3.29 (b). The defects in the reflecting planes can reduce the scattered intensity and thus forming dark features.

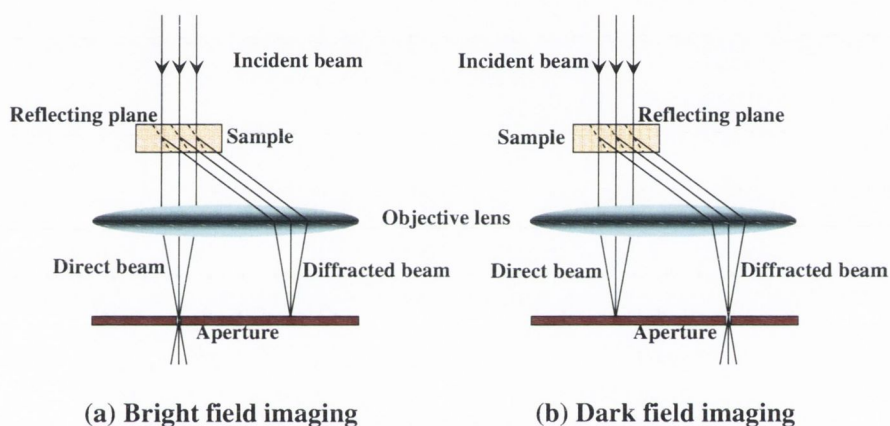


Figure 3.28. Schematic of the two imaging modes (a) bright field imaging and (b) dark field imaging. Reproduced from [16].

3.3.2.2 Instrumentation details

All TEM measurements of $\text{Fe}_3\text{O}_4/\text{MgO}$ and $\text{Fe}_3\text{O}_4/\text{MgAl}_2\text{O}_4$ presented in this work were performed at Institut für Festkörperforschung, Forschungszentrum Jülich GmbH, D-52425 Jülich, Germany. Structural defects were identified by conventional TEM using a Philips CM 20 electron microscope with a side-entry double-tilt goniometer stage and an assortment of specimen holders. This machine was able to operate between 80 and 200 kV in the imaging mode. Diffraction modes include convergent beam diffraction for three-dimensional structure information and micro-diffraction with a minimum probe size of 20nm.

High-resolution images were obtained with a Philips CM 200 electron microscope, which was equipped with a CEOS double hexapole corrector. Adjusting a negative spherical aberration constant, C_s , of $-40 \mu\text{m}$ and using the optimum overfocus setting of the objective lens of 12 nm resulted in a directly interpretable bright-atom contrast and in minimized, sub-Angstrom delocalizations.[17]

In order for the electrons to pass through the sample, it has to be electron transparent. Therefore the sample or the regions to be analyzed have to be sufficiently thin (of the order of hundreds of nanometers) which of course depends on energy of the incident electrons and the density of the sample. In the present work mechanical thinning and Ar ion milling were applied to obtain electron transparent areas within the TEM specimen.

3.3.3 Raman spectroscopy

Raman spectroscopy is an analytical technique based on detection of scattered light from an irradiated sample. A small portion of the scattered light exhibits a slight shift in wavelength due to molecular vibrations in the sample, and this wavelength shift is used to analyze the sample. The interaction between this light and the chemical bonds in the sample is known as the Raman effect. Raman spectra of the different compounds may be used as fingerprints to detect particular species [18,19]. The most common iron oxides and hydroxides such as hematite ($\alpha\text{-Fe}_2\text{O}_3$), maghemite ($\gamma\text{-Fe}_2\text{O}_3$), magnetite (Fe_3O_4) and goethite ($\alpha\text{-FeOOH}$) possess characteristic Raman spectra which are drastically different from each other [20]. In the present work, Raman spectroscopy was used to ascertain the magnetite phase. A qualitative description of the basic principles of Raman spectroscopy and instrumentation details are given in the following sections.

3.3.3.1 Basic principles of Raman spectroscopy

When the sample is irradiated, most of the incident light is scattered at the same wavelength. This "elastic" type of scattering is known as Rayleigh scattering. However, a small fraction of the laser light will excite molecular vibrations in the sample and will be inelastically scattered, or scattered at a slightly different wavelength. The wavelength of the scattered photons can be

higher or lower than the incident photons. This shift in the wavelength can be detected and are expressed in wave numbers. The plot of intensity versus wavelength shifts expressed in wave number (cm^{-1}) is called the Raman spectrum. The spectral lines for higher wavelengths than the incident wavelengths are called 'Stokes lines' and the spectral lines with lower wavelengths are called 'Anti-Stokes lines'. The Raman shift, $\overline{\Delta\nu}$, in wave numbers (cm^{-1}), is calculated using the following equation :

$$\overline{\Delta\nu} = \frac{1}{\lambda_{\text{Incident}}} - \frac{1}{\lambda_{\text{scattered}}} \quad (3.33)$$

where λ is in cm. When a photon is absorbed by a molecule in its ground state, it is excited into a higher virtual energy state and then de-excited to the first excited vibrational energy state. This process gives out a photon with less energy or lower wavelength than the incident photon and forms Stokes lines in the Raman spectrum. This is schematically represented in Figure 3.29. The virtual electronic state is not generally a true electronic state of the molecule but a composite function involving all possible states such as rotational, vibrational, and electronic states [21].

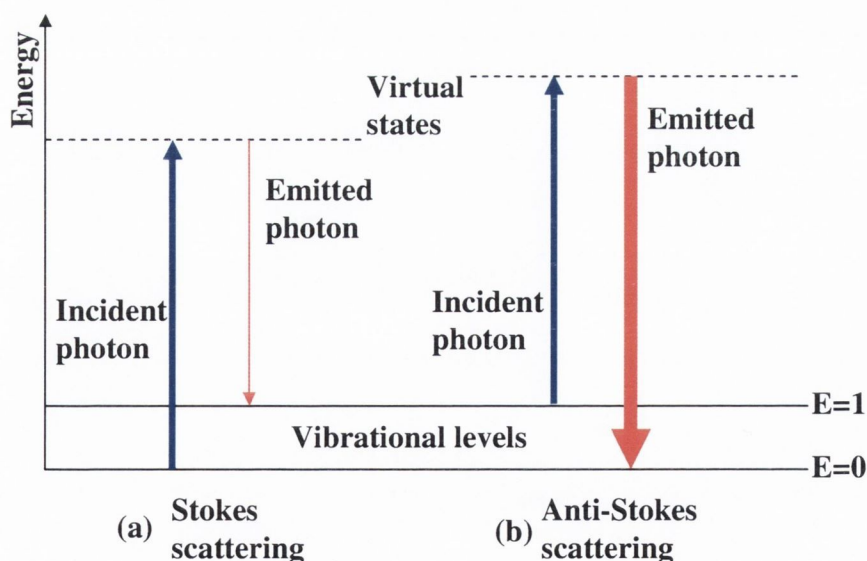
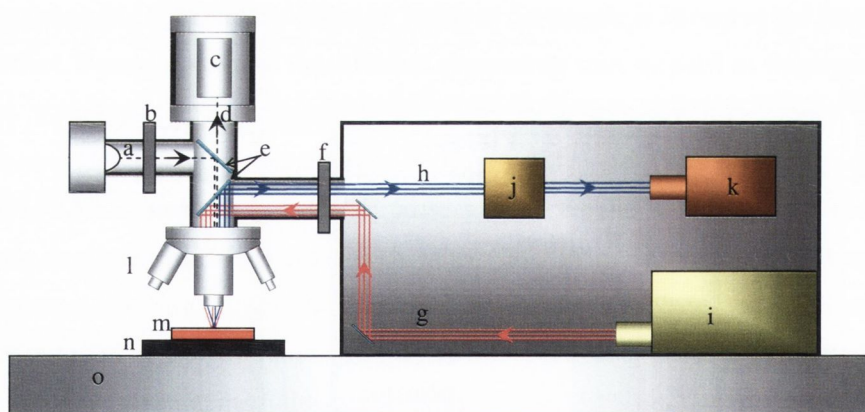


Figure 3.29. Energy level diagram for Raman scattering; (a) Stokes Raman scattering (b) anti-Stokes Raman scattering.

When a molecule in the first vibrational excited state absorbs the incident photon, it will be excited into a virtual energy state and when it de-excites to the ground state it emits a photon with higher energy or shorter wavelength than the incident photon and contributes to the Anti-Stock lines in the Raman spectrum. This is schematically represented in Figure 3.29.

At room temperature the thermal population of vibrational excited states is low, although not zero. Therefore, the initial state of the molecule is the ground state, and the scattered photon will have lower energy (longer wavelength) than the exciting photon. This Stokes shifted scatter is what is usually observed in Raman spectroscopy. Since the Raman spectrum reflects the vibrational energy transitions, which essentially depends on the bonding nature of the molecule, a lot of information regarding the molecular structure can be acquired from the Raman spectrum. Some of the advantages of Raman measurements are (a) no special sample preparation required, (b) relatively quick process (c) compatible with aqueous solutions etc.

3.3.3.2 Instrumentation details of Raman spectrometer



- | | |
|---|---|
| a) white light | h) Scattered laser beam from the sample |
| b) Shutter for white light | i) Ar ⁺ ion laser source |
| c) CCD camera | j) Monochromators |
| d) Bright light reflected from the sample | k) Detector |
| e) Mirros | l) Objective lens |
| f) Shutter for laser | m) Sample |
| g) Incident laser beam | n) Sample Holder |
| | o) Vibration free table |

Figure 3.30. Schematic representation of the Raman spectrometer.

Room temperature Raman measurements were carried out using a Rainshaw 1000 micro Raman system. A schematic diagram of Raman system is given in the figure 3.30. The excitation wavelength used was 514.5nm from an Ar⁺ ion laser (Laser Physics Reliant 150 Select Multi-Line) with maximum power of ~10mW (Although ~3mW power was used for the measurements in order to avoid excessive heating). The laser beam was guided to an objective lens of the Leica Microscope with a specific magnification (50X magnifying objective lens focus the beam into a spot of about 1µm size) using a series of mirrors as shown in the figure. The system was provided with a shutter 'f' as shown in the figure, capable of stopping the incoming and scattered laser beam whenever required. The beam was focused on to the sample by moving the sample holder 'n' as shown in the figure, which was capable of moving in X, Y and Z direction. The scattered laser from the sample was then guided to the detector 'k' as shown in the figure, through monochromators 'j'. A white light source 'a' was provided for observing the sample using a CCD camera 'c'. This was used for the positioning of the sample to select the area of scattering. The laser was isolated from falling on the sample using shutter 'f' when ever CCD camera was used and when laser light was on the white light was isolated using shutter 'b'. (The actual arrangement of the shutters differs from the schematic). The whole unit was properly shielded (not shown in the figure) for the laser and was mounted on a vibrational free table 'o'. The Raman shifts reported for commercial Fe₃O₄ powder are 670cm⁻¹, 540cm⁻¹ and 308cm⁻¹[20].

3.3.4 Vibrating sample magnetometer (VSM) and

Alternating gradient field magnetometer (AGFM)

There are many magnetometers devised for the characterisation of magnetic materials, out of which only three different types of instruments are widely used today. They are the Vibrating sample magnetometer (VSM), Hysteresis meter (HM), and the Alternating gradient field magnetometer (AGFM). In the present work only VSM and AGFM were used for the sample characterisation. The VSM and AGFM are generally used to measure the magnetic properties of materials as a function of magnetic field, temperature and time. Basic theory of operation and details of the instruments used are given in the following sections.

3.3.4.1 Theory of operation

When a material is placed within a uniform magnetic field \mathbf{H} , a magnetic moment \mathbf{m} will be induced in the sample. A plot of the magnetisation \mathbf{M} , which is the total magnetic moments aligned in the direction of field per unit volume and applied field \mathbf{H} is called hysteresis loop of the magnetic material under study. A typical hysteresis loop of a ferromagnet with applied field in the direction of easy axis is given the Figure 3.31. The magnetisation \mathbf{M} reaches saturation value called saturation magnetisation \mathbf{M}_s at a certain applied field. When the field is decreased to zero the sample still holds certain value of magnetisation called the remanence \mathbf{M}_r . Increasing the field in opposite direction will bring the magnetisation to zero at an applied field \mathbf{H}_c which is called coercivity of the material. Further increase in the field will saturate the moments in the applied field. The loop traced has a rectangular shape and exhibits irreversible changes of magnetisation. The ratio of $\mathbf{M}_r/\mathbf{M}_s$ is called squareness ratio (SQR) and is essentially a measure of how square the hysteresis loop is. The hard axis loop is more linear and generally hysteresis free i.e. the magnetisation is more or less reversible. The magnetisation behaviour of the sample at different temperatures, \mathbf{T} , can be understood by

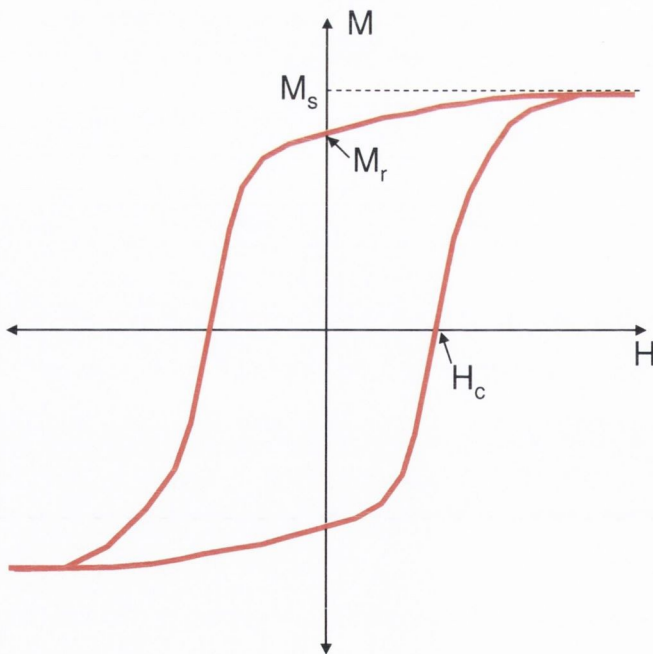


Figure 3.31. A typical hysteresis loop of a ferromagnet with applied field \mathbf{H} in the direction of easy axis.

tracing hysteresis loops at different temperatures or measuring the variation of \mathbf{M} with temperature \mathbf{T} at a constant field \mathbf{H} etc. A discussion on magnetisation of Fe_3O_4 samples and its connection with magnetoresistance behaviour is given in chapters 5 and 6.

As described in the preceding section §3.3.4, there exist many methods for the measurement of magnetic moments. They can be divided into two categories called (a) the inductive technique and (b) the force technique. The detailed explanation is given in the following paragraphs.

(a) Inductive technique

In this technique the voltage induced by a changing flux is measured. The most prevalent examples of magnetometers employing this technique are the hysteresis meter (HM) and Vibrating sample magnetometer (VSM). Since hysteresis meter is not used in the present work only the vibrating sample magnetometer is explained.

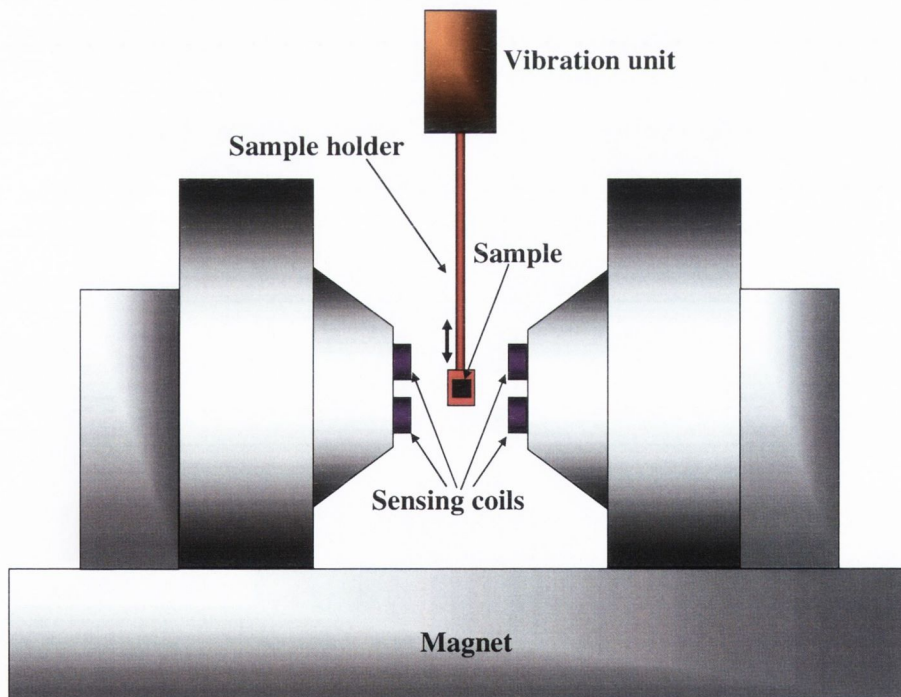


Figure 3.32. Schematic of a VSM measurement setup.

In a VSM generally an electromagnet is employed to provide the DC magnetising field \mathbf{H} (Super conducting magnets are used for generating higher

fields). A sample is placed in between the sensing coils or detection coils (which are suitably placed within the magnetic poles pieces of the electromagnet) and is made to undergo sinusoidal motion i.e. mechanically vibrated. The changing flux emanating from the vibrating magnetised sample induces a signal voltage in the sensing coils. The output measurement displays the magnetic moment \mathbf{M} as a function of the field \mathbf{H} . A schematic diagram of VSM is shown in Figure 3.32.

(b) Force technique

In this technique the force exerted on a magnetised sample in a magnetic field gradient is measured. The two main instruments based on this principle are the Faraday balance and the Alternating gradient force magnetometer (AGFM). Since faraday balance is not used in the present work, operating principle of AGFM is only explained

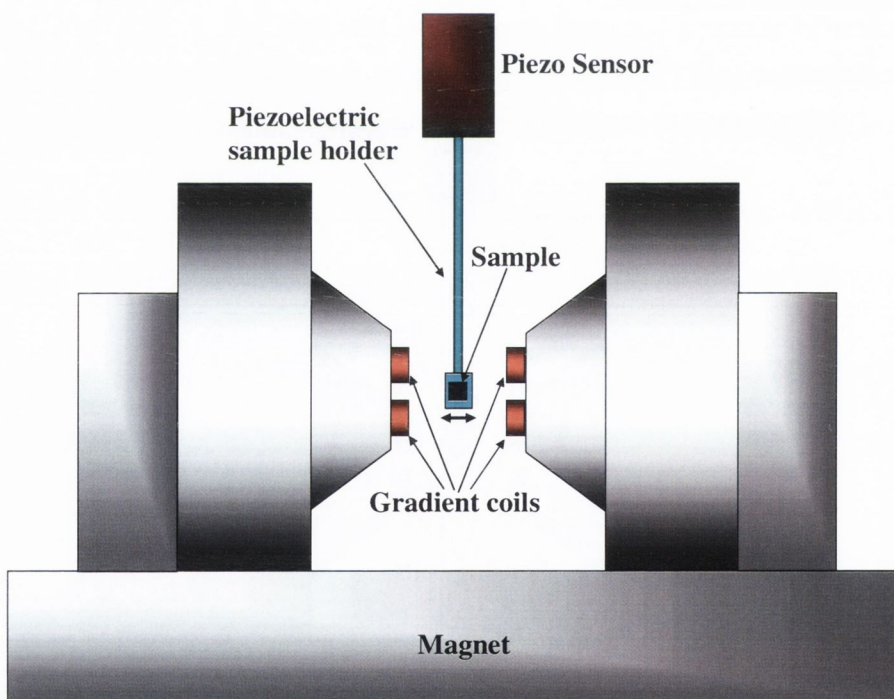


Figure 3.33. Schematic of a AGFM measurement setup.

In an AGFM, the sample is mounted on a piezoelectric transducer which oscillates when the sample is subjected to an alternating magnetic field gradient superimposed on the DC field of an electromagnet as shown in the

Figure 3.33. The alternating field gradient exerts an alternating force on the sample proportional to the magnitude of the gradient field and the magnetic moment of the sample. The resulting deflection of the extension is transmitted to the piezoelectric transducer. The output signal from the piezoelectric element is synchronously detected at the operating frequency of the gradient field. The signal developed by the piezoelectric element is greatly enhanced by operating at or near the mechanical resonant frequency of the assembly. Generally a built-in software function automatically determines the mechanical resonance and sets the appropriate operating frequency for the sample under study.

AGFM is a widely accepted technique in magnetic metrology because of its high sensitivity. The sample size that can be used on the AGFM is smaller in area compared with that of the VSM by a factor of 10 to 100 (typically 1 to 5mm square for the AGFM compared with 6 to 10mm square for the VSM). Therefore, the difference in the signal to noise ratio between the two instruments is usually small. The only case where the AGFM has significantly superior signal to noise ratio to a VSM is when one wants to measure only a very small area sample with very small thickness (1-3nm) and very small magnetisation. The piezoelectric sample holder of the AGFM is fragile and expensive and must be operated at the resonance frequency of the sample holder. Since the resonance frequency depends on the mass of the sample/substrate combination, it is required to re-tune to the resonance frequency for every new sample. If the magnetic moment is very low, then the automatic tuning doesn't work and the user has to do it manually. For AGFM the measured moment is very sensitive to the sample placement due to the gradient field and should be optimized for each sample. The AGFM is also very limited in measuring samples with large magnetic moments.

3.3.4.2 Details of VSM and AGFM used in the present work

Magnetisation measurements were performed in a MicroMag™ Model 3900 VSM system and a MicroMag™ Model 2900 AGFM system manufactured by Princeton Measurements Corporation USA, Model 3900. VSM had high sensitivity (1 μ emu (or 10^{-9} A-m²) at 1 second per point), a fast four-quadrant power supply and a 2 inch laboratory electromagnet with 1 Tesla field. Precision X, Y, and Z translation stages permit fast and accurate sample

placement. Anisotropy measurements are facilitated by a driver here that provides continuous rotation about the Z-axis. Sample holders accommodate a wide variety of thin films, solids, powders and liquids.

Actually the VSM and AGFM units were integrated into the same magnet and control unit. It was able to interchange between the two configurations, with out any complications, whenever required. The Model 2900AGFM system had extremely high sensitivity (10nemu (or $10^{-11}\text{A}\cdot\text{m}^2$) rms-corresponding to less than 50pg of iron) and high speed of measurement (100 ms per point). The system accommodates all types of samples (up to 5x5x2mm: 200mg mass): solids ultra thin films, powders liquids etc.

The VSM/AGFM unit was equipped with a LN2 (Liquid Nitrogen) variable temperature cryostat and a high temperature furnace with fully integrated temperature controller. The calibration of the VSM/AGFM system was done with a Standard Reference Material[®] (SRM) 2853 Magnetic Moment Standard- Yttrium Iron Garnet Sphere (YIG) supplied by National Institute of Standards and Technology (NIST). The sensitivity of VSM system was 1 μemu ($10^{-9}\text{A}\cdot\text{m}^2$) standard deviation (room temperature operation, 1s averaging time) and for AGFM it was 10 nemu ($10^{-11}\text{A}\cdot\text{m}^2$) standard deviation (room temperature operation, 1s averaging time)

3.3.5 Electrical resistivity measurements

In this section, the experimental details of low temperature resistivity and magnetoresistance measurements are given. The DC resistivity of the sample was measured with a HP 34401A Multimeter, in the standard four probe configuration. Electrical contacts were made on the sample using quick drying silver paint (Agar scientific, Batch number 0294) and ultra thin copper wire. The silver paint was diluted with Iso-Butyl-Methyl-Ketone (Agar scientific, Batch number R1272).

The low temperature measurements were carried out using two closed cycle refrigeration (CCR) systems (CTI-Cryogenics 8200 Compressor and Cryodyne Cryocooler, which uses helium as the refrigerant), which are identified here after as CCR 1 and CCR 2. A schematic of the CCR system is given in Figure 3.34. The sample was mounted on a copper sample holder using GE varnish (Oxford Scientific, which is a good thermal conductor but an electrical insulator) and was attached to the cold finger of the cryocooler using

brass screws in CCR 1 and directly screwed in to the cold finger in CCR 2 (for CCR 1 and CCR 2 different types of sample holders were used). Then the cold finger of the cryocooler was covered with a cylinder called the 'radiation shield' which was then covered with another cylinder called the 'vacuum shroud'.

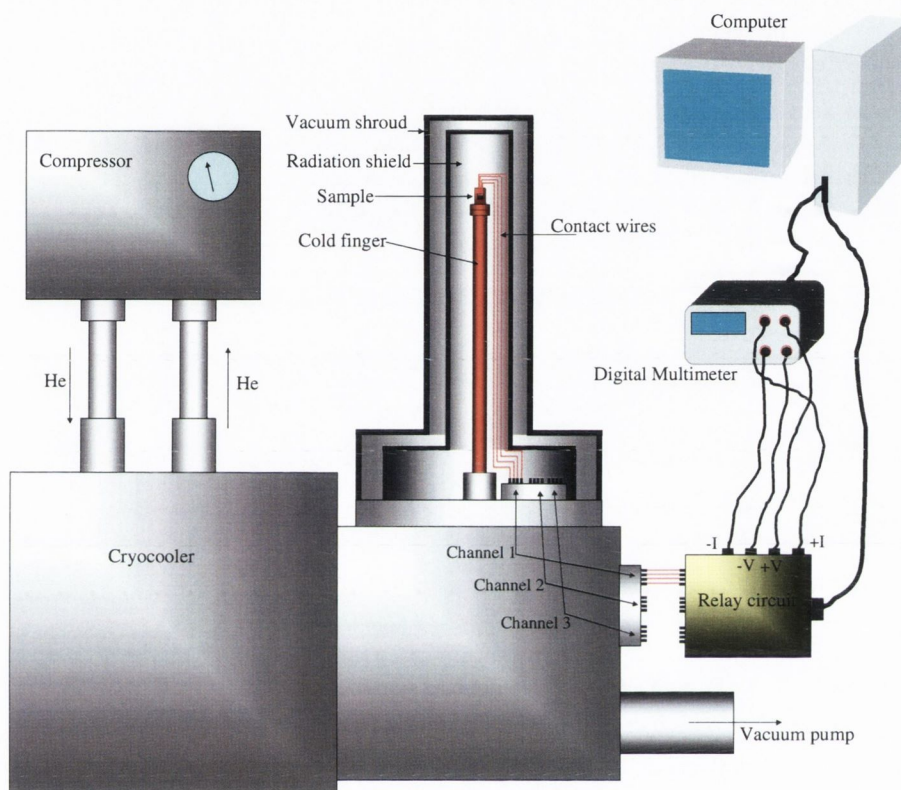


Figure 3.34. Schematic of the CCR Resistivity Measurement system. (not to scale). (Magnet not shown)

The radiation shield provided better temperature stability while vacuum shroud was used for achieving vacuum, with the aid of a rotary pump connected to the system. Electrical connections were made to the multimeter via an electrical feed-through. A relay circuit was also included in the connections to facilitate measurement of up to three samples at a time.

The compressor supplies compressed He gas into the cryocooler and there it expands using the heat supplied from the cold finger and eventually reduces the temperature of the sample stage. The temperature of the sample was controlled by a Lake Shore 330 Temperature Controller, which varied the current in the heating wires wound near to the sample, to counter the cooling

effect of the compressed helium from the compressor. The temperature of the sample stage was monitored using a GaAlAs thermometer with an accuracy of $\pm 0.05\text{K}$. In this manner it was possible to set a fixed temperature or to ramp the temperature with a constant rate, within the temperature range of 30 K to 300 K.



Figure 3.35. Photograph of the CCR 2 system in MR measurement configuration. The measurement head is inserted into the permanent magnet.

The change in electrical resistance of a sample with the application of a magnetic field is called magnetoresistance (MR) and is defined as:

$$\text{MR \%} = \frac{\mathbf{R(H)} - \mathbf{R(0)}}{\mathbf{R(0)}} \quad (3.34)$$

For the measurement of magnetoresistance the cold finger (with sample) was inserted in to a magnetic field. For CCR1, a Multimag (Model: MM-2000-26.5-001) variable field permanent magnet (Magnetic Solutions Ltd, Ireland) with a maximum field strength of 2 Tesla was used. Using this magnet, it was possible to vary the strength of the field with an accuracy of $\pm 1\text{mTesla}$ and orientation of the field with an accuracy of $\pm 0.1\text{degree}$, in a desired direction. Figure 3.35 shows the photograph of CCR1 with its sample stage inserted in to the magnetic field produced by the variable field permanent magnet.

For CCR 2, a 1 Tesla electromagnet (Bruker, Germany, Model: B-E10V) was used for providing the magnetic field. In this system the field orientation was fixed and therefore the sample stage along with the cryocooler was rotated in order to apply field in different directions of the sample. The entire system of CCR1 and CCR 2 were computer controlled and both the R-T and MR measurements were automated. Further details regarding the measurements are furnished in the following chapters.

Bibliography

- [1] W. Braun, Applied RHEED: Reflection High Energy Electron Diffraction During Crystal Growth, Springer Tracts in modern Physics (Springer, Berlin, Vol **154** (1999).
- [2] K. Britze and G. Meyer-Ehmsen, Surf. Sci. **77**, 131 (1978).
- [3] Y. Lee, J. Y. Juang, J. H. Ou, Y. F. Chen, K. H. Wu, T. M. Uen, and Y. S. Gou, Physica B **284-288**, 2099 (2000).
- [4] J.H. Neave, B.A. Joyce, P.J. Dobson, and N. Norton, Appl. Phys. A **31**, 1, (1983).
- [5] I. Hernández-Calderón, H. Höchst, Phys. Rev. B **27** 4961 (1983).
- [6] J.J. Harris, B.A. Joyce, P.J. Dobson, Surf. Sci. **103** L90 (1981).
- [7] C.E.C. Wood, Surf. Sci. **108** L441 (1981).
- [8] J.M. Van Hove, C.S. Lent, P.R. Pukite, P.I. Cohen, J. Vac. Sci. Technol. **B1** 741 (1983).
- [9] D. Lee, S.J. Barnett, A.D. Pitt, M. R. Houlton, G.W. Smith, Appl. Surf. Sci. **50** 428 (1991).
- [10] J. R. Arthur, Surf. Sci. **500**, 189 (2002).
- [11] P. Kidd, P.F. Fewster and N.L. Andrew, J. Phys. D Appl. Phys. **28**, A-133 (1995).
- [12] O. Auciello, A. R. Krauss, In situ real-time characterization of thin films, John Wiley & Sons, Inc (2001).
- [13] A. Krost, G. Bauer and J. Woitok, Optical characterization of epitaxial semiconductor layers, Springer Berlin/Heidelberg/New York, **Chapter 6**, 287 (1995).
- [14] D.B. Williams and C.B. Carter, Transmission Electron Microscopy, Plenum Press, New York, (1996).

- [15] P.B. Hirsch, A. Howie, R.B. Nicholson, D.W. Pashley and M.J. Whelan, Electron Microscopy of thin Crystals, Butterworths London,(1965).
- [16] W. Eerenstein, Spin-Dependent Transport Across Anti-Phase Boundaries in Magnetite Thin Films, PhD thesis, University of Groningen, Netherlands (2003).
- [17] M. Lentzen, Ultramicroscopy **99**, 211 (2004).
- [18] D.L.A. de Faria, S. Venancio Silva and M.T. de Oliveira, J. Raman Spectrosc.**28**, 873 (1997)
- [19] S.J. Oh, D.C. Cook and H.E. Townsend, Hyperfine Interact. **112**, 59(1998)
- [20] L. V. Gasparov, D.B. Tanner, D. B. Romero, H. Berger, G. Margaritondo, L Forro, Phys.Rev.B **62** 7939 (2000)
- [21] M. Pemble, Surface Analysis, John Wiley & Sons, Inc, **Chapter 7**, 299 (1998)

It is always delightful when a great and beautiful idea proves to be consonant with reality.

Einstein 1936

Chapter 4

Strain relaxation behaviour of (100) oriented Fe_3O_4 thin films

4.1 Introduction

During epitaxial growth, the unit cell of a thin film can distort due to elongation or compression of in-plane lattice constants in orthogonal directions depending on the sign of the lattice mismatch. Then the epitaxial system is said to be in a 'strained state'. The strain state of a thin film also depends on the differences in crystal structure symmetry between the film and substrate. Theoretical models predict that epitaxial systems with smaller mismatch will remain in a strained state until a critical film thickness (t_c) is reached and thereafter it will undergo relaxation by generating misfit dislocations [1]. The stoichiometry, strain, defect structure etc. are expected to play a crucial role in determining the physical properties of the epitaxial layers of Fe_3O_4 films.

MgO is an ideal substrate for epitaxy of magnetite (Fe_3O_4) because the difference in oxygen sub-lattice size of MgO and Fe_3O_4 gives a small lattice mismatch of 0.33%. Consequently, there are many investigations dealing with the growth of epitaxial thin films of Fe_3O_4 on MgO using a variety of deposition techniques [2-7]. There are also a few reports concerning the growth of Fe_3O_4 on MgAl_2O_4 , sapphire, Si and GaAs substrates [[8-10]. It has been noted previously [6] that the Fe_3O_4 films grown on MgO (100) show sluggish strain relaxation behaviour, relaxing partially well above the critical thickness of strain relaxation. Even for a thickness of 6.6 μm the relaxation was partial. However, no effort was made to understand the origin of this behaviour.

There are two distinct forms of symmetry breaking in $\text{Fe}_3\text{O}_4/\text{MgO}$ hetero-epitaxy. The first one is due to the fact that the lattice parameter of MgO is half that of Fe_3O_4 leading to disruption of translation symmetry. The other one is due to the reason that Fe_3O_4 ($\text{Fd}\bar{3}\text{m}$) crystal structure is lower in symmetry than MgO ($\text{Fm}\bar{3}\text{m}$). This leads to formation of antiphase boundaries (APB) [2-7]. The details of formation of APBs are discussed in chapter 2.

MgAl_2O_4 has the normal spinel structure and the lattice constant is 0.80831 nm. In the normal spinel structure the Mg^{2+} and Al^{3+} ions occupy the tetrahedral and octahedral sites respectively. For $\text{Fe}_3\text{O}_4/\text{MgAl}_2\text{O}_4$ system the lattice mismatch is much greater (3.9%) and films are found to be relaxed in agreement with the theoretical models. Since MgAl_2O_4 has the same spinel type crystal structure and symmetry as that of Fe_3O_4 , formation of APBs are not expected for the films grown on MgAl_2O_4 . However, the presence of APBs in $\text{Fe}_3\text{O}_4/\text{MgAl}_2\text{O}_4$ system has been reported [11].

The differences in crystal structure and symmetry of the MgO and MgAl_2O_4 substrates with Fe_3O_4 prompted us to look at the strain relaxation behaviour of Fe_3O_4 film on them which will essentially provide information about the role of crystal structure symmetry difference on the strain relaxation behaviour. This information will be very useful in the design of future spin electronic devices and nano-structures based on magnetite.

In this chapter we present the details of our investigations on anomalous strain relaxation behaviour of (100) oriented Fe_3O_4 films grown on MgO (100) and non-anomalous strain relaxation behaviour of (100) oriented Fe_3O_4 films grown on MgAl_2O_4 (100) substrates.

4.2. Experiment

The Fe_3O_4 thin films (thickness: 45-700nm) used in the present study were grown on (100) oriented MgO and MgAl_2O_4 single crystal substrates (cut along $\langle 100 \rangle$ direction within $\pm 0.5^\circ$) using oxygen plasma assisted molecular beam epitaxy, MBE, system (DCA MBE M600) with a base pressure 2×10^{-10} Torr. The substrates were cleaned in-situ at 600°C in 5×10^{-6} Torr oxygen for two hours. Growth of the Fe_3O_4 films was carried out at a substrate temperature of 250°C from a pure metallic Fe source by means of electron beam evaporation and oxygen free radicals generated by the electron cyclotron

resonance (ECR) plasma source. The plasma source was operated at 80 W power in an oxygen partial pressure of 1×10^{-5} Torr. Reflection high energy electron diffraction, RHEED, (STAIB Instruments) was used to monitor the growth mode and growth rate (0.3 \AA/s).

Magnetization measurements were performed using an alternating gradient field magnetometer (Micromag-3900, Princeton Measurements, USA) with a sensitivity of 10^{-8} emu ($10^{-11} \text{ A}\cdot\text{m}^2$). The magnetization versus field (M-H) loops were measured at room temperature by applying the magnetic field (maximum field of 10kOe) in the film plane along the $\langle 100 \rangle$ direction. The diamagnetic contribution from the MgO substrate was subtracted from the measured data by performing a M-H loop of the MgO substrate of similar dimensions as that of thin film sample, in the same field range. The uncertainty in measuring the absolute value of magnetization for the films was about 1 %. Room temperature Raman spectroscopy was performed in the backscattering configuration using Rainshaw 1000 Micro Raman system. The Ar^+ ion laser (514.5 nm) was used for the Raman measurements.

Structural characterization of Fe_3O_4 thin films was done using a multi-crystal high-resolution x-ray diffractometer, HRXRD (Bede-D1, Bede, UK). The HRXRD in double or triple axis configuration was performed to confirm the epitaxial relationship of the $\text{Fe}_3\text{O}_4/\text{MgO}$ and $\text{Fe}_3\text{O}_4/\text{MgAl}_2\text{O}_4$ hetero-epitaxy. The in-plane (\mathbf{a}_{\parallel}) and out-of-plane (\mathbf{a}_{\perp}) lattice parameters were determined from the analysis of ω - 2θ scans measured around the symmetric (200) and asymmetric (311) diffraction planes common to the substrate and thin film.

To study the coherency of the thin film-substrate interface and the morphology of the APBs transmission electron microscopy (TEM) was employed using cross-sectional and plan view samples. Mechanical thinning and Ar ion milling was applied to obtain electron transparent areas within the TEM specimen. Structural defects were identified by conventional TEM using a Philips CM 20 electron microscope operated at 200 kV. High-resolution images were obtained with a Philips CM 200 electron microscope, which was equipped with a CEOS double hexapole corrector.

4.3 Results and discussion

4.3.1 Studies on Fe_3O_4 (100)/MgO (100) system

4.3.1.1 RHEED measurements

Reflection high energy electron diffraction, was used to monitor the growth mode and growth rate.

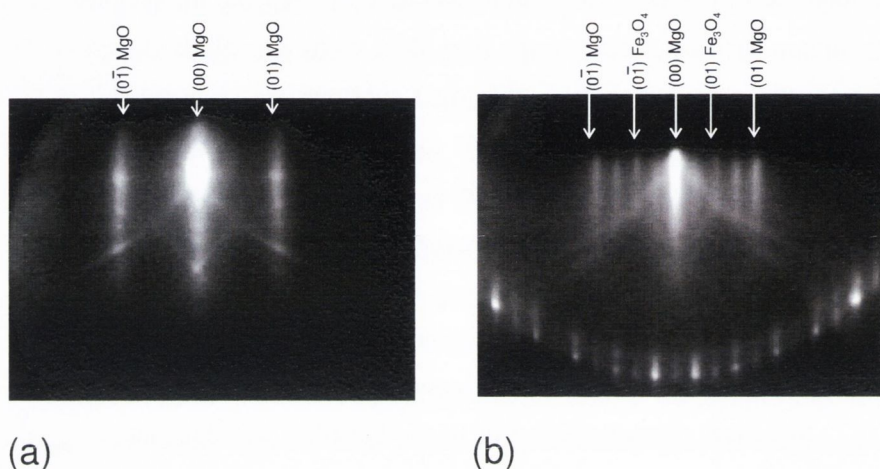


Figure 4.1 RHEED pattern of (a) MgO substrate and (b) 70 nm thick Fe_3O_4 film along the (100) azimuth.

Figure 4.1(a) shows the RHEED pattern of the MgO (100) single crystalline substrate measured along the $\langle 100 \rangle$ azimuth after following the cleaning procedure described in the experimental section. It shows vertical lattice rods and radial Kikuchi lines indicative of well ordered and flat surface. After the growth of two monolayers (ML) of iron oxide thin films, half order lattice rods appear in the RHEED pattern located in the middle of lattice rods corresponding to MgO, indicating the formation of Fe_3O_4 . Figure. 4.1(b) shows the RHEED pattern of a 70 nm thick Fe_3O_4 thin film measured along the $\langle 100 \rangle$ azimuth. The lattice constant of magnetite as determined from RHEED images is $8.4 \pm 0.1 \text{ \AA}$. The appearance of half order streaks is accompanied by the oscillations in the intensity of specularly reflected beam. The RHEED patterns were similar for all other film thicknesses. Period of oscillation corresponds to the growth rate 0.3 \AA/s and confirms that the film growth occurs in a layer-by-layer mode. Figure 4.2 shows RHEED intensity oscillations corresponding to a growth rate of 0.3 \AA/s . Within the window of growth

conditions, we never observed the formation of any iron oxide phase (FeO and γ -Fe₂O₃) other than magnetite.

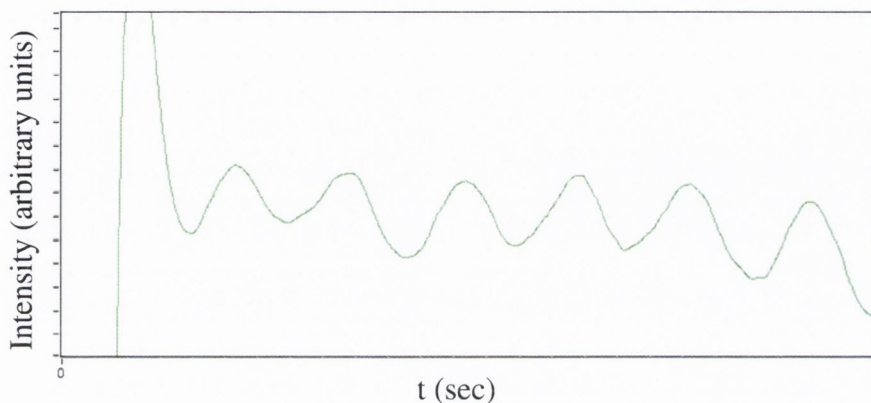


Figure 4.2 RHEED intensity oscillations observed during the growth of Fe₃O₄ film on MgO substrate which gives a growth rate of 0.3 Å/s.

4.3.1.2 Raman spectroscopy

Room temperature Raman spectroscopy was performed in order to ascertain the Fe₃O₄ phase. The excitation wavelength used was 514.5nm from an Ar⁺ ion laser (Laser Physics Reliant 150 Select Multi-Line) with maximum power of ~10mW (Although ~3mW power was used for the measurements in order to avoid excessive heating and oxidation). The laser beam was guided to an objective lens of the Leica Microscope with a specific magnification (50X magnifying objective lens focus the beam into a spot of about 1 μ m size).

The magnetite thin films grown on MgO (100) substrate showed Raman shifts corresponding to Fe₃O₄ phase at 662.82, 533.70 and 302.63 cm⁻¹ (± 0.01 cm⁻¹) wave numbers. The FWHM of the most intense Raman peaks were 33.79, 34.19, 33.92, 33.91 and 36.47 for 70, 120, 200, 400 and 700nm, respectively. No Raman peaks corresponding to the other iron oxide phases were present. The Raman bands are shifted to lower wave number position in comparison with the values observed for bulk single crystal of Fe₃O₄ (which are 670, 540 and 308 cm⁻¹) and are representative of in-plane tensile strain [12]. Raman measurements therefore confirm that films grown have magnetite phase and indicates the presence of strain within the film. Figure 4.3 shows Raman shifts observed for Fe₃O₄ films having various thicknesses grown on MgO substrate and the results are tabulated in Table.4.1.

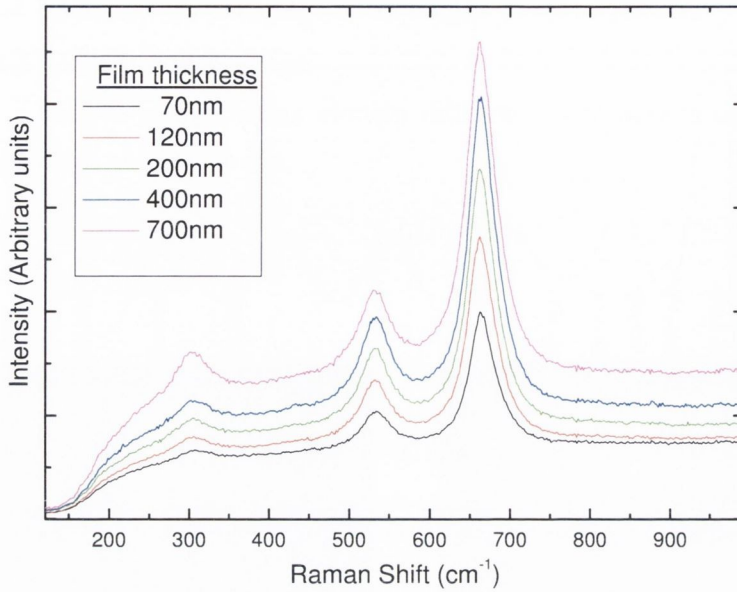


Figure 4.3 Raman shifts observed for Fe_3O_4 films having various thicknesses grown on MgO substrate. Curves are shifted on the vertical axis for clarity.

Sample	Raman Shift (cm^{-1})		
	($\pm 0.01\text{cm}^{-1}$)		
Bulk Fe_3O_4	670	540	308
70 nm Fe_3O_4	662.8	533.7	302.6
120 nm Fe_3O_4	662.8	533.7	302.6
200 nm Fe_3O_4	662.8	533.7	302.6
400 nm Fe_3O_4	662.8	533.7	302.6
700 nm Fe_3O_4	662.8	533.7	302.6

Table 4.1 Raman shifts observed for Fe_3O_4 films having various thicknesses grown on MgO substrate.

4.3.1.3 Magnetization measurements

Magnetization measurements on different thickness magnetite films showed that it was possible to saturate the films of thickness greater than 120 nm with a moderate magnetic field (5-8 kOe). The saturation magnetization, M_S , measured at room temperature for the Fe_3O_4 films (>120 nm) on MgO

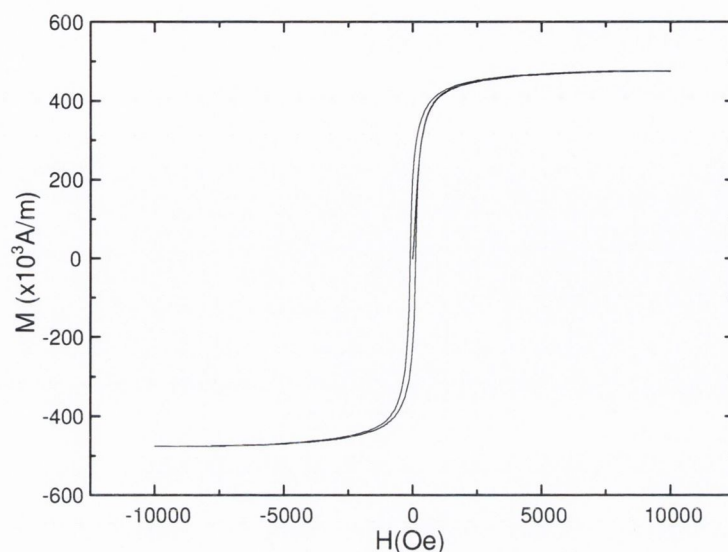


Figure 4.4 Magnetization curve obtained for 700 nm epitaxial magnetite film grown on MgO substrate.

Sample	Thickness (nm)	M_s (10kOe) $\times 10^3$ (A/m)
Fe ₃ O ₄ /MgO	45	468
	120	472
	200	475
	400	473
	700	475

Table 4.2 Summary of the magnetization (M) at 10kOe field for the epitaxial magnetite films as a function of film thickness.

substrates was found to be 475×10^3 A/m within the experimental uncertainty of 1%, which includes the error in thin film volume estimate. The observed values of M_s are in agreement with the M_s value for bulk magnetite (480×10^3 A/m). For smaller thickness films, the magnetization (M) values attained for a 10 kOe field were lower than the saturation magnetization (M_s) of bulk magnetite, displaying a finite slope at higher fields. The observation of

a reduced \mathbf{M} and the inability to saturate epitaxial Fe_3O_4 films has been attributed to the presence of APBs [6,7]. An increase in \mathbf{M} and a reduction in slope of the \mathbf{M} - \mathbf{H} curves at higher fields with increasing thickness suggests an increase in separation between the APBs. The magnetization results are in line with previous reports [6,7]. Figure 4.4 shows the magnetization curve obtained for a 700 nm film and the results obtained from films with various thicknesses are summarised in Table 4.2.

4.3.1.4 Resistivity measurements

In addition to the magnetization measurements, resistivity as a function of temperature was investigated in these films. Resistivity values for these films measured at 300 K were found to decrease with an increase in thickness. For film thickness above 120 nm, the resistivity values didn't show much variation.

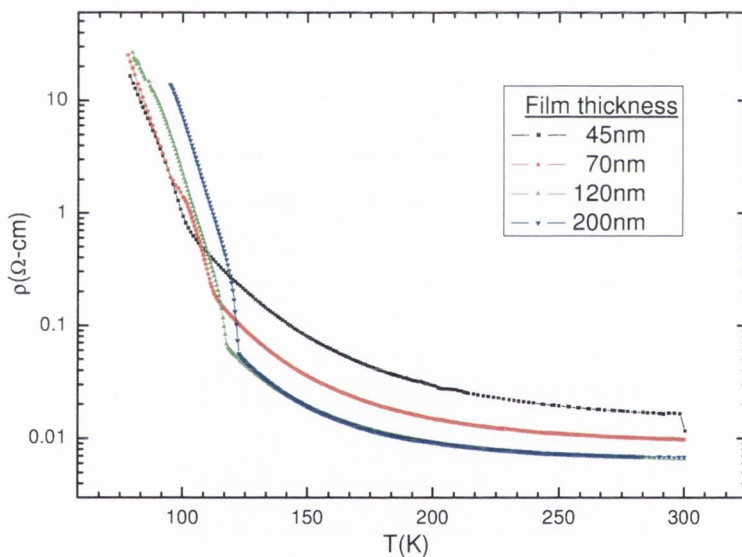


Figure 4.5 Verwey transition observed for Fe_3O_4 films having various thicknesses grown on MgO substrate.

The Verwey transition temperature for these films was found to be thickness dependent; being 108 K ($\pm 0.5\text{K}$) for the 45 nm film and 120 K ($\pm 0.5\text{K}$) for the 700 nm film. Figure 4.5 shows Verwey transition observed in films with various thicknesses. Since Verwey transition is very sensitive to the Fe_3O_4 film

Sample	Thickness (nm)	Resitivity at 300 K (Ohm-cm)	Verwey Transition Temperature (K)
Fe ₃ O ₄ /MgO	45	0.015	108.0
	70	0.0100	114.0
	120	0.0071	117.5
	200	0.0069	118.2
	400	0.0068	120.0
	700	0.0069	120.5

Table 4.3 Summary of the resistivity values at 300K and Verwey transition temperatures observed for the epitaxial magnetite films as a function of film thickness.

stoichiometry (see chapter 2), the observation of Verwey transition confirms that the films are stoichiometric. The enhancement in resistivity with reduction in film thickness is due to a decrease in APB domain size or increase in APB density with reduction in thickness [13]. The resistivity results also support our conclusion that the separation between the APBs in Fe₃O₄/MgO films is thickness dependent and it increases with an increase in film thickness. The resistivity results are summarized in Table 4.3.

4.3.1.5 HRXRD measurements

Figure.4.6 shows the ω - 2θ scans (measured in triple-axis configuration at room temperature) for the (200) and (400) symmetric Bragg reflections of MgO and film respectively for different thickness (70-700 nm) Fe₃O₄ films.

The horizontal axis in the figure is shown with reference to the Bragg angle of the (200) reflection for MgO substrate. The curves are shifted along the vertical axis for clarity. The bottom and top most curves belong to 70 nm and 700 nm thickness respectively. The full width at half of maximum (FWHM) of the film peak decreases with increasing film thickness, up to a thickness of 200 nm, and remains constant for further increase in thickness. The FWHM for film peak was found to be 0.03 to 0.015° for 70 nm and 700 nm thick films respectively. The FWHM for the film peaks are comparable to that of the substrate (0.008-0.009°). The value of a_{\perp} for the Fe₃O₄ thin films was determined from the separation of film-substrate peaks (0.14605°) and was

found to be 0.83717 nm within the experimental accuracy (± 0.00005 nm). Independent ω -rocking curves for film and substrate peaks indicated that the mosaic spread in the Fe_3O_4 thin films was comparable to that of the substrate.

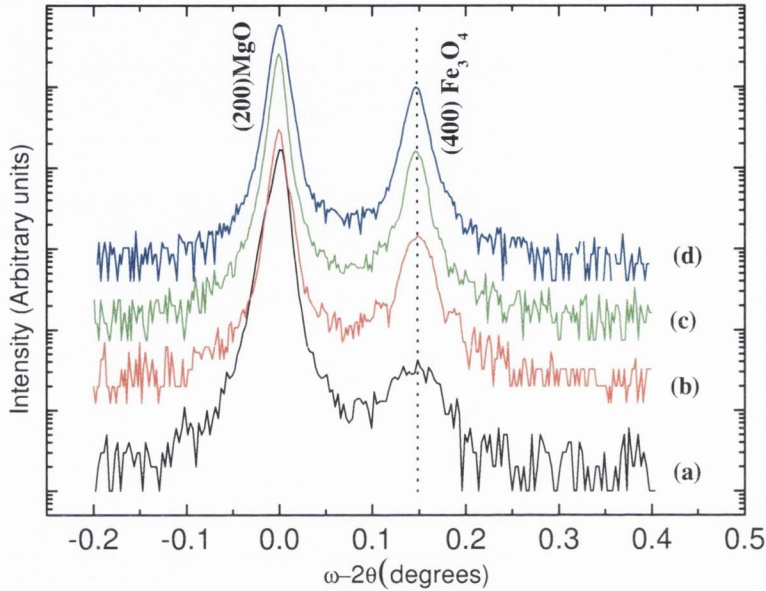


Figure 4.6 The ω - 2θ scans for Fe_3O_4 films with different thickness on MgO (100) substrates, measured for symmetric (200) Bragg reflection common to substrate and thin film. Curves **a**, **b**, **c** and **d** corresponds to 70, 200, 400 and 700 nm film thickness respectively. Curves are shifted on the vertical axis for clarity.

The ω - $n\theta$ ($n=5.18$) scans (measured in double axis configuration at room temperature) for the (311) asymmetric Bragg reflection of MgO which is common to the (622) reflection of the Fe_3O_4 film, in grazing exit geometry ($\omega=62.5685$, $2\theta=74.6582$), are shown in Figure.4.7. A value other than 2 of the angular ratio $2\theta/\omega$ was required to detect the thin film peak through a single ω - $n\theta$ scan. This is due to the reason that the position of reciprocal lattice point, RLP, of thin film in the reciprocal space is not in a straight line with substrate RLP position due to the strain tilt. Detailed explanation of this point is given in chapter 3, section 3.3. In addition to grazing exit (GE) geometry, asymmetric scans were also performed using a grazing incidence (GI) geometry. From the analysis of GE and GI asymmetric scans we obtained the in-plane and out-of-plane lattice parameters of the films. FWHM of the film peaks were found to be 0.025, 0.16, 0.158 and 0.158° for 70, 200, 400 and 700

nm thickness films respectively. The $a_{||}$ was found to be 0.8426 nm for all the films, within the experimental accuracy, exactly twice the substrate lattice constant. The values of a_{\perp} are consistent with the values estimated through independent symmetric ω - 2θ scans.

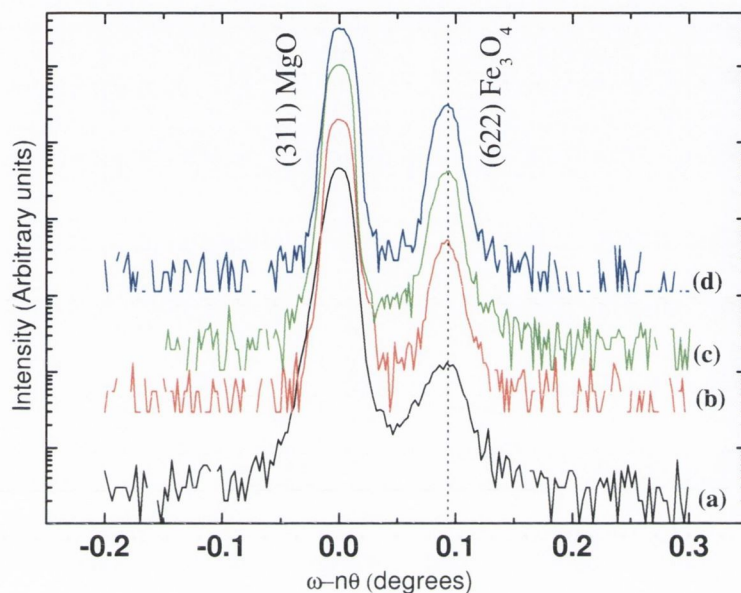


Figure 4.7. The ω - $n\theta$ scans for Fe_3O_4 films with different thickness on MgO (100) substrates, measured for asymmetric (311) Bragg reflections common to substrate and thin film. Curves **a**, **b**, **c** and **d** corresponds to 70, 200, 400 and 700 nm film thickness respectively. For asymmetric (311) Bragg reflection measurements, the grazing exit geometry was used. Curves are shifted on the vertical axis for clarity.

A representative two-dimensional contour plot of x-ray diffraction intensity as a function of reciprocal lattice vectors $\mathbf{Q}(\mathbf{x})$ and $\mathbf{Q}(\mathbf{z})$ for the 700 nm thick Fe_3O_4 film on MgO performed around the (200)/(400) Bragg reflection is shown in Figure 4.8. The reciprocal lattice vectors $\mathbf{Q}(\mathbf{x})$ and $\mathbf{Q}(\mathbf{z})$ represent the in-plane (110) and out-of-plane (100) directions respectively. The position of intense substrate peak is adjusted to the bulk MgO ($a=0.4213$ nm) position. The strong sharp peak corresponds to (200) reciprocal lattice point (RLP) of MgO and other weaker one at higher $\mathbf{Q}(\mathbf{z})$ position corresponds to the (400) RLP of Fe_3O_4 thin film. Both the substrate and thin film RLPs show a broadening along the $\mathbf{Q}(\mathbf{x})$ direction which is indicative of mosaic spread in the MgO crystal. The mosaic spread in the Fe_3O_4 thin film is comparable to that of

the substrate. The value of a_{\perp} for the Fe_3O_4 thin film determined from the film peak position along $Q(z)$ direction in the RSM and film-substrate peak separation (0.14605°) from independent ω - 2θ scan is 0.83717 nm.

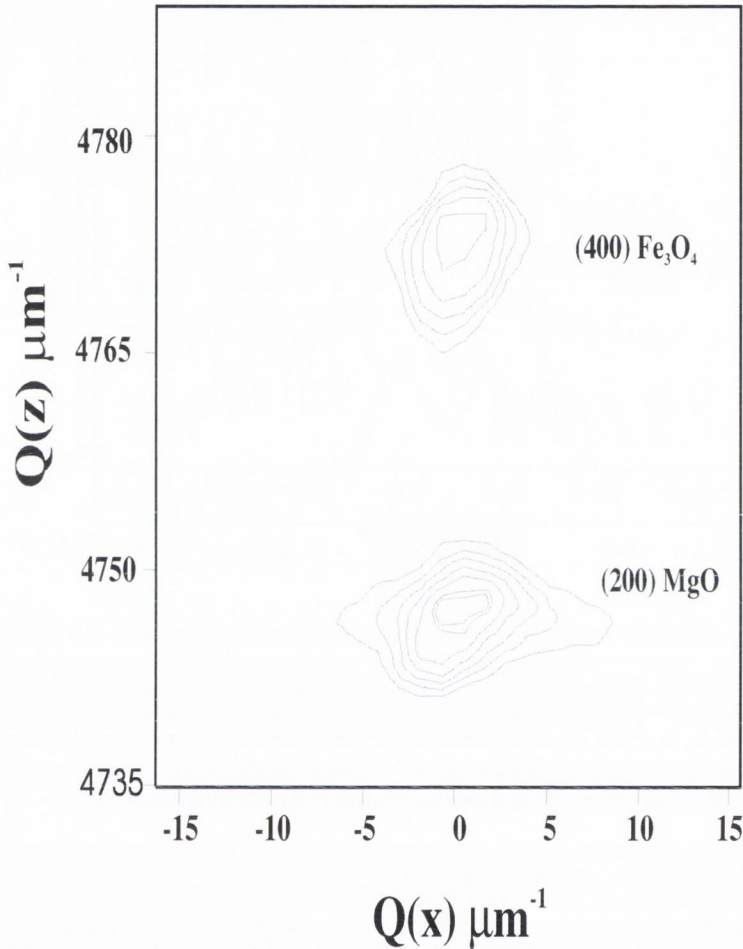


Figure.4.8 Reciprocal space map of 700 nm thick Fe_3O_4 film on MgO measured for symmetric (200)/(400) Bragg reflections common to substrate and thin film.

The HR-XRD results show that the films grown on MgO remain fully coherent up to 700 nm thickness on the MgO (100) substrate. This was the largest thickness we could grow with the MBE due to the small growth rate (0.3 \AA/s) used. Moreover, we were concerned with growing films under identical conditions to make sure that there were no variations in the film quality that could complicate the comparison of the strain relaxation behaviour.

From the detailed structural characterization, we infer that the films grown on MgO substrates remains fully coherent up to 700 nm thickness. The lack of strain relaxation in Fe₃O₄/MgO up to 700 nm thickness is a totally unexpected result. For Fe₃O₄ films on MgO (100) we expected a significant amount of strain relaxation at a thickness of 700 nm, which is much greater than the estimated value of critical thickness, t_c , (60 nm) for strain relaxation on the basis of widely used Mathew and Blakeslee's (M-B) model [1], details of which is given in the discussion part.

4.3.1.6 TEM Studies

To check the coherency of the interface we performed TEM studies on Fe₃O₄ films. Figure 4.9 shows a cross-sectional TEM bright field image of a Fe₃O₄-MgO interface. According to the (220) two beam imaging conditions chosen, APBs are characterized by distinct contrast fluctuations. The network of APBs is observed to be denser close to the interface. The typical separation between APBs within the upper part of the film is about 100 nm. This is also confirmed by the plan-view image, which shows the upper part of the film (Figure 4.10 and figure 4.11). Again (220) two beam imaging conditions were applied to visualize the APBs. Due to their inclination towards the electron beam, some of the APBs display fringe contrast. Apart from the APBs no structural defects, such as dislocations were observed, no matter which imaging condition was chosen. The high resolution electron micrograph (Figure 4.12) displays the interface between the MgO substrate and the Fe₃O₄ film. White atom contrast was obtained according to the negative Cs imaging conditions chosen. The interface was observed to be completely coherent.

The network of APBs is formed during the coalescence of the initial spinel nuclei [2,3,6]. While the oxygen sublattice of different islands coalesces without forming any defects, various arrangements of cations in the spinel islands result in the formation of APBs. In our case, the systematic variation of separation between APBs, across the film thickness is contrary to previous reports[3,13]. Earlier reports suggested that the separation between APBs increases with film thickness and is uniform for a given thickness. However, the results reported by them [3,13] refer to a plan-view configuration; therefore, the information related to the size in the growth direction is not accessible. The size evolution of structurally shifted domains is not an

uncommon feature and has been reported previously by other researchers for the case of GaAs/Si and GaAs/GaAs [14,15].

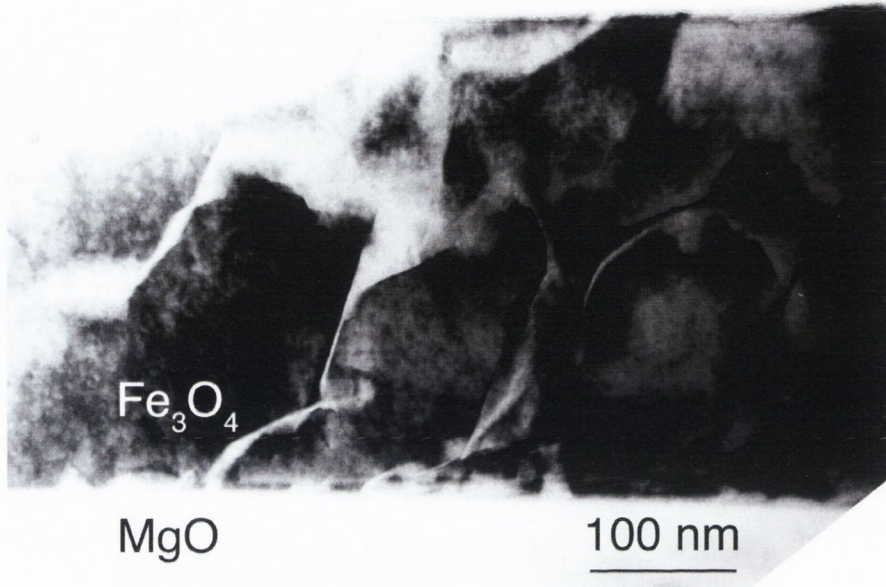


Figure.4.9. Cross-sectional TEM image of 400 nm $\text{Fe}_3\text{O}_4/\text{MgO}$ recorded under two beam conditions for (2-20) spinel diffraction showing the presence of APBs in the Fe_3O_4 film.

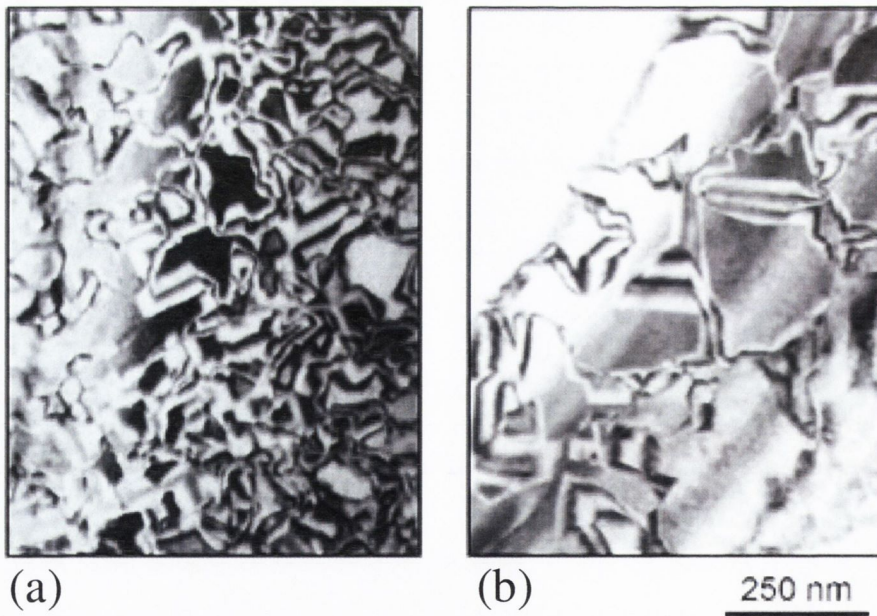


Figure.4.10. Plan-view bright field electron micrograph taken with (220) two beam imaging conditions showing the network of APBs in a (a) 200 nm and (b) 700nm Fe_3O_4 film grown on MgO substrate.

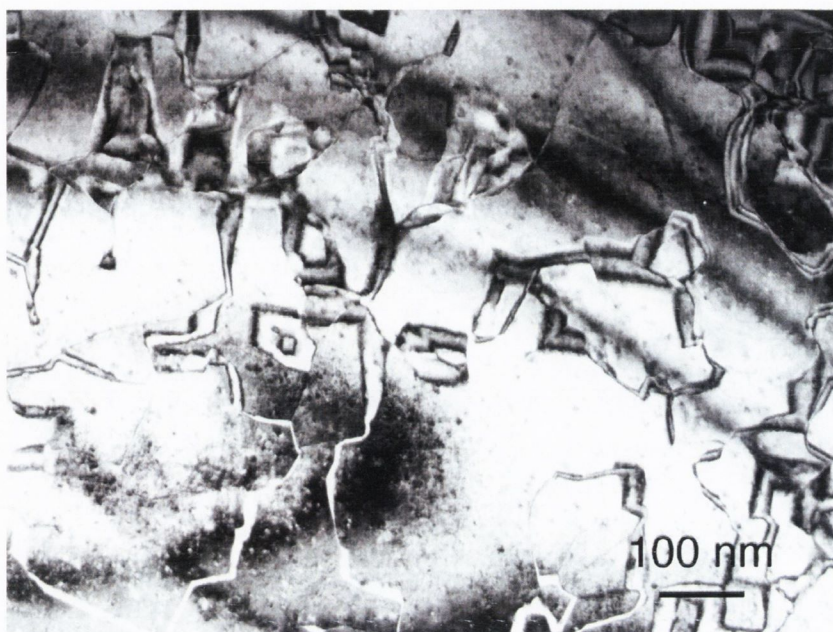


Figure.4.11. Plan- view bright field electron micrograph taken with (220) two beam imaging conditions showing the network of APBs in a 400 nm Fe₃O₄ film grown on MgO substrate.

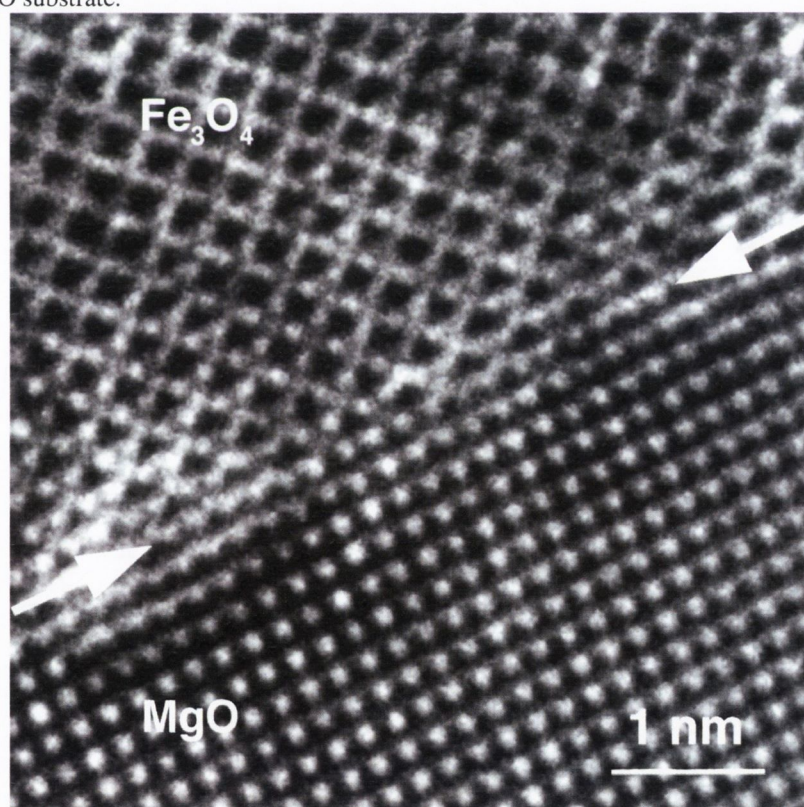


Figure.4.12. High resolution cross-section TEM image of 400 nm Fe₃O₄/MgO in (100) orientation taken with a Cs=-40 μ m and at overfocus. Accordingly, white atom contrast is obtained. Arrows mark the Fe₃O₄-MgO interface.

The driving force for the reduction of the density of APBs can be the minimization of the total energy which implies a minimization of the APB area. Another possibility to explain the size evolution is the fusion of two APBs on different $\langle 110 \rangle$ planes, e.g. if two APBs grow along $\langle 011 \rangle$ and $\langle 0\bar{1}1 \rangle$ direction, they may merge at some thickness depending on their separation at the point of nucleation.

4.3.1.7 Discussion

In order to look at the anomalous strain relaxation behaviour of $\text{Fe}_3\text{O}_4/\text{MgO}$ heteroepitaxy, it is important to furnish the details of critical thickness, t_c , prediction for this system. At thermodynamic equilibrium, misfit dislocations appear at the interface of strained layer heterostructure when the strained layer is thick enough that it is energetically favourable for the mismatch to be accommodated by a combination of elastic strain and interfacial misfit dislocations [16,17]. There are many reports on calculations and discussions of the equilibrium critical thickness t_c [1,17-21]. One of the widely accepted models is Matthews and Blakeslee (MB) model [1].

MB model is formulated by considering the two important forces acting on the dislocation lines which are F_ϵ and F_1 as shown in the figure 4.13. F_ϵ is the force exerted by the misfit strain and F_1 is the tension in the dislocation line. Their analysis shows that, in the case of layers A and B whose elastic constants are equal and isotropic, and also thickness of the layers $t_A = t_B$, then there arises three possible geometries of dislocations as indicated in the figure 4.13 as (a), (b) and (c).

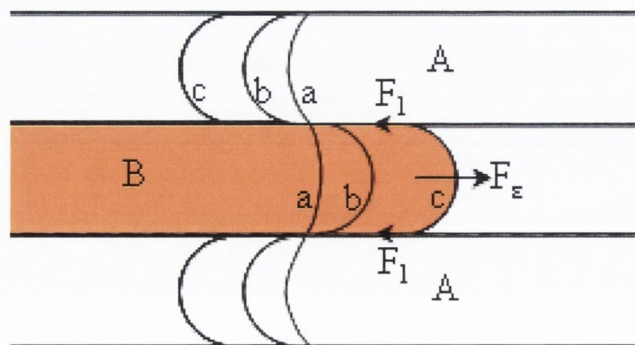


Figure. 4.13. Three possible dislocation geometries in multilayers. (a) coherent (b) critical (c) incoherent. Reproduced from [1]

The dislocation geometry **(a)** corresponds to the coherent case where $F_{\varepsilon \max}$ (the maximum value of F_{ε}) is less than $2 F_1$, **(b)** corresponds to the critical case where $F_{\varepsilon \max} = 2 F_1$ and **(c)** corresponds to the incoherent case where $F_{\varepsilon \max} > 2 F_1$. The critical thickness at which $F_{\varepsilon \max} = 2 F_1$ is given as:

$$t_c = \frac{b}{4\pi(1+\nu)e} \left[\ln\left(\frac{t_c}{b}\right) + 1 \right] \quad (4.1)$$

Where **b** is the Burger vector, **e** is the misfit strain ($e = (a_{TF} - a_S)/a_S$, a_{TF} and a_S being the film and substrate lattice parameters) and ν is the Poisson ratio. The MB model was refined by Fischer, Kuhne and Richter (FKR), by taking into consideration the interaction between dislocations employing the image force approach [16]. Critical thickness t_c estimated using the approach yields better agreement with the observed results. The critical thickness given by this model is :

$$t_c = \frac{b \cos \lambda}{e} \left[1 + \ln\left(\frac{t_c}{b}\right) \left(\frac{1 - \frac{\nu}{4}}{4\pi(1+\nu)\cos^2 \lambda} \right) \right] \quad (4.2)$$

where λ is the angle between the Burger vector and the direction in the interface normal to the dislocation line. By using the experimentally obtained value of $\nu = 0.30$ (estimated by measuring a_{\parallel} and a_{\perp} from the asymmetric Bragg reflection performed in grazing exit and grazing incidence geometries) and Burger vector values of 0.59580 nm, this model gives a value of t_c of 70 nm for the Fe_3O_4/MgO system. Figure 4.14 shows the calculated equilibrium in-plane strain, ε_{\parallel} ,

$$\varepsilon_{\parallel} = \frac{a_{Fe_3O_4 TF} - a_{Fe_3O_4 bulk}}{a_{Fe_3O_4 bulk}} \quad (4.3)$$

using the FKR-model for Fe_3O_4 films on MgO as a function of thickness along with the measured experimental data.

It is evident from this figure that the observed and calculated values are not in agreement. For Fe_3O_4/MgO hetero-epitaxy, no relaxation is observed up to 700 nm. This thickness is about an order of magnitude larger than predicted

by the FKR model. In an earlier study, Margulies et al [6] have mentioned about the partial relaxation of strain in films much thicker than the critical thickness of strain relaxation. Even at 6.6 μm thickness the films do not exhibit fully relaxed state. Although, they noticed this feature, the issue of anomalous strain relaxation behaviour was not addressed, as this was not the main focus of their investigations. Kale et al [9] explained some of the anomalous features observed in the magnetic properties of Fe_3O_4 films on MgO and MgAl_2O_4 substrates on the basis of critical thickness calculations. It was not clear from their investigations that whether the $\text{Fe}_3\text{O}_4/\text{MgO}$ films did exhibit anomalous or normal strain relaxation behaviour as no details on the structural characterization was provided.

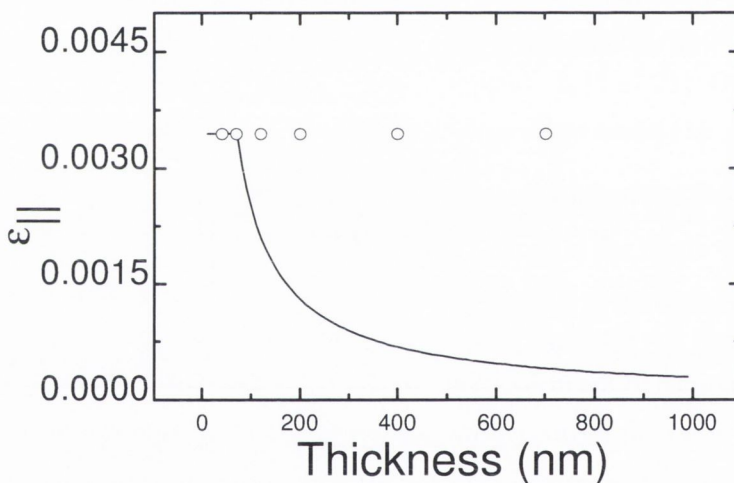


Figure.4.14 Comparison of experimentally observed values of the in-plane strain, $\epsilon_{||}$, with the FKR model predictions for the Fe_3O_4 films grown on MgO (100) substrates as a function of thickness. The solid line is the theoretical prediction and scattered points are experimentally observed values.

In order to understand the driving force that enables the film to maintain this large amount of elastic energy in $\text{Fe}_3\text{O}_4/\text{MgO}$ hetero-epitaxy, we need to analyse the crystal structure differences between MgO and Fe_3O_4 . One could suggest that the structure of Fe_3O_4 accommodates the strain by deviation from stoichiometry. Such deviations should result in a lattice constant change. However, this explanation has to be discarded due to the fact that the volume of the magnetite unit cell in our films, which is sensitive to deviations from

stoichiometry, remains constant. In addition to structural investigations the Verwey temperature of the films was also measured using the four-probe resistivity technique. As the Verwey temperature is highly sensitive to deviations from stoichiometry, its presence in all the films (Table.4.3) further confirms that the films consist of stoichiometric magnetite.

Another reason for the lack of strain relaxation at much greater thickness in this hetero-epitaxial system is possibly related to the difference between the crystal symmetry of the film and substrate, which leads to the formation of APBs. APBs can be formed due to the different translation and rotational symmetries of Fe_3O_4 and MgO . There are two kinds of APBs resulting from the disruption of translation symmetry. These correspond to half and quarter lattice constant shifts along the $\langle 100 \rangle$ and $\langle 110 \rangle$ directions respectively. The third type of APB results from the disruption of rotational symmetry, which is equivalent to an out-of-plane shift by a quarter of a lattice period. The structure and formation of these APBs are discussed in chapter 2.

We suggest that the presence of APBs influences the strain relaxation behaviour of the Fe_3O_4 films. Although the symmetry faults leading to APBs formation are easy to figure out, the detailed structure of the APBs on the atomic level is unclear. At present, there is not enough experimental data to provide an understanding of the issue. The region around an APB could be nearly stoichiometric or substantially non-stoichiometric since the spinel structure itself contains a large amount of vacant A and B sites. Therefore, the total energy of the APB depends on its shape, size, number of erroneous bonds, nearest neighbour interaction and the atomic arrangement in its vicinity. The APB is a static defect and one might expect that when the growth of the first monolayer (ML) of Fe_3O_4 is completed, these domains would grow vertically, so that the film thickness does not affect the density of the APBs. However, this is not the case as reported by others [13].

Our results suggest that the presence of APBs is responsible for the observed strain relaxation behaviour. It is reasonable to expect that the mechanical properties of a single APB are different for the two directions: along and perpendicular to the APB's plane. The growth of APBs is also known to be strongly anisotropic with respect to the film surface, i.e. the density of APBs with planes directed substantially perpendicular to the surface of the film is significantly different to that of the APB's with planes

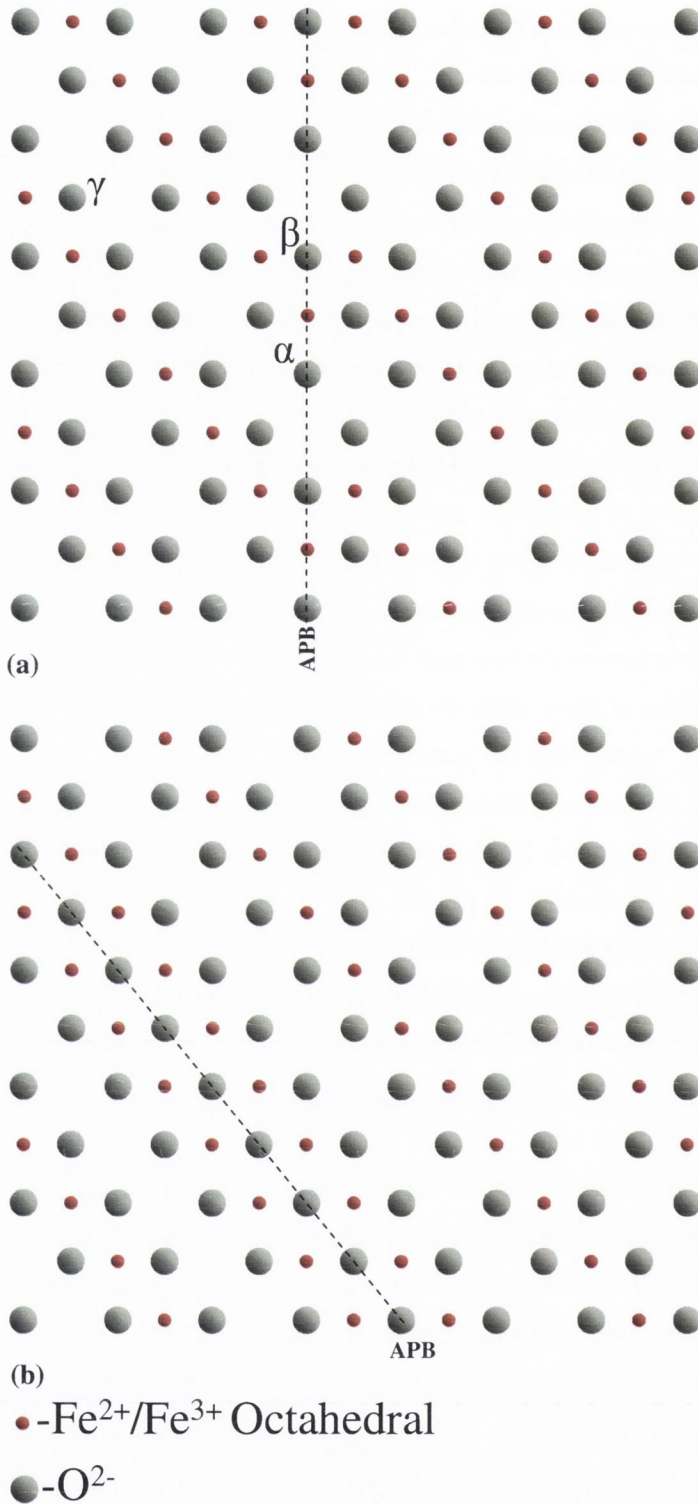


Figure. 4.15 Schematic diagram of an antiphase boundary formed in Fe₃O₄ films grown on MgO (100) substrate assuming a perfect oxygen sublattice; (a) with $\frac{1}{2}$ [100] shift vector along the $\langle 010 \rangle$ direction and (b) $\frac{1}{4}$ $\langle 100 \rangle$ shift vector along $\langle 1-10 \rangle$ direction.

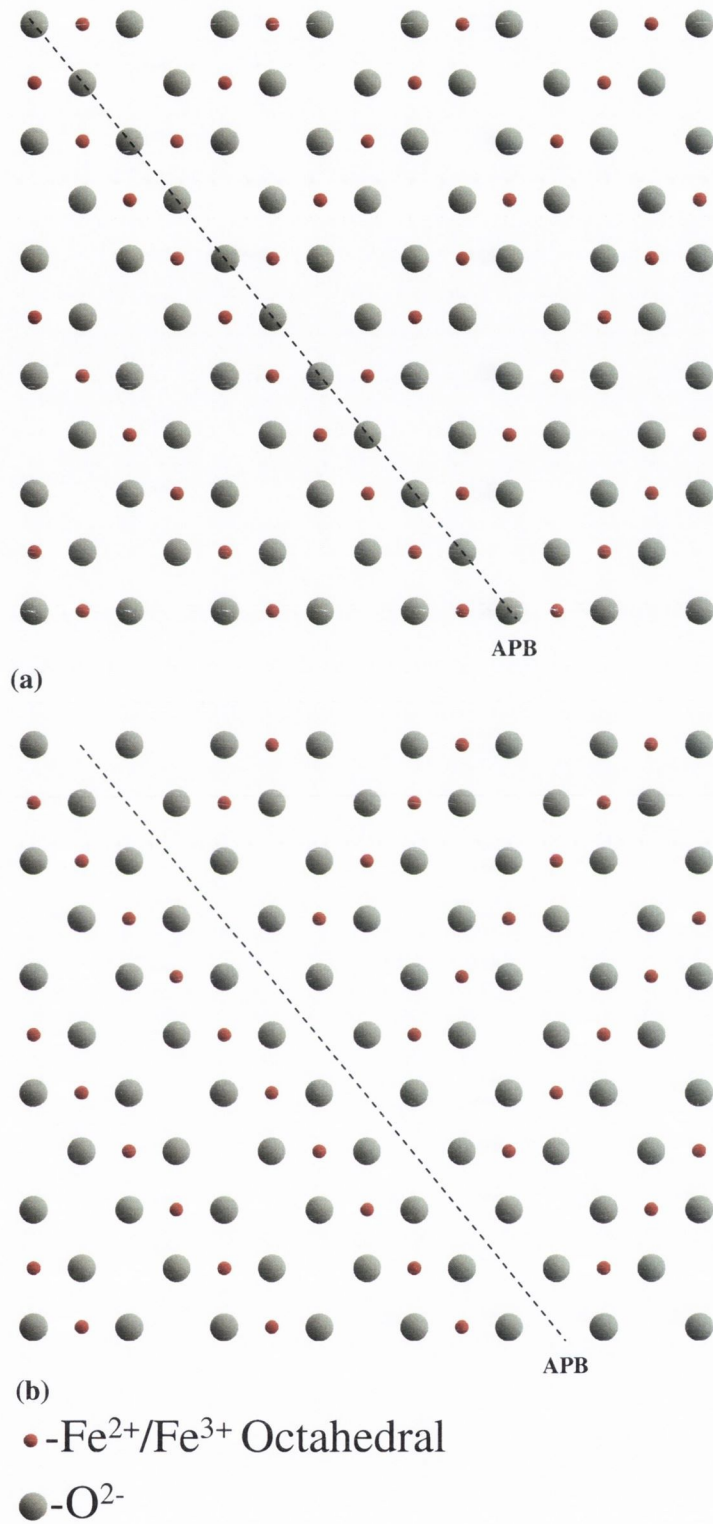


Figure. 4.16 Schematic diagram of a rotational type antiphase boundary aligned along [110] direction showing two different possibilities of (a) higher coordination for anions at the boundary and (b) lower coordination for anions at the boundary.

substantially parallel to the surface. Consequently, elastic properties of the film in the direction perpendicular to its surface are different from those along the surface. Therefore the entire film no longer has the elastic properties of a material with cubic symmetry but rather of one with a lower symmetry. In terms of the elasticity tensor ($E_{\sigma\mu\nu}$), the tensor of bulk magnetite has 3 components similar to that of any cubic material whereas the $\text{Fe}_3\text{O}_4/\text{MgO}$ film must have a greater number of components. Therefore the model of strain relaxation that fits well for cubic/isotropic material without APBs does not necessarily fit ones with lower symmetry of elasticity tensor. This suggests that the presence of APBs will affect the strain relaxation behaviour in the $\text{Fe}_3\text{O}_4/\text{MgO}$ system. Our mechanism involves the consideration, that there is no reason why APB should be based on a perfect oxygen sublattice. The models of APBs do invariably assume that the oxygen sublattice is stoichiometric and is in perfect match with that of the substrate. There is no justification for this assumption. On the contrary one should expect that this is not the case. We shall illustrate this point using several examples of APBs. Figure 4.15 (a) shows the APB based on the $1/2\langle 100 \rangle$ lateral displacement fault. The direction of the APB in this example is along $\langle 010 \rangle$. Figure 4.15 (a) shows the hypothetical "perfect" APB in which the anionic sublattice is perfect. In general, a perfect APB will be unstable due to charge pileup. Therefore, one could expect that the cations will be redistributed to achieve a local charge neutrality. If one considers the details of the film growth process, it should be expected that on the contrary, some anion positions should be vacant. Indeed growth of the film implies that the MgO surface is showered by Fe atoms and they react with the oxygen in the environment of the chamber to form magnetite. With this mechanism in mind, the oxygen pressure in the chamber is adjusted to form the correct phase of iron oxide. The oxygen pressure required for the growth of a particular iron oxide is representative of the reactivity of iron on the surface. Now we can appreciate that the surface reactivities (affinity of oxygen) of the sites α and β are different. It is also different from the reactivity of the sites away from the APB (e.g. site γ). One should expect that the sites α are likely to remain vacant as they are located away from the Fe ions and thus oxygen affinity at these is reduced. Another example is shown in Figure 4.15 (b). This involves the APB formed by $1/4\langle 110 \rangle$ lateral displacement fault that is directed along $\langle 1-10 \rangle$. In this case the anions located

directly at the APB have a different cationic coordination than those in the area away from the APB, again prompting a different reactivity. Moreover, even for the APB based on the same type of fault and having the same boundary direction, there are numerous possibilities for defects in the anionic lattice. Figures 4.16 (a) and (b) shows two possible cases of the APB caused by a rotation fault and aligned along $\langle 110 \rangle$. One can appreciate that in the case of Figure 4.16 (a) the coordination number of anions at the APB is greater than that away from the APB. The situation is reversed in the case of Figure 4.16 (b). At present there is not enough experimental data to provide atomic scale information on the APB structure, however it is clear that the common assumption of the perfect oxygen lattice is unlikely to be correct. One should further expect that APB with vacant oxygen sites develop a compressive strain in the film. Such a compressive strain should have a strong implication on the strain relaxation behaviour in the $\text{Fe}_3\text{O}_4/\text{MgO}$ (100) hetero-epitaxial system. Therefore, the film containing APBs can be represented by areas having a different sign of strain. i.e. the domains under an in-plane tensile strain due to lattice mismatch, joined by the boundaries imposing a compressive strain onto the domains. This alteration of areas within the film having opposite kind of stress will reduce the overall strain experienced by the film and decreases the free energy of the system. It enables the system to maintain the fully strained state much above the t_c . It has been noted previously [22,23] that in thin films containing structurally shifted domains, a compressive strain develops at the domain boundaries. This is a situation similar to the one in super-lattice hetero-structures where one can grow an overlayer of large mismatch on a substrate by growing it in alternation with the layer of another material that compensates for the mismatch strain. The effective stress experienced by the film will be strongly influenced by the density of APBs and their orientation and size. Therefore, depending on the density of the APBs and their type, one can observe a pattern of strain relaxation critical thickness for the films containing APBs.

We could further propose that the composition of the APB and the number of defects in it could be affected by the strain. For example, it is known that the affinity of the Fe surface to oxygen is affected by the value of stress in the Fe film [24]. One would therefore expect that the stoichiometry of the APB and the number of defects and vacancies in the film may be affected through

the feedback mechanism. The feedback could be either positive or negative, thereby creating additional defects in the APBs, which respectively act to reduce or increase the overall strain in the film.

Further, due to the anisotropic stress accommodation by APBs, as the density of APBs decreases with film thickness, the in-plane strain that is

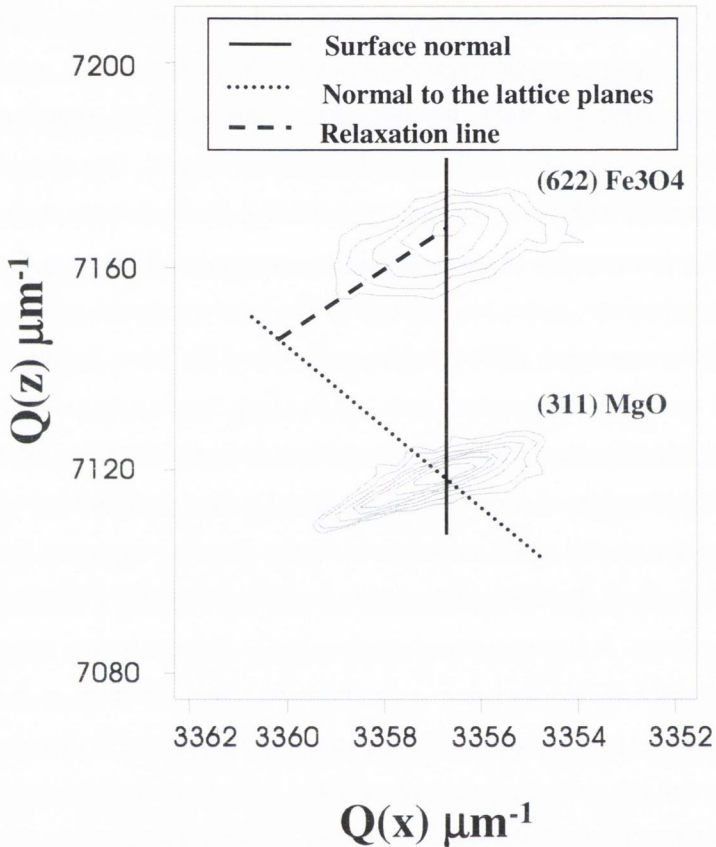


Figure 4.17 Reciprocal space maps around the (311)/(622) Bragg reflection in grazing exit geometry for 700 nm thick Fe₃O₄ thin films on MgO (100) substrate. The vertical line shows the direction normal to the growth plane and the dashed line show the direction of relaxation. Direction normal to the (311) planes are also shown. Along the x-axis $Q(x)$ is plotted ($a_{\parallel} = \sqrt{2} \times 10^4 / Q(x)$) and $Q(z)$ along the y axis ($a_{\perp} = 3 \times 10^4 / Q(z)$)

induced by them, according to our model, changes with thickness. Therefore the upper part of the film close to the surface and its lower part close to the interface will have different strain values. This must be reflected in small changes of in-plane and out-of-plane lattice constants as a function of depth within the film and therefore, smearing of the diffraction peaks, as evident from the broadening of the FWHM for thin film peak observed in triple-axis

geometry (311) rocking curves. The FWHM was found to be 0.0064 to 0.0077° for a thickness of 400 and 700nm respectively. Broadening of reciprocal lattice points (RLP) in a reciprocal space map can provide information regarding the absence or presence of strain or compositional gradients. Figure.4.17 shows a reciprocal space map for the 700 nm Fe₃O₄ film on MgO measured for the (311) Bragg planes in grazing exit geometry ($\omega=62.5685$, $2\theta=74.6582$). The reciprocal lattice vectors $\mathbf{Q}(\mathbf{x})$ and $\mathbf{Q}(\mathbf{z})$ represent the in-plane (110) and out-of-plane (100) directions respectively (details are given in chapter 3). The position of the intense substrate peak is adjusted to the bulk MgO ($a_s=0.4213$ nm) position. From the position of the thin film reciprocal lattice point in the RSM along the $\mathbf{Q}(\mathbf{x})$ and $\mathbf{Q}(\mathbf{z})$ directions, we find that the in-plane lattice parameter of the film is 0.8426 nm, and it is exactly twice the substrate lattice constant. Figure.4.17 also shows the direction of the relaxation line. The relaxation line can be calculated analytically and it depends on the surface orientation and the elastic properties of the layers as well as the Bragg reflection considered [25]. From the figure it is clear that the layer RLP broadens in the direction of the relaxation line. The broadening along the relaxation line is indicative of the presence of a strain gradient in the layer without affecting the stoichiometry. However, if a composition gradient was present in the layer then one expects broadening of the RLP towards the substrate RLP.

This result demonstrates the link between the APBs and the status of strain relaxation. However, since the details of the structure of the APB and their exact orientation are not known at present, it is not possible to make any definitive suggestions on the functional relationship between the APB density and the strain relaxation behaviour. We have summarized the calculated and observed strain relaxation values in Table.4.4 for the Fe₃O₄ films grown on MgO substrates. Our model of stress accommodation by APBs in epitaxial magnetite films also explains the lack of relaxation in much thicker films by Margulies et al [6].

Another possibility for the failure of critical thickness predictions in the case of Fe₃O₄/MgO is possibly related to the impediment of dislocation movement by the large Peierls force, that creates an activation barrier [26]. There are modified forms of M-B model, which attempt to explain the large critical thickness for low misfit hetero-structures grown at low temperatures

[26]. The effect of this is to raise the critical thickness at low growth temperatures. By extrapolation of this argument, it is possible that high growth temperature or post growth treatment could reduce the Peierls barrier and therefore reduce the critical thickness that will approach the M-B model prediction. Chidambarro et al [27] have obtained a good agreement between the calculated critical thickness based on the above considerations and the observed values for the Si-Ge/Si system. Liu et al [28], have shown that low temperature grown pseudomorphic InGaAs/GaAs hetero-structures can be relaxed by a high temperature post growth treatment, which reduces the Peierls barrier. In our case post growth high temperature annealing or high temperature growth, which could shed light on this aspect are not feasible due to the reason that at higher temperatures Mg diffuses into Fe_3O_4 and forms a MgFe_2O_4 phase[29]. This will alter the lattice mismatch and hence the critical thickness. Therefore, we have not attempted to explore this issue. Moreover, our study suggests that the strain relaxation behaviour depends on the density of APBs.

Sample	Thickness	Strain Relaxation predicted by FKR model (%)	Observed % strain relaxation (%)
$\text{Fe}_3\text{O}_4/\text{MgO}$	45	0	0
	70	0	0
	120	39	0
	200	62	0
	400	80	0
	700	88	0

Table 4.4 Summary of the predicted and observed strain relaxation values for the epitaxial magnetite films as a function of film thickness.

4.3.2 Studies on $\text{Fe}_3\text{O}_4(100)/\text{MgAl}_2\text{O}_4(100)$ system

4.3.2.1 RHEED measurements

The Fe_3O_4 films on $\text{MgAl}_2\text{O}_4(100)$ of varying thickness in the range of 5-120 nm were deposited under identical growth conditions. RHEED intensity oscillations were observed during the initial stage of the film growth. The intensity oscillations abruptly disappeared beyond the 6 nm thickness.

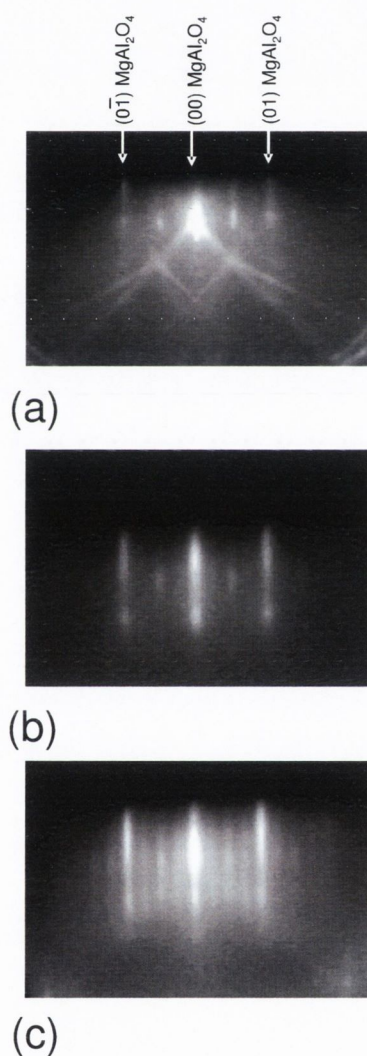


Figure 4.18 RHEED patterns of (a) (100) oriented MgAl_2O_4 substrate, (b) 5 nm and (c) 120 nm thick Fe_3O_4 films measured along the $\langle 100 \rangle$ azimuth.

The absence of RHEED intensity oscillation is a signature of growth mode crossover from 2-dimensional (layer-by-layer) to 3-dimensional (island-

like) growth. Figure 4.18 (a) shows the RHEED pattern of the MgAl_2O_4 (100) substrate measured along the $\langle 100 \rangle$ azimuth prior to growth of the Fe_3O_4 film. Half order lattice rods are also present along with the (00) and (01) lattice rods. Figures. 4.18 (b) and 4.18 (c) shows the RHEED patterns of 5 and 120 nm Fe_3O_4 films respectively. The 5 nm film shows the same separation between the (00) and (10) lattice rods which represents pseudomorphic growth of Fe_3O_4 . For the 120 nm Fe_3O_4 film, this separation is smaller and corresponds to an increase in the in-plane lattice constant of the film. The lattice constant estimated from the RHEED is 0.84 (± 0.05) nm. Reduction in the separation between the RHEED streaks for film thickness beyond 5nm suggest that the strain relaxation takes place or strain in the film is reduced.

4.3.2.2 Raman spectroscopy

Figure 4.19 shows Raman shifts obtained as described earlier for Fe_3O_4 films having various thicknesses grown on MgAl_2O_4 substrate and results are tabulated in table.4.5. No Raman peaks corresponding to the other iron oxide phases were present. The Raman bands are shifted to lower wave number position in comparison with the values observed for bulk single crystal of Fe_3O_4 (which are 670, 540 and 308 cm^{-1} ($\pm 0.01\text{cm}^{-1}$)) for films having small thickness and as the thickness increases the values are shifting towards the bulk values. Figure 4.20 shows the variation of most intense peak position with thickness. The FWHM of most intense peak (670 cm^{-1}) were 30.22, 31.18, 30.57 cm^{-1} for 15, 60, 120 nm films respectively. This result suggests the occurrence of strain relaxation with increasing film thickness. Apart from the Raman bands observed in bulk and thin film Fe_3O_4 grown on MgO (100) substrate, here two additional bands are observed (Table 4.5). These additional Raman bands could be occurring due to the APBs formed by misfit dislocations where the stoichiometry can be quite different from the rest of the sample. The formation of APBs due to misfit dislocations will be discussed in the following sections. Raman measurements therefore confirm that films grown have magnetite phase and indicates the presence of strain relaxation within the film.

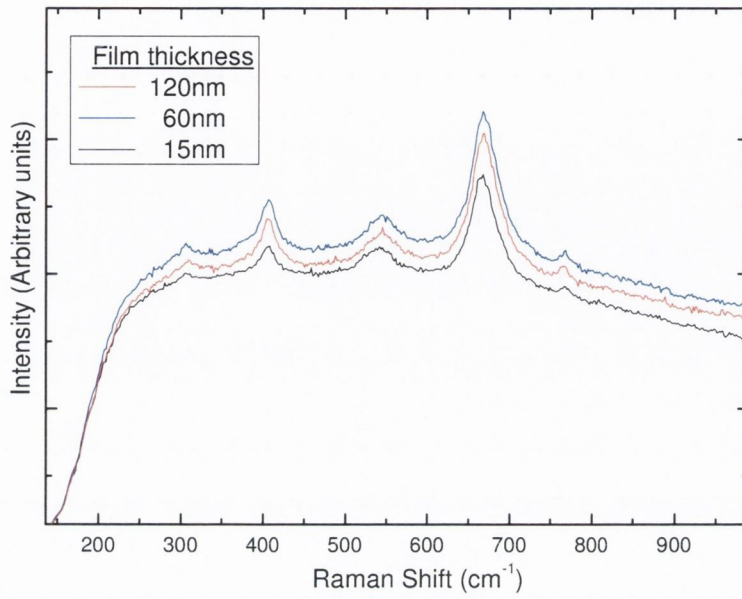


Figure 4.19 Raman shifts observed for Fe₃O₄ films having various thicknesses grown on MgAl₂O₄ substrate. Curves are shifted on the vertical axis for clarity.

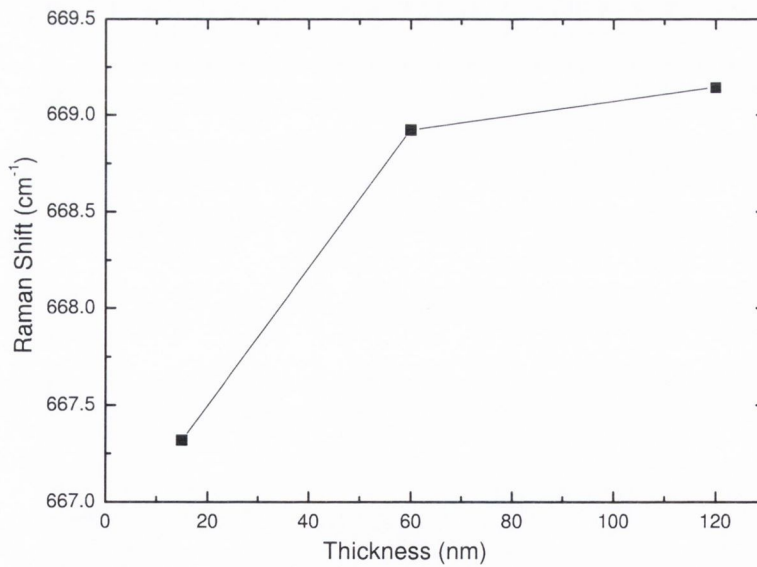


Figure 4.20 Variation of most intense Raman peak position with thickness.

Sample	Raman Shift (cm^{-1})				
	($\pm 0.01 \text{cm}^{-1}$)				
Bulk Fe_3O_4	670	540	308		
15 nm Fe_3O_4	667.31	539.7	305.8	764.7	405
60 nm Fe_3O_4	668.92	544.7	309.3	766.4	406
120 nm Fe_3O_4	669.14	545.1	306.6	768.1	406

Table 4.5 Raman shifts observed for Fe_3O_4 films having various thicknesses grown on MgAl_2O_4 substrate.

4.3.2.3 Magnetization measurements

Fe_3O_4 films grown on MgAl_2O_4 substrates were much easier to saturate compared to films grown on MgO substrates. Figure 4.21 shows the magnetization curve obtained for a 120 nm film and the results obtained from films with various thicknesses are summarised in Table 4.6. The films show lower saturation magnetisation compared to the saturation magnetisation of bulk Fe_3O_4 ($480 \times 10^3 \text{ A/m}$)

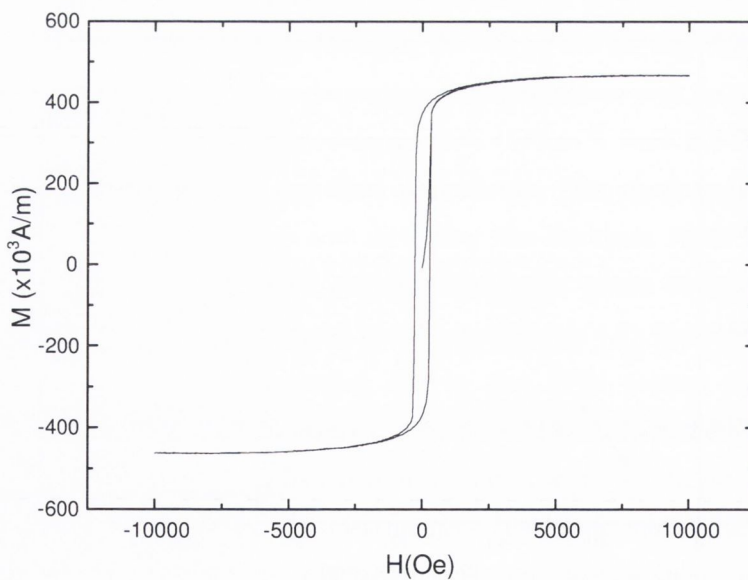


Figure 4.21 Magnetization curve obtained for 120 nm epitaxial magnetite film grown on MgAl_2O_4 substrate.

Sample	Thickness (nm)	Ms (10kOe) $\times 10^3$ (A/m)
Fe ₃ O ₄ /MgAl ₂ O ₄	15	473
	60	460
	120	466

Table 4.6 Summary of the magnetization (Ms) at 1 Tesla field for the epitaxial magnetite films as a function of film thickness.

4.3.2.4 Resistivity measurements

Figure 4.22 shows resistivity as a function of temperature for a 70 nm and a 120 nm Fe₃O₄ film grown on MgAl₂O₄ substrates. Resistivity values for these films measured at 300 K were found to decrease with an increase in thickness. The resistivity values observed at 300K for these films are 0.0099 and 0.0088 for 70nm and 120nm film respectively.

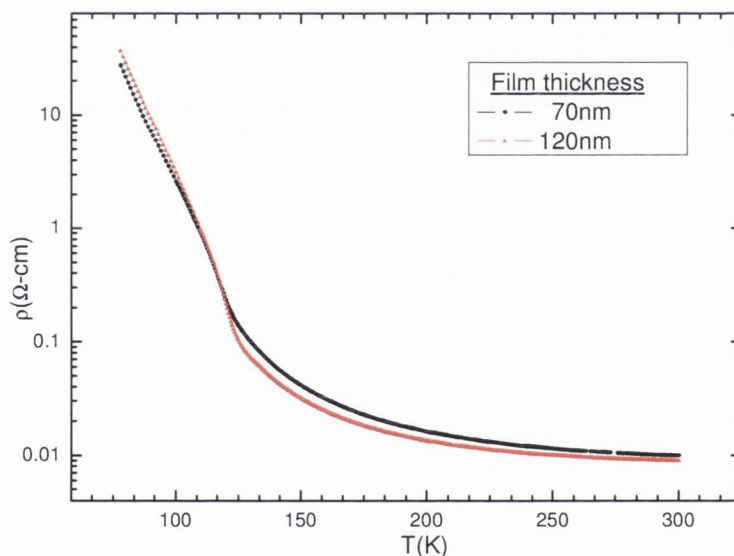


Figure 4.22 Verwey transition observed for 70 and 120 nm Fe₃O₄ films grown on MgO substrate.

The Verwey transition temperature for these films were found to be 122 K (± 0.5 K) and 123 K (± 0.5 K) for 70 and 120 nm films respectively and are

higher than Fe_3O_4 films deposited on MgO substrates. The value of Verwey transition temperature is near to the value observed for bulk Fe_3O_4 (~123). The observation of the Verwey transition confirms that films are stoichiometric.

4.3.2.5 HRXRD measurements

To know precisely the extent of strain relaxation for thickness above 15 nm we employed the HRXRD technique. Figure 4.23 shows the ω - 2θ scans of 15, 60 and 120 nm Fe_3O_4 films grown on MgAl_2O_4 oxide substrate measured for (400) Bragg planes. The curves are shifted on the vertical axis for clarity. The full width at half of maximum (FWHM) of the thin film peaks are 0.301 , 0.08 and 0.076° respectively. The substrate-film peak separation decreases with the increase in thickness. The a_\perp determined from the film-substrate peak separation are 0.84568 , 0.84413 and 0.84088 nm for 15, 60 and 120 nm films respectively.

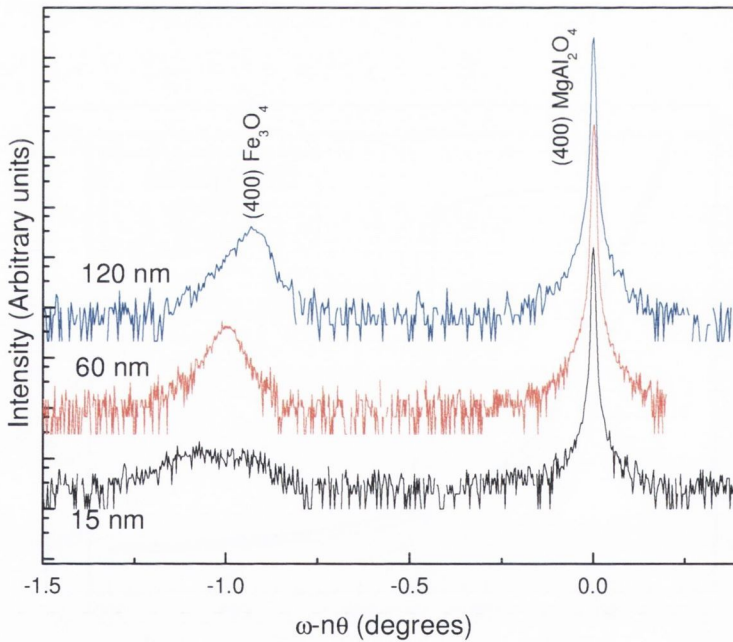


Figure 4.23. The ω - 2θ scans of 15, 60 and 120 nm Fe_3O_4 film on (100) MgAl_2O_4 substrate measured for symmetric (400) Bragg reflection. Curves are shifted on the vertical axis for clarity.

Figure 4.24 shows ω - $n\theta$ scans measured for the asymmetric (622) Bragg planes in the grazing exit geometry for the 60 and 120 nm thick films. The experimentally measured angular ratios of the angle made by the x-ray to the detector (2θ) and sample (ω) was 2.4 and 2.2 for the 60 and 120 nm films respectively. A value other than 2 was required to detect the thin film peak through a single ω - $n\theta$ scan due to the strain tilt. The $a_{||}$ determined from the (622) scan is 0.834 and 0.8371 nm for 60 and 120 nm films respectively. This corresponds to a relaxation of 70 and 95%. The in-plane and out-of-plane lattice parameters determined from the asymmetric (622) scans agrees well with the estimates of strain relaxation for the n -ratio used to perform the asymmetric scans. The strain relaxation was measured as a function of thickness in Fe_3O_4 thin films grown on MgAl_2O_4 and it was found that the amount of strain relaxation increases with the increase in thickness.

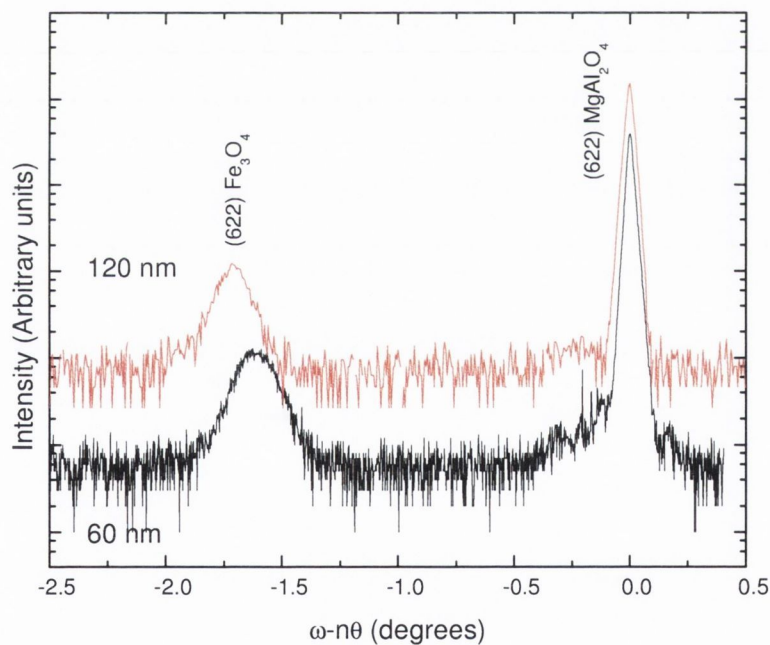


Figure 4.24. The ω - $n\theta$ scans of 60 and 120 nm Fe_3O_4 film on (100) MgAl_2O_4 substrate measured for asymmetric (622) Bragg reflection, measured in the grazing exit geometry.

From the $a_{||}$ and a_{\perp} lattice constant values obtained through the analysis of RSM and individual ω - 2θ scans for the Fe_3O_4 films grown on MgO and MgAl_2O_4 substrates, strain relaxation is exhibited from 6 nm thickness.

4.3.2.6 Discussion

Figure.4.25 shows the calculated equilibrium in-plane strain, $\epsilon_{||}$, using FKR-model for Fe_3O_4 films on MgAl_2O_4 substrate as a function of thickness along with the measured experimental data. The observed relaxation behaviour was in agreement with the estimated values for Fe_3O_4 films grown on MgAl_2O_4 unlike $\text{Fe}_3\text{O}_4/\text{MgO}$ hetero-epitaxy which doesn't show relaxation even up to 700 nm. Calculated and observed strain relaxation values are given in Table.4.7. Due to large misfit of 3.9% between Fe_3O_4 and MgAl_2O_4 , the epitaxial films above the critical thickness will be relaxed generating misfit dislocations (MDs). The large density of MDs can produce stacking faults.

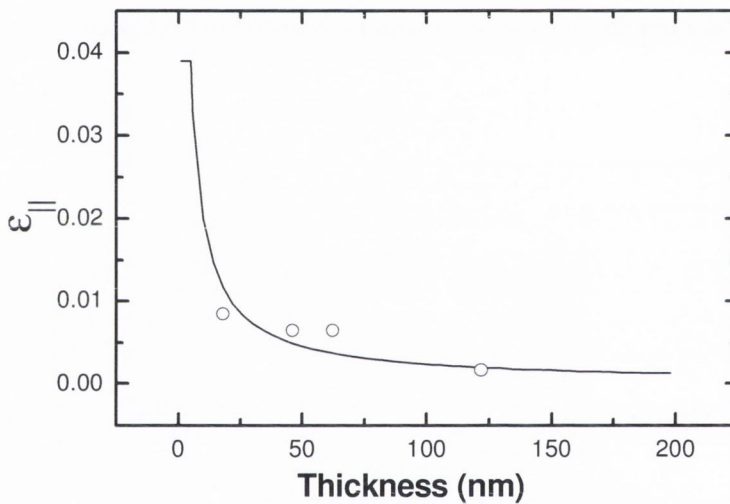


Figure.4.25 Comparison of experimentally observed values of the in-plane strain, $\epsilon_{||}$, with the FKR model predictions for the Fe_3O_4 films grown on MgAl_2O_4 (100) substrates as a function of thickness. The solid line is the theoretical prediction and scattered points are experimentally observed values.

Such a feature has been reported for other spinel films grown on MgAl_2O_4 with a similar misfit [30]. Since MgAl_2O_4 has the same spinel type crystal structure and symmetry as that of Fe_3O_4 , formation of APB is not expected for the films grown on MgAl_2O_4 . However, presence of the APBs in $\text{Fe}_3\text{O}_4/\text{MgAl}_2\text{O}_4$ system has been reported [11]. Figure 4.26 shows plan-view TEM images observed for 70 and 200nm Fe_3O_4 thin films grown on MgAl_2O_4 substrates.

Sample	Thickness	Strain Relaxation predicted by FKR model (%)	Observed % strain relaxation (%)
Fe ₃ O ₄ /MgAl ₂ O ₄	40	87	60
	60	91	84
	120	95	95.6

Table 4.7 Summary of the predicted and observed strain relaxation values for the epitaxial magnetite films as a function of film thickness.

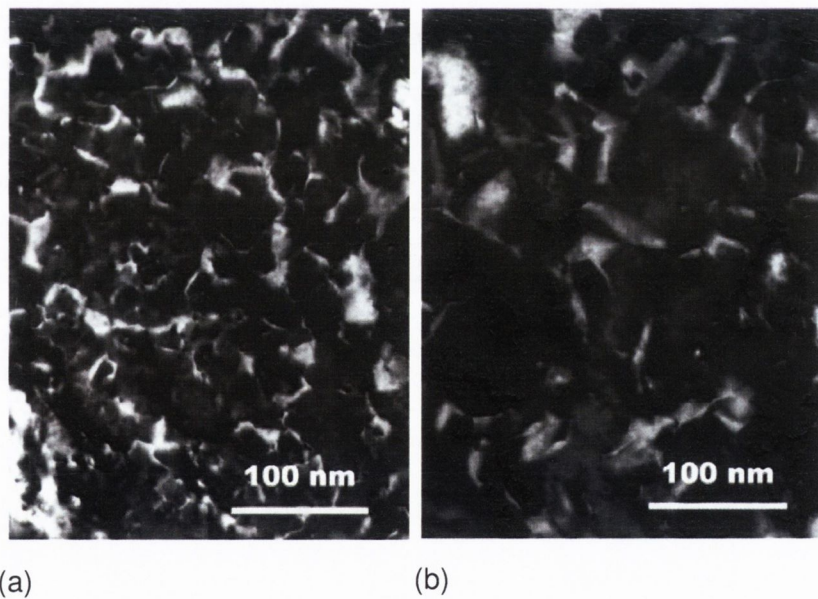


Figure 4.26 Plan-view TEM images observed for (a) 70nm and (b) 200nm Fe₃O₄ thin films grown on MgAl₂O₄ substrates.

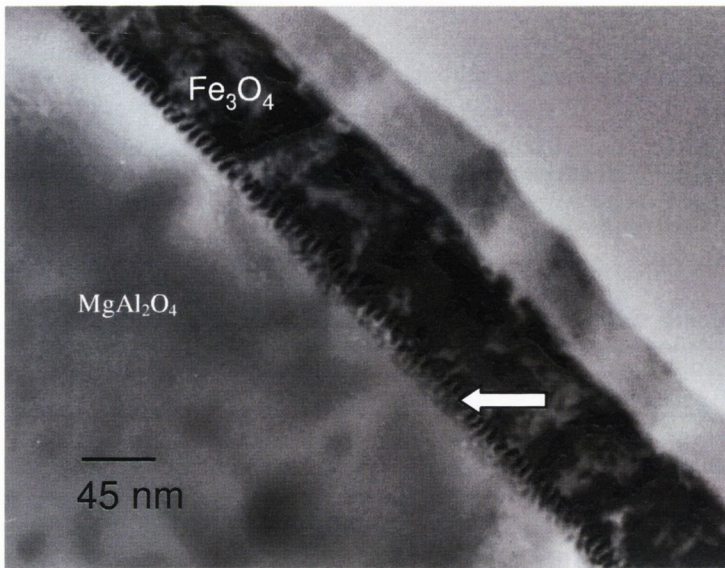


Figure 4.27 The cross-section TEM image of 70nm Fe_3O_4 film on MgAl_2O_4

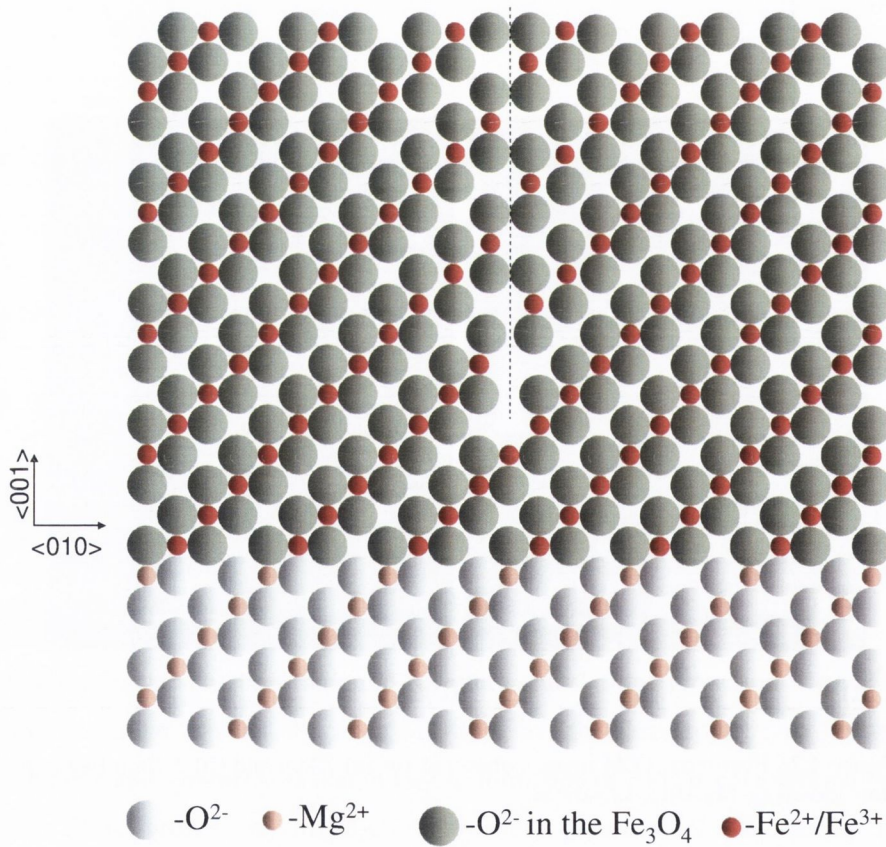


Figure. 4.28 Schematic diagram of an antiphase boundary formed in Fe_3O_4 films grown on MgAl_2O_4 (100) substrate due to the stacking fault with one missing row of oxygen. The APB is indicated with a dashed line.

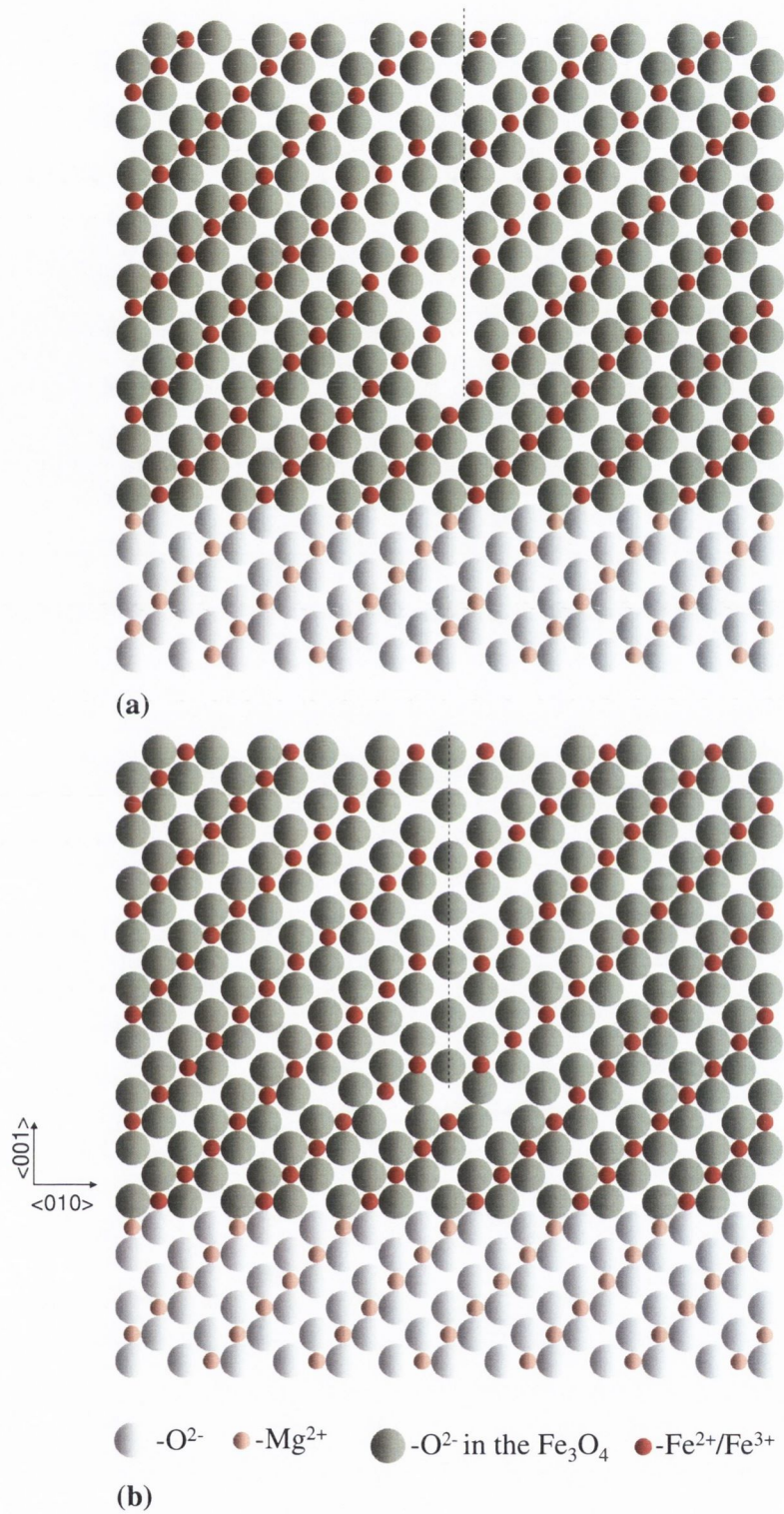


Figure 4.29 Schematic diagrams of two possible configurations of antiphase boundaries formed in Fe_3O_4 films grown on $MgAl_2O_4$ (100) substrate due to the stacking fault with two missing rows of oxygen. The APB is indicated with a dashed line.

Both images were obtained using a 220 imaging vector. TEM images clearly show APBs and the density of APBs decreasing with increasing thickness as observed in the case of Fe_3O_4 grown on MgO substrates. Figure 4.27 shows the cross-section TEM image of 70nm Fe_3O_4 film on MgAl_2O_4 substrate which clearly shows stacking faults generated by misfit dislocations. We suggest that the formation of APBs in $\text{Fe}_3\text{O}_4/\text{MgAl}_2\text{O}_4$ systems are due to the stacking faults generated because of strain relaxation. Out of many possible formations two cases are demonstrated below.

Figure 4.28 shows (100) plane of $\text{Fe}_3\text{O}_4/\text{MgAl}_2\text{O}_4$ system with a stacking fault formed by missing one row of oxygen. It is clear from the figure that the cation lattice is disrupted across the dislocation line which essentially forms an APB. Figure 4.29 show two possible APB configurations generated because of a stacking fault with two missing oxygen rows, although at this point it is difficult to know the exact APB configurations which will result in $\text{Fe}_3\text{O}_4/\text{MgAl}_2\text{O}_4$ system due to the lack of experimental detail. The reduction of the density of APBs with increasing thickness as observed in TEM images can be due to the minimization of the total energy by the minimization of the APB area. Also the reduced saturation magnetization observed could be because of antiferromagnetically coupled APBs.

In the previous section (§4.3.1.7) we argued that the absence of strain relaxation in Fe_3O_4 films grown on MgO substrates even up to ten times higher than the critical thickness is due to the presence of APBs. On the other hand, Fe_3O_4 films grown on MgAl_2O_4 show strain relaxation and follow the theoretical prediction. Even though no APB formation is expected in films grown on MgAl_2O_4 , which has the same spinel type crystal structure and symmetry that of Fe_3O_4 , APBs were nevertheless observed. The fundamental difference between the APB formation in $\text{Fe}_3\text{O}_4/\text{MgO}$ and $\text{Fe}_3\text{O}_4/\text{MgAl}_2\text{O}_4$ is that in the former system APBs are formed due to the difference in lattice symmetry between Fe_3O_4 and MgO and latter system the APBs are formed due to the stacking faults generated by strain relaxation.

4.4 Conclusions

From the strain relaxation studies of epitaxial Fe_3O_4 thin films grown on $\text{MgO}(100)$ and MgAl_2O_4 substrates we infer that the films grown on MgO

(100) substrate remain fully coherent up to much greater thickness than predicted by the FKR model (~70 nm), whereas the films grown on MgAl_2O_4 substrates shows a behaviour consistent with the model predictions. The observed strain relaxation behaviour is attributed to the differences in the crystal structure symmetry between MgO and Fe_3O_4 . Due to the lower crystal symmetry of the spinel structure of Fe_3O_4 compared to that of MgO , APBs are formed and lead to the formation of areas within the film that have opposite sign of stress. The stress compensation by the APBs reduces the effective stress experienced by the films. The reduction in effective stress experienced by the film depends strongly on the nature and density of APBs. Even though APBs are not expected in Fe_3O_4 films grown on MgAl_2O_4 , TEM studies revealed the presence of APBs. We suggest that these APBs are formed not because of symmetry difference but because of the stacking faults generated by strain relaxation due to large mismatch between the thin film and substrate.

Bibliography

- [1] J. W. Matthews and A. E. Blakeslee, *J. Cryst. Growth* **27**, 118 (1973)
- [2] S.K. Arora, R.G.S. Sofin and I.V. Shvets, *Phys. Rev. B* **72**, 134404 (2005).
- [3] W. Eerenstein, T. T. M. Palstra, T. Hibma and S. Celotto, *Phys. Rev. B* **66**, 201101 (2002)
- [4] J. P. Hong, S.B. Lee, Y.W. Jung, J.H. Lee, K.S. Yoon, K.W.. Kim, C.O. Kim and C.H. Lee, *Appl. Phys. Lett.* **83**,1590 (2003)
- [5] M. Ziese, *Phys. Rev. B* **62**, 1044 (2000)
- [6] D. T. Margulies, F. T. Parker, F. E. Spada, R. S. Goldman, J. Li, R. Sinclair and A. E. Berkowitz, *Phys. Rev. B* **53**, 9175 (1996)
- [7] T. Hibma, F.C. Voogt, L. Niesen, P.A.A. van der Heijden, W.J.M. de Jonge, J.J.T.M. Donkers and P.J. van der Zaag, *J. Appl. Phys.* **85**, 5291 (1999).
- [8] S.M. Watts, K. Nakajima, S. van Dijken and J.M.D. Coey, *J. Appl. Phys.* **95**, 7465 (2004).
- [9] S. Kale, S. M. Bhagat, S. E. Loafland, T. Scabarozi, S. B. Ogale, A. Orozco, S. R. Shinde, T. Venkatesan, B. Hannyoy, B. Mercey and W. Prellier, *Phys. Rev. B* **64**, 205413 (2001); M. Zeise, R. Hohne, H. C. Semmelhack, H. Reckentin, N. H. Hong and P. Esquinazi, *Eur. Phys. J. B* **28**, 415 (2002)
- [10] D. Reisinger, M. Schonecke, T. Brenninger, M. Opel, A. Erb, L. Alff and R.Gross, *J. Appl. Phys.* **94**, 1857 (2003)
- [11] C.A. Kleint, M.K. Krause, R. Hhne, M. Lorenz, H.C. Semmelhack, A. Schneider, D. Hesse, H. Sieber, J. Taubert and W. Andr, *J. Phys IV*, **7C1**, 593 (1997).
- [12] L. V. Gasparov, D.B. Tanner, D. B. Romero, H. Berger, G. Margaritondo and L. Forro, *Phys. Rev. B* **62**, 7939 (2000)
- [13] W. Eerenstein, T. T. M. Palstra, T. Hibma and S. Celotto, *Phys. Rev. B* **68**, 014428 (2003).
- [14] O. Ueda, T. Soga, T. Jimbo and U. Umeno, *Appl. Phys. Lett.* **55**, 445 (1989).
- [15] Yuan Li and L.J. Giling, *J. Cryst. Growth* **163**, 203 (1996).

- [16] A. Fischer, H. Kuhne and H. Richter, Phys. Rev. Lett. **73**, 2712 (1994)
- [17] G.C. Osbourn, IEEE J. Quantum Electron. **QE-22**, 1677 (1986).
- [18] B.W. Dodson and J.Y. Tsao, Appl. Phys. Lett. **51**, 1325 (1987); **52**, 852 (1988)
- [19] A. Fischer and H. Richter, Appl. Phys. Lett. **64**, 1218 (1994)
- [20] D.C. Houghton, Appl. Phys. Lett. **57**, 1434 (1990); **57**, 2124 (1990).
- [21] R. Hull, J.C. Bean, D.J. Werder and R.E. Leibenguth, Phys. Rev. B **40**, 1681(1989)
- [22] A. Biswas, M. Rajeswari, R.C. Srivastava, Y.H. Li, T. Venkatesan, R.L. Greene and A.J. Millis, Phys. Rev. B **61** 9665 (2000).
- [23] R.Koch, J. Phys. Condens. Matter **6**, 9519 (1994); R. Koch, D. Winau and K.H. Rieder, Phys. Scr. T **49B**, 539 (1993).
- [24] S. Murphy, G. Mariotto, N. Berdunov and I.V. Shvets Phys. Rev. B **68**, 165419 (2003).
- [25] P. Kidd, P.F. Fewster and N.L. Andrew, J. Phys. D Appl. Phys. **28**, A-133 (1995).
- [26] B.A. Fox and W.A. Jesser, J. Appl. Phys. **68**, 2801 (1990).
- [27] D. Chidambarao, G.R. Srinivasan, B. Cunningham and C.S. Murthy, Appl. Phys. Lett. **57**, 1001 (1990).
- [28] W.X. Liu, A.A. Hopgood, B.F. Usher, H. Wang and N.St.J. Braithwaite, J. Appl. Phys. **94**, 7496 (2003).
- [29] K.A. Shaw, E. Lochner and D.M. Lind, J. Appl. Phys. **87**, 1727 (2000).
- [30] Y. Suzuki, G. HU, R.B. van Dover and R.J. Cava, J. Magn. Magn. Mat. **191**, 1 (1999)

Chapter 5

Magnetoresistance enhancement in epitaxial magnetic films grown on vicinal substrates

5.1 Introduction

The presence of antiphase boundaries (APBs) in epitaxial Fe_3O_4 films introduces local structural modifications and alters the magnetic interactions at the boundary making them predominantly antiferromagnetic [1, 2]. This strongly affects the magnetic and electronic properties of the epitaxial Fe_3O_4 films. Because of the presence of APBs, magnetization shows an anomalous behaviour and it is difficult to saturate the films even with strong magnetic fields of up to several Tesla (T), although the anisotropy field is only ~ 300 Oe for bulk Fe_3O_4 [3]. Ultra thin Fe_3O_4 films (below 5 nm) exhibit superparamagnetic behaviour [4]. The magnetoresistance (MR) behaviour of magnetite thin films has been widely studied in films on different substrates like MgO and MgAl_2O_4 [5-8]. Compared to bulk magnetite, epitaxial Fe_3O_4 films show a greater MR which is difficult to saturate even in strong magnetic fields. So far, the magnitude of MR observed in epitaxial films has not exceeded 8% for a magnetic field strength of 2 Tesla. The unusual MR behaviour of Fe_3O_4 films is attributed to the presence of APBs and a spin valve mechanism was proposed by Eerenstein et al [6]. They have modelled the observed MR across the APBs employing a hopping conductivity model in which the spin-polarized transport occurs across the antiferromagnetic interface between two ferromagnetic chains. This model predicts a large MR effect

across a single boundary. However, due to the random network of APBs obtained in Fe₃O₄/MgO hetero-epitaxy, this effect is greatly smeared and it is not possible to obtain any quantitative information.

In this study we have employed a new approach which allows for a selective extraction of the contribution of the antiphase boundaries from the total MR. In our study the MgO substrate has a miscut with respect to a low-index plane (100). If annealed under suitable condition, presence of miscut facilitates the formation of surfaces with atomic height steps. In this case the islands of Fe₃O₄ forming at different atomic terraces nucleate independently from each other. Consequently, as the nucleation islands grow there is a significant chance that antiphase boundaries are formed along the step edges of the atomic terraces. Calculating the probability of APBs forming along a given step edge relies on certain assumptions in relation to the mechanism of nucleation of magnetite on MgO. This is explained below.

5.1.1 Calculation of the probability of APB formation

The crystal structure of magnetite is based on the fcc oxygen sub-lattice, similar to the oxygen sub-lattice of MgO. In this sub-lattice some of the tetrahedral interstices (so-called A-sites) and some of the octahedral interstices (so-called B-sites) are occupied by the Fe²⁺ and Fe³⁺ ions. The (100) atomic planes containing A- and B-sites are positioned in alternation and are separated by 0.1049nm. Thus, the separation between the planes containing the like sites (A-A or B-B), is 0.2099nm. In the atomic planes containing B-sites the Fe ions are positioned in rows along the (110) directions. The separation between the ions within the rows is 0.3nm and the separation between the rows is 0.6 nm. Details of the Fe₃O₄ crystal structure is given in chapter 2.

The key assumption in calculating the probability of APB formation is nucleation mechanism of magnetite. For example, if the nucleation on one of the two terraces separated by step edge starts at the atomic plane of A-sites, and the nucleation on the other one starts at the atomic plane of B-sites, then ABP is formed with certainty. This is clear because in the structure of magnetite, atomic planes separated by 0.2099nm are planes of like interstices. Yet the body of experimental evidence coming e.g. from the STM studies suggests that there is a large energy difference between the surfaces of A- and B-site terminations. Usually the B-site terminated surfaces are observed [9,10].

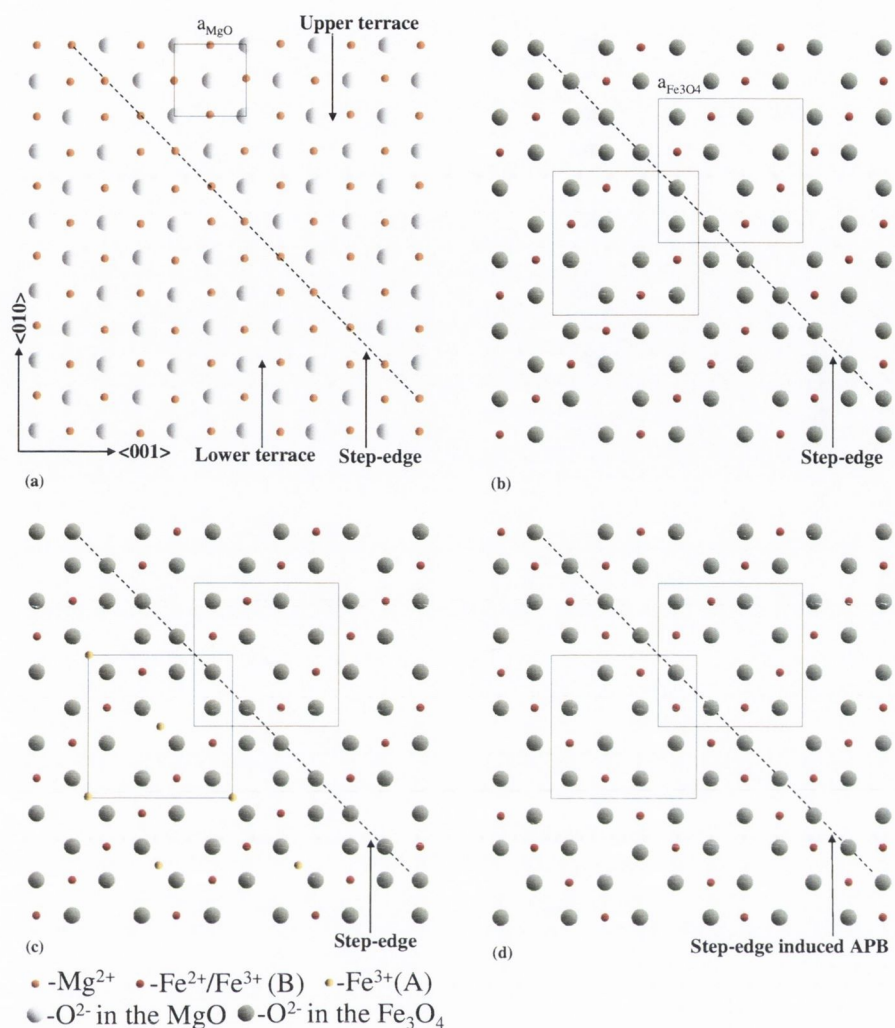


Figure.5.1. Example for the formation of a step induced APB. (a) MgO (100) surface with a monoatomic step directed along $\langle 011 \rangle$ (b) formation of the first B site layer on both the upper and lower terrace with nucleation rows parallel to each other (c) formation of the second layer on the lower terrace which is an A site plane (d) formation of the third layer on the lower terrace which is a B site plane with nucleation rows perpendicular to the upper terrace and hence the formation of step induced APB.

The type of surface termination is sensitive to the sample preparation conditions. Regardless of any preparation condition, the two terminations are virtually never observed simultaneously on the same surface. Most of the STM data have been obtained on single crystals of magnetite, and not on $\text{Fe}_3\text{O}_4/\text{MgO}$ films. Still, the data suggest that the likelihood of nucleation by A- and B-site planes simultaneously can be discounted. Let us first consider the case of nucleation by B-sites which is preferred by the STM studies. Across a monoatomic step on the (100) surface of MgO, there are 32 possible

combinations of positioning the nucleation islands of Fe_3O_4 on two neighbouring terraces. To see if they result in the formation of the APB we need to compare the positions of atoms in the third Fe atomic layer on the lower terraces with the positions of the atoms of the first Fe layer on the upper terrace. Of the 32 possible combinations, 16 have the nucleation rows of first B-site layer on the upper terrace parallel to the ones on the lower terrace. All these 16 combinations result in the formation of APBs.

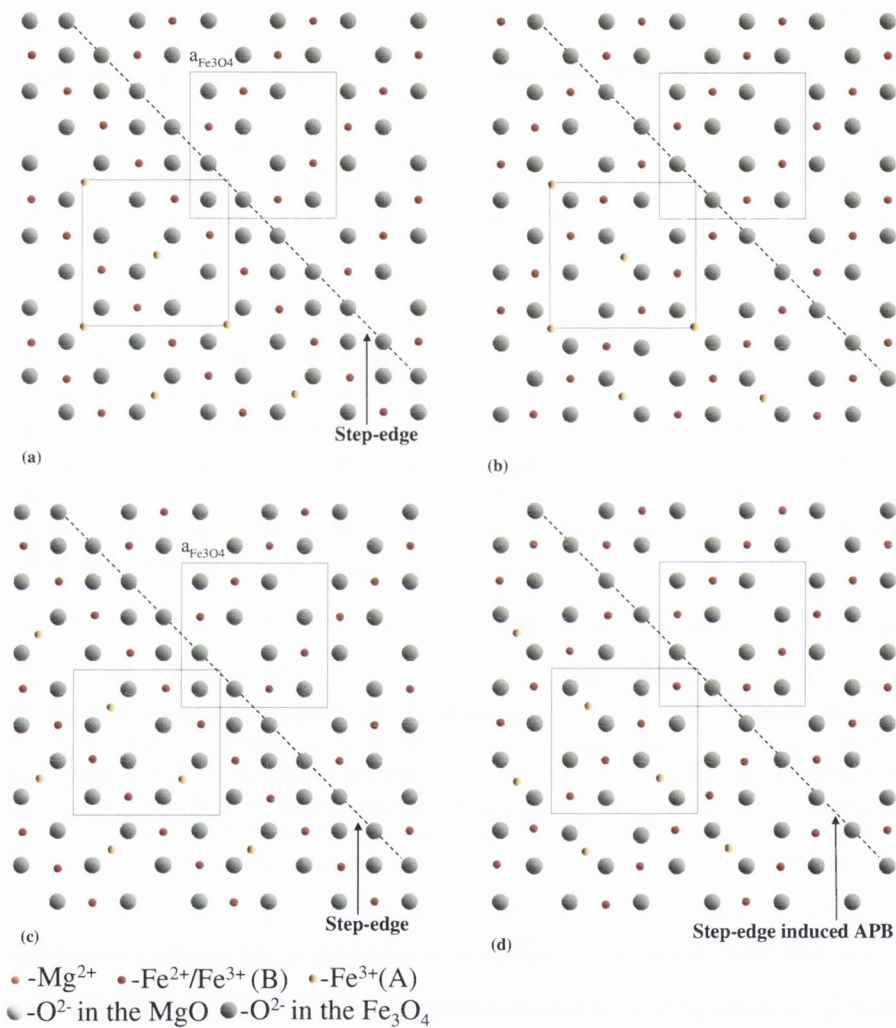


Figure.5.2 Two possible combinations of step induced APB formation of which one forms an APB and the other does not. (a) formation of the first B site layer on both the upper and lower terrace with nucleation rows perpendicular to each other with the second A site plane on the lower terrace (b) formation of third layer on lower terrace which is a B site plane with nucleation rows parallel to the upper terrace and no formation of a step induced APB (c) formation of the first B site layer on both the upper and lower terrace with nucleation rows perpendicular to each other with a different orientation of the second A site layer compared to (a). (d) shows the

formation of the third layer on the lower terrace which is a B site plane with the nucleation rows parallel to the upper terrace and formation of a step induced APB.

One such example is shown in Figure.5.1. Figure 5.1(a) shows the MgO (100) surface with a monoatomic step directed along $\langle 011 \rangle$. Figure 5.1(b) shows the formation of first B site layer on both upper and lower terrace with nucleation rows parallel to each other. Figure 5.1(c) shows the formation of second layer on the lower terrace which is an A site plane. Figure 5.1(d) shows the formation of third layer on lower terrace which is a B site plane with nucleation rows perpendicular to the upper terrace and hence the formation of step induced APB. The remaining 16 combinations have the rows of the first B site layer on the upper plane perpendicular to the rows of the first B site layer on the lower plane. Of these 16 combinations, 8 result in the formation of the APBs and the remaining 8 do not. Figure.5.2 shows two of such combinations. Figure 5.2(a) shows the formation of first B site layer on both the upper and lower terrace with nucleation rows perpendicular to each other. Figure 5.2(a) also shows the second layer on the lower terrace which is an A site plane. Figure 5.2(b) shows the formation of the third layer on the lower terrace which is a B site plane with nucleation rows parallel to the upper terrace and no formation of a step induced APB. Figure 5.2(c) shows the formation of the first B site layer on both the upper and lower terrace with nucleation rows perpendicular to each other with a different orientation of the second A site layer compared to Figure 5.2(a). Figure 5.2(d) shows the formation of the third layer on the lower terrace which is a B site plane with nucleation rows parallel to the upper terrace and formation of a step induced APB. Therefore, the analysis shows that there is 75% chance of forming APB along the step edge if the nucleation starts at the B-sites. Considering the second case when the nucleation starts at the A-sites, it is possible to have 64 combinations, out of which only 8 combinations form APBs. So the total chance of forming APBs in this case will be 87.5%. Whether the magnetite nucleates at A- or B-sites, or even if there is nucleation at both sites simultaneously, one could see that there is a very high chance of formation of APBs along step edge.

Therefore, as the density of the APBs aligned along the step edges is greater than in the perpendicular direction, one expects to find a difference in the MR for current driven along and perpendicular to the direction of the step edges. It is important to emphasise that in the case of the film grown on the

MgO (100) substrate the crystallographic anisotropy makes no contribution to the measurements. Indeed, the two orthogonal directions on the (100) surface of a cubic crystal always correspond to equivalent crystallographic directions (e.g. (110) and (1-10)). Consequently, we decided to perform experiments on the MgO (100) substrate. In this study we measure the MR of Fe₃O₄ thin films for different substrate miscut angles and compare the results of MR along- and perpendicular to the step-edge direction. The substrate microstructure is known to be strongly influenced by pre-deposition treatment [11,12] and is expected to play an important role in determining the density of APBs in Fe₃O₄ films. The effects of pre-deposition annealing duration on the MR properties of Fe₃O₄ films grown on vicinal MgO (100) substrates are also presented.

We should point out that there has been some effort to improve the MR of magnetite films by utilizing a microscopic step edge array on surfaces patterned by means of lithography [13]. The authors observed an enhancement in the MR that was not high in the low fields and was due to the spin dependent electron transport across the magnetic clusters formed at the step edges.

5.2. Experiment

Fe₃O₄ thin films used in the present study have been grown on (100) oriented MgO single crystal substrates using an oxygen plasma assisted molecular beam epitaxy (MBE) with a base pressure 5×10^{-10} Torr. We used two kinds of MgO (100) substrates: the first ones are low-vicinal (100) oriented single crystal substrates with a nominal miscut within ± 0.5 degrees along an arbitrary direction and the other set of substrates had a 2 degrees miscut on (100) oriented substrate along $\langle 011 \rangle$ direction within the accuracy of ± 0.1 degrees. The substrates were chemically cleaned prior to their insertion into the growth chamber and then cleaned in-situ at 600°C in UHV for 1 hour followed by annealing in 1×10^{-5} Torr oxygen for 5 hours duration. Growth of the Fe₃O₄ films have been carried out by means of electron beam evaporation of pure metallic Fe (99.999%) in presence of free oxygen radicals generated by the ECR (Electron Cyclotron Resonance) plasma source (OSPrey Plasma Source, Oxford Scientific, UK). The plasma source was operated at 80W in an oxygen atmosphere of 1×10^{-5} Torr. Reflection high-energy electron diffraction (RHEED) was employed to confirm the epitaxial growth and establish the

growth mode. The presence of the RHEED intensity oscillations confirms that the films grow in a layer-by-layer mode ($0.3\text{\AA}/\text{s}$). To check the effects of pre-deposition annealing duration on the MR properties of Fe_3O_4 films, the substrates were annealed at 600°C for 3, 5, 9 and 13 hours duration and then the Fe_3O_4 films were grown with the same growth parameters as depicted above.

For electrical resistivity and magneto-resistance measurements a standard dc-four probe technique was employed. The sample was mounted on a copper block fitted onto a cold finger of the closed cycle refrigerator. Temperature of the sample stage was monitored using a GaAlAs thermometer and controlled within ± 0.05 K. For magneto-transport measurements, the cold finger was inserted into a variable field permanent magnet (Multimag, Magnetic Solutions Ltd, Ireland). Using this magnet it was possible to vary the strength (maximum field of 2 Tesla) and orientation of the magnetic field in a desired direction. The magnetoresistance results reported here were obtained by keeping the direction of magnetic field and current parallel to each other unless otherwise stated. The MR is defined as; $\text{MR}\% = [\text{R}(\text{H}) - \text{R}(0)/\text{R}(0)] * 100$, where $\text{R}(\text{H})$ and $\text{R}(0)$ are the resistances of the sample with and without field respectively. To determine the magnetoresistance anisotropy, the measurements were carried out by passing current in two directions, which are orthogonal to each other i.e. along and perpendicular to the direction of step edges.

Structural characterization of Fe_3O_4 thin films was done using a multi-crystal high-resolution x-ray diffractometer, HRXRD (Bede-D1, Bede, UK). The HRXRD in double or triple axis configuration was performed to confirm the epitaxial relationship of the $\text{Fe}_3\text{O}_4/\text{MgO}$ hetero-epitaxy. The miscut of the samples was measured using the high-resolution x-ray diffraction (HRXRD) technique. To determine the miscut of the sample, the ω -rocking curves were performed at (200) Bragg reflection of substrate at several azimuths. From the variation in incidence angle required to achieve the Bragg condition with the sample azimuth and fitting it using a sine function we determine the amplitude and direction of miscut.

Magnetization measurements were performed using an alternating gradient field magnetometer (Micromag-3900, Princeton Measurements, USA) with a sensitivity of 10^{-8} emu. The diamagnetic contribution from the MgO

substrate was subtracted from the measured data by performing a M-H loop of the MgO substrate of similar dimensions as that of thin film sample, in the same field range. The uncertainty in measuring the absolute value of magnetization for the films was about 1% at room temperature

5.3 Results and discussion

5.3.1 RHEED measurements

In the present study we provide comparative result on two 45nm thick Fe_3O_4 films grown on low- and high-vicinal MgO (100) substrates hereafter referred to as samples 1 and 2 respectively. Low and high-vicinal samples had a miscut of 0.5° and 2.0° , respectively, along the $\langle 011 \rangle$ direction. Figure 5.3 shows the RHEED images of the high-vicinal UHV heat treatment, recorded in $\langle 011 \rangle$ directions (Figure 5.3(a) and 5.3(b)). Small changes observed in the separation of vertical streaks are due to variations in incidence angle of the electron beam for different azimuths.

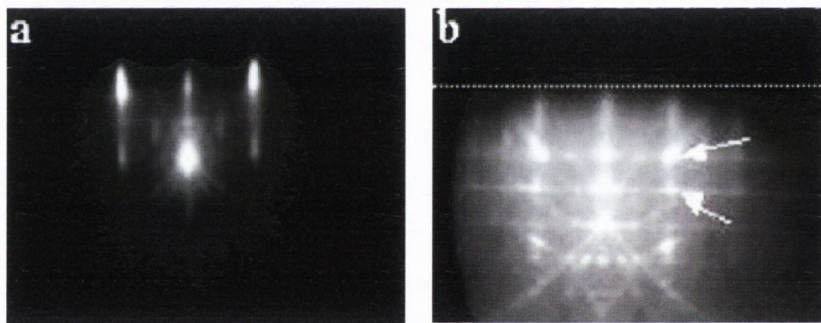


Figure 5.3 RHEED images of high-vicinal MgO (100) substrate after the UHV heat treatment measured in $\langle 011 \rangle$ azimuths at room temperature with an incident electron beam directed (a) along the step edges and (b) perpendicular to the step edges. Variations in the streak separation are due to the small changes in incidence angle of the electron beam for different azimuths. The dashed line in image (b) represents the shadow edge.

Figures 5.3(a) and (b) correspond to the case when electron beam is incident parallel or perpendicular to the step edge directions, respectively. For the case when the electron beam is incident along the step edges, the vertical lattice rods and sharp Kikuchi lines are observed. Sharp horizontal Kikuchi lines are observed only when the direction of incident electron beam is perpendicular to the step edges, which represents increased inelastic scattering due to the

presence of atomic steps. These horizontal Kikuchi lines were found to have a tilt with respect to the shadow edge and were used to determine the average miscut angle of the substrate, which comes out to be 2.05° . We also checked the surface tilt from the position of the two diffracted spots marked with arrows in Figure 5.3(b).

The average surface tilt or miscut angle can be calculated from the spot separation using the following equation [14,15] (see chapter 2 for details):

$$\theta_c = \frac{\langle \theta_e \rangle}{2\pi/sd - 1} \quad (5.1)$$

where $\langle \theta_e \rangle$ is the average exit angle of the two diffraction spots, d is the planer spacing and s denotes the spot separation in reciprocal lattice units. This analysis gives a miscut angle of 2.1° . Figure 5.4 (a) and (b) shows the RHEED pattern recorded after the growth of 45nm Fe_3O_4 film on high-vicinal MgO (100) substrate. Additional streaks corresponding to Fe_3O_4 are situated in the middle of the MgO streaks. Other features are quite similar to those of the substrate for the case when the electron beam is incident along the step edges. For the incident beam direction perpendicular to the step edges there are additional features observed, and there are slashes alongside the vertical rods due to the additional periodicity arising from the terrace width.

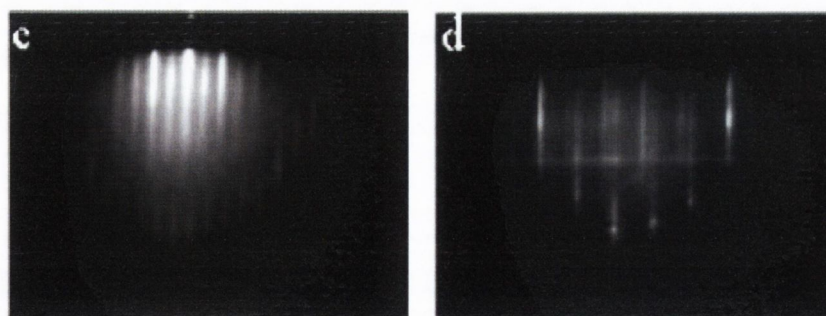


Figure 5.4 RHEED images of 45nm Fe_3O_4 film grown on high-vicinal MgO (100) substrate with (a) incident electron beam directed along the step edges and (b) perpendicular to the step edges.

The average terrace width determined from the separation between the slashes and the diffraction streaks for the film is $5.69 (\pm 0.5\text{nm})$ nm. The average miscut for sample 1 was found to be 0.5° within the accuracy of RHEED measurements. However, due to the larger terrace width of 24.05nm for this

sample, the additional slashes corresponding to the terraces were not observed. Instead, a broadening of steaks was noted. The estimated values of average miscut angles for both the samples were in good agreement with the results obtained through HRXRD measurements. HRXRD results showed that the average miscut angle for the substrate and the film after the growth were the same.

5.3.2 HRXRD measurements

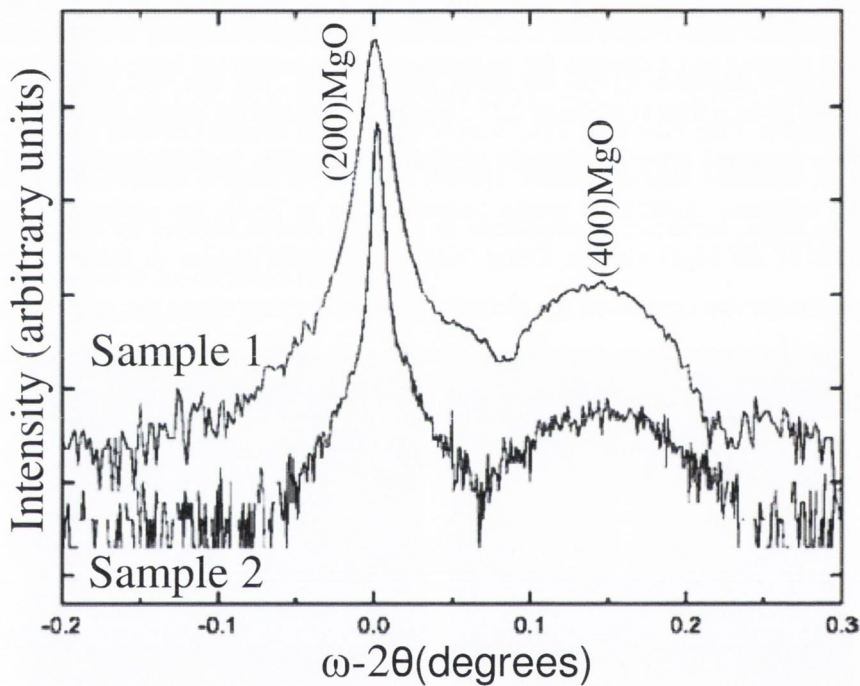


Figure 5.5 The ω - 2θ scans of Sample 1 and Sample 2 measured relative to the (200) Bragg reflection of MgO.

Figure 5.5 shows the ω - 2θ rocking curves measured at room temperature for (200) and (400) Bragg reflections of the substrate and thin film respectively for Sample 1 (45 nm Fe_3O_4 film on low-vicinal MgO substrate) and Sample 2 (45 nm Fe_3O_4 film grown on 2° vicinal MgO substrate). The horizontal axis in the

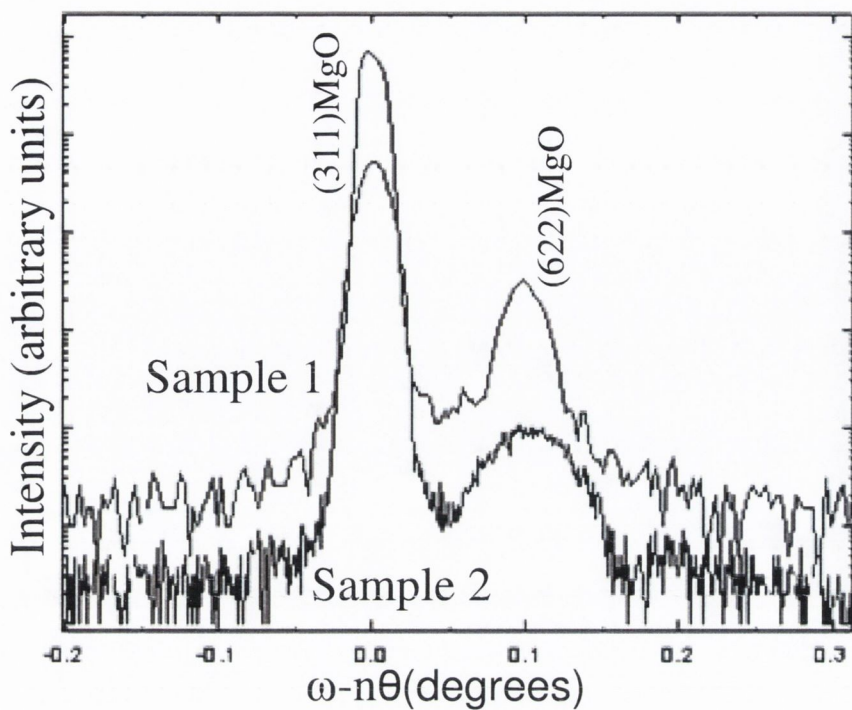


Figure 5.6 The ω - $n\theta$ grazing exit scans of Sample 1 and Sample 2 measured relative to the (311) Bragg reflection of MgO.

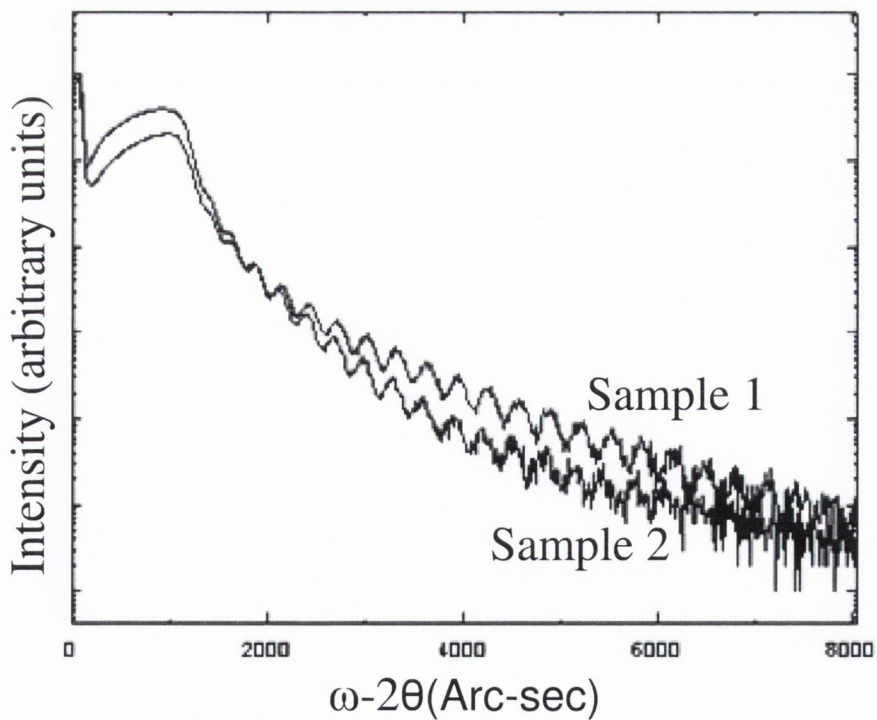


Figure 5.7 The reflectivity scans of Sample 1 and Sample 2.

figure is shown with reference to the Bragg angle for symmetric (200) reflection of MgO substrate. The curves are shifted along the vertical axis for clarity. From the separation between the film and substrate Bragg peaks we determine the out-of-plane lattice constant. For both the samples it is found to be 0.8372 nm. The full width at half maximum for the thin film peak is found to be 0.065 and 0.077 degrees for Sample 1 and Sample 2 respectively. The larger FWHM of the thin film peak for sample 2 represents additional scattering contribution arising from the presence of step edges.

The in-plane lattice parameters of the films were determined from the asymmetric (622/311) Bragg reflections. Figure 5.6 shows the ω - $n\theta$ grazing exit scans for sample 1 and sample 2. We found that the in-plane lattice constant of the Fe₃O₄ thin film (0.84236 nm) is twice that of the MgO substrate (0.4213 nm). The FWHM for the thin film peak is found to be 0.021 and 0.042 degrees for Sample 1 and Sample 2 respectively. From the in-situ RHEED and ex-situ HRXRD characterization, we infer that the films grow pseudomorphically and maintain one-to-one registry with the MgO substrate. The unit cell volume of the film is a good indication of the film stoichiometry and is consistent with bulk magnetite suggesting that the films are stoichiometric. Figure 5.7 shows the reflectivity scans of sample 1 and sample 2. The thickness measured from the scans are 45nm(\pm 2nm).

5.3.3 Magnetization measurements

Figure 5.8 shows the in-plane hysteresis loops measured at room temperature for both samples. Saturation magnetization (M) values attained for samples 1 and 2 at 1 T field were found to be 468 and 445 $\times 10^3$ A/m. These values are smaller than the saturation magnetisation value of bulk Fe₃O₄ (480 $\times 10^3$ A/m). It was not possible to saturate both the samples with the maximum available field strength of 1 T with the measurement set up. Observation of reduced magnetization and finite slope seen at higher fields is indicative of the presence of areas with frustrated exchange. Observation of reduced M and inability to saturate epitaxial Fe₃O₄ films is attributed to the presence of APBs [3,4]. The reduction in M with increasing miscut angle is related to the step edges which enable the formation of additional APBs. The

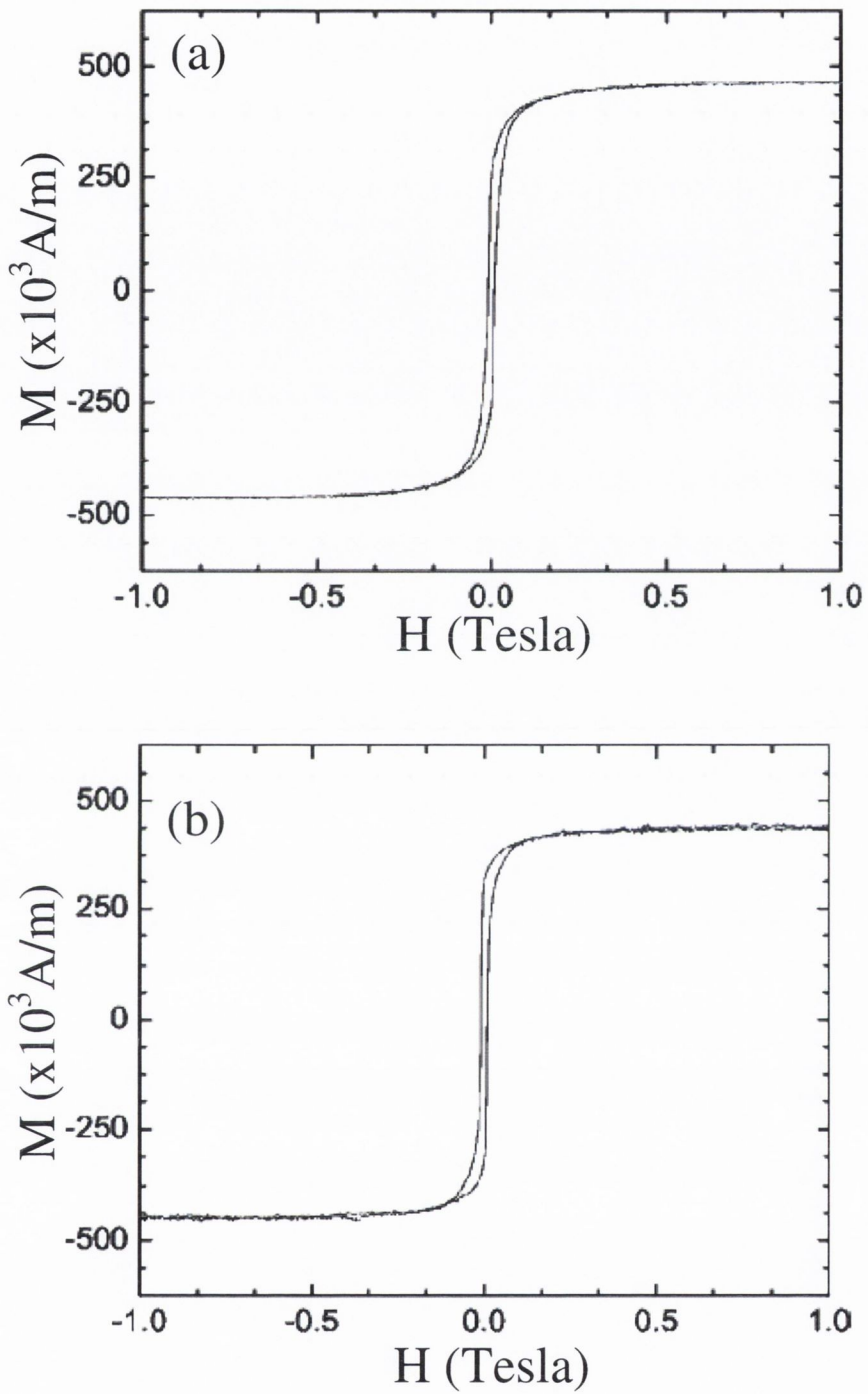


Figure 5.8 Hysteresis loops of (a) Sample 1 and (b) Sample 2 measured at room temperature with an in-plane applied field.

observed reduced magnetic moment is suggestive of an increased number of APBs.

For 0.5° and 2° miscuts along the $\langle 011 \rangle$ direction of MgO (100) substrate the average terrace width is 24.05 and 5.96 nm respectively. This corresponds to a step density of 4.2×10^5 and $1.6 \times 10^6 \text{ cm}^{-1}$ respectively for sample 1 and 2. By considering this number density of APB and a width of 0.42 nm (by assuming that at the APB one bond from each side of the boundary contributes to the frustrated exchange) we estimate the area of the frustrated volume to be ~ 1.52 and 5.6% for samples 1 and 2 respectively. However, we observe a 2.28 and 7% reduction in magnetic moment for samples 1 and 2 respectively. The additional enhancement of area with frustrated magnetic moment is possibly due to the presence of natural shifted APBs at the terraces.

5.3.4 Magnetoresistance measurements

Sample 1 exhibited a Verwey transition at 108 K and its magnetoresistance was studied as a function of temperature. Figure.5.9 shows the magnetoresistance measured in the $\langle 010 \rangle$ direction at 150 K and 108 K as a function of magnetic field applied in the film plane. The MR is found to increase with decreasing temperature and is substantially higher near the Verwey transition temperature (T_v). The MR shows a linear dependence on applied magnetic field. Figure.5.10 shows the MR results obtained for this sample measured at the Verwey transition (108 K) in the $\langle 010 \rangle$ direction, along and perpendicular to the step edges. In all the cases the magnetic field is applied in the film plane and parallel to the current direction. The MR at 2 Tesla field measured perpendicular to the step edges is found to be 7.54%, which is 2.69 and 1.93% higher than the MR along the $\langle 010 \rangle$ and along the step edges directions respectively. The enhancement in the MR is more prominent at lower temperatures, particularly in the Verwey transition region. Some difference between the curves measured along the $\langle 010 \rangle$ and the miscut directions is expected. Indeed, these two directions are crystallographically in-

equivalent as the miscut direction is effectively along $\langle 011 \rangle$ direction.

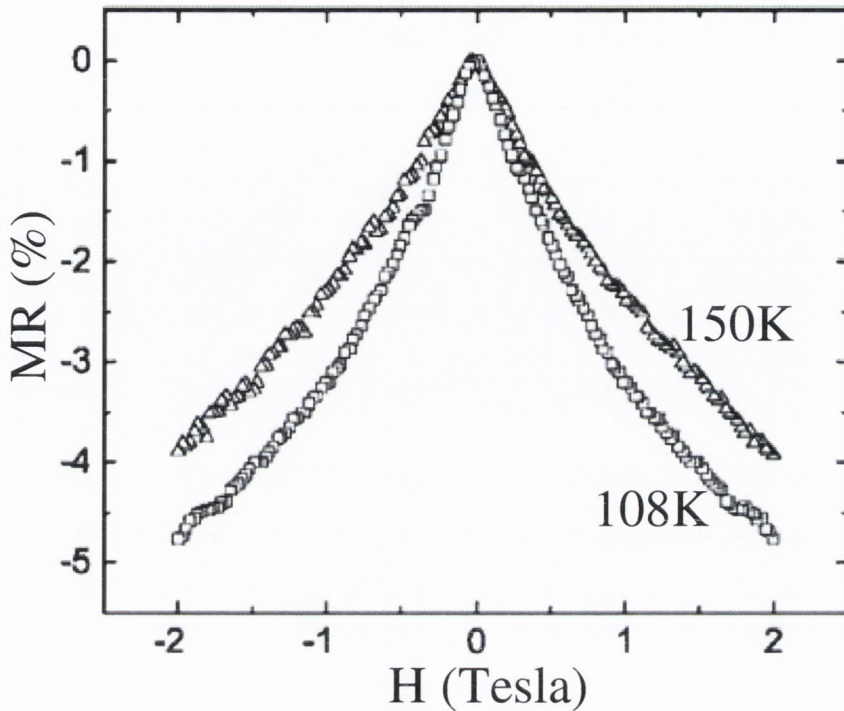


Figure 5.9 Magnetoresistance of sample 1 at 150K and 108K with magnetic field applied in the film plane along $\langle 010 \rangle$ direction.

However, two directions, along and perpendicular to the miscut, are crystallographically equivalent, consequently no anisotropy in transport properties between these two directions is expected. We suggest that the anisotropy results from the preferential alignment of APBs along the step edges as explained in the introduction. Thus, formed APBs enhance the spin dependent scattering and influence the MR properties.

Results on Sample 1 demonstrate that it is possible to control the MR properties of magnetite thin films and introduce MR anisotropy provided the density and orientation of APBs is controlled. Figure.5.11 shows the temperature variation of resistivity measured along and perpendicular to the step edges for Sample 2. The Verwey temperature for both directions is found to be 109.8 K (± 0.5 K). The resistivity across the step edges is about 2 times greater than the resistivity along the step edges (at 130K ρ was found to be 8.6 and 13.6 m Ω cm along and perpendicular to the step edges respectively). The resistivity versus temperature dependency for the Fe₃O₄ films show an activated behaviour with an activation energy of ~ 30 meV above the Verwey

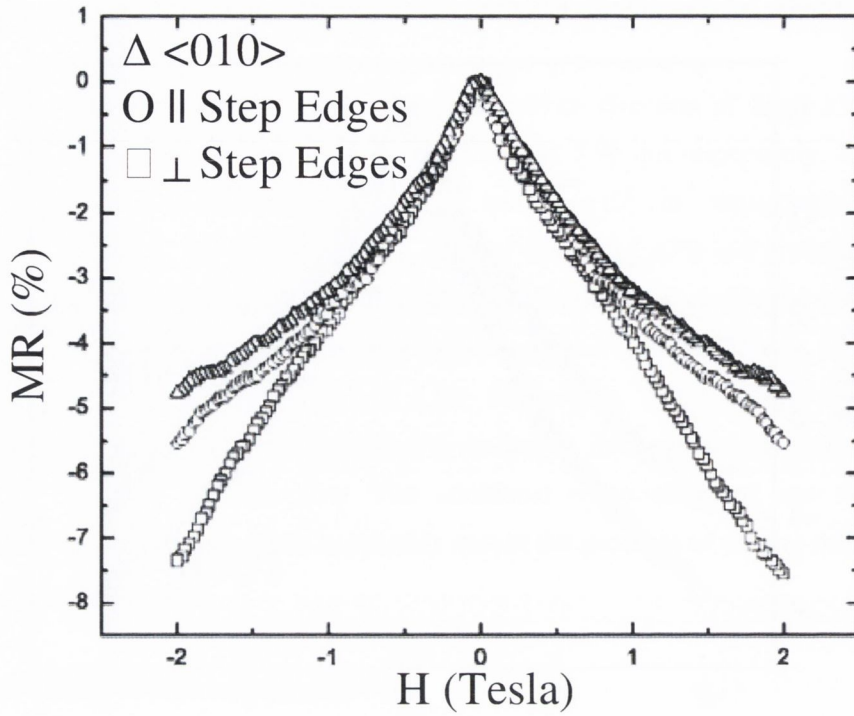


Figure 5.10 Magnetoresistance of sample 1 measured at Verwey transition temperature (108K) in the $\langle 010 \rangle$, along and perpendicular to the step edge directions.

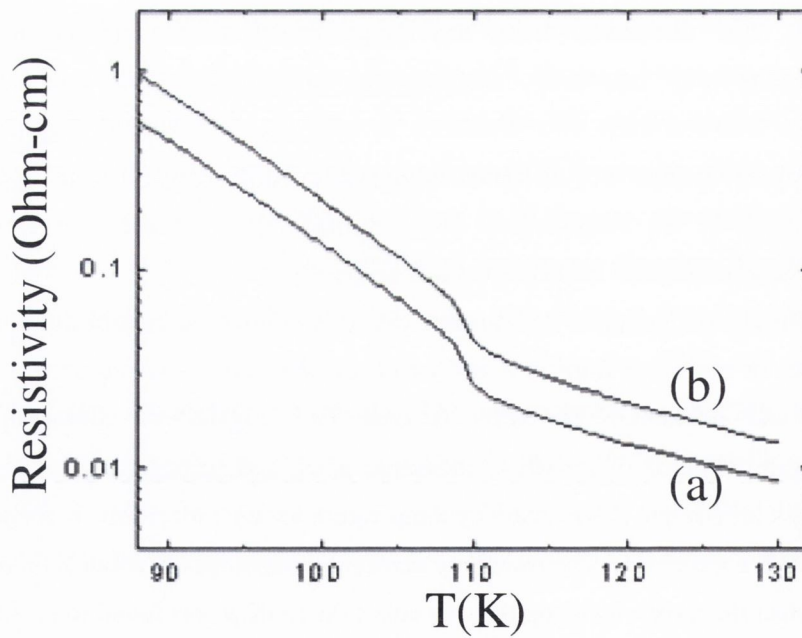


Figure 5.11 Resistivity as a function of temperature measured (a) along and (b) perpendicular to the step edges for sample 2.

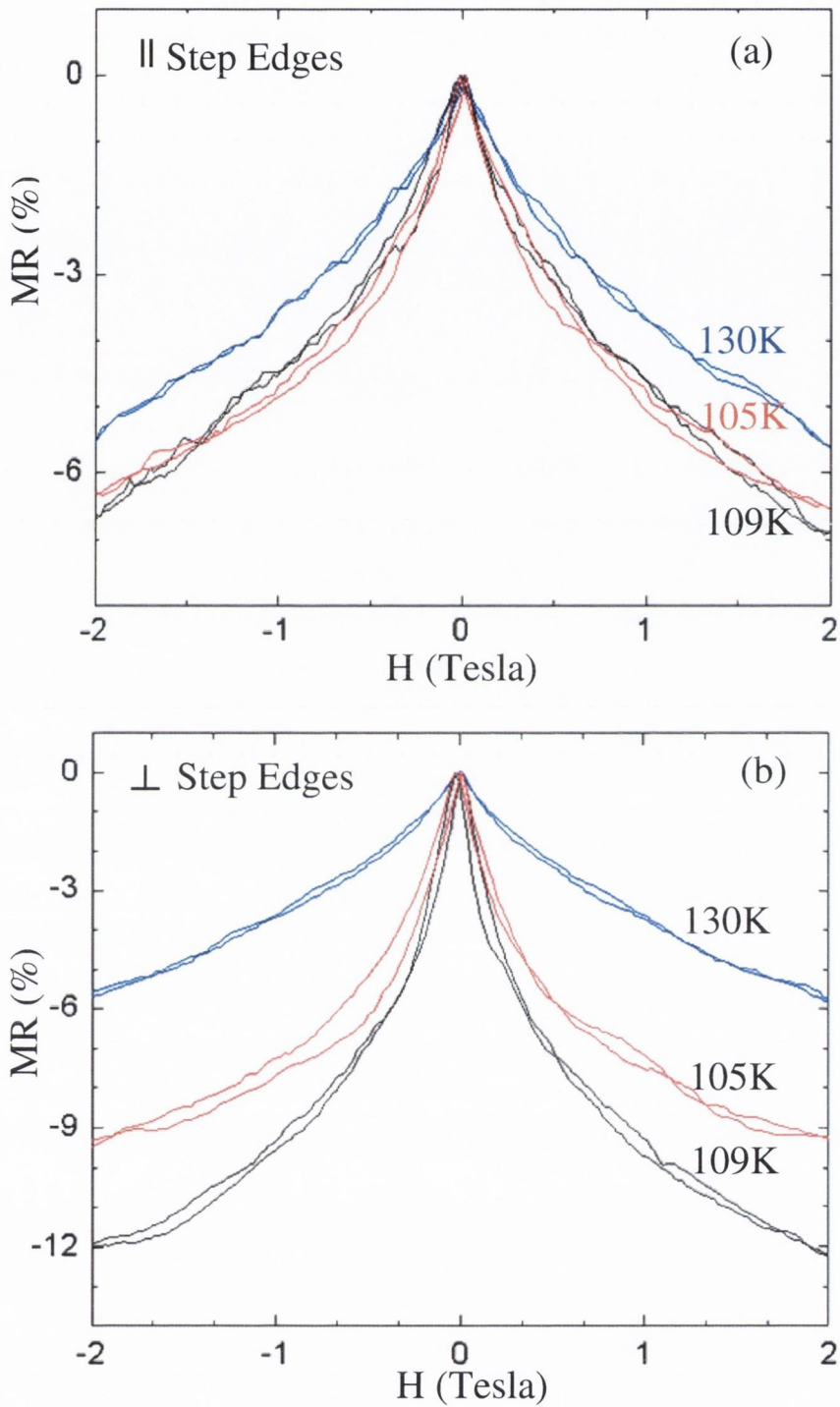


Figure 5.12 Magnetoresistance as a function of applied in-plane magnetic field for Sample 2, measured at different temperatures (a) along and (b) perpendicular to the direction of step edges. The direction of current and magnetic field are parallel to each other.

transition temperature for both directions. Below the Verwey transition temperature the activation energies are found to be 56 and 61 meV along and perpendicular to the step edges respectively. The resistivity anisotropy remains persistent throughout the whole temperature range. The enhancement in resistivity across the step edges is due to a significant increase in the density of APBs formed at the step edges that produces an additional scattering of charge carriers traversing across the step edges. This substantially reduces the mobility of charge carriers across the step edges and an anisotropic mobility with respect to the relative direction of current and step edges is observed. The resistivity for sample 1 showed similar behaviour. At 130 K the resistivity was found to be 4.68 and 5.09 m Ω cm when measured along and perpendicular to the step edges. The lower resistivity obtained for sample 1 as compared with sample 2 demonstrates that the step edges facilitate the formation of APBs. This further supports our conclusion based on magnetization reduction. Conduction properties of Fe₃O₄ thin films possessing APBs has been studied by Eerenstein et al [6], within the framework of a one-dimensional hopping model. The conductivity predicted by this model is proportional to t^2 , where t ($t=t_0\cos\phi_{nm}$) is the transfer integral (see chapter 2 for details). According to this model the presence of local structural and spin disorder at the APB reduces the transfer integral. This suggests that, in the case of vicinal substrate where the APBs are formed predominantly at the step edges, one expects a reduction in the conductivity across the step edge direction, which is in line with the experimental observations.

Magnetoresistance of Sample 2 was studied as a function of temperature along and perpendicular to the direction of the step-edges. Figure. 5.12 shows the representative MR curves for Sample 2 measured along and perpendicular to the step edges at 130, 109 and 105 K respectively. The MR is found to be strongly anisotropic with respect to the direction of the step-edges: the MR perpendicular to the step edges is significantly higher than along the step edge direction.

The magnitude of MR for both directions is found to increase with a decrease in temperature and peaks at the Verwey transition temperature (109 K (± 0.5 K)). A further decrease in the temperature leads to a lowering of the MR for both directions.

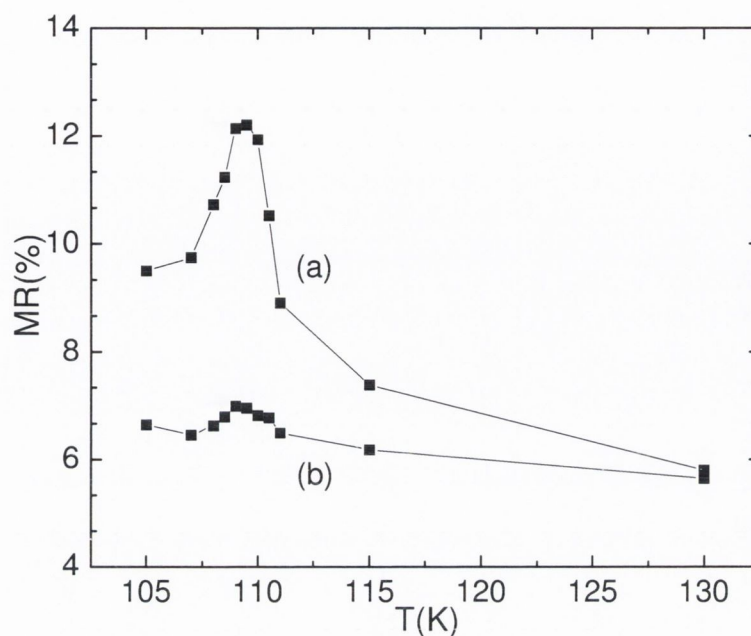


Figure 5.13 Temperature dependence of the MR (a) perpendicular and (b) along the step-edges for Sample 2.

The maximum value of MR is observed in the Verwey transition region, which is 12.2% at 2 Tesla field and 9.7% at 1 Tesla field. These values of MR are 5.4% and 4.4% higher than the corresponding values observed along the step edges. The MR at 2 Tesla field for Sample 2 is found to be 4.8% higher than that of the low miscut sample. The difference in MR along and perpendicular to the step edges is significantly higher only at the low temperatures mainly in the vicinity of the Verwey transition. The remarkable result is that there is a significant enhancement in the low field MR. The MR shows a steep rise up to a field of 0.7 T. For higher magnetic fields (>0.7 T) there is a cross over to shallower field dependence. However, the field dependence of MR along the step edges did not show this change over. Figure 5.13 shows the temperature variation of the MR (2 T) measured along and perpendicular to the step edges. The anisotropy in MR, $MR_{SE} = MR_{\perp} - MR_{\parallel}$, represents the contribution arising due to the step edges and is shown in the Figure 5.14. The anisotropy in MR is observed only below 150K and peaks at the Verwey transition.

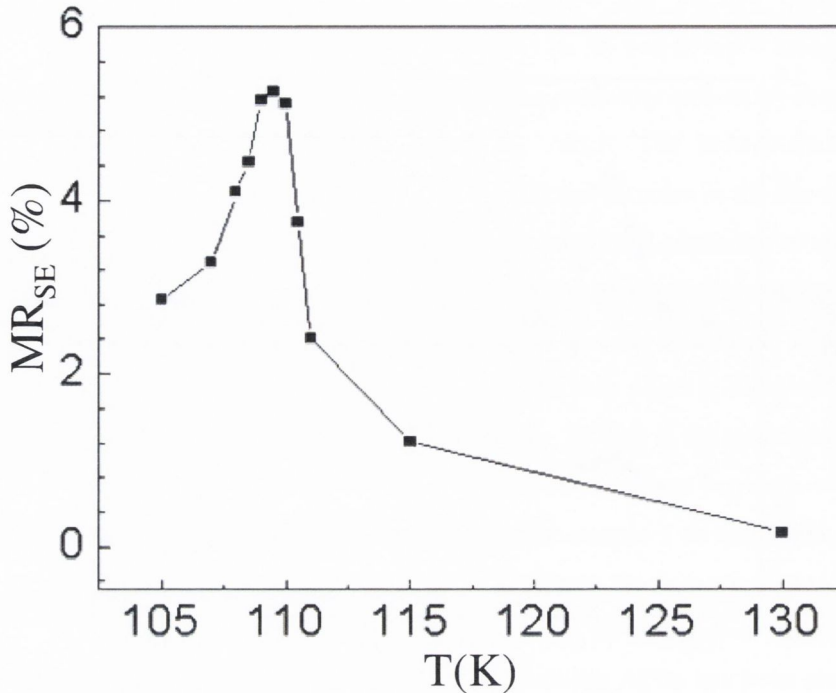


Figure 5.14 The difference in MR observed along and perpendicular to the step edge directions, representing the step-edge induced contribution to MR, as a function of temperature.

5.3.5 Effects of substrate pre-deposition annealing on the MR behaviour of Fe₃O₄ films grown on vicinal MgO (100) substrate

In our study we have also noticed that the MR enhancement depends strongly on the way the substrate surface has been treated prior to the growth of the magnetite film. This subsequently determines the nature of the film microstructure as well as the nature and density of APBs that will strongly affect the MR properties. The studies presented in this section were obtained for the optimised substrate annealing conditions. Details of the substrate annealing conditions and its influence on the MR properties are discussed in this section.

The Fe₃O₄ thin films were grown on (100) oriented MgO single crystal substrates having 2° ($\pm 0.05^\circ$) miscut along the $\langle 011 \rangle$ direction. In the present study we used four representative samples named, Sample 2, Sample 3, Sample 4 and Sample 5 each of 45nm thickness (Sample 2 is the same sample used in

the previous study). Prior to Fe_3O_4 film growth the MgO substrates were annealed at 600°C for 5, 3, 9 and 13 hours duration for sample 2, sample 3, sample 4 and sample 5, respectively. First one hour of annealing for each sample was performed under UHV conditions and the remaining time in oxygen at a pressure of 5×10^{-5} Torr. Structural characterization of the samples was performed using a high-resolution X-ray diffractometer. Miscut of the samples was determined from the variation in Bragg angle for the symmetric diffraction measured for different azimuths.

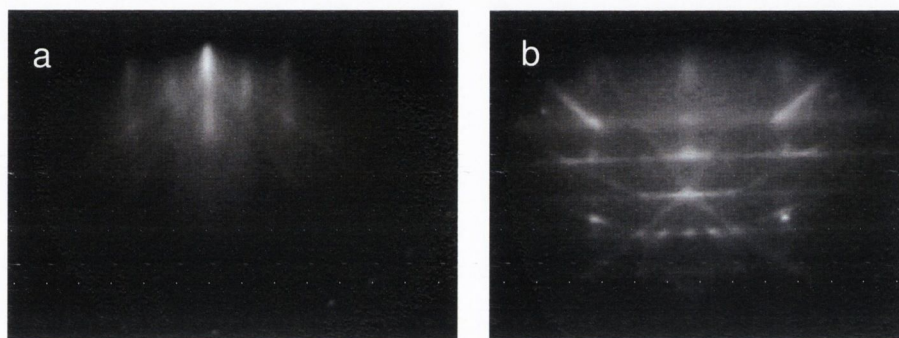


Figure 5.15 RHEED images of high vicinal MgO substrate (Sample 3) after the UHV heat treatment recorded along $\langle 110 \rangle$ direction which corresponds to the case when electron beam is incident (a) along the step edges and (b) perpendicular to the step edges.

The RHEED image obtained for the substrate of Sample 2 recorded at room temperature after 5 hours of heat treatment is shown in Figure.5.3. Figure 5.3.(b) shows that the vertical lattice rods and the horizontal Kikuchi lines are sharper and prominent. The same image obtained for the substrate of Sample 3 (Figure 5.15) showed weak features. The horizontal Kikuchi lines are observed only when the direction of the incident electron beam is directed across the step edges and represents increased inelastic scattering due to the presence of atomic steps [16]. RHEED images of the substrates of Sample 4 and Sample 5 are not different from Figure.5.3 hence not shown. The average miscut angle determined for the substrates from the separation of diffraction spots marked with arrows in the RHEED pattern and tilting of Kikuchi lines with reference to shadow edge is $\sim 2.1^\circ$ and agrees well with the miscut angle found from the HRXRD measurements. This corresponds to a step height of 0.21 nm. After the growth of Fe_3O_4 film on these substrates pre-annealed for

different time duration, the miscut angle for the films were found to be same as that of the substrate within the accuracy of RHEED measurements.

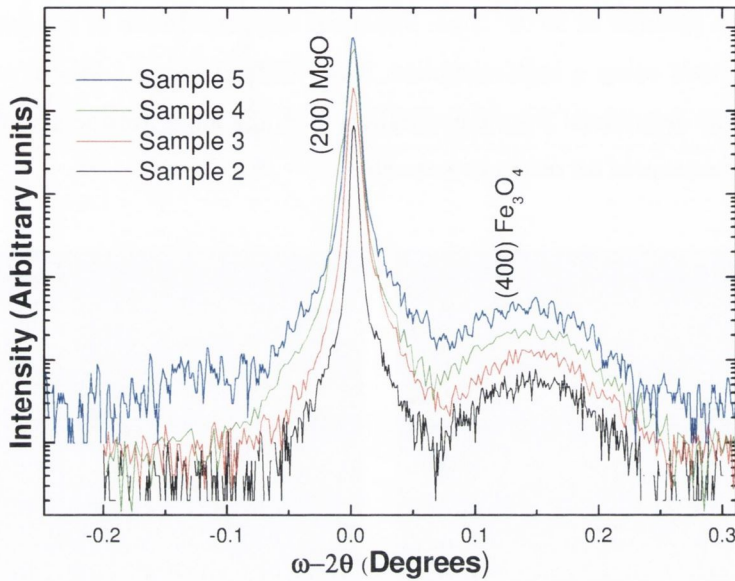


Figure 5.16 The ω - 2θ scans of Sample 2, Sample 3, Sample 4 and Sample 5, measured relative to the (200) Bragg reflection of MgO.

The structural characterisation of the films was performed using HRXRD. The ω - 2θ scans performed for symmetric (200) (figure 5.16) and asymmetric (311) Bragg reflections gave in-plane and out-of-plane lattice constants values of 0.8426 nm and 0.8372 nm respectively for the Fe_3O_4 films. This indicates that the films are fully strained with a tetragonally distorted unit cell.

Resistivity measurements on these samples revealed a clear Verwey transition near 109 K (± 1 K) for both along and perpendicular to the step edge directions. Figure 5.17 shows the resistivity as a function of temperature for Sample 2, Sample 3, Sample 4 and Sample 5. The resistivity was found to have an activated behaviour with an activation energy of ~ 30 meV and 60 meV above and below the Verwey transition temperatures (T_v) respectively. The percentage difference in resistivity along and across the step edges at 130 K are 55%, 34%, 54%, and 43% for Sample 2, Sample 3, Sample 4, and Sample 5 respectively.

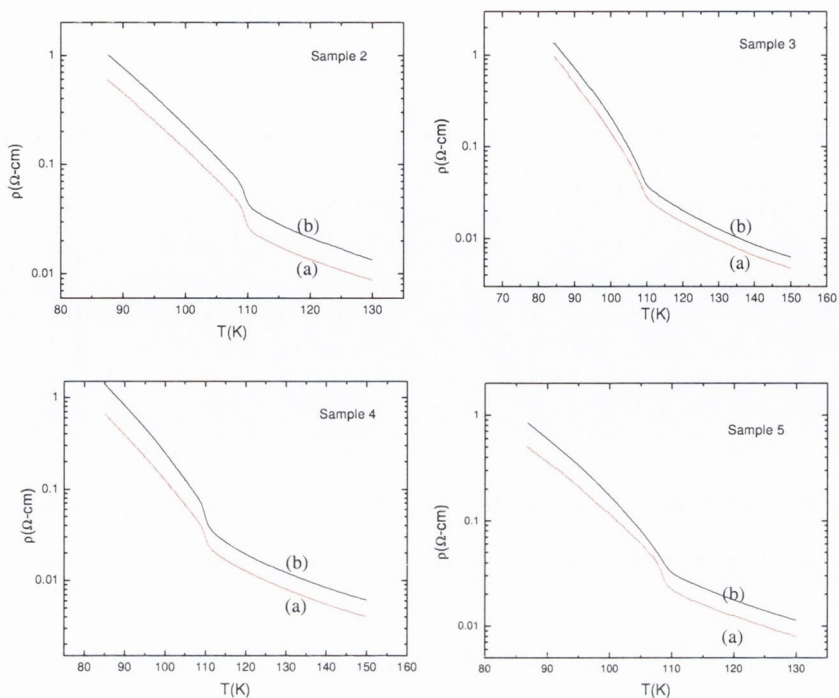


Figure 5.17 Resistivity as a function of temperature measured (a) along and (b) perpendicular to the step edges for Sample 2, Sample 3, Sample 4 and Sample 5..

Magnetoresistance for all the samples were measured from room temperature down to 77 K for the direction of current along and perpendicular to the step edges while keeping the direction of magnetic field parallel to the current direction. MR was found to increase with the decreasing temperature and was highest at Verwey transition temperature (T_v) for both directions. Figures 5. 18 (a) and (b) show the MR at 130K for all the samples with current driven in the direction across and along the step edges respectively. Figures 5. 19 (a) and (b) show the MR at T_v and Figures 5. 20 (a) and (b) show the MR at 105K. Figure 5.21 shows the MR measured at 2 Tesla field in all samples at different temperatures in the direction along and across the step edges. All samples showed a clear peak near to T_v which is due to the abrupt changes in the thermodynamic quantities accompanied with the first order Verwey transition. Figure 5.22 shows the difference in MR (MR_{SE}) at T_v (109 ± 1 K) observed between current and field direction along and across the step edges at 2 Tesla field, with different annealing time.

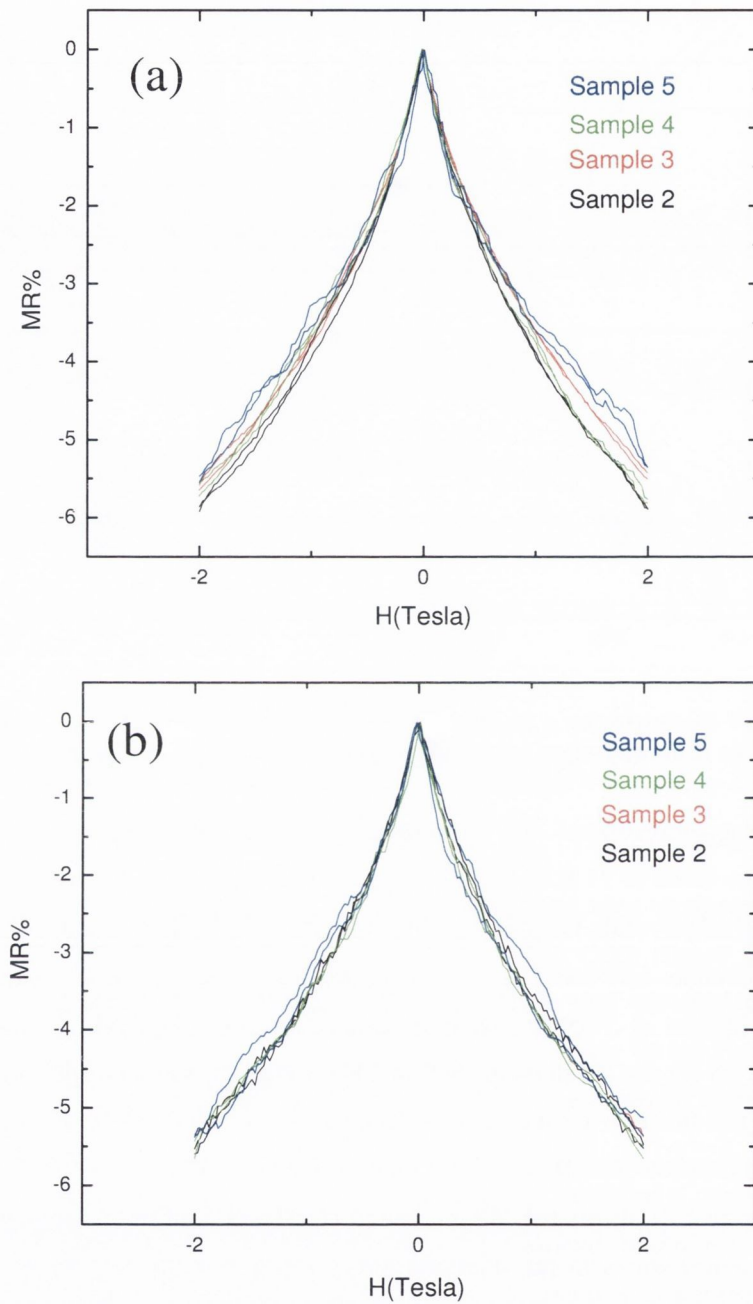


Figure 5.18 Magnetoresistance MR of Sample 2, Sample 3, Sample 4 and Sample 5 measured at 130K for the current and field direction (a) perpendicular to the step edges and (b) along the step edges.

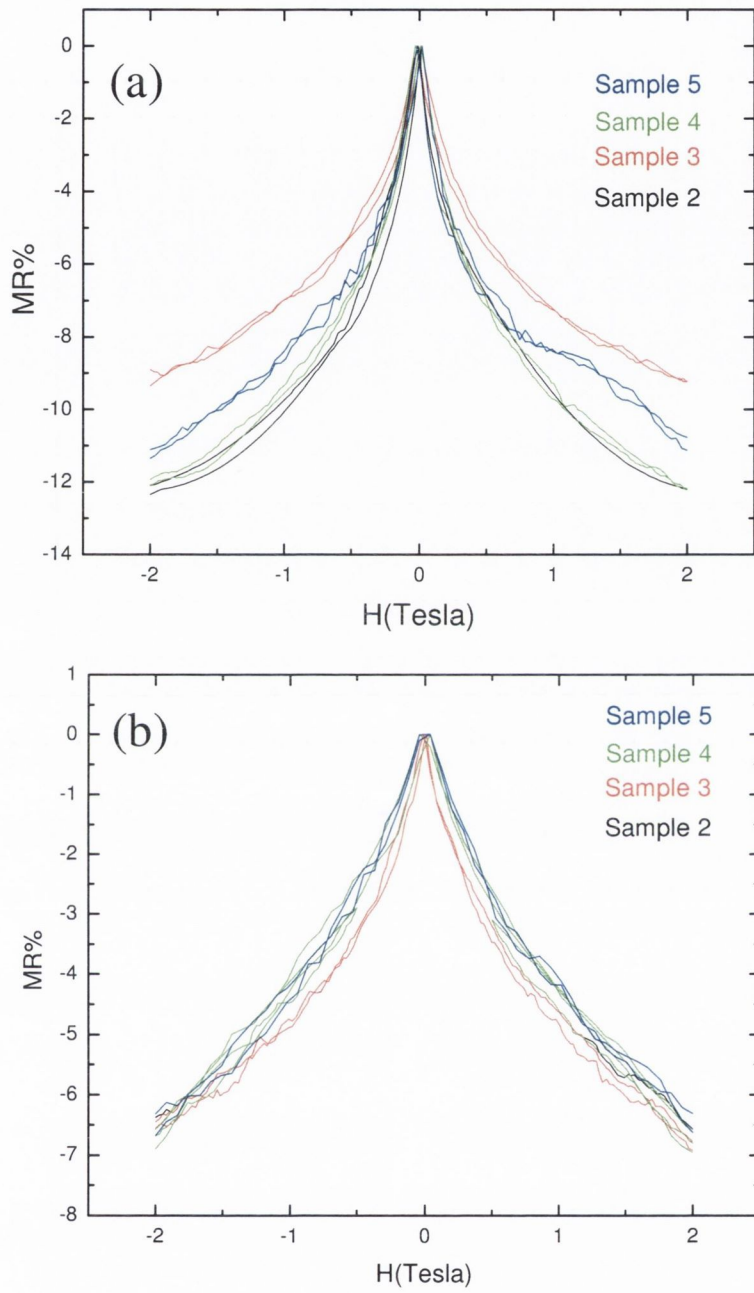


Figure 5.19 Magnetoconductance MR of Sample 2, Sample 3, Sample 4 and Sample 5 measured at Verwey transition (T_v) for the current and field direction (a) perpendicular to the step edges and (b) along the step edges.

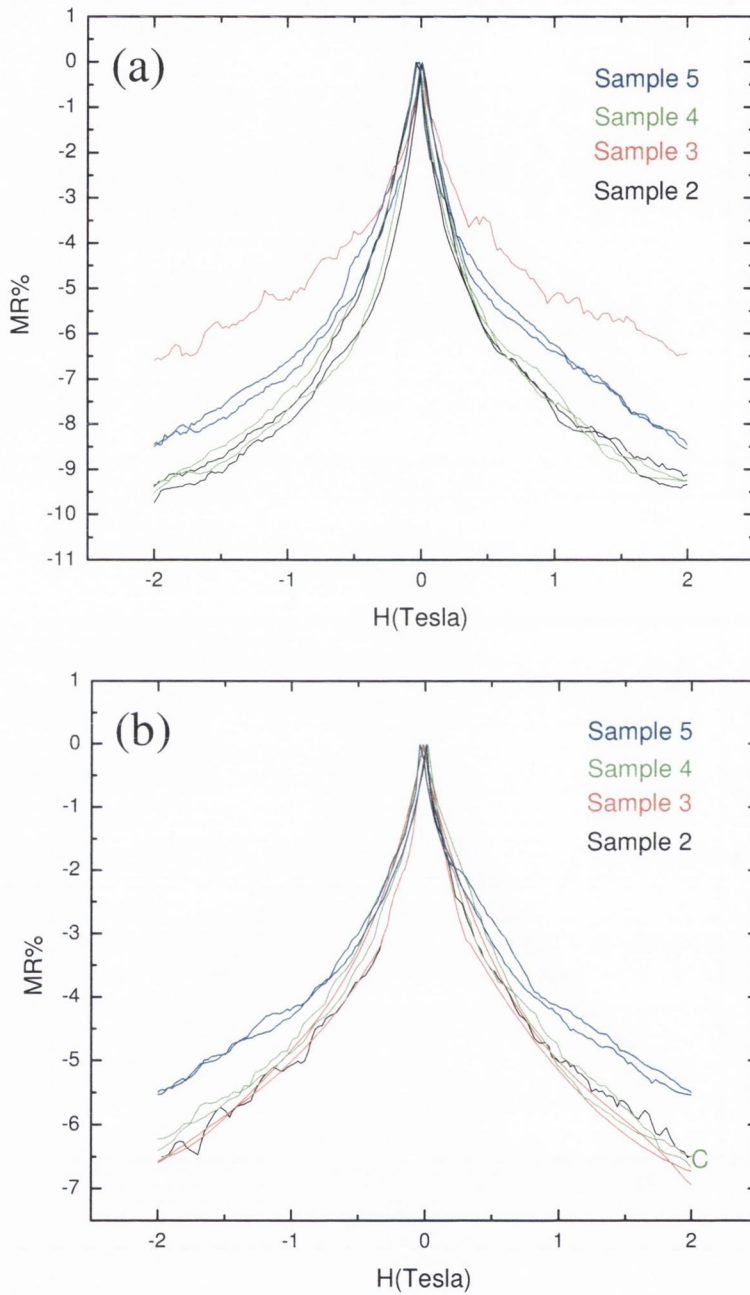


Figure 5.20 Magnetoresistance MR of Sample 2, Sample 3, Sample 4 and Sample 5 measured at 105 K for the current and field direction (a) perpendicular to the step edges (b) along the step edges.

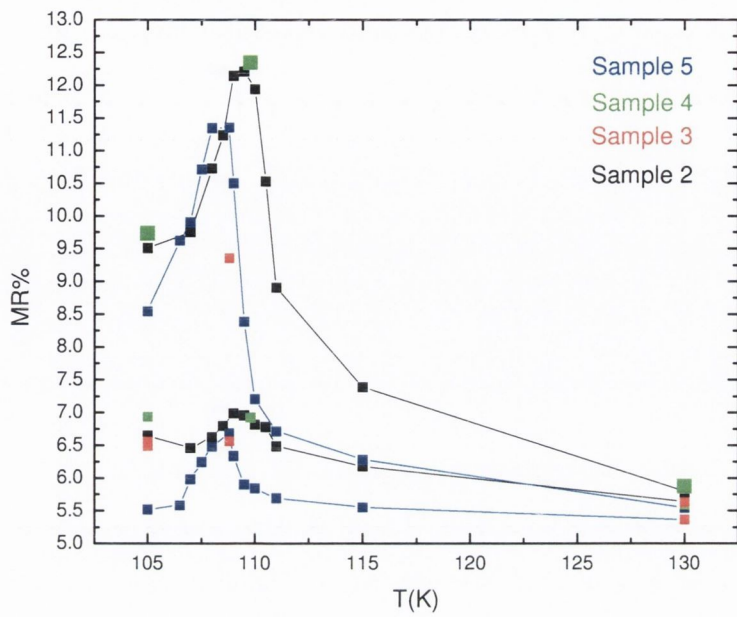


Figure 5.21 Magnetoresistance MR at 2 Tesla field of *Sample C* as a function of temperatures for the current and field direction across (a) and along (b) the step edges.

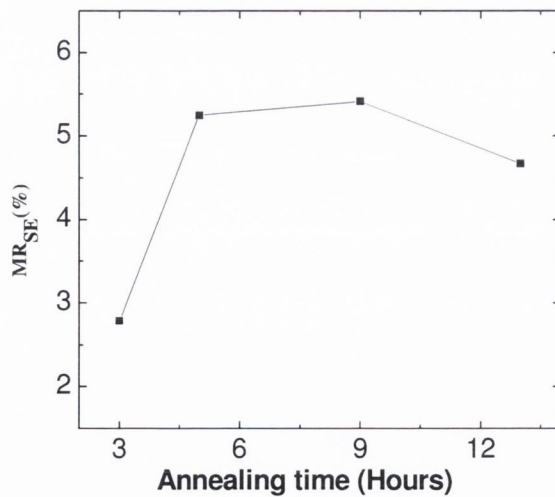


Figure 5.22 Difference in Magnetoresistance measured along and across the step edges (MR_{SE}) of Sample 2, Sample 3, Sample 4 and Sample 5 measured at Verwey transition (T_v) at 2 Tesla field as a function of annealing time. In all the cases the magnetic field is parallel to the current direction.

5.3.6 Discussion

The observed value of MR is higher than any of the previously reported MR values for epitaxial magnetite films [6-8,13]. Previous efforts by Ziese et al [13,17] to enhance the MR of epitaxial Fe_3O_4 films grown on patterned MgO and MgAl_2O_4 substrates having step edge array (80-120 nm step height and 10-20 μm wide stripes) have not yielded substantial MR increase. They found that the anisotropy in MR with reference to the step edge direction was not large (1.8% at 3T, 80K) for the case of films grown on patterned MgO substrates, whereas they obtained relatively larger MR anisotropy for films grown on patterned MgAl_2O_4 (5% at 3 T,105K). They attributed the results on patterned MgO to the presence of larger density of APBs within the stripe. For films grown on patterned MgAl_2O_4 , the disorder at step edges enhances the spin scattering leading to a larger anisotropy in MR, since the effect due to step edges is not smeared by the APBs. Recently, Bollero et al [18] have reported that due to the presence of APBs within the film, Fe_3O_4 films grown on bicrystal MgO (100) substrate having a 28° grain boundary did not yield any enhancement in MR across the grain boundary. In our case, due to the preferential alignment of step edges along the direction perpendicular to the miscut, APBs are formed due to the presence of atomic height steps (0.21 nm) on MgO substrate. The terrace width (24.05 and 5.96 nm for 0.5° and 2° miscut, respectively) is quite small in comparison to the width of step edge array used by Ziese et al [13,17]

The MR behaviour of epitaxial magnetite thin films containing APBs has been analysed by Eerenstein et al. [6] and Zeise and Blythe [7] within one-dimensional models. Concerning the MR of the Fe_3O_4 films on vicinal substrates, we noticed that contrary to the prediction of the models, the field dependence of MR deviates from a linear behaviour below a certain temperature (130 K). The above models assume quite a simplified spin structure of APB whereas the spin structure could be more complex. The spin dependent scattering across the APB will be strongly influenced by spin structure and the strain fields associated with it. Furthermore, to explain the temperature and field dependence of MR, variations in the mismatch strain with the temperature and presence of the Verwey transition also need to be considered. If the additional MR induced by the step edges arises due to the spin polarized tunnelling (SPT) across the APBs, one expects the MR to scale

with the spin polarization, \mathbf{P} . The dependence of spin polarization on magnetization (\mathbf{M}) is complex but we use Julliere's model [19] within the first approximation ($\mathbf{P} \propto \mathbf{M}$), this predicts MR as;

$$\text{MR} = \frac{P^2}{(1+P^2)} \quad (5.2)$$

From (5.2), one would expect the MR to follow the relation :

$$\text{MR} \propto - \left(\frac{M_g}{M_s} \right)^2 \quad (5.3)$$

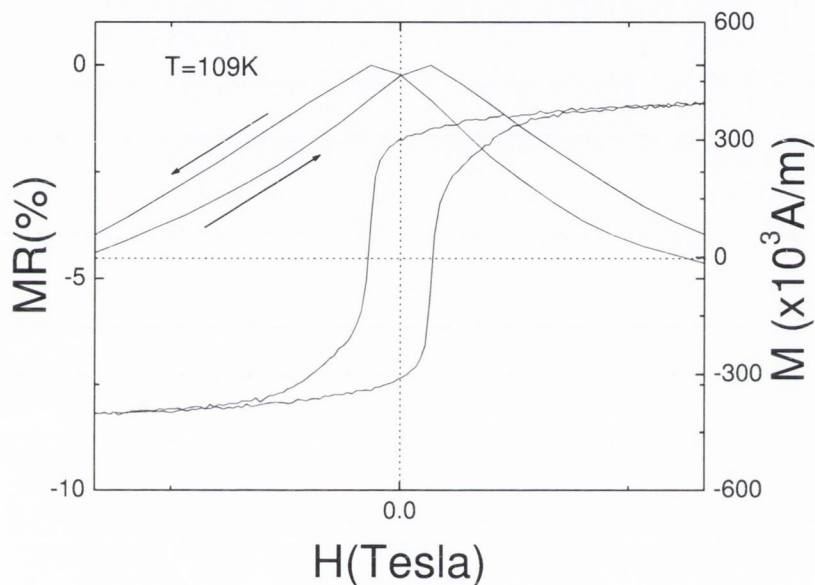


Figure 5.23 Magnetoresistance as a function of applied magnetic field for sample 2 measured across the step edges at 109 K along with the magnetization loop at the same temperature. Arrows indicate the direction of field.

where M_g and M_s are the global magnetization (or the net magnetisation of the sample at a particular field value) and saturation magnetization, respectively. This model is quite successful in explaining the MR behaviour of devices made of bicrystal or grain boundary junctions [13,20,21]. Figure 5.23 show the magnetization and MR in low field across the step edges. The MR peaks at the coercivity fields of the film ($H_c = 0.0205$ Tesla). A similar correlation with the coercive field was noted throughout the temperature range. To check the validity of the model yielding the dependence (5.3), we plot MR against the squared magnetisation normalized to the saturation magnetization, $-\left(\frac{M_g}{M_s}\right)^2$

(Figure.5.24). Only a small fraction of the observed low field MR can be explained on the basis of relation (5.3). The observation of a two step transition from a sharp low field MR to a gradual high field MR (the crossover field being much greater than the coercive field) for our case cannot be explained within the simplified picture of Julliere's model [19]. The model assumes that

the extent of SPT depends on barrier conductance and relative orientation of magnetization directions of uniformly magnetized spin systems on each side of the boundary, which are magnetically decoupled. In our case, the situation is more complicated due to the reason that the magnetization vectors across an APB are closely related. Moreover, the tunnelling probability could be affected from the variations in local magnetization within the domain, atomic arrangement and spin configuration of the APBs, terrace width, etc. Although, our observations are not in agreement with the relation (5.3), the MR contribution arising from SPT cannot be completely ruled out. In order to

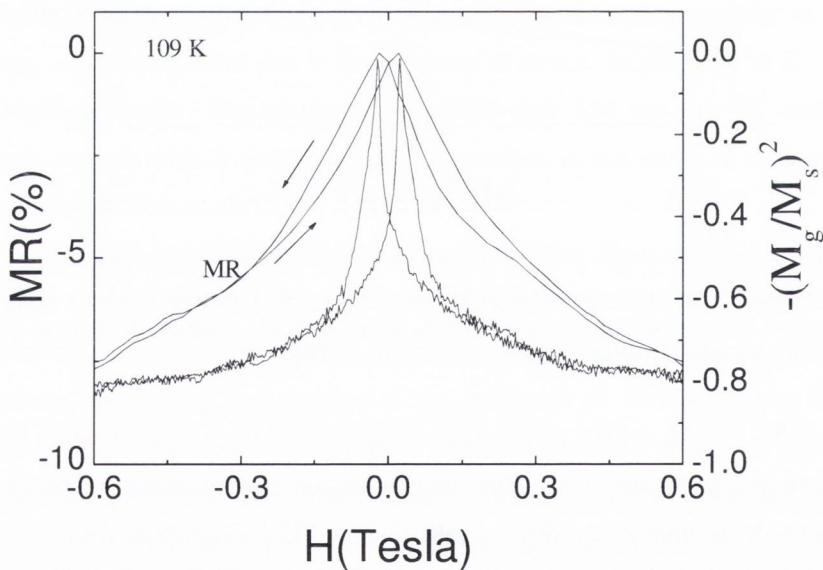


Figure 5.24 Magnetoresistance of sample 2 along with the bulk magnetization normalized to the saturation magnetization $-(M_g/M_s)^2$ as a function of applied magnetic field measured across the step edges at 109 K. Arrows indicate the direction of field increase.

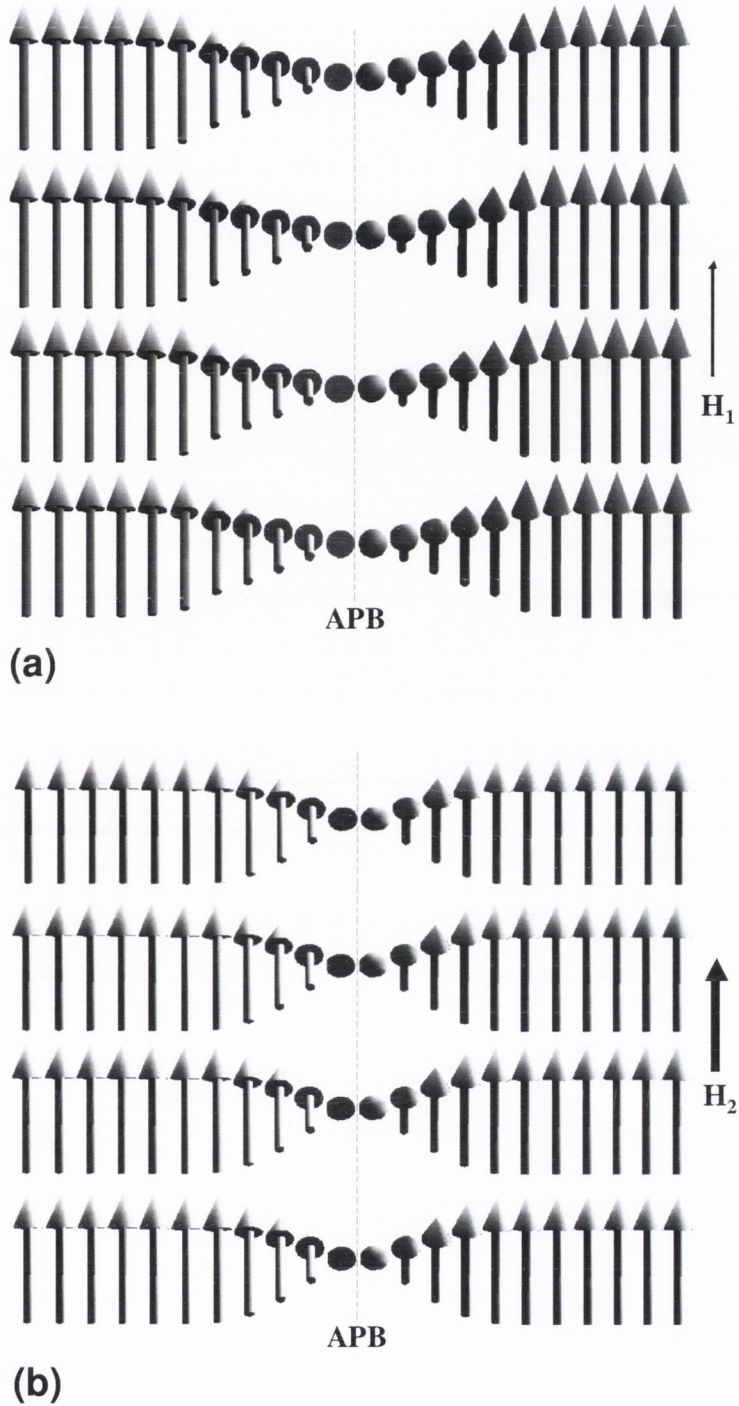


Figure 5.25 Spin structures of one of the magnetic sublattices of magnetite across an antiphase boundary, for (a) weak and (b) strong magnetic fields respectively, showing the variations in domain wall widths with an applied magnetic field.

explain the MR in the films we consider spin dependent scattering at the antiphase boundaries. Such scattering results from the spin-spin interaction. The second mechanism of the scattering could be that the lattice deformation takes place at the APB resulting from the magnetostriction. The magnetostriction is altered by the external magnetic field that changes the scattering. Needless to say, the scattering at the APBs is additional to the other spin-dependent scattering taking place within the grains. The misaligned direction of spins at the APB leading to the spin scattering is a result of two factors: the frustrated exchange across the APB and the interaction with the domains adjacent to the APB. With increasing magnetic field, the magnetic domains adjacent to the APBs pull against the frustrated exchange interaction and reduce the magnetic inhomogeneity at the APB and consequently the scattering induced by it. This model explains the observations in the higher magnetic field (above 1 T) whereby the MR increases with the field and yet the magnetisation is virtually saturated. Indeed the volume of the region with frustrated exchange at the boundaries is very small by comparison with the overall volume of the sample. Therefore, the more collinear alignment of the spins at the APB has no significant effect on \mathbf{M}_g . Still, these APBs with increased co-linearity of the spins become less effective in scattering electrons. The model is schematically presented in Figure 5.25. For simplicity, only one of the magnetic sublattice of magnetite is shown. The Figures 5.25 (a) and (b) schematically show the situation with smaller and greater field values respectively. Figure 5.25 (b) shows that the width of the area with misaligned spins is reduced when a stronger magnetic field is applied. In a recent investigation it was shown that the extent of exchange coupling induced by the APBs depends on the thermo-magnetic history of the sample [22]. Our results also suggest that the APBs are non-stoichiometric with defects expected at both cationic and anionic sublattices [23].

The above mechanism is based on the same concept of magnetoresistance caused by spin dependent scattering as applied in spin valves. An alternative mechanism of the anisotropy of MR can be constructed in particular with the view to explain the temperature dependence of the magnetoresistance. In our experiments the MR increases substantially in the vicinity of the Verwey transition and the MR anisotropy develops at the same time. The increase in MR at the Verwey transition is not unusual and is

reported by several other researchers in thin films and bulk single crystal of magnetite [7,8, 21]. To explain the presence of MR peak in the vicinity of Verwey transition, Girdin and co-workers [24] used the established facts regarding the transport in Fe_3O_4 and thermodynamic arguments related to the Verwey transition. Tracing the discontinuous changes in enthalpy and entropy with resistivity, they proposed that the jump in MR can be described as $\varphi^* = \Delta\mathbf{M}\mathbf{H}/k_{\text{B}}\delta\mathbf{T}_{1/2}$, where $\Delta\mathbf{M}$ is the change in magnetization across \mathbf{T}_{v} and $\delta\mathbf{T}_{1/2}$ is the full-width at half maximum of the MR peak at \mathbf{T}_{v} . They correlated the MR peak amplitude with the discontinuous changes in magnetization (0.1% decrease) and the width of transition. Small decreases in magnetization could be related to the partial condensation of optical phonon modes. In a recent report, Ogale et al.[8] has reported the presence and absence of MR peak in magnetite thin films of (100) and (111) orientations respectively. Their data emphasize the role of strong electron-phonon coupling and polaronic correlation effects in context of the carrier transport in Fe_3O_4 . These observations explain the gross feature of temperature dependence in our case, but not the difference in the magnitude of MR for two directions reported here. As discussed below, the observed results can be explained by the anisotropy in magnetoelastic properties of the films induced by the presence of APBs and the subsequent modifications to the polaronic states.

For a start we should point out that the Verwey transition in our films is of the first order as indeed expected for stoichiometric magnetite. This is confirmed by the presence of the hysteresis in the temperature dependencies of magnetisation and resistivity. In our study (see chapter 4 for details) we have shown that the presence of APBs affects the elastic property of the films and enables them to maintain a fully strained state up to thickness much greater than those estimated from the mismatch strain, as there is compressive strain at the domain boundaries. Because of the highly directional nature of step edge induced APBs in the films grown on vicinal substrates the elastic properties of the film will be anisotropic. This suggests that the magnetoelastic response of these films will depend on the relative orientation of the magnetic field and step edges. Therefore, the magnetostriction anisotropy will cause distinctly different modifications of internal stress and correspondingly the phonon spectra for the two directions: along and perpendicular to the step edges. In

addition to anisotropic elastic properties, the structural disorder associated with the APB modifies the cationic coordination and affects the nearest- and next nearest- neighbour Coulomb interactions energies that are responsible for the short- and long- range ordering of carriers.

Given the magnetoelastic coupling, the application of a magnetic field will affect the coupled phonon-magnon modes as well as the nearest- and next-nearest neighbour interactions energies differently along the two directions. Consequently, this alters the electron-phonon coupling and broadens the polaronic bands in an anisotropic way that directly affects the formation of a charge ordered state. The polaronic hopping energy, which is proportional to the inverse square of the optical phonon frequency will be affected by the application of a magnetic field via coupled phonon-magnon modes. Decrease in activation energy across the step edges in our case reflects the softening of magnon modes and correspondingly the phonon-magnon modes due to the applied magnetic field. Moreover, the variations in mismatch strain due to differences in the thermal expansion coefficients of Fe_3O_4 and MgO and strain associated with the cubic-monoclinic structural phase transition at the Verwey temperature will also have an influence on the charge ordering process. In light of above suggestions, the application of a magnetic field will suppress the formation of a charge ordered state across the step edges to a greater extent than along them leading to a larger amplitude of MR across the step edges. The above physical picture explains qualitatively the observed anisotropy in the MR peak magnitude, but the precise mechanism is not clear at this time.

The increase in MR with increasing annealing time suggests the formation of sharp atomic step-terrace structure which acts as a template for the formation of APBs with out of plane shifts across the steps. The formation of sharp horizontal Kikuchi lines in the RHEED image after 5 hours of annealing confirms the same. The increase in resistivity difference along and across the step edges with the annealing time and increase in MR anisotropy represents the increased APB density which in turn is related to the surface microstructure of the substrate. Annealing MgO substrates at higher temperatures leads to step-bunching [11, 25]. Our previous analysis suggests that the probability of APB formation is significantly lower if the height of the bunched steps on MgO substrate is an even multiple of monoatomic step height [6]. So the annealing temperature was kept constant at 600°C for all the

substrates. The slight decrease in MR for longer annealing time (13 hours) in Sample D is possibly due to the segregation of impurities like Ca on the surface of MgO. Longer annealing duration and high temperature annealing can cause the segregation of Ca on the surface of MgO substrate [25]. The Ca segregation will give rise to an increase in the stress energy of the surface. To release this energy, steps are found to be bent around the segregated Ca or in other words Ca impurity restricts the azimuth of the step line [26]. The bending of steps around the Ca segregation can greatly hinder the formation of highly directional out-of-plane shifted APBs. The optimum duration of substrate annealing was found to be 5-9 hours at 600°C and 5×10^{-5} Torr oxygen pressure with one hour in UHV prior to the insertion of oxygen.

5.4 Conclusion

In summary, we have observed a strong anisotropy in the MR in close correlation with the direction of current and step-edges in epitaxial Fe₃O₄ films grown on vicinal MgO (100) substrate. Magnetization measurements clearly demonstrate the formation of a greater number of antiferromagnetically coupled antiphase boundaries due to the presence of step edges in the vicinal substrate. We describe two mechanisms for the observed difference in MR along two equivalent crystallographic directions on the surface. The first one is based on spin dependent electron scattering along the APBs. The second mechanism suggests a difference in the reduction of magnetisation values along and across the APBs resulting from the difference in magnetoelastic properties. Magnetoresistance properties of epitaxial Fe₃O₄ films on vicinal MgO substrate show a direct dependence on the substrate annealing duration. The increased annealing time (5-9 hours) significantly modifies the surface morphology MgO substrate and in turn provides a better template for the formation of APBs of Fe₃O₄ thin films deposited. Further increase in annealing time (13 hours) leads to a slight decrease in MR which could be due to impurity segregation on the surface.

The increase in the low field MR due to the step induced spin scattering in Fe₃O₄ films is an important result to realize future spin-electronics applications of magnetic nano-structures. We wish to point out that the differences in the values of MR reported for Fe₃O₄ films are linked to the

microstructural properties and strongly depend on the miscut magnitude and direction. Antiphase boundaries are expected to form in various other spinel materials as well as numerous non-spinel films provided the substrate for the epitaxial film growth is chosen correctly. Therefore, we suggest that the observed increase in magnetoresistance is not necessarily limited to magnetite films only. It is likely that magnetoresistance of some other epitaxial films could be enhanced in the same way if the films are grown on vicinal substrates and the pattern of antiphase boundaries with preferential orientation is formed.

Bibliography

- [1] D.T. Margulies, F.T. Parker, M.L. Rudee, F.E. Spada, J.N. Chapman, R.A. Aitchison and A.E. Berkowitz, *Phys. Rev. Lett.* **79**, 5162 (1997) ;
- [2] W.Eerenstein, "Spin-Dependent transport across anti-phase boundaries in Magnetite films" PhD thesis (2003)
- [3] D. T. Margulies, F. T. Parker, F. E. Spada, R. S. Goldman, J. Li, R. Sinclair and A. E. Berkowitz, *Phys. Rev. B* **53**, 9175 (1996)
- [4] F.C. Voogt, T.T.M. Palstra, L. Niesen, O.C. Rogojuanu, M.A. Janes and T. Hibma, *Phys. Rev. B* **57**, 8107 (1998).
- [5] X.W. Li, A. Gupta, Gang Xiao and G.Q. Gong, *J. Appl. Phys.* **83**, 7049 (1998).
- [6] W.Eerenstein, T.T.M Palstra, S.S. Saxena, and T. Hibma, *Phys. Rev. Lett.* **88**, 247204(2002).
- [7] M. Ziese, and J. Blythe, *J. Phys. Condens. Matter* **12**, 13 (2000).
- [8] S.B. Ogale, K. Ghosh, R.P. Sharma, R.L. Greene, R. Ramesh and T. Venkatesan, *Phys. Rev. B* **57**, 7823 (1998).
- [9] G. Mariotto, S. Murphy and I.V. Shvets, *Phys. Rev. B* **66**, 245426 (2002)
- [10] I.V. Shvets, G. Mariotto, K. Jordan, N. Berdunov, R. Kantor and S. Murphy, *Phys. Rev. B* **70**, 155406 (2004)
- [11] S.L. King, M.R. Wilby and I.W. Boyd, *Mater.Sci. Eng. B* **37** 162(1996)
- [12] S.L King, L.G. Coccia and I.W. Boyd, *Appl. Surf. Sci.* **86** 134.(1995)
- [13] M.Ziese, R. Hohne, H.C. Semmelhack, K.H. Han, P. Esquinazi and K.Zimmer, *J. Magn. Magn. Mat.* **279**, 331 (2004).
- [14] W.Braun, *Applied RHEED: Reflection High Energy Electron Diffraction During Crystal Growth*, Springer Tracts in modern Physics (Springer, Berlin, Vol **154** (1999).
- [15] H. Abe, M. Kanemura, T. Egawa, Y. Nabetani, T. Kato and T matsumoto, *J. Cryst.Growth* **241/215**,595(2000)
- [16] S K Arora, R.G.S Sofin and I.V Shvets, *Phys. Rev. B*, **72**,134404 (2005)
- [17] M.Ziese, R. Hohne,N.H Hong, J. Dienelt, K. Zimmer and P.Esquinazi, *J. Magn. Magn. Mat.* **242-245**, 450 (2002).
- [18] A. Bollero, M.Ziese, P.Esquinazi, k. Dorr and I. Monch, *J. Magn. Magn.*

- Mat. **290-291**, 1134 (2005).
- [19] M. Julliere, Phys. Lett. **54A**, 225 (1975).
- [20] M. Sussiau, F. Nguyen-Van-Dau, P. Galtier and A. Schuhl, Appl. Phys. Lett. **69**, 857 (1996).
- [21] J.E. Evetts, M.G. Blamire, N.D. Mathur, S.P. Isaac, B.S. Teo, L.F. Cohen and L. macmanus-Driscoll, Phil. Trans. R. Soc. Lond. A **356**, 1593 (1998).
- [22] S.K. Arora, R.G.S. Sofin, A. Nolan and I.V. Shvets, J. Magn. Magn. Mat. **286**, 463 (2005).
- [23] Y. Zhou, X. Jin and I.V. Shvets, J. Magn. Magn. Mat. **286**, 346 (2005).
- [24] V.V. Gridin, G.R. Hearne and J.M. Honig, Phys. Rev. B. **53**, 15518, (1996).
- [25] K. Fukui and Y. Iwasawa, Surf. Sci. **441**, 529 (1999).
- [26] H. Ota, K. Sakai, R. Aoki, N. Ikemiya and S. Hara, Surf. Sci. **150**, 357-358 (1999).

Chapter 6

Strain relaxation behaviour and magnetotransport properties of (110) oriented Fe_3O_4 thin films

6.1 Introduction

Fe_3O_4 (110) epitaxial films, grown on MgO (110) substrates, are extensively used as a pinning layer in spin valves like Co/Cu/Co/ Fe_3O_4 structures and as a bottom electrode in tunnel junctions like CoFe/AlO_x/ Fe_3O_4 trilayer structures [1,2]. Since the magnetic easy axis and hard axis lie along $\langle \bar{1}10 \rangle$ and $\langle 001 \rangle$ directions on the surface plane, the MR properties are expected to show different trends due to the difference in the magnetization (M) curves. Previous reports on MS and MR behaviour of Fe_3O_4 (110) epitaxial films grown on MgO(110) substrate, show a sharp rectangular magnetic hysteresis loop when field is applied along $\langle \bar{1}10 \rangle$ easy axis and 0.65% MR at 120°C (Verwey temperature T_v) with an applied field of 0.1 Tesla [3]. To our knowledge there are no detailed reports on the comparison of MR measured along $\langle \bar{1}10 \rangle$ and $\langle 001 \rangle$ direction in (110) oriented Fe_3O_4 thin films. Previous reports on Fe_3O_4 /MgO (110) hetero epitaxial systems show that films are fully strained [1-4].

In this chapter, we present a detailed study of strain relaxation behaviour and crystallographic direction dependence of MR in (partially strain relaxed) Fe_3O_4 (110) films having different thickness grown on MgO (110) substrates. The high resolution X-ray diffraction studies show that films are partially strain relaxed. MR studies as a function of temperature and thickness

on these films reveal that the field dependency of MR shows drastically different features when measured with current and field along $\langle \bar{1}10 \rangle$ and $\langle 001 \rangle$ directions. MR along the $\langle 001 \rangle$ direction is found to be higher than MR measured along the $\langle \bar{1}10 \rangle$ direction and also MR values reported for Fe_3O_4 films at 1 Tesla field apart from films deposited on vicinal MgO substrates (see chapter 5). The observed anisotropy in MR behaviour of Fe_3O_4 films is related to the strain relaxation status of the film, antiphase boundaries (APBs) and magnetocrystalline anisotropy of Fe_3O_4 films.

6.2. Experiment

The Fe_3O_4 thin films (thickness:20-200nm) were grown on (110) oriented MgO single crystal substrates (cut along $\langle 110 \rangle$ direction within $\pm 0.5^\circ$) using oxygen plasma assisted molecular beam epitaxy, MBE, system (DCA MBE M600). The growth details can be found in the previous chapters. Reflection high energy electron diffraction, RHEED, was used to monitor the growth mode and growth rate (0.3 \AA/s).

Magnetization measurements were performed using an alternating gradient field magnetometer (Micromag-3900, Princeton Measurements, USA) with a sensitivity of 10^{-8} emu. The magnetization verses field (M-H) loops were measured at room temperature by applying the magnetic field (maximum field of 1 Tesla) in the film plane along the $\langle 001 \rangle$ direction and $\langle \bar{1}10 \rangle$ directions. The low temperature magnetization measurements were carried out using a Quantum Design MPMS-XL SQUID magnetometer. Room temperature Raman spectroscopy was performed in the backscattering configuration using Rainshaw 1000 Micro Raman system. The Ar^+ ion laser (514.5 nm) was used for the Raman measurements.

Structural characterization of Fe_3O_4 thin films was done using a multi-crystal high-resolution x-ray diffractometer, HRXRD (Bede-D1, Bede, UK). The HRXRD in double or triple axis configuration was performed to confirm the epitaxial relationship of the $\text{Fe}_3\text{O}_4/\text{MgO}$ hetero-epitaxy. The out-of-plane (\mathbf{a}_\perp) lattice parameter was determined from the analysis of ω - 2θ scans measured around the symmetric (220) diffraction planes common to the substrate and thin film. Since the (110) surface is of lower symmetry with two lattice parameters ($\mathbf{d}_{001} = \mathbf{a}_{\text{Fe}_3\text{O}_4}$ and $\mathbf{d}_{110} = \sqrt{2}\mathbf{a}_{\text{Fe}_3\text{O}_4}$) orthogonal to each other,

asymmetric scans were performed on two different in-planes to find the in-plane lattice constants. The in-plane lattice constant of thin film $a_{\parallel} = d_{001}$, was measured by performing asymmetric scans on (222) and (444) diffraction planes of the substrate and thin film and $a_{\parallel} = d_{110}$, was measured by performing asymmetric scans on (400) and (800) diffraction planes of the substrate and thin film.

For electrical resistivity and magneto-resistance measurements a standard dc-four probe technique was employed. The sample was mounted on a copper block fitted onto a cold finger of the closed cycle refrigerator. Temperature of the sample stage was monitored using a GaAlAs thermometer and controlled within ± 0.05 K. For magneto-transport measurements, the cold finger was inserted into an electromagnet (Bruker, Germany, Model:B-E10V). Using this magnet it was possible to vary the field strength maximum up to 1 Tesla. Orientation of the magnetic field in a desired direction was set by rotating the sample stage. The magnetoresistance results reported here were obtained by keeping the direction of magnetic field and current parallel to each other unless otherwise stated. The MR is defined as; $MR\% = [R(H) - R(0)/R(0)] * 100$, where $R(H)$ and $R(0)$ are the resistances of the sample with and without field respectively. To determine the magnetoresistance anisotropy, the measurements were carried out by passing current in two directions, which are orthogonal to each other i.e. along $\langle 001 \rangle$ and $\langle -110 \rangle$ directions.

6.3 Results and discussion

6.3.1 RHEED measurements

Figures 6.1(a) and (b) show the RHEED pattern of the MgO (110) single crystalline substrate measured along the $\langle 001 \rangle$ and $\langle \bar{1}10 \rangle$ azimuths respectively, after following the cleaning procedure described in the experimental section. It shows vertical lattice rods and radial Kikuchi lines indicative of a well ordered and flat surface.

Figures 6.1(c) and (d) show the RHEED pattern after the growth of 200 nm thick Fe_3O_4 thin film measured along the $\langle 001 \rangle$ and $\langle \bar{1}10 \rangle$ azimuth respectively. The appearance of half order streaks was accompanied by the oscillations in the intensity of secularly reflected beam. The period of oscillation corresponds to the growth rate 0.3 \AA/s and confirms that the film

growth occurs in a layer-by-layer mode. Figures 6.2 (a) and (b) show the RHEED pattern after the growth of 20 nm thick Fe_3O_4 thin film measured along the $\langle 001 \rangle$ and $\langle \bar{1}10 \rangle$ azimuth respectively.

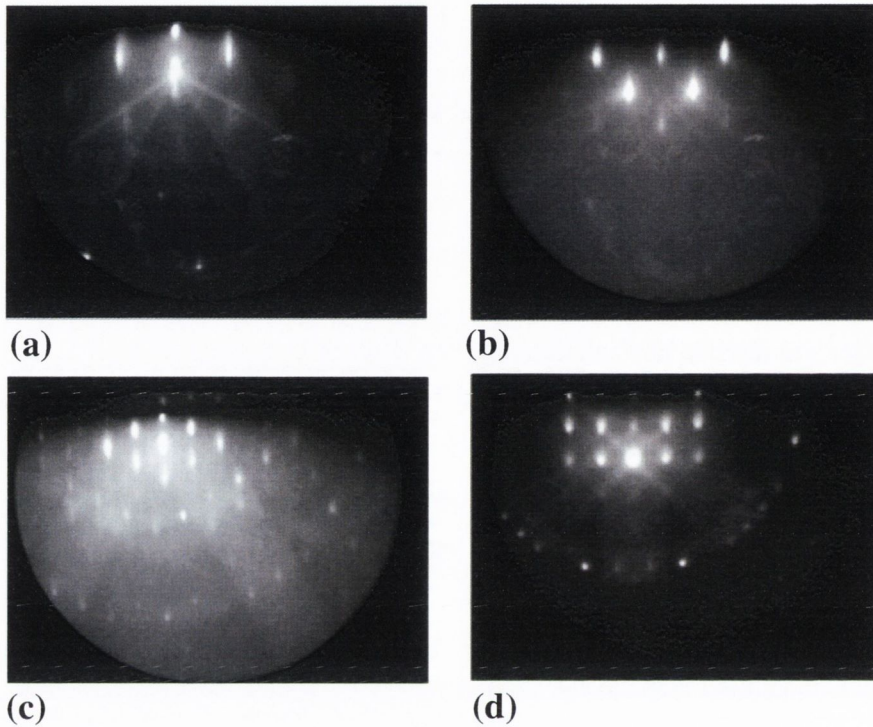


Figure 6.1 RHEED pattern of (a) MgO substrate with electron beam directed along $\langle 001 \rangle$ azimuth (b) along $\langle \bar{1}10 \rangle$ azimuth (c) and (d) after the growth of 200 nm thick Fe_3O_4 film along $\langle 001 \rangle$ and $\langle \bar{1}10 \rangle$ azimuths respectively.

6.3.2 Raman spectroscopy

Room temperature Raman spectroscopy was performed in order to ascertain the Fe_3O_4 phase. The excitation wavelength used was 514.5 nm from an Ar^+ ion laser (Laser Physics Reliant 150 Select Multi-Line) with maximum power of ~ 10 mW (Although ~ 3 mW power was used for the measurements in order to avoid excessive heating and oxidation).

The magnetite thin films grown on MgO (110) substrate showed Raman shifts corresponding to the Fe_3O_4 phase. Figure 6.2 shows Raman shifts observed for Fe_3O_4 films having various thicknesses grown on MgO substrate and the results are tabulated in Table.6.1. The most intense Raman peak is

shifted to lower wave number position in comparison with the values observed for bulk

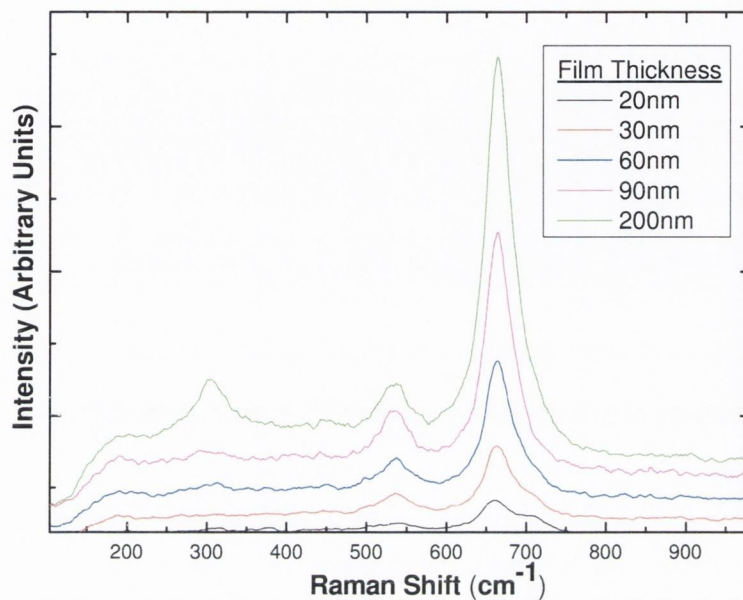


Figure 6.2 Raman shifts observed for Fe_3O_4 (110) films having various thicknesses grown on MgO (110) substrate. Curves are shifted on the vertical axis for clarity.

Sample	Raman Shift (cm^{-1})			
		($\pm 0.01\text{cm}^{-1}$)		
Bulk Fe_3O_4	670	FWHM	540	308
20 nm Fe_3O_4	661.92	36.27	534	311
30 nm Fe_3O_4	662.42	39.14	536	
60 nm Fe_3O_4	664.05	33.94	536	308
90 nm Fe_3O_4	664.45	33.33	534	302
200 nm Fe_3O_4	664.99	32.69	534	305

Table 6.1 Raman shifts observed for Fe_3O_4 (110) films having various thicknesses grown on MgO (110) substrate.

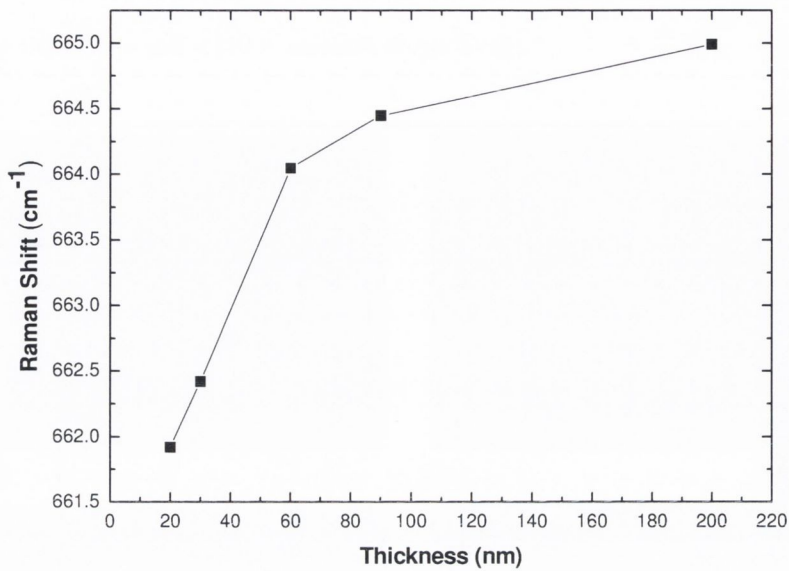


Figure 6.3 Variation of most intense Raman peak position with thickness.

single crystal of Fe_3O_4 (which are 670, 540 and 308 cm^{-1} ($\pm 0.01\text{cm}^{-1}$)) for films having small thickness and as the thickness increases the values are shifting towards the bulk values. Figure 6.3 shows the variation of most intense peak position with thickness. No Raman peaks corresponding to the other iron oxide phases were present. This result suggests the occurrence of strain relaxation with increasing film thickness. There is a shoulder in the most intense peak of 20 and 30 nm film which could arise from the oxidation of the film. Raman measurements therefore confirm that the films are magnetite and indicate the presence of strain relaxation within the film.

6.3.3 HRXRD measurements

Figure 6.4 shows the reflectivity scans of Fe_3O_4 films grown on MgO (110) substrates with different thickness. The thicknesses measured from the scans are 20, 30, 60, and 90 nm ($\pm 2\text{nm}$). The thickness values determined from reflectivity measurements are in good agreement with t estimated from observed growth rate from RHEED intensity oscillations. Figure 6.5 shows the ω - 2θ scans (measured in triple-axis configuration at room temperature) for the

(220) and (440) symmetric Bragg reflections of MgO and film respectively for different thickness (20-200 nm) Fe_3O_4 films. The horizontal axis in the

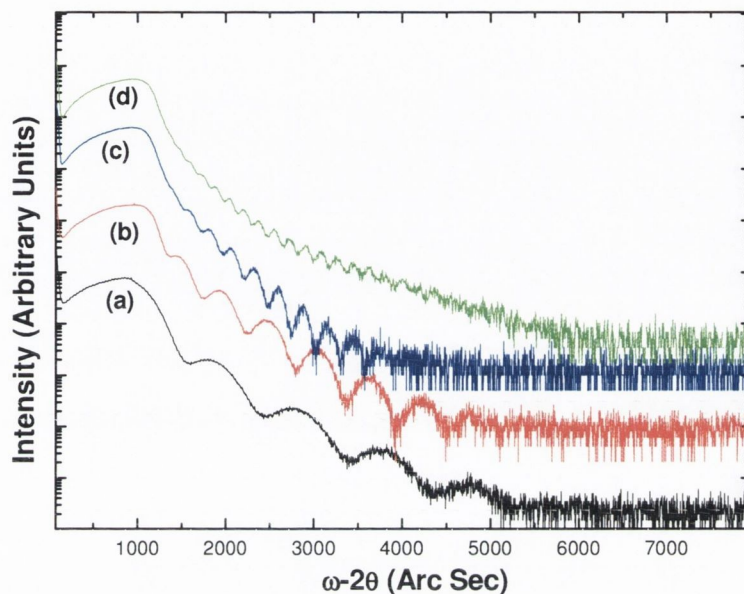


Figure 6.4 The reflectivity scans for of Fe_3O_4 films grown on MgO (110) substrates with thickness (a) 20 nm (b) 30 nm (c) 60 nm and (d) 90 nm.

figure is shown with reference to the Bragg angle of the (220) reflection for the MgO substrate. The curves are shifted along the vertical axis for clarity. The bottom and top most curves belong to 20 nm and 200 nm thickness respectively. The full width at half of maximum (FWHM) of the film peak was found to decrease with increasing film thickness. The FWHM for film peak was found to be 0.34, 0.19, 0.099, 0.056 and 0.0249° for 20 nm, 30 nm, 60nm, 90nm and 200 nm thick films respectively. The value of a_{\perp} for the Fe_3O_4 thin films was determined from the separation of film-substrate peaks and was found to be increasing with increasing film thickness. Figure 6.6 shows the variation of a_{\perp} with thickness. Independent ω -rocking curves for film and substrate peaks indicated that the mosaic spread in the Fe_3O_4 thin films was comparable to that of the substrate.

The ω - $n\theta$ scans (measured in double axis configuration at room temperature) for the (222) and (400) asymmetric Bragg reflections of MgO which is common to the (444) and (800) reflections of the Fe_3O_4 film, in

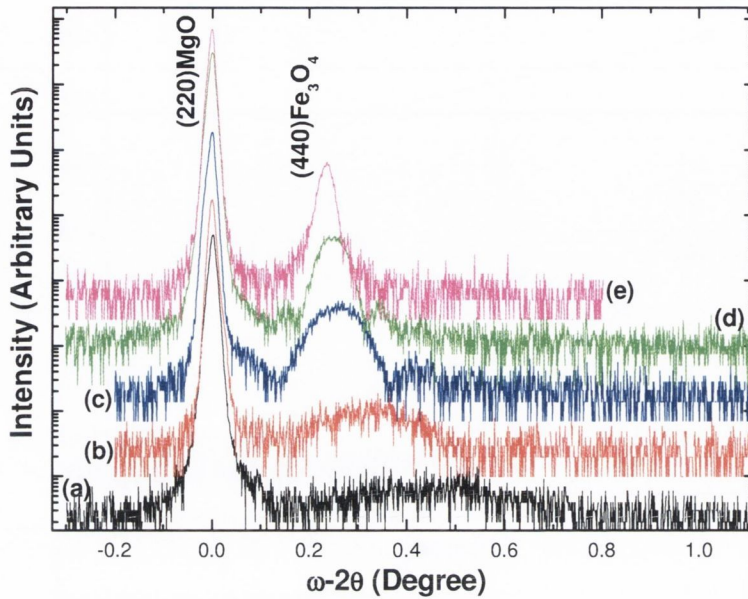


Figure 6.5 The ω - 2θ scans for Fe_3O_4 films with different thickness on MgO (110) substrates, measured for symmetric (220) Bragg reflection common to substrate and thin film. Curves **a**, **b**, **c**, **d** and **e** corresponds to 20, 30, 60, 90 and 200 nm film thickness respectively. Curves are shifted on the vertical axis for clarity.

grazing exit geometry ($\omega_{222}=74.562147$, $2\theta_{222}=78.59$ and $\omega_{400}=91.9985$, $2\theta_{800}=93.997$), are shown in Figures 6.7 and 6.8 respectively. In the (222) grazing exit scans, the FWHM for film peak was found to be 0.047 , 0.0128 , 0.009 and 0.00688° for 30 nm, 60nm, 90nm and 200 nm thick films respectively and in the (400) grazing exit scans, FWHM for film peak was found to be 0.0089 , 0.0057 , 0.00518 and 0.00367° for 30 nm, 60nm, 90nm and 200 nm thick films respectively. The FWHM for the substrate peak in (222) grazing exit scans was 0.0058° and for (200) grazing exit scans it was 0.0032° .

In addition to grazing exit (GE) geometry, asymmetric scans were also performed using grazing incidence (GI) geometry. From the analysis of GE and GI asymmetric scans we obtained the in-plane lattice parameters of the films in two orthogonal directions ($\langle 001 \rangle$ and $\langle \bar{1}10 \rangle$). The a_{\parallel} was found to be 1.19160 ($\langle \bar{1}10 \rangle$) and 0.8426 nm ($\langle 001 \rangle$) for 30nm film, within the experimental accuracy, exactly twice the substrate lattice constant. For all other films the a_{\parallel} is found to be decreasing and approaching towards the bulk value, with increasing thickness.

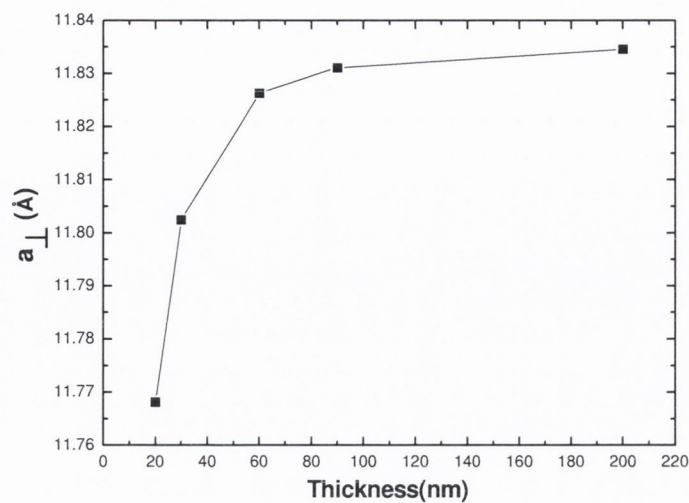


Figure 6.6 Variation of out of plane lattice constant (a_{\perp}) with thickness.

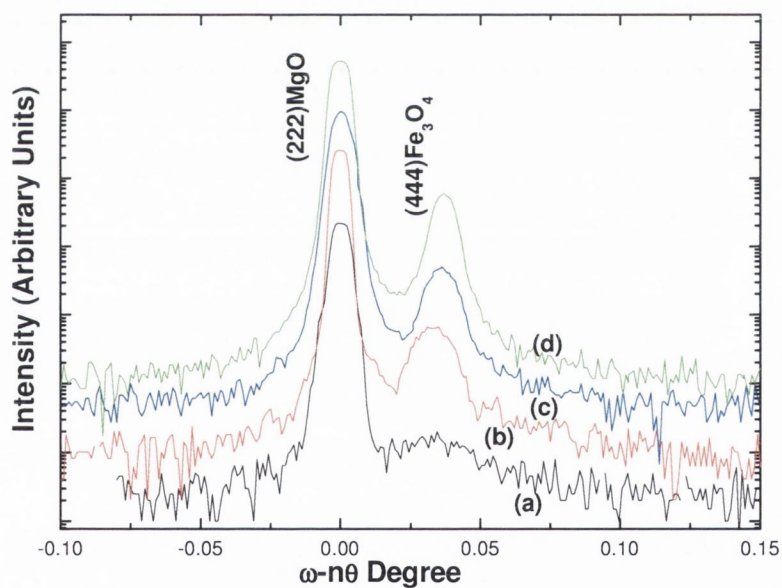


Figure 6.7. The ω - ν scans for Fe_3O_4 films with different thickness on MgO (110) substrates, measured for asymmetric (222) Bragg reflections common to substrate and thin film. Curves **a**, **b**, **c** and **d** correspond to 30, 60, 90 and 200 nm film thickness respectively. For asymmetric (222) Bragg reflection measurements, the grazing exit geometry was used. Curves are shifted on the vertical axis for clarity.

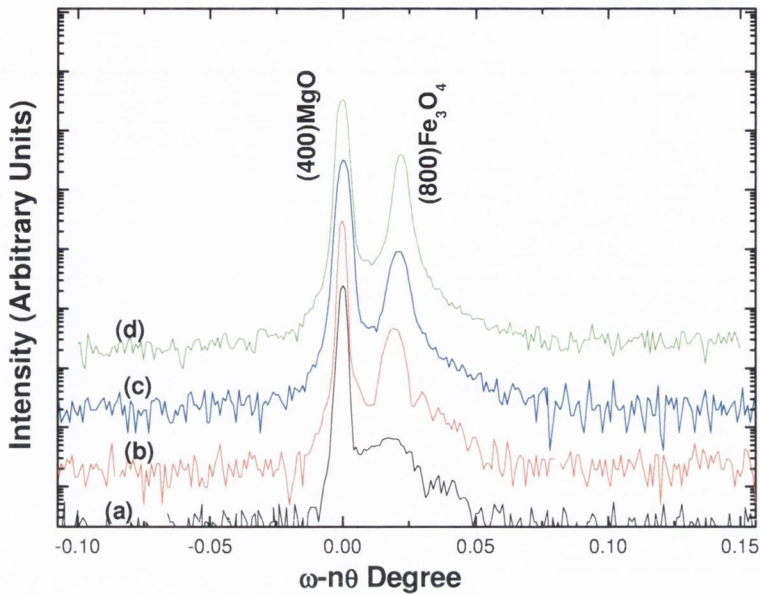


Figure 6.8. The ω - $n\theta$ scans for Fe_3O_4 films with different thickness on MgO (110) substrates, measured for asymmetric (400) Bragg reflections common to substrate and thin film. Curves **a**, **b**, **c** and **d** corresponds to 30, 60, 90 and 200 nm film thickness respectively. For asymmetric (400) Bragg reflection measurements, the grazing exit geometry was used. Curves are shifted on the vertical axis for clarity.

Figures 6.9 and 6.10 show the variation of a_{\parallel} with film thickness along $\langle \bar{1}10 \rangle$ and $\langle 001 \rangle$ respectively. The smaller value of a_{\perp} observed in the case of 20nm film could be due to the oxidation which is also evident from the observation of additional Raman bands. The observed strain relaxation along $\langle 001 \rangle$ direction was 4.83 , 2.76, 0.7 and 0% for 200, 90, 60, and 30nm films respectively. The observed strain relaxation along $\langle 110 \rangle$ direction was 4.29 , 2.35, 1 and 0.39% for 200, 90 60, and 30nm films respectively.

The detailed structural characterization of the Fe_3O_4 films grown on MgO (100) substrates, shows that films undergo strain relaxation above 30nm thickness and the amount of strain relaxation increases with the increase in thickness. The amount of relaxation is found to be 12% and 18% higher in the $\langle 001 \rangle$ direction compared to $\langle \bar{1}10 \rangle$ direction for 200nm and 90nm film and 60 nm thick film showed 30% less relaxation along $\langle 001 \rangle$ direction compared to $\langle \bar{1}10 \rangle$ direction.

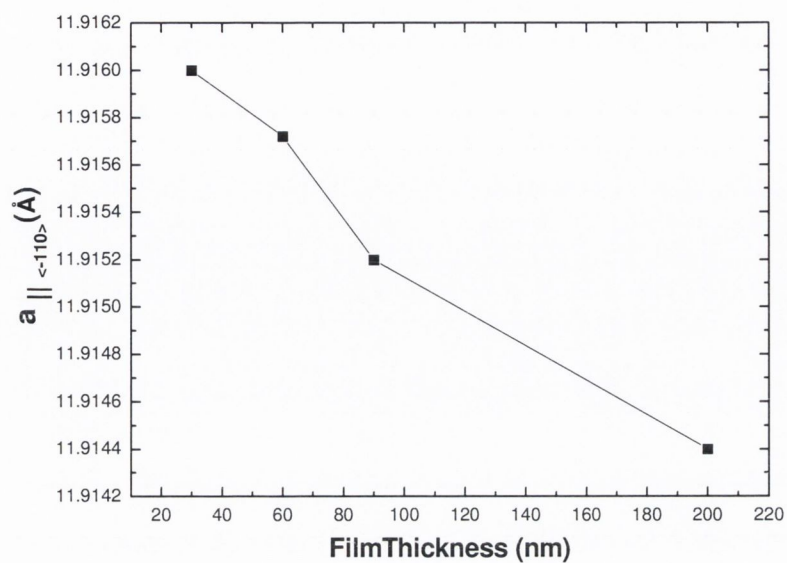


Figure 6.9. Variation of in-plane lattice constant ($a_{||}$ along $\langle -110 \rangle$ direction) with thickness.

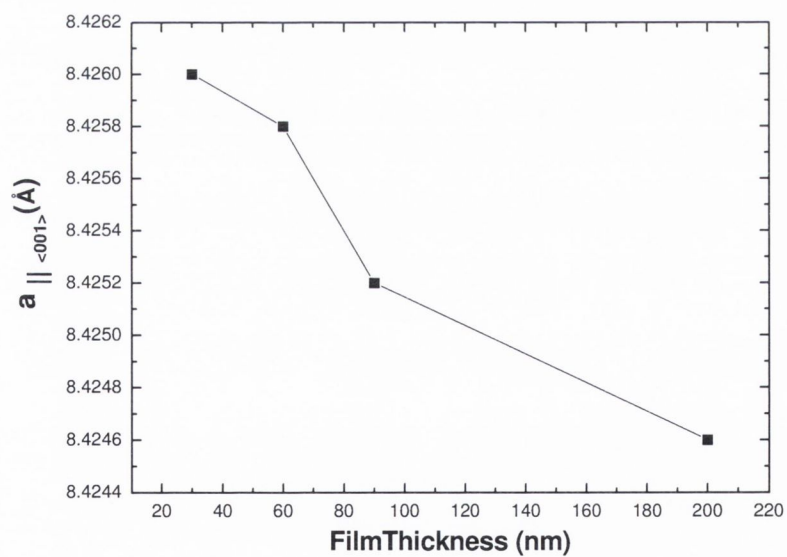


Figure 6.10 Variation of in-plane lattice constant ($a_{||}$ along $\langle 001 \rangle$ direction) with thickness.

6.3.4 Resistivity measurements

The resistivity as a function of temperature was investigated in these films. The Verwey transition temperature was found to be thickness dependent. Figure 6.11 shows variation of resistivity with temperature. The Verwey transition was observed in films with thickness greater than 20nm. Since Verwey transition is very sensitive to the Fe_3O_4 film stoichiometry (see chapter 2), the presence of the Verwey transition confirms that the films are stoichiometric. The absence of Verwey transition for a 20 nm film is in line with the previous reports [5] regarding the observation of no Verwey transition in lower thickness films grown on MgO (100) substrates. Resistivity values for these films were found to decrease with an increase in thickness. For film thickness above 90 nm, the resistivity values didn't show much variation. The resistivity results and Verwey transition temperatures are summarized in Table 6.2.

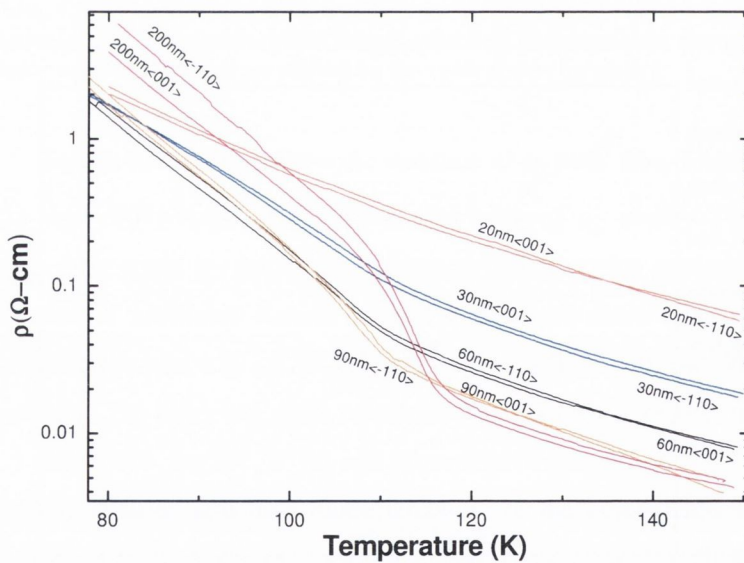


Figure 6.11 Verwey transition observed for Fe_3O_4 films having various thicknesses grown on MgO (110) substrate in $\langle \bar{1}10 \rangle$ and $\langle 001 \rangle$ directions.

Sample	Thickness (nm)	Resitivity at 150 K (Ohm-cm)	Verwey Transition Temperature (K)
Fe ₃ O ₄ /MgO	20	0.064	-----
	30	0.019	108
	60	0.008	109
	90	0.0046	110.6
	200	0.0043	116.2

Table 6.2 Summary of the resistivity values at 300K and Verwey transition temperatures observed for the epitaxial magnetite films as a function of film thickness.

6.3.5 Magnetization measurements

Magnetization measurements were performed on samples with different thickness with magnetic field aligned in $\langle \bar{1}10 \rangle$ and $\langle 001 \rangle$ directions. Figures 6.12, 6.13 and 6.14 show magnetization curves obtained at room temperature for films with various thickness in $\langle \bar{1}10 \rangle$ and $\langle 001 \rangle$ directions respectively. The magnetization curves obtained at room temperature in the $\langle \bar{1}10 \rangle$ direction show an easy axis behaviour and in the $\langle 001 \rangle$ direction show hard axis behaviour, which is in line with the previous reports [4].

Sample	Thickness (nm)	Ms (10kOe) $\times 10^3$ (A/m)	Hc (10kOe) (Oe)
Fe ₃ O ₄ /MgO	20	877	265
	30	623	727
	60	410	550
	90	482	500
	200	481.6	303

Table 6.3 Summary of the saturation magnetization (Ms) and coercivity field for the magnetite films grown on MgO (110) substrates as a function of film thickness, measured along $\langle \bar{1}10 \rangle$ easy axis direction.

Sample	Thickness (nm)	Ms (10kOe) $\times 10^3$ (A/m)	Hc (10kOe) (Oe)
Fe ₃ O ₄ /MgO	20	903	96
	30	608	99
	60	437	91
	90	483	161
	200	467	115

Table 6.4 Summary of the saturation magnetization (Ms) and coercivity field for the magnetite films grown on MgO (110) substrates as a function of film thickness, measured along $\langle 001 \rangle$ hard axis direction.

The Magnetization results obtained from films with various thicknesses are summarised in Tables 6.3. and 6.4. The saturation magnetization of the 200nm film was found to be 480×10^3 A/m in $\langle \bar{1}10 \rangle$ direction and 467×10^3 A/m in $\langle 001 \rangle$ direction and showed very high values for 20 and 30 nm films. A kink was observed in the $\langle \bar{1}10 \rangle$ easy axis magnetization curves which are prominent in lower thickness films and vanishes as thickness is increased.

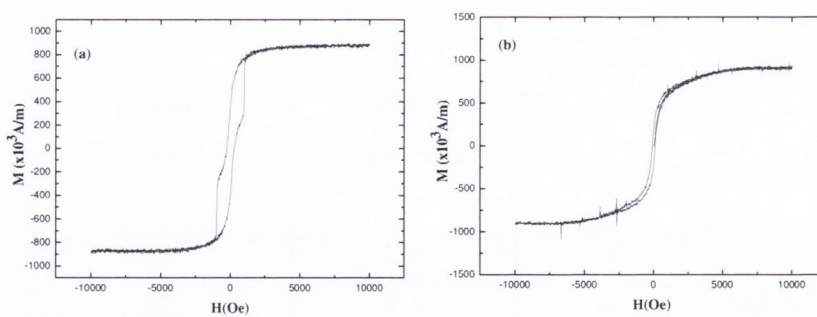


Figure 6.12 Magnetization curve obtained for 20 nm magnetite film grown on MgO (110) substrate with in plane field directed along (a) $\langle -110 \rangle$ and (b) $\langle 001 \rangle$ directions.

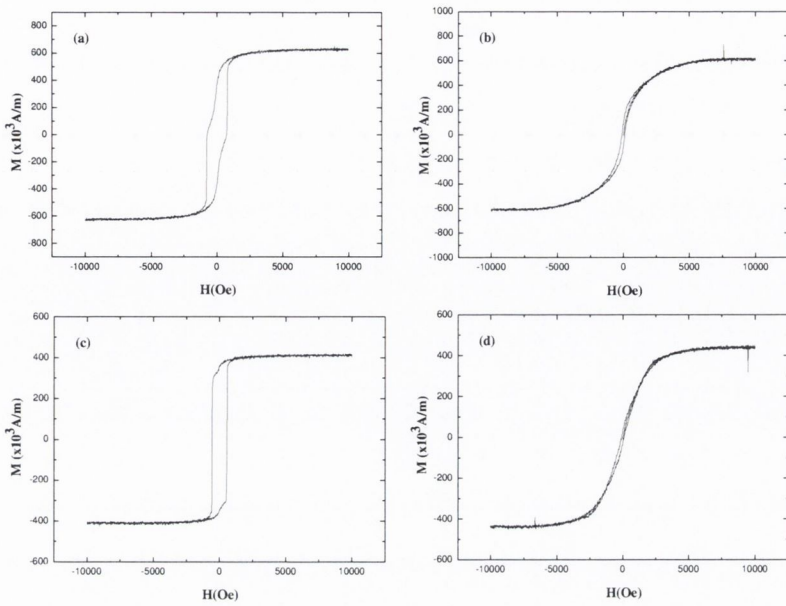


Figure 6.13 Magnetization curve obtained for (a) 30 nm magnetite film grown on MgO (110) substrate with in plane field directed along $\langle \bar{1}10 \rangle$ and (b) $\langle 001 \rangle$ directions (c) 60 nm magnetite film grown on MgO (110) substrate with in plane field directed along $\langle \bar{1}10 \rangle$ and (d) $\langle 001 \rangle$ directions.

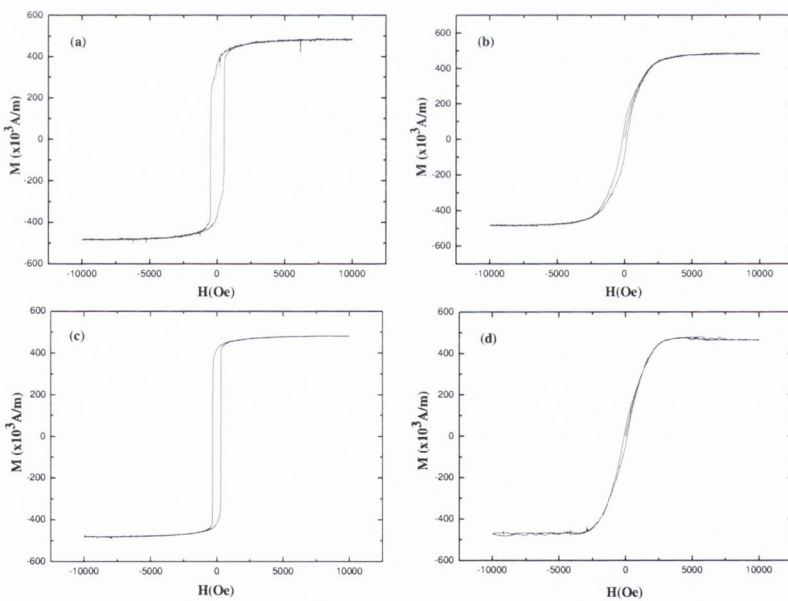


Figure 6.14 Magnetization curve obtained for (a) 90 nm magnetite film grown on MgO (110) substrate with in plane field directed along $\langle \bar{1}10 \rangle$ and (b) $\langle 001 \rangle$ directions (c) 200 nm magnetite film grown on MgO (110) substrate with in plane field directed along $\langle \bar{1}10 \rangle$ and (d) $\langle 001 \rangle$ directions.

6.3.6 Magnetoresistance measurements

Magnetoresistance (MR%) measurements were carried out in an in-plane configuration. The current was directed along the $\langle \bar{1}10 \rangle$ easy axis direction and $\langle 001 \rangle$ hard axis direction. The magnetic field was parallel to the direction of current. Figure 6.15 and 6.16 show the magnetoresistance curves obtained along the $\langle \bar{1}10 \rangle$ direction at different temperatures, for a 200nm and 20nm Fe_3O_4 films respectively. MR% was found to increase with decrease in temperature for both the films. The MR% was found to be maximum at the Verwey transition ($T_v = 116 \text{ K}$) which is 4% for the 200nm film. The MR curves for 200nm film showed maximum resistance at the coercive field (H_c) of the film and a gradual increase in MR with the increase in field was found. For the 20nm film a sharp low field MR (or switching) was observed which was prominent at low temperature. Films with other thickness also showed behaviour similar to the 200nm film.

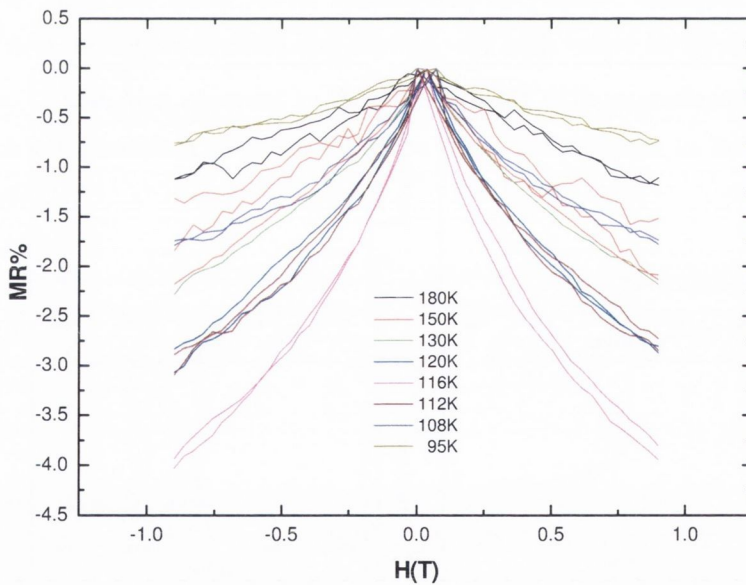


Figure 6.15 Magnetoresistance curves measured at different temperatures for a 200 nm magnetite film grown on MgO (110) substrate with in plane field and current directed along $\langle \bar{1}10 \rangle$ direction.

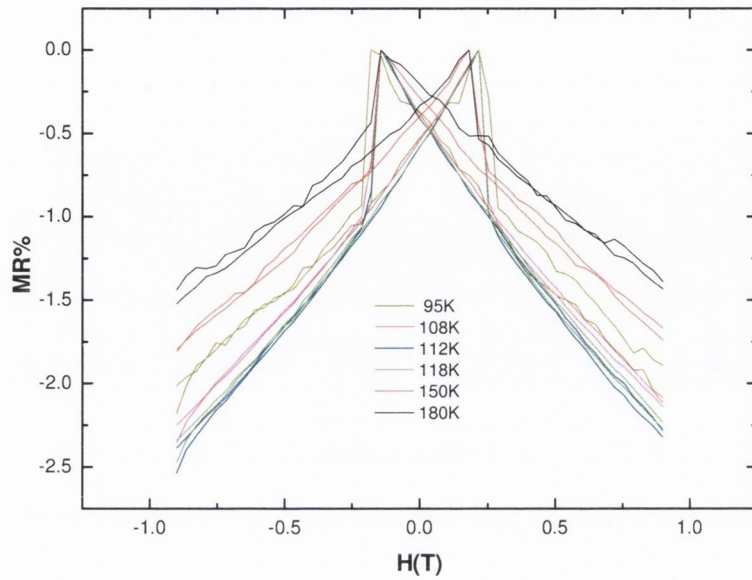


Figure 6.16 Magnetoresistance curves measured at different temperatures for a 20 nm magnetite film grown on MgO (110) substrate with in plane field and current directed along $\langle \bar{1}10 \rangle$ direction.

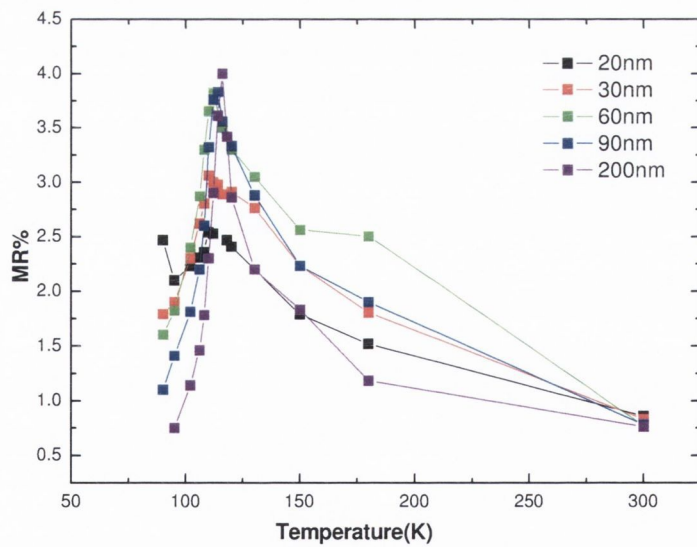


Figure 6.17 MR% observed for magnetite films grown on MgO (110) substrate having different thickness, at 1 Tesla field, as a function of temperature. Magnetic field and current directed along $\langle \bar{1}10 \rangle$ direction.

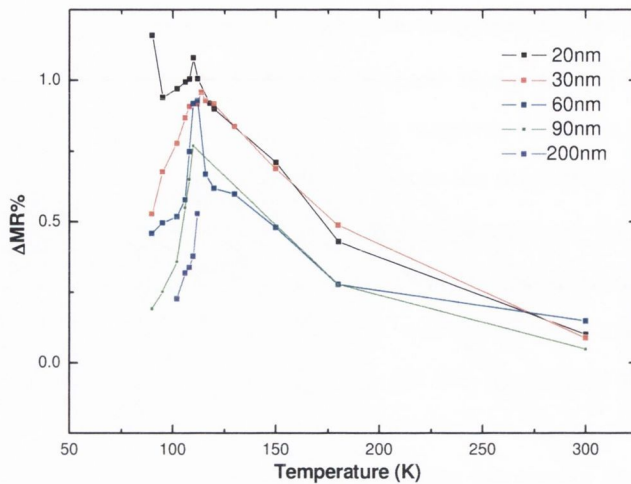


Figure 6.18 $\Delta MR\%$ (width of the switching) observed at the switching field for magnetite films having different thickness grown on MgO (110) substrates, as a function of temperature. Magnetic field and current directed along $\langle \bar{1}10 \rangle$ direction.

The MR% values at 1T field as a function of temperature for films with different thickness are shown in Figure 6.17. MR% near the Verwey transition was found to increase with increase in thickness. The switching effect was prominent for films with lower thickness. The change in MR ($\Delta MR\%$) at the switching field was found to increase with decreasing thickness. Figure 6.18 shows the variation of width of the switching ($\Delta MR\%$), at the switching field, as a function of temperature for films with various thickness. The width of the switching also shows a peak value near the Verwey transition temperature. 20nm film showed 1% ΔMR at 110K and at 0.252 T switching field.

Figures 6.19 and 6.20 show the magnetoresistance curves obtained at different temperatures, for 200nm and 20nm Fe_3O_4 films with field and current directed along $\langle 001 \rangle$ direction. The MR% in $\langle 001 \rangle$ direction at 1T field as a function of temperature for films with different thickness is shown in the Figure 6.21. Similar to the $\langle \bar{1}10 \rangle$ case, MR% was found to increase with decreasing temperature and to peak near the Verwey transition temperature (T_v). MR% was found to increase with thickness.

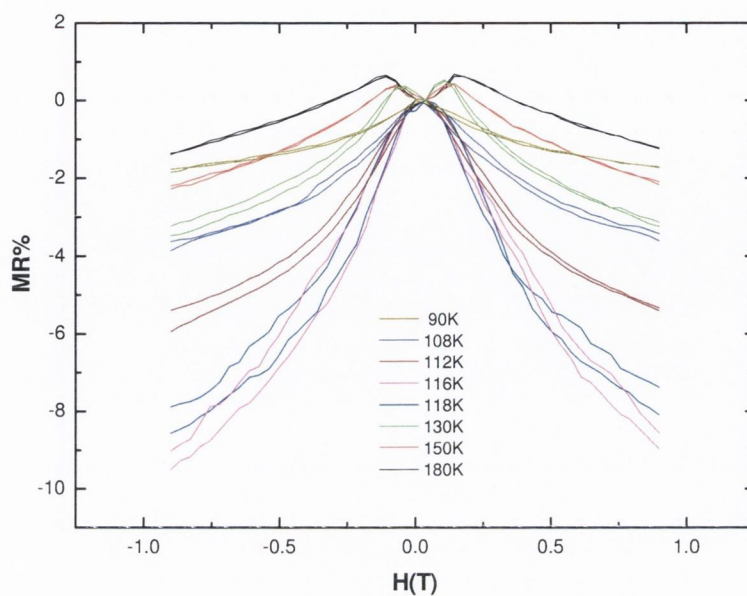


Figure 6.19 Magnetoresistance curves measured at different temperatures for a 200 nm magnetite film grown on MgO (110) substrate with in plane field and current directed along $\langle 001 \rangle$ direction.

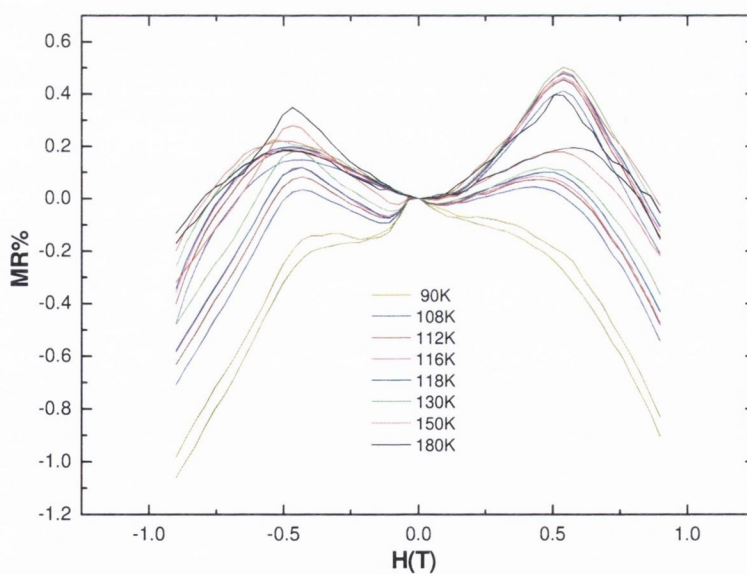


Figure 6.20 Magnetoresistance curves measured at different temperatures for a 20 nm magnetite film grown on MgO (110) substrate with in plane field and current directed along $\langle 001 \rangle$ direction.

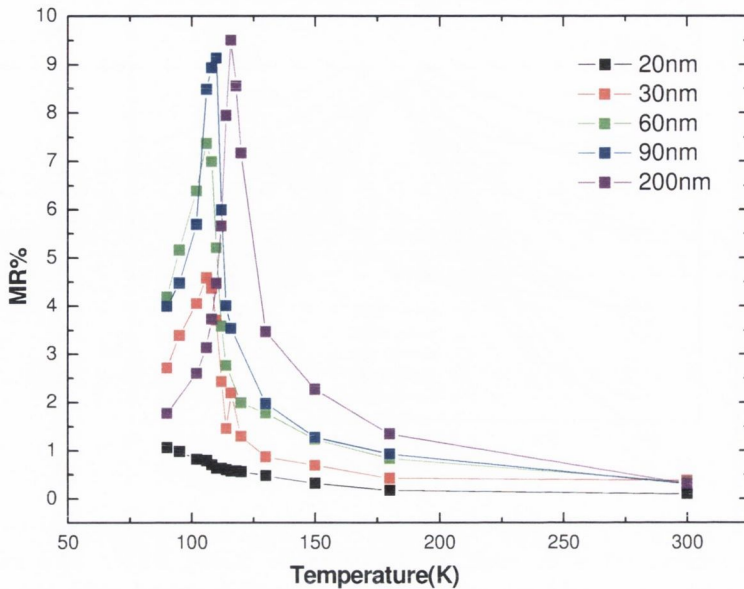


Figure 6.21 MR% observed for magnetite films grown on MgO (110) substrate having different thickness, at 1Tesla field, as a function of temperature. Magnetic field and current directed along $\langle 001 \rangle$ direction.

The 200nm film showed 9.5% MR at the Verwey transition ($T_v = 116$ K). This value of MR% is found to be 5.5% higher compared to MR% measured along $\langle \bar{1}10 \rangle$ direction and to MR values reported for Fe_3O_4 films with various orientations and thicknesses at 1 Tesla field, apart from the films deposited on vicinal MgO substrates [6,7]. Field dependency of MR shows drastically different features compared to the MR along $\langle \bar{1}10 \rangle$ direction. Above Verwey transition temperature MR curves showed a ‘butterfly shape’ with two symmetric peaks arising across the zero field (Figure 6.19 and 6.20). The separation between the peaks decreases as the temperature is lowered and vanishes at the Verwey transition. Figure 6.22 shows the variation of the separation (ΔH) between the symmetric peaks across the zero field. Below the Verwey transition temperature the shape of the MR curves were the same as in the case of MR curves observed in the $\langle \bar{1}10 \rangle$ direction. The separation between the peaks was found to increase with decreasing thickness.

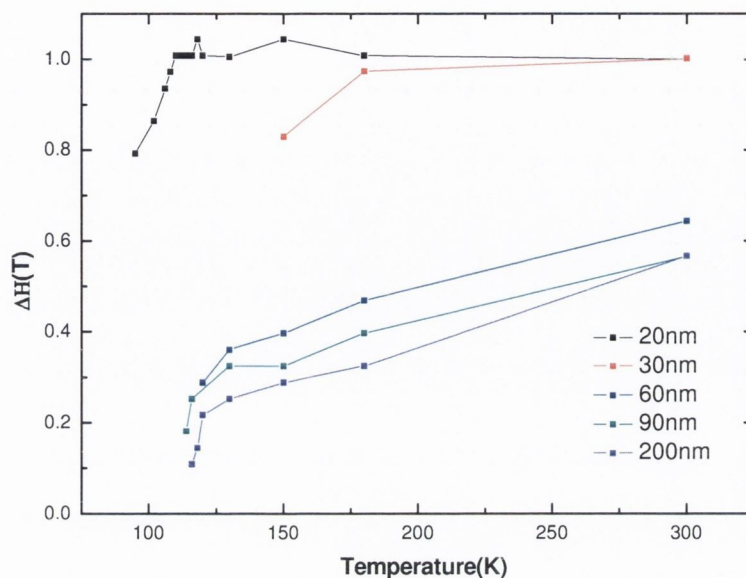


Figure 6.22 Variation of the separation (ΔH) between the symmetric peak values of MR% observed for magnetite films having different thickness grown on MgO (110) substrates, as a function of temperature. Magnetic field and current directed along $\langle 001 \rangle$ direction.

6.3.7 Discussion

From the strain relaxation studies of epitaxial Fe_3O_4 thin films grown on MgO(100) substrates (see chapter 4) we found that the films remain fully coherent up to much greater thickness than predicted by the FKR model (~ 70 nm), whereas the films grown on MgAl_2O_4 (100) substrates show a behaviour consistent with the model predictions. The observed strain relaxation behaviour is attributed to the presence of APBs which form areas within the film that have opposite sign of stress. The stress compensation by the APBs reduces the effective stress experienced by the films. The reduction in effective stress experienced by the film depends strongly on the nature and density of APBs. From the high resolution XRD measurements we found that the Fe_3O_4 films grown on MgO (110) substrates show partial strain relaxation with increasing thickness. APBs are expected to form in the case of Fe_3O_4 films grown on MgO (110) substrates as well. During the layer by layer growth

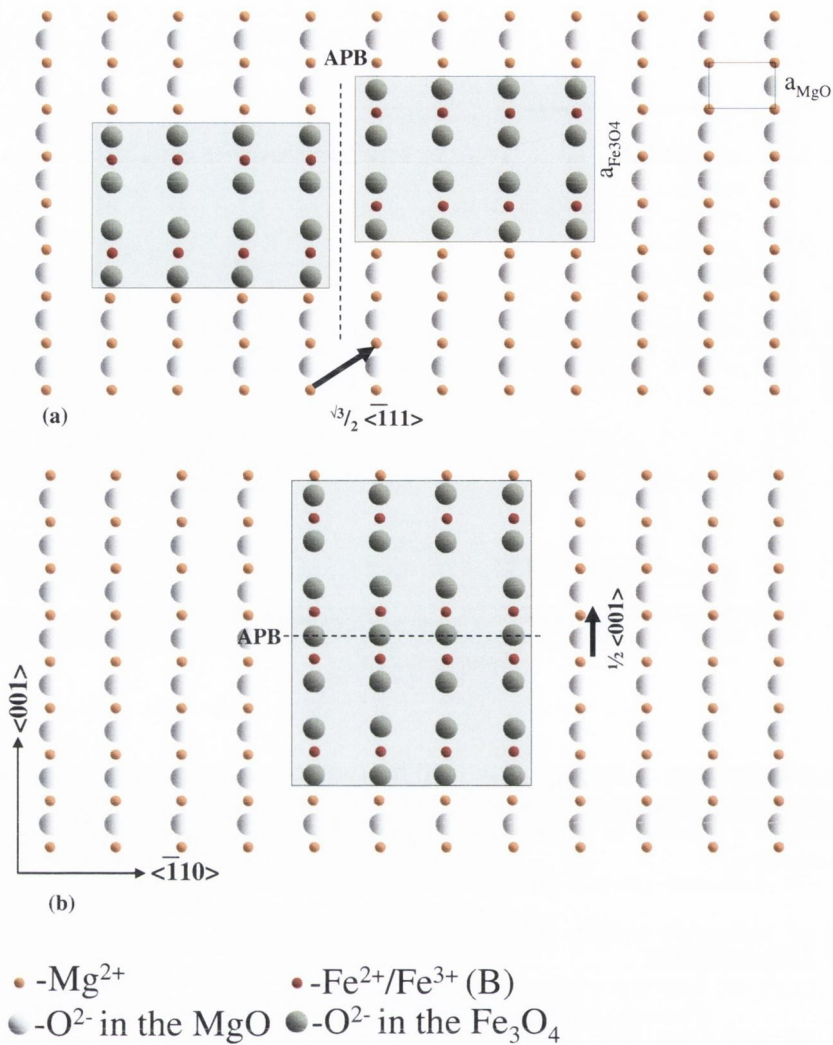


Figure 6.23 Schematic illustration of APB formation with (a) $\sqrt{3}/2 \langle \bar{1}11 \rangle$ shift vector in the $\langle \bar{1}10 \rangle$ direction and (b) by $1/2 \langle 001 \rangle$ shift vector in the $\langle 001 \rangle$ direction for (110) oriented Fe₃O₄ films grown on MgO (110) substrates.

mode, adjacent Fe₃O₄ monolayers may be shifted by $\sqrt{3}/2 \langle \bar{1}11 \rangle$ or $\sqrt{3}/2 \langle \bar{1}\bar{1}\bar{1} \rangle$ shift vectors in the $\langle \bar{1}10 \rangle$ direction and by $1/2 \langle 001 \rangle$ shift vector in the $\langle 001 \rangle$ direction. The islands separated by these shift vectors can eventually form APBs when they coalesce. Figure 6.23 shows the possible APB formation in $\langle \bar{1}10 \rangle$ and $\langle 001 \rangle$ directions. In the case of Fe₃O₄ films grown on MgO (100) substrates the adjacent monolayers can be related with 7 shift vectors ($1/4 \langle 110 \rangle$, $1/4 \langle \bar{1}\bar{1}0 \rangle$, $1/2 \langle 100 \rangle$, $1/4 \langle 101 \rangle$, $1/4 \langle 10\bar{1} \rangle$, $1/4 \langle 011 \rangle$ and $1/4 \langle 01\bar{1} \rangle$) which can form [8-10] APBs whereas there are only 3 possible shift vectors which can give rise to APBs during the growth of

Fe_3O_4 films on MgO (110) substrates. This give rise to 40% more probability for the formation of APBs in the Fe_3O_4 films grown on a MgO (100) oriented substrate than (110) oriented substrate. Therefor we can expect less density of APBs in the case of (110) oriented Fe_3O_4 films compared to (100) orientated films and this difference in density could be one of the reasons for the observed strain relaxation in films grown on MgO (110) substrates and not in MgO(100), although the strain relaxation observed in 200nm film is only 4.83% which is very small compared to 95% relaxation of 120 nm Fe_3O_4 film grown on MgAl_2O_4 .

Magnetization measurement in the $\langle \bar{1}10 \rangle$ easy axis directions shows a kink which was prominent in lower thickness films and vanishes as thickness is increased. These observed kinks could be arising due to the different coercivity values of strained and relaxed volume fractions with in the film. Also there is a possibility of contributions from stoichiometrically different volume fractions in lower thickness films due to the possible oxidation which is evident from the observation of additional Raman Bands in the Raman spectrum and a lower out of plane lattice constant from HRXRD measurements for the 20nm film. The very high values of saturation magnetization in 20 and 30nm films could be arising from the uncompensated magnetic moments in the surface and interface or unquenched orbital moments within the film. Another possibility is the breaking of the strong antiferromagnetic exchange interaction between the Fe^{3+} ions in A site and B site. The exact mechanism is not known at the moment. More detailed magnetic measurements are required to propose a conclusive model.

Magnetoresistance curves obtained in the $\langle \bar{1}10 \rangle$ direction show switching behaviour which is prominent for the films with lower thickness and at low temperature. Figure 6.24 shows the MR curve superimposed with magnetization loop, both measured at room temperature for a 20 nm film. From the figure it is clear that the observed switching is associated with the difference in the coercivity values of strained and relaxed volume fractions or stoichiometrically different volume fractions within the film. As the film thickness increases the kinks in the magnetization curves are found to disappear and MR curves also showed a corresponding decrease in the switching effect.

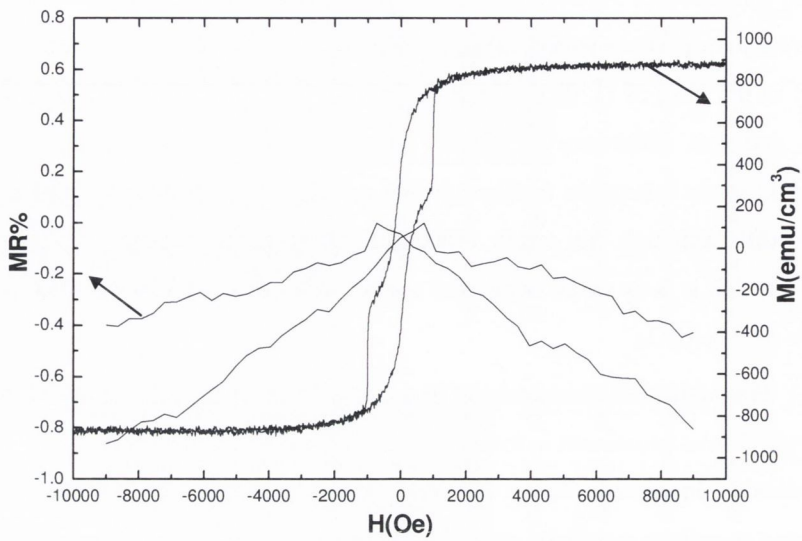


Figure 6.24 Magnetoresistance curve obtained at room temperature for a 20 nm film measured along $\langle \bar{1}10 \rangle$ direction superimposed with Magnetization curve obtained at room temperature with field directed along $\langle \bar{1}10 \rangle$ easy axis. Arrows shows the vertical scale corresponding to the curve.

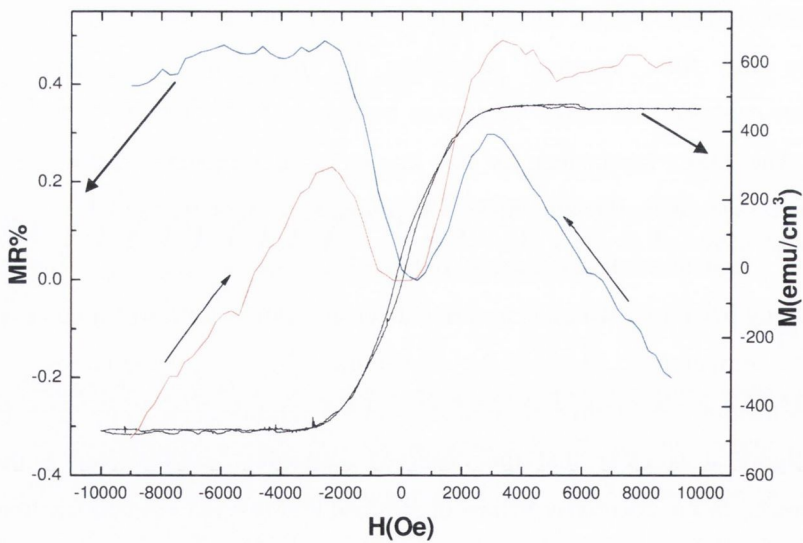


Figure 6.25 Magnetoresistance curve obtained at room temperature for a 200 nm film measured along $\langle 001 \rangle$ direction superimposed with Magnetization curve obtained at room temperature with field directed along $\langle 001 \rangle$ hard axis.

The butterfly shaped magnetoresistance curves obtained above room temperature in the $\langle 001 \rangle$ direction can be explained on the basis of spin orbit coupling. Figure 6.25 shows the MR curve observed at room temperature superimposed with magnetization loop measured at room temperature for a 200nm film. It is evident from the figure that the resistivity maximum is occurring near the anisotropy field (H_A).

To explain this MR behaviour, we need to consider contributions of different factors in to the collective behaviour of MR. The conductivity of Fe_3O_4 is proportional to the square of the transfer integral: $\sigma \propto t^2$. Previous studies have shown that t , depends on the angle between two spins on neighbouring ions [11,12, see chapter 2], which is given by:

$$t = t_0 \cos \frac{\phi}{2} \quad (6.1)$$

where ϕ is the angle between the two spins. In the case of ferromagnetic alignment, the two spins are parallel and the transfer integral has its maximum value t_0 . In the case of anti-ferromagnetic alignment the transfer integral becomes zero. This is the case at the APBs when an anti-ferromagnetic coupling is present. Considering two spin chains separated by an antiferromagnetic boundary with a field along a hard magnetization axis, Eerenstein et al, [13] obtained

$$\cos^2 \phi = \frac{(HM_s)^2}{4KW_{AF}} \quad \text{when } H < H_A \quad (6.2)$$

$$\cos^2 \phi = \frac{HM_s - K}{W_{AF}} \quad \text{when } H > H_A \quad (6.3)$$

where H is the applied magnetic field, M_s is the saturation magnetisation and $W_{AF} = A_{AF}^2 / A_F d^2$ (where A_F is the exchange stiffness constant, A_{AF} is the exchange stiffness constant for the antiferromagnetic exchange interaction at the boundary and d is the distance between two neighbouring spin chains along the boundary). K is the anisotropy constant coming from uniaxial anisotropy energy density term. From Equations 6.2 and 6.3 it is clear that for a field below the anisotropy field, H_A , the conductivity across the antiferromagnetically coupled APB will change quadratically with the field and is approximately linear for higher fields. This implies that the decreasing resistivity will be having a quadratic dependence to the applied field

in the low field regime ($H < H_A$) and a sharp linear variation for high field. Therefore in the low field regime the resistivity contribution from other factors will dominate the resistivity variation due to the spin polarised transport across the antiferromagnetically coupled APBs. Figure 6.26 shows the MR curve observed at 180 K for a 200 nm film with a field and current applied along $\langle 001 \rangle$ hard axis direction. It is clear from the Figure 6.26 that MR after the anisotropy fields (the field at which we observe the resistivity maxima, denoted by case (b) and case (d)) varies approximately linearly with the field. In figure 6.26, MR shows saturation behaviour after crossing the anisotropy field at room temperature. This could be because of the low spin polarization at room temperature which eventually will affect the scattering mechanism across the APBs. The MR contribution of antiferromagnetically coupled APBs in the high field regime will be discussed later in this section. Before that we will discuss the resistivity contributions from other factors which gives a positive MR in the low field. The main contributions to the MR are from anisotropic magneto resistance (AMR), ordinary magneto resistance OMR and Domain wall resistance.

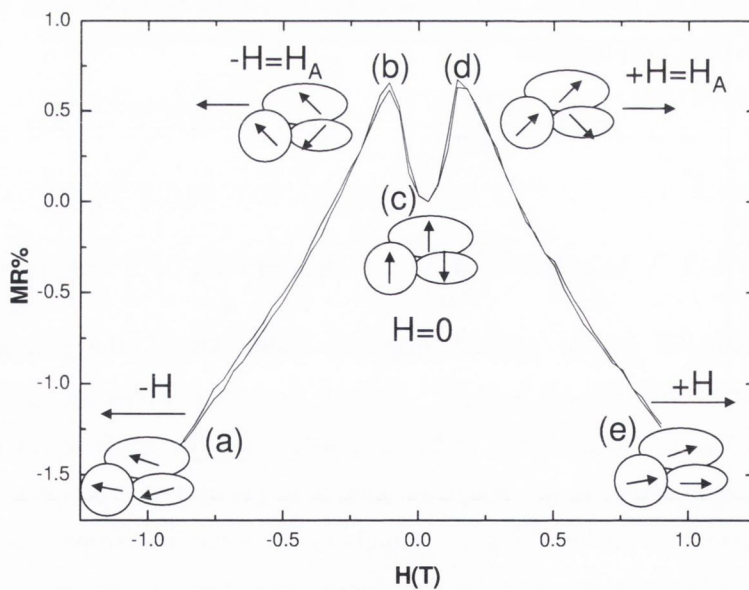


Figure 6.26 Magnetoresistance curve obtained at 180K for a 200 nm film measured along $\langle 001 \rangle$ hard axis direction superimposed with schematic model of magnetized domains.

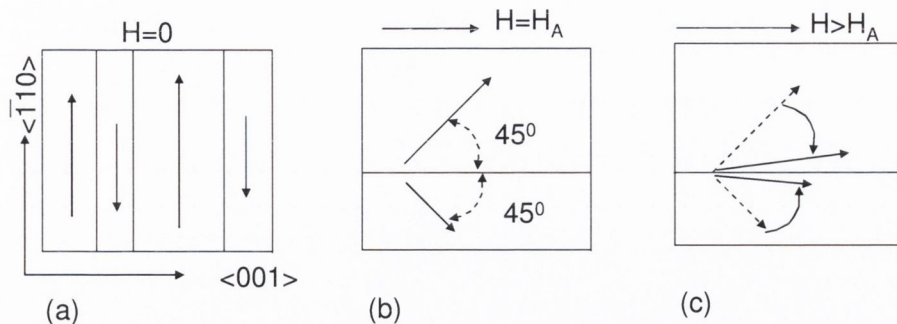


Figure 6.27 Changes in the domain structure during the increase in magnetic field along $\langle 001 \rangle$ hard axis. (a) with zero field (b) at anisotropy field (c) above anisotropy field.

On the (110) oriented Fe_3O_4 film surface, the magnetic hard axis lies along $\langle 001 \rangle$ direction. We can consider different magnetic domains within the film which are aligned in the easy axis direction ($\langle \bar{1}10 \rangle$), when applied field is zero. This is shown in the figures 6.26 and 6.27 as case (c) and case (a), respectively. When the field increases in the hard axis, $\langle 001 \rangle$ direction the domains will merge and try to align in the $\langle \bar{1}11 \rangle$ medium axis direction, which is at an angle 45° with the field and easy axis directions. Therefore at the anisotropy field we can consider mainly two domains with magnetisations separated by 90° . This is shown in Figure 6.26 and 6.27 as case (b) (or (d)) and (b), respectively. After crossing the anisotropy field the magnetisation will rotated towards the applied field along $\langle 001 \rangle$ and will align parallel to the field at saturation field. The case at which the magnetisation is rotated nearly parallel to the field is shown as case (a) (or case (e)) and case (c) in Figures 6.26 and 6.27, respectively. Therefore we can assume that there will be a component of magnetisation directed along the $\langle 001 \rangle$ direction which is the direction of flow of current and applied field. There will be another component directed along the $\langle \bar{1}10 \rangle$ direction which is perpendicular to the direction of current.

The resistivity of a ferromagnet depends on the angle between the magnetization M and the electric current J . This phenomenon is called anisotropic magnetoresistance (AMR) and is caused by the spin-orbit interaction [14-18]. The microscopic origin of electrical transport in ferromagnetic metals was explained on the basis Smit's results of investigations of magnetoresistance in ferromagnetic materials [15]. The starting point of the analysis was the two current model of conduction in

transition metals proposed by Mott [19]. The theory was further refined by Campbell et al., Jaoul et al., Potter and Malozemoff.[20-23]. Even though this theory is developed for metals, still it can be applied in the case of magnetite, which is a strongly correlated metal with significant polaronic effects, because the basic assumptions of the theory is band transport and general characteristics of atomic d states which are fulfilled in magnetite.

In the case of ferromagnetic transition metals like Fe, Co, Ni etc the band structure is split into two different sub-bands representing the different orientations of the electron spins i.e., electrons with magnetic moments parallel or antiparallel to the total magnetisation. When the 3d band is not fully filled, scattering of 4s electrons to the 3d band is probable. The current of 4s electrons with small effective mass m^*_s is predominant compared to the low mobility 3d electrons with large effective mass m^*_d . In Smit's model it was assumed that, due to the magnetic field and spin orbit interaction, there will be an anisotropic mixing of $d(\uparrow)$ and $d(\downarrow)$ states. This mixing depends on the magnetization direction, i.e., the direction of the net spin density. Therefore, the magnetization direction determines the density of unoccupied d states at the Fermi level. This gives rise to a magnetization-direction dependent s-d scattering rate, which dominates the resistance. As a result, the resistivity tensor of a saturated sample is determined by the angle α between the electrical current I and the magnetization M . The AMR is defined as :

$$\left[\frac{\Delta\rho}{\rho} \right]_{\parallel-\perp} = \frac{\rho_{\parallel} - \rho_{\perp}}{\rho_{ave}} \quad (6.4)$$

where $\rho_{ave} = \frac{\rho_{\parallel}}{3} + \frac{2\rho_{\perp}}{3}$ and ρ_{\parallel} and ρ_{\perp} denote the longitudinal ($\mathbf{M} \parallel \mathbf{J}$)

and transverse resistivity ($\mathbf{M} \perp \mathbf{J}$), respectively.

The magnetoresistance of a cubic ferromagnet can be expanded as a series in the direction cosines α_i of the magnetisation and β_i of the current [18].

$$\begin{aligned} \frac{\Delta\rho}{\rho} = & \mathbf{R}_1[\alpha_1^2\beta_1^2 + \alpha_2^2\beta_2^2 + \alpha_3^2\beta_3^2 - 1/3] + 2\mathbf{R}_2[\alpha_1\alpha_2\beta_1\beta_2 \\ & + \alpha_2\alpha_3\beta_2\beta_3 + \alpha_3\alpha_1\beta_3\beta_1] + \mathbf{R}_3[s - c] + \mathbf{R}_4[\alpha_1^4\beta_1^2 \\ & + \alpha_2^4\beta_2^2 + \alpha_3^4\beta_3^2 + 2s/3 - 1/3] \\ & + 2\mathbf{R}_5[\alpha_1\alpha_2\beta_1\beta_2\alpha_3^2 + \alpha_2\alpha_3\beta_2\beta_3\alpha_1^2 + \alpha_3\alpha_1\beta_3\beta_1\alpha_2^2] \end{aligned} \quad (6.5)$$

Where $\Delta\rho$ is the change in resistivity, $s = \alpha_1^2\alpha_2^2 + \alpha_2^2\alpha_3^2 + \alpha_3^2\alpha_1^2$, R_i 's are phenomenological constants and c is a numerical constant depending on the easy axis direction. If the domains are equally distributed among the easy axes then the constant $c=1/4$ for $\langle 110 \rangle$ easy axis and $c=0$ for $\langle 100 \rangle$ easy axis. There are conflicting reports on the easy axis direction of magnetite films published with $\langle 100 \rangle$ easy axes [24, 25] and $\langle 110 \rangle$ easy axis [26]. Our magnetization measurements show that, above the Verwey temperature on (110) oriented Fe_3O_4 thin films the easy axis is along $\langle \bar{1}10 \rangle$, which agrees with ref [3]. Therefore using Equation 6.5, the MR with current in the direction of $\langle 001 \rangle$ direction and magnetisation along $\langle 001 \rangle$ and $\langle \bar{1}10 \rangle$ directions can be written as

$$\left[\frac{\Delta\rho}{\rho} \right]_{\parallel} = \frac{2R_1}{3} - \frac{R_3}{4} + \frac{2}{3}R_4 \quad (6.6)$$

$$\left[\frac{\Delta\rho}{\rho} \right]_{\perp} = \frac{R_3}{4} \quad (6.7)$$

Therefore AMR can be calculated as

$$\left[\frac{\Delta\rho}{\rho} \right]_{\parallel-\perp} = \frac{2R_1}{3} + \frac{2R_4}{3} - \frac{R_3}{2} \quad (6.8)$$

In Mott's two current model the majority (\uparrow) and minority (\downarrow) electrons are assumed to constitute two parallel conduction channels and the associated currents are assigned with resistivities ρ_{\uparrow} and ρ_{\downarrow} , respectively. If spin-flip scattering with resistivity $\rho(\uparrow\downarrow)$ is taken into account, the total resistivity ρ is given by :

$$\rho = \frac{\rho_{\uparrow}\rho_{\downarrow} + \rho_{\uparrow\downarrow}(\rho_{\uparrow} + \rho_{\downarrow})}{\rho_{\uparrow} + \rho_{\downarrow} + 4\rho_{\uparrow\downarrow}} \quad (6.9)$$

If $\Delta\rho_{\uparrow}$ and $\Delta\rho_{\downarrow}$ denote the resistivity changes of the majority and minority channels between the longitudinal and transverse directions, respectively then the AMR can be written as

$$\rho = \frac{\rho_{\uparrow}\Delta\rho_{\downarrow} + \rho_{\downarrow}\Delta\rho_{\uparrow} + \rho_{\uparrow\downarrow}(\Delta\rho_{\uparrow} + \Delta\rho_{\downarrow})}{\rho_{\uparrow}\rho_{\downarrow} + \rho_{\uparrow\downarrow}(\rho_{\uparrow} + \rho_{\downarrow})} - \frac{\Delta\rho_{\uparrow} + \Delta\rho_{\downarrow}}{\rho_{\uparrow} + \rho_{\downarrow} + 4\rho_{\uparrow\downarrow}} \quad (6.10)$$

It is generally found that the resistance changes are a function of the channel resistivities themselves leading to the general expressions [24]

$$\Delta\rho_{\uparrow} = \gamma_{\uparrow\uparrow}\rho_{\uparrow} + \gamma_{\uparrow\downarrow}\rho_{\downarrow} \quad (6.11)$$

$$\Delta\rho_{\downarrow} = \gamma_{\downarrow\uparrow}\rho_{\uparrow} + \gamma_{\downarrow\downarrow}\rho_{\downarrow} \quad (6.12)$$

The coefficients (γ) were calculated by Malozemoff [23] using a simple atomic state model. For majority up spin doublet e_g band and down spin minority t_{2g} triplet band equation 6.11 becomes

$$\Delta\rho_{\uparrow} = -\frac{3}{4}\left[\frac{\lambda^2}{(\mathbf{H}_{\text{ex}} - \Delta_{\text{cf}})^2} - \frac{\lambda^2}{\Delta_{\text{cf}}^2}\right]\rho_{\uparrow} + \frac{3}{4}\left[\frac{\lambda^2}{(\mathbf{H}_{\text{ex}} - \Delta_{\text{cf}})^2}\right]\rho_{\downarrow} \quad (6.13)$$

where Δ_{cf} denotes the crystal field splitting, \mathbf{H}_{ex} the exchange field splitting and λ is a constant proportional to the spin orbit coupling constant. From equation 6.13 the AMR in the two band model can be written as

$$\left[\frac{\Delta\rho}{\rho_0}\right]_{\parallel-\perp} = \gamma_{\text{eff}}(\chi - 1) \quad (6.14)$$

$$\text{where } \gamma_{\text{eff}} = \frac{-\gamma_{\downarrow\downarrow} + \gamma_{\uparrow\downarrow}\chi(1 + 4\delta) - 4\gamma_{\uparrow\uparrow}\chi\delta^2}{[1 + \delta(1 + \chi)][1 + \chi + 4\chi\delta]} \quad (6.15)$$

$$\chi = \frac{\rho_{\downarrow}}{\rho_{\uparrow}} \text{ and } \delta = \frac{\rho_{\uparrow\downarrow}}{\rho_{\downarrow}} \quad (6.16)$$

In the case of Fe_3O_4 which is a half metal, the Fermi energy is located in the minority $t_{2g\downarrow}$ band and a gap is formed in the majority band. Considering only the minority $t_{2g\downarrow}$ band and using the Equation 6.12 the AMR can be calculated as:

$$\left[\frac{\Delta\rho}{\rho_0}\right]_{\parallel-\perp} = \gamma_{\downarrow\downarrow} = -\frac{3}{4}\left[\frac{\lambda}{\Delta_{\text{cf}}^2}\right] \quad (6.17)$$

Using the value of $\Delta_{\text{cf}} = 1.75$ eV, $\lambda = 0.04$ for Fe_3O_4 [27] a value of AMR = -0.04% was obtained from equation 6.17 by Ziese [18]. He argued that since the observed value is too small and has the opposite sign to the experimental value (0.5% for current along $\langle 100 \rangle$ direction on a (001) oriented magnetite thin film grown on MgO (001) substrate), the contribution of majority $e_{g\uparrow}$ band has to be considered and consequently the band structure will be similar to Equations 6.14 and 6.15. The positive AMR means $\rho_{\parallel} > \rho_{\perp}$. Therefore a positive AMR contribution can be considered in low field magnetoresistance with ρ_{\parallel} increasing with the magnetisation component in the direction of the current and

ρ_{\perp} reducing. Although the contribution of AMR, which is very small, will be visible in the low field, it will be dominated by APB contribution in the high field.

The ordinary magnetoresistance (OMR) is due to the Lorentz force, which bends the conduction electrons away from the electric field direction, increasing the resistivity of a conductor with increasing magnetic field [28]. The magnitude of the OMR is proportional to the square of the magnetic induction \mathbf{B} ($\mathbf{B}=\mathbf{H}+4\pi\mathbf{M}$). The OMR contribution will be high in the beginning when the magnetization component in the perpendicular direction to the current is more than in the parallel direction and as the magnetisation component in the perpendicular direction decreases the OMR contribution also decreases.

Domain walls (DWs) are intriguing objects in ferromagnetic materials with electronic properties distinct from that of ferromagnetic domains. DW is an interface between uniformly magnetised regions (domains) with different magnetisation directions [29]. The length scale over which the magnetisation direction changes is determined by material parameters such as the exchange and magnetic anisotropy energies [29]. The scattering of spin polarised electrons while crossing the domain wall will give a resistivity contribution which will reduce with the annihilation of the domains with increasing field. Another important factor is reduction of spin polarization due to the DWs. Because of the small non-adiabaticity of the spin polarised electrons in traversing the wall, there is a possibility of mixing of the up spin and down spin channels within the domain walls which will reduce the resistance as the domain wall width increases [29]. So the domain wall resistance is expected to increase as the wall region is narrowed during the annihilation of the DWs. It is clear that, in the low field region during the annihilation of domain walls the wall width is expected to reduce and give a positive contribution to the MR.

Therefore it is evident from our discussion in the previous paragraphs that at low fields the positive contribution of AMR, OMR and domain wall magnetoresistance (DWMR) effects (which dominates the contribution from APB scattering) to the resistivity of the sample is prominent and shows a positive MR. After crossing the anisotropy fields the magnetization rotates and aligns with the field. Thereafter the APB scattering contribution to the MR dominates and shows a negative MR. The butterfly shape of the MR curve vanishes as the temperature is lowered through the Verwey transition. Figures

6.28 (a) (b) and (c) shows the magnetization curves obtained for a 200 nm film above, at, and below the Verwey transition temperature (T_v) with field directed along $\langle 001 \rangle$ direction. The curves above T_v show a hard axis behaviour and below T_v show an easy axis behaviour. So it is evident from our data that near T_v , there is a hard axis to easy axis transition taking place in the $\langle 001 \rangle$ direction. Figures 6.29 (a), (b) and (c) show the same magnetization curves but with the field directed along the $\langle \bar{1}10 \rangle$ direction: no transition is observed. The switching of the magnetisation direction in Fe_3O_4 during the Verwey transition is related to the changes in sign of the anisotropic constants and associated structural phase transition from cubic to monoclinic phase [30]. There are previous reports on the sign change of anisotropic constant K_1 for (100) oriented magnetite thin films during the Verwey transition [4,31]. In the cubic phase the magnetocrystalline anisotropy energy is given by

$$E_K = K_0 + K_1 s + K_2 \alpha_1^2 \alpha_2^2 \alpha_3^2 \quad (6.18)$$

where s is same parameter used in Equation 6.5 and α_i are the direction cosines of the magnetisation with crystallographic axes. Since \mathbf{R}_3 and \mathbf{R}_4 are expansion coefficients of $\Delta\rho/\rho$ in s (Equation 6.5) and \mathbf{K}_1 is the expansion coefficient of anisotropy energy in s , we can consider that \mathbf{R}_3 and \mathbf{R}_4 are proportional to \mathbf{K}_1 and cause the sign change of the anisotropic magnetoresistance in the equation 6.8, which implies

$$\left[\frac{\Delta\rho}{\rho} \right]_{\perp} = \frac{\mathbf{R}_3}{2} < \left[\frac{\Delta\rho}{\rho} \right]_{\parallel} = \frac{2\mathbf{R}_1}{3} - \frac{\mathbf{R}_3}{4} + \frac{2\mathbf{R}_4}{3} \quad (6.19)$$

Therefore below the Verwey transition the AMR has a negative sign and will cause the resistance to decrease with field. The OMR contribution will be less because of the small component of magnetisation in the direction perpendicular to the direction of current of $\langle 001 \rangle$. Thus the change from hard axis to easy axis in the $\langle 001 \rangle$ direction clearly explains the observed change in the behaviour of MR curves while passing through Verwey transition. The hard axis to easy axis transition along with the Verwey transition could be one of the reasons for the high MR observed in the $\langle 001 \rangle$ direction compared to the $\langle \bar{1}10 \rangle$ direction.

The main factor governing the MR behaviour at high fields is antiferromagnetic coupling of Fe ions across the APBs. In chapter 2 we have

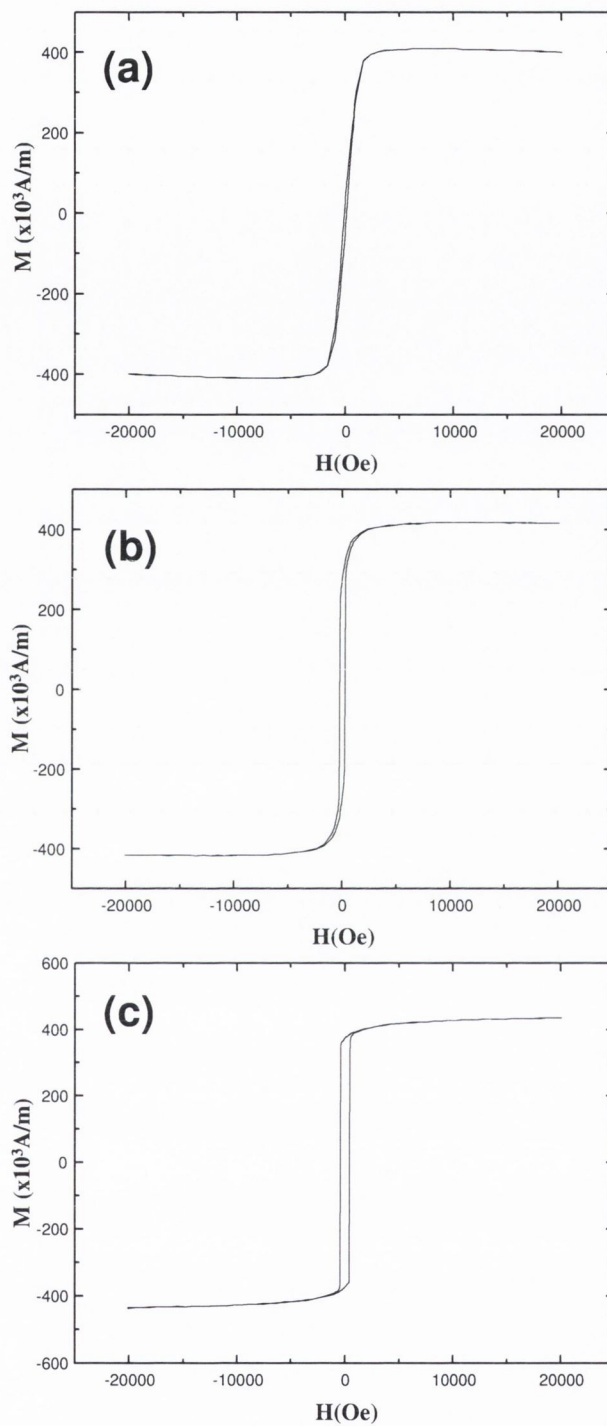


Figure 6.28 magnetization curves obtained for a 200nm film at (a) $T=150\text{K}$ at (b) $T_V=116\text{K}$ and (c) $T=90\text{K}$ (T_V Verwey transition temperature) with field directed along the $\langle 001 \rangle$ direction.

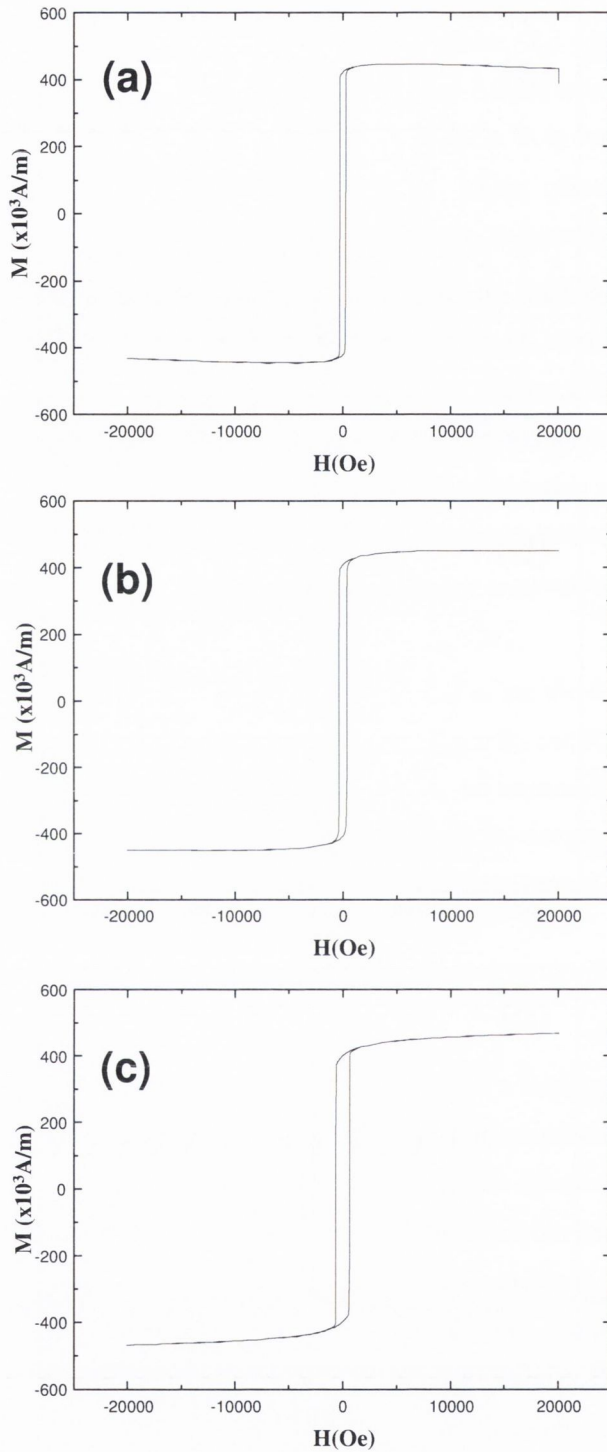


Figure 6.29 magnetization curves obtained for a 200nm film at (a) $T=150\text{K}$ (b) $T_v=116\text{K}$ and (c) $T=90\text{K}$ (T_v Verwey transition temperature) with field directed along the $\langle 110 \rangle$ direction.

shown that the prominent antiferromagnetic exchange across APBs is the 180° Fe-O-Fe strong antiferromagnetic super exchange. From Figure 6.23 it is clear that APBs formed due to the $1/2\langle 001 \rangle$ type of shift towards $\langle 001 \rangle$ direction give a 108° Fe-O-Fe antiferromagnetic super exchange but not in the $\langle \bar{1}10 \rangle$ direction due to the $1/4\langle 111 \rangle$ type of shifts. So we can expect more strong antiferromagnetically coupled APBs in the $\langle 001 \rangle$ direction compared to the $\langle \bar{1}10 \rangle$ direction. This difference could be one of the reasons for the difference in the MR along these two directions, and the higher MR along $\langle 001 \rangle$ direction. Another factor to look at is the APB formation due to strain relaxation. In chapter 4 it was demonstrated that APBs can be formed due to the misfit dislocations produced by strain relaxation in Fe_3O_4 films grown on MgAl_2O_4 substrates. The same model can be applied for Fe_3O_4 (110) films grown on MgO (110) substrates also, since the films show a partial strain relaxation. Figure 6.30 shows the possible APB formation due to misfit dislocations. Figure 6.30 (a) shows the formation of a misfit dislocation due to a missing row of oxygen atoms so that the strain is released in $\langle \bar{1}10 \rangle$ direction. It is clear that no APB is formed across the dislocation line.

It is clear from Figure 6.30(b) that the APB is formed across the dislocation line. Therefore from this analysis we can show that density of APBs formed due to the misfit dislocation will be more in the direction $\langle 001 \rangle$ than the $\langle \bar{1}10 \rangle$. Also it is clear from the analysis that there exists 180° Fe-O-Fe antiferromagnetic superexchange across these APBs formed along $\langle 001 \rangle$ direction. The presence of these high density of antiferromagnetically coupled APBs could be the reason for lower value of M_s obtained for 200nm film.

Another important aspect to look at is the effect of strain in the spin polarisation. In Fe_3O_4 , the high conductivity results only from the partially filled minority-spin Fe (B-site) 3d band. This band is dominated by three off-axial $3d-t_{2g}$ orbitals, which is consistent with the geometry of the spinel structure that the conducting B-site strings are along the six off-axial $\langle 110 \rangle$ directions. For the majority spin, the Fe (B-site) $3d-e_g$ band, which is characterized by insignificant overlaps between axial e_g orbitals of the nearest Fe (B-site) neighbors, is 0.14 eV below the Fermi level with relatively narrow bandwidth. This results in an insulating majority spin with a band gap of 0.54 eV at the Fermi level, being the same order of magnitude as that of many semiconductors.

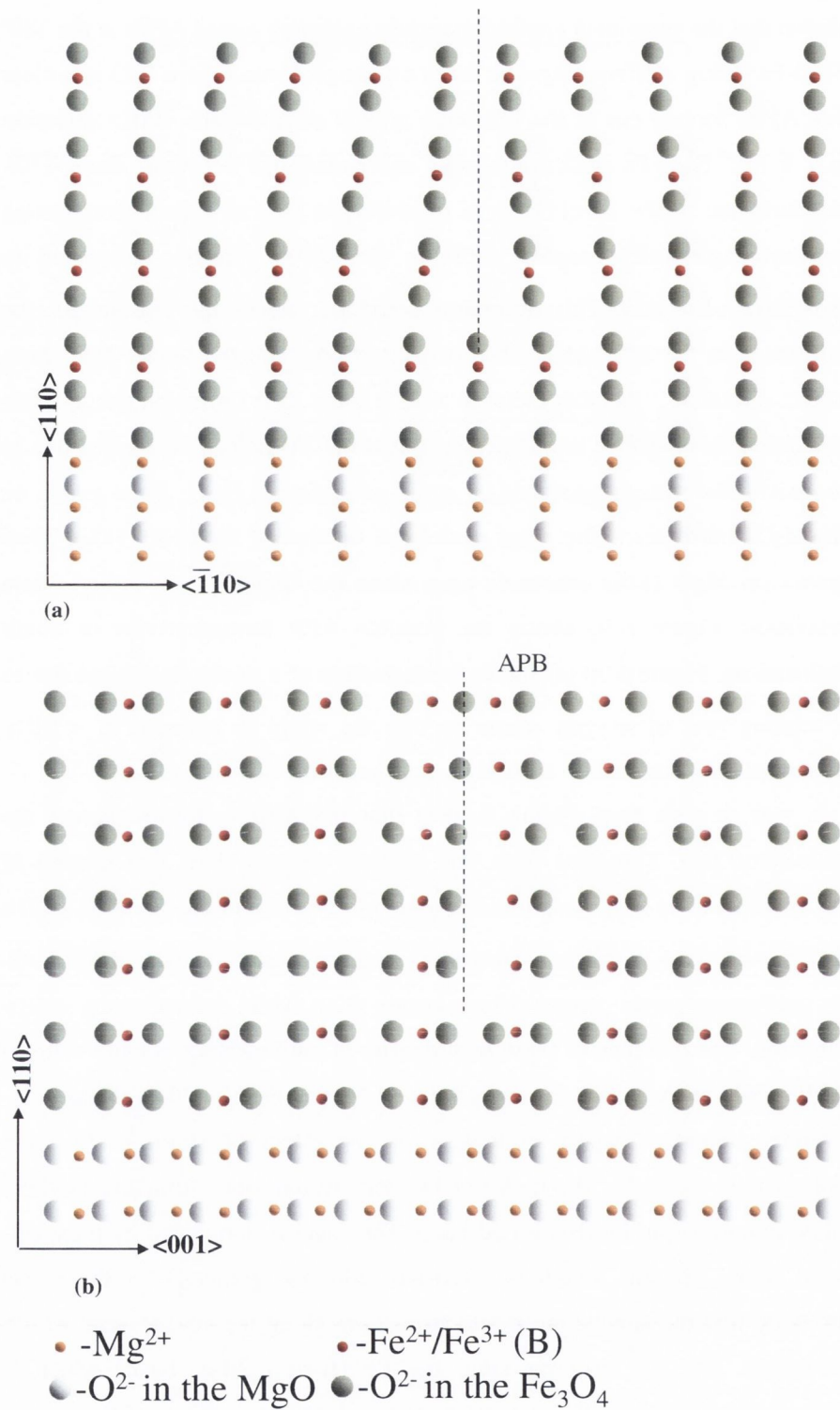


Figure 6.30 (a) Formation of a misfit dislocation due to a missing row of oxygen so that strain is released in $\langle \bar{1}10 \rangle$ direction. There is no APB formation. (b) formation of misfit dislocation due to a missing row of oxygen so that strain is released in the $\langle 001 \rangle$ direction, and leading to the formation of APB.

Jeng et al [32] have calculated the electronic structure and magnetocrystalline anisotropy energies of Fe_3O_4 under both compressive and extensive strains along $\langle 001 \rangle$ direction from first principles by using the linear muffin-tin orbital (LMTO) method. It is found that uniaxial strain has significant effects on both the electronic structure and magnetocrystalline anisotropy of magnetite. Compared to the unstrained state, the most visible change in the strained state is in the majority-spin Fe (B-site) $3d-e_g$ band near the Fermi level and the minority-spin Fe (B-site) $3d-e_g$ band between 1 and 2.5 eV. For the majority spin, the width of the Fe (B-site) $3d-e_g$ band becomes larger under both strains (compressive as well as extensive) and the band top exceeds the Fermi level and almost touches the lower edge of the upper A-site $3d-e_g$ band. For the minority spin, all band edges already overlap and form a large conduction band for both the strains. In particular, as the strain is applied, the insulating band gap of the majority spin is reduced due to the broadening of the B-site Fe 3d band and the half-metallic behaviour of the cubic magnetite eventually turns into normal metal behaviour in the high-strain states or, in other words, the spin polarization is affected by the strain. There are several recent calculations on the surface electronic structure of the Fe_3O_4 [33, 34, 35] and Fe_3O_4 (111)/MgO (111) interface [36], indicating the modification of surface electronic band structure due to the various surface reconstructions. The density functional theory (DFT) calculation by Fonin et al. [33] shows that Jahn-Teller distortion of the surface atoms of Fe_3O_4 (100) surface is opening a band gap in the majority spin channel between -0.4 eV and -0.1 eV. This depletion of states in the majority spin channel is accompanied by occupation of states in the minority spin channel, which is referred as spin flip, resulting in a substantial reduction of the magnetic moments of the surface Fe(B) atoms. Therefore the calculation gives the evidence for a half-metal to metal transition at the Fe_3O_4 (100) surface. The electronic states in the majority spin-channel responsible for the reduction of spin polarization are dominated by dx^2-y^2 states of surface Fe (B). Similar results are obtained using *ab initio* calculations, which indicates the substantial reduction in the magnetic moment and half metal to metal transition at the Fe_3O_4 (100) [34] and Fe_3O_4 (111) [35] surface due to the surface atomic relaxations. The DFT calculation of the electronic structure predict strong bonding across the polar oxide interface of

Fe_3O_4 (111)/MgO (111), with metallic states present in the band gap of the O interface layers [36].

In (110) oriented Fe_3O_4 thin films the amount of strain will be different along two crystallographically different directions such as $\langle 001 \rangle$ and $\langle \bar{1}10 \rangle$ directions. Moreover in our case the films are partially strain relaxed. 200nm and 90 nm films show 12% and 18% more relaxation along $\langle 001 \rangle$ direction compared to $\langle \bar{1}10 \rangle$ direction. As per the above discussion, the anisotropic strain in these directions should be affecting the extent of spin polarisation. A higher degree of spin polarization along with high density of antiferromagnetically coupled APB formation along $\langle 001 \rangle$ direction compared to $\langle \bar{1}10 \rangle$ direction, could lead to the observed MR anisotropy and enhanced MR along $\langle 001 \rangle$ direction.

6.4 Conclusion

A detailed study of strain relaxation behaviour and crystallographic direction dependence of MR in (partially strain relaxed) Fe_3O_4 (110) films having different thickness grown on MgO (110) substrates has been carried out. The high resolution XRD measurements and Raman measurements show that the films are partially strain relaxed. The relaxation found increases with increasing thickness. The amount of relaxation is found to be 12% and 18% higher in the $\langle 001 \rangle$ direction compared to $\langle \bar{1}10 \rangle$ direction for the 200 nm and 90 nm films and showed 30% less relaxation along $\langle 001 \rangle$ direction compared to $\langle \bar{1}10 \rangle$ direction for the 60nm film. Fe_3O_4 (110) films grown on MgO (110) substrates can form APBs. Our analysis shows that there is 40% higher probability in the formation of APBs in (100) oriented Fe_3O_4 films grown on MgO (100) compared to (110) oriented films grown on MgO (110) substrates. This low probability of formation of APBs could be one of the reasons for the observation of partial strain relaxation in (110) oriented films. The room temperature magnetization along the $\langle \bar{1}10 \rangle$ easy axis direction shows kinks which are prominent for films with lower thickness and diminishes as the thickness is increased. This is attributed to the different coercivity arising from strained and partially relaxed volume fractions. There is a possibility of a contribution from stoichiometrically different volume

fractions in lower thickness films due to the possible oxidation which is evident from the observation of additional Raman Bands in the Raman spectrum and lower out of plane lattice constant measured from HRXRD measurements for the 20nm film.

Magnetoresistance measurements show different behaviour in $\langle 001 \rangle$ and $\langle \bar{1}10 \rangle$ directions. The MR along $\langle 001 \rangle$ directions shows a butterfly shaped curve above the Verwey temperature and changes shape through the Verwey transition. The observation of butterfly shaped curves are attributed to the AMR, OMR and DWMR effects which dominate the MR contribution of APBs at low fields. At high fields the contribution of APBs to MR dominates and resistance decreases with increasing field. The low temperature magnetization measurements show that there exists a hard axis to easy axis transition in the $\langle 001 \rangle$ direction, whereas in the $\langle \bar{1}10 \rangle$ direction it is not observed. The 200 nm film showed 9.5% MR at Verwey transition ($T_v = 116$ K). This value of MR% is found to be 5.5% higher than the MR% measured along the $\langle \bar{1}10 \rangle$ direction and to MR values reported for Fe_3O_4 films with various orientations and thicknesses at 1 Tesla field, apart from the films deposited on vicinal MgO substrates.

The formation of APBs during the growth due to the symmetry difference is analysed. The analysis shows that the APBs formed in the $\langle 001 \rangle$ direction forms 180° Fe-O-Fe antiferromagnetic superexchange but not in the $\langle \bar{1}10 \rangle$ direction. This could give a higher density of antiferromagnetically coupled APBs in the $\langle 001 \rangle$ direction than in the $\langle \bar{1}10 \rangle$ direction and could be one of the reasons for the high MR along the $\langle 001 \rangle$ direction. Possibilities of formation of APBs with misfit dislocations are explored. The analysis shows that the misfit dislocations in the $\langle 001 \rangle$ direction will lead to the formation of APBs while misfit dislocations along $\langle \bar{1}10 \rangle$ will not. This eventually will increase the APB density along $\langle 001 \rangle$ direction compared to the $\langle \bar{1}10 \rangle$ direction. The spin polarized electron transport across the antiferromagnetically coupled APBs formed along $\langle 001 \rangle$ direction, could be one of the reasons for the observation of higher MR values. Another possible explanation for MR anisotropy is the strain induced modification of band structure of Fe_3O_4 films. Jeng et al [32] have calculated the electronic structure and magnetocrystalline anisotropy energies of Fe_3O_4 under both compressive and extensive strains

along $\langle 001 \rangle$ direction from first principles by using the linear muffin-tin orbital (LMTO) method and it was found that, as the strain is applied, the insulating band gap of the majority spin is reduced due to the broadening of the B-site Fe 3d band and the half-metallic behaviour of the cubic magnetite eventually turns into normal metal behaviour in the high-strain states or, in other words, the spin polarization is reduced by the strain. (110) oriented Fe_3O_4 films grown on MgO (110) substrates show partial strain relaxation and the percentage relaxation is found to be higher in $\langle 001 \rangle$ direction compared to $\langle \bar{1}10 \rangle$ direction in 200nm and 90 nm films. A difference in spin polarization due to anisotropic strain along with high density of antiferromagnetically coupled APB formation due to strain relaxation induced misfit dislocations could be another reason for the enhancement of MR observed in the $\langle 001 \rangle$ direction compared to $\langle \bar{1}10 \rangle$ direction. Films with lower thickness showed switching behaviour in the MR curves measured along the $\langle \bar{1}10 \rangle$ direction, which diminished with increasing thickness. This is related to the different coercivity values within the film, which were reflected in the magnetization curves as kinks.

Bibliography

- [1] H. Matsuda, S. Okamura, T. Shiosaki, H. Adachi and H. Sakakima, *J. Appl. Phys.*, **98**, 063903(2005).
- [2] H. Matsuda, M. Takeuchi, H. Adachi, M. Hiramato, N. Matsukawa, A. Odagawa, K. Setsune and H. Sakakima. *Jpn. J. Appl. Phys.* **41** L387(2002)
- [3] H. Matsuda, H. Sakakima, H. Adachi, A. Odagawa and K. Setsune, *J. Mater. Res.*, **17**, 1985(2002).
- [4] D. T. Margulies, F. T. Parker, F. E. Spada, R. S. Goldman, J. Li, R. Sinclair, and A. E. Berkowitz, *Phys. Rev.* **53**, 9175 (1996).
- [5] S. P. Sena, R. A. Lindley, H. J. Blythe, Sauer Ch, M. Al-Kafarji and G. A. Gehring, *J. Magn. Magn. Mater.* **176**, 111(1997). **97**, 10D315 (2005)
- [6] R.G.S Sofin, S K Arora and I.V Shvets *J. Appl. Phys*
- [7] S K Arora, R.G.S Sofin and I.V Shvets *Phys. Rev. B*, **72**, 134404 (2005).
- [8] D.T. Margulies, F.T. Parker, M.L. Rudee, F.E. Speda, J.N. Chapman, P.R. Aitchison and A.E. Berkowitz. *Phys. Rev. Lett.* **79**, 5162 (1997).
- [9] F.C Voogt, T.T.M. Palstra, L. Niesen, O.C. Rogojanu, M.A. James and T. Hibma, *Phys. Rev. B*. **57**, 08107 (1998).
- [10] T. Hibma, F.C. Voogt, L. Niesen, P.A.A. van der Heijden, W.J.M. de Jonge, J.J.T.M. Donkers, P.J. van der Zaag, *J. Appl. Phys*, **85**, 5291 (1999).
- [11] P.W. Anderson and H. Hasegawa, *Phys. Rev.* **100**, 675 (1955).
- [12] K. Kubo and N. Ohata, *J. Phys. Soc. Japan* **33**, 21 (1972).
- [13] W. Eerenstein, T.T.M. Palstra, S.S. Saxena and T. Hibma *Phys. Rev. Lett.* **88**, 247204(2002).
- [14] T. R. McGuire and R. I. Potter, *IEEE Trans. Magn.* **MAG-11**, 618 (1973).
- [15] J. Smit, *Physica (Amsterdam)* **16**, 612 (1951)
- [16] R. I. Potter, *Phys. Rev. B* **10**, 4626 (1974).
- [17] R. P. van Gorkom, J. Caro, T. M. Klapwijk, and S. Radelaar, *Phys. Rev. B* **63** 134432 (2001).
- [18] M. Ziese, *Phys. Rev. B* **62**, 1044 (2000).
- [19] N. F. Mott. *Proc. Royal Soc. London* **153A**, 699 (1936).
- [20] I.A Canobell, A. Fert, and O. Jaoul, *J. Phys.* **C 3**, S 95 (1971)]
- [21] O. Jaoul, I.A. Campbell and A. Fert, *J. Magn. Magn. Mater.* **5**, 23 (1977).

- [22] R.I. Potter, Phys. Rev. B 10 4626 (1974).
- [23] A.P. Malozemoff, Phys. Rev. B. 34, 1853 (1986).
- [24] Y. Suzuki, H.Y. Hwang, S-W. Cheong, and R.B van Dover Appl. Phys. Lett. **71** 140(1997)
- [25] J O'Donnell, M. Onellion, M.S. Rzechowski, J.N. Eckstein and I Bosovic, Appl.Phys Lett. **72**,1775(1998).
- [26] K Steenbeck and R Hiergeist Appl.Phys Lett.**75**,1778(1999)
- [27] S.F Alvarado, M. Erbudak and P. Munz, Phys. Rev. B **14**,2740 (1976).
- [28] J. P. Jan, Solid State Phys. **5**, 1 (1957).
- [29] A.D Kent, J. Yu, U. Rudiger and S.S.P. Parkin, J. Phys: Condens. Matter, **13** R461 (2001).
- [30] B. A. Calhoun, Phys. Rev. **94**(6),1577 (1954).
- [31] M. Ziese and H.J Blythe, J. Phys: Condens. Matter, **12** 13 (2000).
- [32] Horng-Tay Jeng and G. Y. Guo, Phys. Rev. B **65**, 094429 (2002).
- [33] M. Fonin, R. Pentcheva, Yu. S. Dedkov, M. Sperlich, D. V. Vyalikh, M. Scheffler, U. Rüdiger and G. Güntherodt, Phys. Rev. **72**,104436 (2005)
- [34] C. Cheng, Phys. Rev. **71**, 52401 (2005)
- [35] L. Zhu, K. L. Yao and Z. L. Liu. Phys. Rev. **74**, 35409 (2006)
- [36] V. K. Lazarov, M. Weinert, S. A. Chambers, and M. Gajdardziska-Josifovska, Phys. Rev. **72**, 195401 (2005)

*One thing I have learned in a long life: that all our science,
measured against reality, is primitive and childlike –and yet it is the
most precious thing we have*

Einstein 1951

Chapter 7

Conclusions

Magnetite, Fe_3O_4 is a common and stable half metallic oxide. Due to its relatively high Curie Temperature (T_C) and its electronic properties, Fe_3O_4 , represents one of the promising materials for spin electronic devices. Most of these applications will employ this material in the form of thin films. To realise these applications, one requires good control over the stoichiometry and precise knowledge of the strain status of the films. The stoichiometry, strain, defect structure etc are expected to play a crucial role in determining the magneto-transport and magnetic properties of Fe_3O_4 films. MgO is an ideal substrate for epitaxy of magnetite (Fe_3O_4) because the difference in oxygen sub-lattice size of MgO and Fe_3O_4 gives a small lattice mismatch of 0.33%. There are two distinct forms of symmetry breaking in $\text{Fe}_3\text{O}_4/\text{MgO}$ hetero-epitaxy. The first one is due to the fact that the lattice parameter of MgO is half that of Fe_3O_4 leading to disruption of translation symmetry. The other one is due to the reason that Fe_3O_4 ($\text{Fd}\bar{3}\text{m}$) crystal structure is lower in symmetry than MgO ($\text{Fm}\bar{3}\text{m}$). As a result, MgO rotated by 90° about an axis perpendicular to the interface falls in itself but Fe_3O_4 does not. This leads to the formation of antiphase boundaries, APBs. The details of the formation of APBs are discussed in chapter 2.

During epitaxial growth, the unit cell of a thin film can distort due to elongation or compression of in-plane lattice constants in the orthogonal directions depending on the sign of the lattice mismatch. When such occurs the epitaxial system is said to be in a 'strained state'. Theoretical models predict that epitaxial systems with smaller mismatch will remain in a strained state

until a critical film thickness (t_c) is reached and thereafter it will undergo relaxation by generating misfit dislocations. It has been previously reported that Fe_3O_4 films grown on MgO (100) show sluggish strain relaxation behaviour, relaxing partially well above the critical thickness of strain relaxation. Even for a thickness of $6.6 \mu\text{m}$ the relaxation was partial. However, no effort was made to understand the origin of this behaviour. MgAl_2O_4 has the normal spinel structure and the lattice constant is 0.80831 nm . For the $\text{Fe}_3\text{O}_4/\text{MgAl}_2\text{O}_4$ system the lattice mismatch is much greater (3.9%) and films are found to be relaxed in agreement with the theoretical models. Since MgAl_2O_4 has the same spinel type crystal structure and symmetry as Fe_3O_4 , the formation of APBs is not expected for films grown on MgAl_2O_4 . However, the presence of the APBs in the $\text{Fe}_3\text{O}_4/\text{MgAl}_2\text{O}_4$ system has been reported previously. The differences in crystal structure and symmetry of the MgO and MgAl_2O_4 substrates with Fe_3O_4 prompted us to look at the strain relaxation behaviour of Fe_3O_4 films grown on the substrates which will essentially provide information about the role of crystal structure symmetry difference on the strain relaxation behaviour. This information will be very useful in the design of future spin electronic devices and nano-structures based on magnetite.

In chapter 4 we presented the details of our investigations on anomalous strain relaxation behaviour of (100) oriented Fe_3O_4 films grown on MgO (100) and non-anomalous strain relaxation behaviour of (100) oriented Fe_3O_4 films grown on MgAl_2O_4 (100) substrates. From the strain relaxation studies of epitaxial Fe_3O_4 thin films grown on MgO (100) and MgAl_2O_4 substrates we infer that the films grown on MgO (100) substrate remain fully coherent up to much greater thickness than predicted by the Fischer, Kuhne and Richter (FKR) model ($\sim 70 \text{ nm}$), whereas the films grown on MgAl_2O_4 substrates shows a behaviour consistent with the model predictions. The observed strain relaxation behaviour is attributed to the differences in the crystal structure symmetry between MgO and Fe_3O_4 . Due to the lower crystal symmetry of the spinel structure of Fe_3O_4 compared to that of MgO , APBs are formed and lead to the formation of areas within the film that have opposite sign of stress. The stress compensation by the APBs reduces the effective stress experienced by the films. The reduction in effective stress experienced by the film depends strongly on the nature and density of the APBs. Even though

APBs are not expected in Fe_3O_4 films grown on MgAl_2O_4 , TEM studies revealed the presence of APBs. We suggest that these APBs are formed not because of symmetry difference but because of the stacking faults generated by strain relaxation due to large mismatch between the thin film and substrate.

The presence of antiphase boundaries (APBs) in epitaxial Fe_3O_4 films introduces local structural modifications and alters the magnetic interactions at the boundary, making them predominantly antiferromagnetic. This strongly affects the magnetic and electronic properties of the epitaxial Fe_3O_4 films. The magnetoresistance (MR) behaviour of magnetite thin films has been widely studied before in films on different substrates like MgO and MgAl_2O_4 . Compared to bulk magnetite, epitaxial Fe_3O_4 films show a greater MR which is difficult to saturate even in strong magnetic fields. So far, the magnitude of MR observed in epitaxial films has not exceeded 8% for a magnetic field strength of 2 Tesla. The unusual MR behaviour of Fe_3O_4 films is attributed to the spin-polarized transport across the antiferromagnetically coupled APBs. This model predicts a large MR effect across a single boundary. However, due to the random network of APBs obtained in $\text{Fe}_3\text{O}_4/\text{MgO}$ hetero-epitaxy, this effect is greatly smeared and it is not possible to obtain any quantitative information.

In chapter 5 we present the details of a new approach which allows for a selective extraction of the contribution of the antiphase boundaries from the total MR. In our study the MgO substrate has a miscut with respect to a low-index plane (100). If annealed under suitable condition, the presence of miscut facilitates the formation of surfaces with atomic height steps. In this case the islands of Fe_3O_4 forming at different atomic terraces nucleate independently from each other. Consequently, as the nucleation islands grow there is a significant chance that antiphase boundaries are formed along the step edges of the atomic terraces. Our results showed a strong anisotropy in the MR in close correlation with the direction of current and step-edges in epitaxial Fe_3O_4 films grown on vicinal MgO (100) substrates. Magnetization measurements clearly demonstrate the formation of a greater number of antiferromagnetically coupled antiphase boundaries due to the presence of step edges present in a vicinal substrate. We describe two mechanisms for the observed difference in MR along two equivalent crystallographic directions on the surface. The first one is based on spin dependent electron scattering along the APBs. The second

mechanism suggests a difference in the reduction of magnetisation values along and across the APBs resulting from the difference in magnetoelastic properties. Magnetoresistance properties of epitaxial Fe_3O_4 films on vicinal MgO substrate show a direct dependence on the substrate annealing duration. The increased annealing time (5-9 hours) significantly modifies the surface morphology MgO substrate and inturn provides a better template for the formation of APBs in the deposited Fe_3O_4 thin films. Further increase in annealing time (13 hours) leads to a slight decrease in MR which could be due to impurity segregation on the surface.

In chapter 6 we presented a detailed study of the strain relaxation behaviour and crystallographic direction dependence of MR in Fe_3O_4 (110) films having different thickness grown on MgO (110) substrates. The high resolution XRD measurements and Raman measurements show that the films are strain relaxed. The relaxation is found to increase with increasing thickness. Fe_3O_4 (110) films grown on MgO (110) substrates can form APBs. The adjacent monolayers can be related by three shift vectors which are $\sqrt{3}/2 \langle \bar{1}11 \rangle$ or $\sqrt{3}/2 \langle \bar{1}\bar{1}\bar{1} \rangle$ shift vectors in the $\langle \bar{1}10 \rangle$ direction and by $1/2 \langle 001 \rangle$ shift vectors in the $\langle 001 \rangle$ direction, whereas on a MgO (100) surface there can be 7 possible shift vectors which eventually form APBs. Therefore there is a 40% higher probability of the formation of APBs in (100) oriented Fe_3O_4 films grown on MgO (100) compared to (110) oriented films grown on MgO (110) substrates. This low probability of formation of APBs could be one of the reasons for the observation of relaxation in (110) oriented films.

Magnetoresistance measurements show different behaviour in $\langle 001 \rangle$ and $\langle \bar{1}10 \rangle$ directions. The MR along $\langle 001 \rangle$ directions shows a butterfly shaped curve above the Verwey temperature and changes shape thorough the Verwey transition. The observation of butterfly shaped curves are attributed to the AMR, OMR and DWMR effects which dominates the MR contribution of APBs at low fields. At high fields the contribution of APBs to MR dominates and resistance decreases with increasing field. The low temperature magnetization measurements show that there exists a hard axis to easy axis transition in the $\langle 001 \rangle$ direction whereas in the $\langle \bar{1}10 \rangle$ direction it is not observed. The 200nm film showed 9.5% MR at Verwey transition ($T_v = 116$ K). This value of MR is found to be 5.5% higher compared to the MR

measured along $\langle \bar{1}10 \rangle$ direction and to MR values reported for Fe_3O_4 films with various orientations and thicknesses at 1 Tesla field apart from the films deposited on vicinal MgO substrates.

The possibilities of formation of APBs with misfit dislocations were explored. The analysis shows that the misfit dislocations in the $\langle 001 \rangle$ direction will lead to the formation of APBs while misfit dislocations along the $\langle -110 \rangle$ will not. This eventually will increase the APB density along $\langle 001 \rangle$ direction compared to $\langle \bar{1}10 \rangle$ direction. The reduced M_s along the $\langle 001 \rangle$ direction compared to $\langle \bar{1}10 \rangle$ is direct evidence for the formation of a higher density of APBs along the $\langle 001 \rangle$ direction. The spin polarized electron transport across the antiferromagnetically coupled APBs formed along the $\langle 001 \rangle$ direction could be one of the reasons for the observation of higher MR values. Another possible explanation for MR anisotropy is the strain induced modification of band structure of Fe_3O_4 films. Recently reported band structure calculations show that, as the strain is applied, the insulating band gap of the majority spin is reduced due to the broadening of the B-site Fe 3d band and the half-metallic behaviour of the cubic magnetite eventually turns into normal metal behaviour in the high-strain states or, in other words, the spin polarization is reduced by the strain. (110) oriented Fe_3O_4 films grown on MgO (110) substrates show partial strain relaxation and the percentage relaxation is found to be higher in the $\langle 001 \rangle$ direction compared to the $\langle \bar{1}10 \rangle$ direction in 200nm and 90 nm films. A difference in spin polarization due to anisotropic strain along with high density of antiferromagnetically coupled APB formation due to strain relaxation induced misfit dislocations could be another reason for the enhancement of MR observed in the $\langle 001 \rangle$ direction compared to the $\langle \bar{1}10 \rangle$ direction. Films with lower thickness showed switching behaviour in the MR curves measured along the $\langle \bar{1}10 \rangle$ direction, which is found to diminish with increasing thickness. This is related to the different coercivity values within the film which was reflected in the magnetization curves as kinks.

Future work

Our investigations demonstrate that Fe_3O_4 films deposited on vicinal MgO (100) substrates show an enhancement and anisotropy of magnetoresistance (MR). The increase in the low field MR due to the step induced spin scattering in Fe_3O_4 films is an important result to realize future spin-electronics applications of magnetic nano-structures. Antiphase boundaries are expected to form in various other spinel materials as well as numerous non-spinel films provided the substrate for the epitaxial film growth is chosen correctly. Therefore, we suggest that the observed increase in magnetoresistance is not necessarily limited to magnetite films only. It is likely that magnetoresistance of some other epitaxial films could be enhanced in the same way if the films are grown on vicinal substrates and the pattern of antiphase boundaries with preferential orientation is formed. Our study suggests that as the angle of miscut of the vicinal substrate is increased the density of APBs increases. In our study we were not able to optimise the growth of stoichiometric magnetite on vicinal MgO substrates with high miscut angles ($>5^\circ$). The films didn't show the Verwey transition and structural characterisation with high resolution XRD showed a higher Fe to O ratio than that of Fe_3O_4 . It is a very important aspect to study the growth process of magnetite or other oxides on high vicinal substrates and its implications on the physical properties of the thin films deposited.

Though Fe_3O_4 films deposited on vicinal substrates show a clear enhancement and anisotropy in MR at low temperature, the room temperature MR is less than 2%. To explore these results in an application point of view, a different approach has to be considered. One of the different possible approaches to construct a magneto-resistive medium is by depositing a ferromagnetic or a ferrimagnetic layer A on a non-magnetic vicinal substrate S and further deposition of a partially closed or fractional layer B of a non magnetic material above A, as shown in Figure 7.1. The first magnetic layer A is deposited in such a way that the top surface of the layer retains the step structure and will form a vicinal surface for the growth of the fractional non-magnetic layer B (spacer layer) which covers only a part of the magnetic layer and will form a nanowire aligned along the step edges. Then a further

antiferromagnetic layer C is deposited above the spacer nanowire B and uncovered magnetic layer A. In this way the magnetic layer A can be divided into two portions A1 and A2. Here layer A2 is exchange coupled to antiferromagnetic layer C unlike A1 which is separated from layer C by a spacer layer B. Therefore, magnetization of the layer A2 is pinned unlike the magnetization of the layer A1. This will lead to a situation where the spin polarized current through the layer A1 and A2 will find more spin scattering centers at the interfaces of A1 and A2 (when the spins in both sections are antiferromagnetically aligned) providing a high resistance path. By aligning the spins in A1 and A2 with an external magnetic field the resistance can be drastically reduced which essentially gives rise to a higher MR. The materials and growth parameters will need to be optimized to get the desired effect.

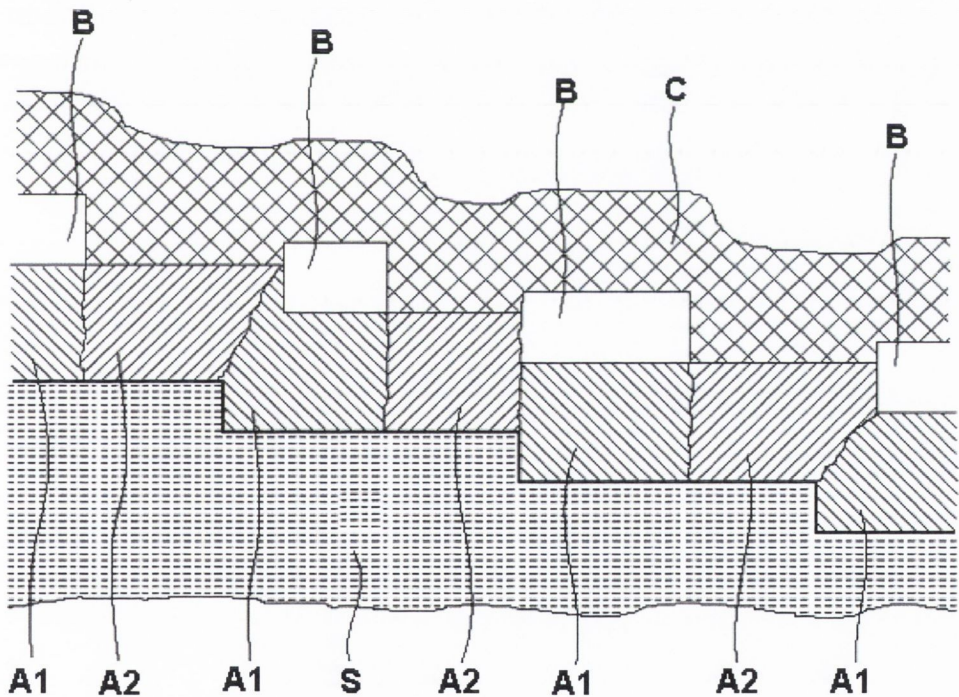


Figure 7.1. Cross sectional view of the proposed magneto-resistive medium.

Our studies on (110) oriented Fe_3O_4 films grown on MgO (110) showed a very high magnetoresistance at Verwey temperature in $\langle 001 \rangle$ direction compared to $\langle -110 \rangle$ direction. This observed magnetoresistance is

higher than any other reported values of MR for Fe_3O_4 films at 1T field except for the films grown on vicinal substrate. The higher MR is attributed to the spin polarized electronic transport across the antiferromagnetically coupled APBs which are generated by misfit dislocation due to strain relaxation. The reduction in spin polarization due to the strain driven band structure modifications is another reason for the MR anisotropy. It should be feasible to study the magneto transport properties of Fe_3O_4 films grown on (110) oriented vicinal MgO substrates that will increase the APB density and hence the MR value. A detailed structural characterisation can be done using the high resolution TEM which will give more insight to the formation of APBs and the anisotropic APB density.

Previous band structure calculations of Fe_3O_4 ignored the presence of defects, especially the oxygen vacancies [1, 2, 3]. Physical properties of magnetite can be greatly affected by the change in stoichiometry or by the presence of crystal defects. Creation of one oxygen vacancy at the B site can create one Fe^{2+} ion. This should affect the properties like electrical conduction in magnetite. It is worth pursuing a systematic study on the effect of defects and off stoichiometry in magnetite thin films as well as bulk samples.

Bibliography

- [1] Z. Zhang and S. Satpathy, Phys. Rev. B **44**, 319 (1991)
- [2] V. N. Antonov, B. N. Harmon, and V. P. Antropov, A. Ya. Perlov, and A.N. Yaresko, Phys. Rev. B **64**, 134410 (2001)
- [3] P. W. Anderson, Phys. Rev. B **102**, 1008 (1956)

A scientist is a mimosa when he himself has made a mistake and a roaring lion when he discovers a mistake of others

Einstein